PERMEABILITY MODELING OF ENGINEERING TEXTILES USED IN COMPOSITE MATERIALS

Mohamed Karaki

THESE

Pour l'obtention du grade de

DOCTEUR DE :

L'UNIVERSITÉ DE TECHNOLOGIE DE TROYES

SPÉCIALITÉ : MATÉRIAUX, MÉCANIQUE, OPTIQUE ET NANOTECHNOLOGIE

Mohammad KARAKI

14 Décembre 2017

PERMEABILITY MODELING OF ENGINEERING TEXTILES USED IN COMPOSITE MATERIALS

MODÉLISATION DE LA PERMÉABILITÉ DES TISSUS À BASE DE NAPPES TISSÉES POUR MATÉRIAUX COMPOSITES

JURY

SOULAT Damien	Professeur des Universités	Rapporteur
SOBOTKA Vincent	Professeur des Universités	Rapporteur
AYAD Rezak	Professeur des Universités	Examinateur
KELLIL Kamel	Maitre de conférences	Examinateur
TROCHU François	Professeur	Examinateur
YOUNES Rafic	Professeur	Directeur de thèse
LAFON Pascal	Professeur des Universités	Directeur de thèse

REMÉRCIEMENTS

Ce travail de recherche a été fait au sein de l'Université de Technologie de Troyes (UTT) en coordination avec le laboratoire de Composite à Haute Performance (CCHP) de l'école polytechnique de l'université de Montréal

Je tiens tout d'abord à remercier Professeur Pascal LAFON et Professeur Rafic YOUNES, directeurs de cette thèse. Ils ont suivi ce travail de recherche avec beaucoup d'attention, en lui donnant les orientations nécessaires. Leur disponibilité, ainsi que leurs conseils et forte implication dans les moments difficiles ont largement contribué à l'aboutissement de cette thèse.

J'adresse mes sincères remerciements à Professeur François TROCHU, pour m'avoir fait l'honneur d'être un co-directeur pour ma thèse. Ce travail n'aurait sans doute pas vu le jour sans son support continu lors de ma présence au sein de l'école Polytechnique de Montréal. Ceux-ci vont aussi à l'endroit de Monsieur Nicolas JUILLARD, président de la compagnie Texonic, pour avoir aimablement offert des tissus qui ont été la base des travaux expérimentaux.

Merci aimable pour Ali HALLAL, Ahmad FAYAD, Ali KOBEYSI, Amine HAYEK, Alaa KOBEYSI and Yousef BERRO qui ont attribué au niveau des simulations numériques. Des remerciements spéciaux pour Ali HALLAL qui m'a assisté gracieusement en laissant ses empreintes sur plusieurs parties de la thèse.

Merci pour les compagnies Chomarat, Saertex, Tissa, et 3TEX pour les tissus offerts pour les mesures de perméabilité.

Merci S. HILAL, P. CAUSSE et Professeur TROCHU pour offrir des figures de microtopographie qui ont servi a démontré des hypothèses au chapitre 7.

Merci Nicolas VERNET pour ton aide, tes conseils et ta formation dans la préparation des échantillons et les mesures. Merci Christian-Charles Martel pour ton support continu au niveau du labo ainsi que ton bonne humeur.

Merci pour tout l'équipe de CCH, tous les doctorants et permanents pour leur soutien quotidien au cours de ce travail de recherche.

Je voudrais remercier mes parents et frères d'être ce qu'ils sont. J'aimerais ici remercier ma mère pour son soutient qui m'a permis d'apprécier ses qualités humaines très précieuses.

J'adresse un merci profond, à mon épouse, Zeinab qui a fait preuve de patience et de réconfort jusqu'à la dernière minute.

Table de Matières

List of figures

Liste des Tableaux

Nomenclature

Symbol	Definition	Symbol	Definition
ε	Porosity	$K_{0°}$	Macroscopic permeability warp direction
ε_{eff}	Effective porosity	$K_{90°}$	Macroscopic permeability weft direction
V_{fy}	Intra yarn fiber volume fraction	K_L	Microscopic longitudinal permeability
V_f	Fiber volume fraction	K_T	Microscopic transversal permeability
V_{f0}	V_f for non compacted fabrics	K_{reg1}	Permeability of region 1
V_{fi}	V_f for compacted fabrics	$K_{reg1.w}$	Permeability of region 1 in 0° flow
$V_{f(reg1)}$	Volume fraction of region 1	$K_{reg1.f}$	Permeability of region 1 in 90° flow
$V_{f(reg2)}$	Volume fraction of region 2	K_{reg2}	Permeability of region 2
H	Fabric thickness	H_i	Fabric thickness on V_{fi}
H_0	Fabric thickness prior to compaction	h_w	Warp yarn thickness
h_f	Weft yarn thickness	ρ_s	Surface density of the fabric
Q	Resin flow	ρ	Material density
$V_{f(meso.f)}$	volume fractions of mesopores in weft direction	$V_{f(meso.w)}$	volume fractions of mesopores in warp direction
$V_{f\,(reg1)}$	Volume fraction of region 1	$V_{f\,(reg2)}$	Volume fraction of region 2

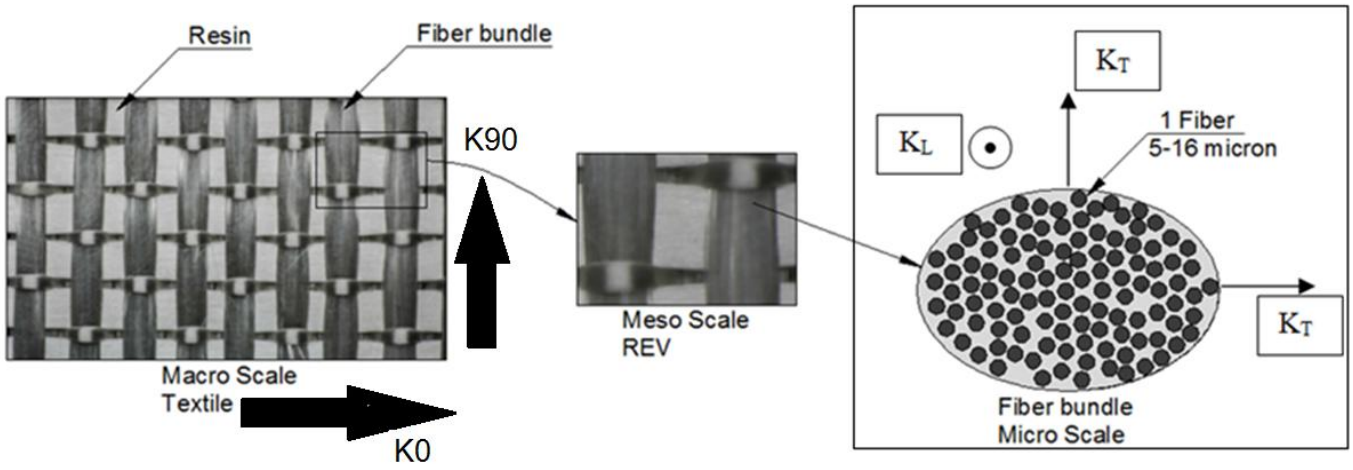

1 Chapter 0: Résumé de la thèse

Outre que ce chapitre, la thèse est divisée en huit chapitres, y compris le chapitre de l'introduction. Le deuxième chapitre présente une revue sur les méthodes de prédiction de la perméabilité. Au chapitre 3, une analyse comparative analytique, numérique et expérimentale, de la perméabilité microscopique des torons de fibre unidirectionnelle est réalisée. Les chapitres 4 et 5 montrent une description des méthodologies sélectionnées pour les mesures en plan et à travers l'épaisseur, et décrivent les spécifications des tissus et les mesures de perméabilité. Le chapitre 6 présent le modèle analytique prédisant la perméabilité dans le plan pour différents tissus NCF et 3D-orthogonal. Le chapitre 7 présente une analyse numérique de la perméabilité pour les tissus unidirectionnels, NCF et tissés taffetas. Enfin, le chapitre 8 tire les conclusions de ce travail et trace des perspectives d'avenir.

Les matériaux composites sont connus par la combinaison de deux matériaux hétérogènes ayant des propriétés complémentaires. Le premier est le renfort fibreux et le second est connu sous le nom de matrice. En général, le tissu ou le renfort soutient toute la rigidité et la résistance nécessaire dans le composite, la matrice entoure le tissu et le protège contre les attaques chimiques et environnementales. Les propriétés de la matrice ont un module d'élasticité inférieur et une élongation supérieure à celui du renfort, ce qui permet de bénéficier de toutes les propriétés de la fibre lors de la transmission de la charge dans la partie composite. Selon les matériaux sélectionnés et le traitement, les propriétés mécaniques et les usages des matériaux composites sont variables. Les propriétés des tissus dépendent de deux variables principales : le matériau des fibres du tissu et l'architecture du tissage. Le Tableau 1 montre certaines propriétés des matières premières par rapport aux matériaux métalliques traditionnels.

Plusieurs procédés sont utilisés dans la fabrication des pièces composites, selon l'application, le coût, la quantité et de nombreux autres critères, un processus de fabrication adéquat est sélectionné. Les procédés sous l’acronyme LCM (Liquid Composite Molding) sont groupés sous deux grandes catégories : l’injection (RTM et variantes) et l’infusion (LRI et variantes), comme cet acronyme l’indique, ces procédés

impliquent l'introduction de la matrice sous forme liquide dans le renfort fibreux. Ces méthodes sont considérées comme des techniques de fabrication composite prometteuse en raison de leur coût relativement faible, leur temps de cycles de production réduit, leur répétabilité et leur capacité à fabriquer des pièces de formes complexes.

Propriété des matériaux	Densité (Kg/m3)	Module axial (GPa)	Module transverse (GPa)	Module de cisaillement (GPa)	Résistance à la traction (MPa)	Résistance (compression axiale) (MPa)
E-glass	2600	72	72	30	2100	1500
S2-glass	2650	87	87	36	3500- 2850	3000- 2450
AS4carbon	1800	231	15	15	3500	3000
IM7carbon	1800	276	19	27	5180	3200
Kevlar	1400	80 - 110	7 - 10	5	3500	2900
Spectra	970	80 - 110	7 - 10	5	2400- 3200	
Fer	7800	200	200	70	200 - 1800	200 - 1000
Aluminium	2700	70	70	40	150 - 600	100>
Epoxy LY556	1200	3.35	3.35	1.24	80	120
Polyester S-15080 L	1100	4	4	-	50	-

Tableau 1 Propriétés mécaniques de différents matériaux

Un problème important apparaît dans LCM en raison de la présence de vides et de zones sèches qui causent différents types de défauts dans la partie fabriquée. La présence de vides a une influence sur les propriétés mécaniques. Alors que, dans une partie bien fabriquée, après un remplissage de moule parfait, les vides macroscopiques et microscopiques sont minimisés. Les paramètres influençant le comportement de remplissage sont la géométrie du moule, la viscosité de la résine, la température du moule, le placement des orifices d'injection, et enfin le paramètre le plus critique est l'évaluation de la perméabilité du tissu.

Les logiciels tels que PAM-RTM [6], LIMS [7] et Polyworx [8] permettent de prédire le comportement de remplissage, d'obtenir les temps de remplissage et les formes du front d'écoulement. Ceux-ci nécessitent certaines entrées :

- Le dessin de la pièce
- La viscosité de la résine
- Le tenseur de perméabilité

Ainsi, l'étape la plus critique dans les procédés de fabrication composites à base d'injection / infusion consiste à simuler le flux de résine en fonction des positions d'injection, de la pression d'écoulement à l'entrée et la vitesse. La loi de Darcy a été généralisée pour pouvoir être applique en milieux poreux anisotropes, et est utilisée dans la modélisation du flux de résine des fluides comme le montre l'équation(1) :

$$\bar{u} = -\frac{K}{\mu}\nabla P \tag{1}$$

Où ū est la vitesse de Darcy, μ la viscosité du fluide, ∇P le gradient de pression et K le tenseur de perméabilité du milieu poreux. Le tenseur de perméabilité pour les tissus est généralement orthotrope, donc le tenseur de perméabilité dans le système de coordonnées principal (1, 2, 3)(équation(2)) pourra se réduire à :

$$\begin{pmatrix} K_1 & 0 & 0 \\ 0 & K_2 & 0 \\ 0 & 0 & K_3 \end{pmatrix} \tag{2}$$

Où (1, 2) sont les directions dans le plan et (3) la direction à travers l'épaisseur. (0°, 90°) sont utilisées pour désigner la perméabilité dans le plan avec les directions chaine et trame respectivement.

Dans cette étude, l'objectif principal est d'obtenir les valeurs de perméabilité dans le plan de la manière la plus précise, la plus simple et la plus robuste. Pour ce faire, une série d'objectifs secondaires sont énumérés ci-dessous :

1. Une étude comparative est menée pour sélectionner les meilleurs modèles pour prédire la perméabilité des torons fibreux unidirectionnels.
2. La perméabilité dans le plan est mesurée pour onze tissus d'architectures différentes. Ces mesures sont réalisées à l'aide d'une méthode expérimentale bien connue, convenue internationalement, fiable et efficace.
3. En raison du manque de données sur les spécifications et la perméabilité des tissus, des paramètres géométriques détaillés sont fournis pour chaque tissu, comme entrée pour les modèles numériques FE élémentaires analytiques.
4. Élaborer un modèle analytique simple, précis et facile à appliquer pour prédire la perméabilité dans le plan.
5. Développer une méthode de simulation numérique simple et rapide pour prédire la perméabilité dans le plan.

En plus des objectifs mentionnés, notez que la perméabilité à travers l'épaisseur a également été mesurée pour sept tissus en offrant les paramètres géométriques nécessaires pour des travaux futuristes.

Dans une deuxième étape une étude bibliographique étendue est présentée sur les méthodes d'évaluation de la perméabilité. Différentes méthodes ont été utilisées pour évaluer le tenseur de perméabilité : expérimental, méthodes numériques et analytiques. L'Illustration 1 montre les différentes régions aux différentes échelles dans un tissu.

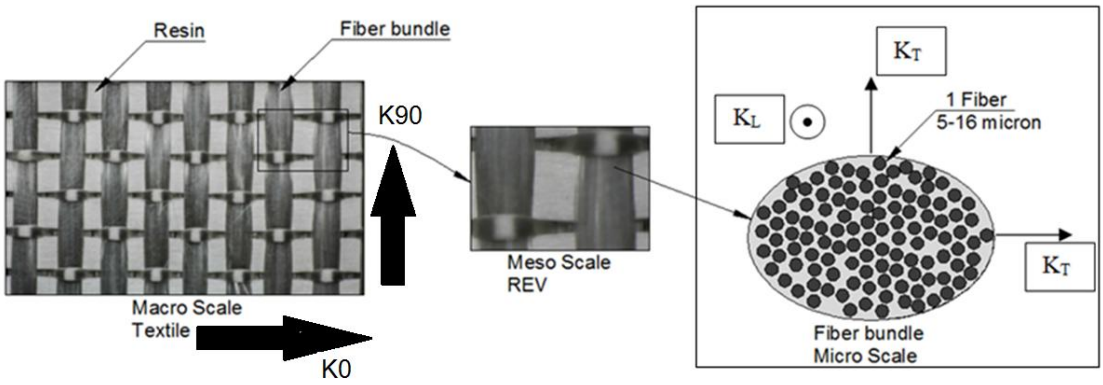

Illustration 1 Échelles des tissus

Lors d'un travail de modélisation, la prise en compte de l'architecture à double échelle des tissus est impérative pour obtenir des résultats fiables. Après plusieurs années, en essayant de prédire sans trop de succès, la perméabilité des renforts fibreux, compte tenu seulement d'une seule échelle de porosité, les recherches se sont naturellement orientées vers la prise en compte d'une architecture à double échelle. En fait, la présence de micropores entre les fibres réduit la perméabilité par rapport à une prédiction à une échelle unique. La quantité de réduction dépend de l'arrangement entre les micropores et les mésopores ; en d'autres termes, elle est dépendante de l'architecture des tissus.

Nous présentons ici différents types de mesures de perméabilité en distinguant les mesures dans les directions du plan et à travers l'épaisseur. Dans un procédé de fabrication, la résine est généralement injectée ou infusée dans un tissu sec sous une pression constante ou à débit constant.

La perméabilité dans le plan est mesurée expérimentalement de différentes façons. Les méthodes peuvent être classées par la procédure de mesure, le dispositif de mesure et le fluide utilisé :

- radial ou longitudinal, en fonction de la position de la porte d'entrée, voir l'Illustration 1 pour la perméabilité dans le plan,
- Saturé ou insaturé, selon que la préforme est saturée de résine ou sèche lors de la mesure de la perméabilité,
- Pression constante à l'entrée ou vitesse constante pendant l'injection,
- Type de liquide injecté,
- Appareil de mesure.

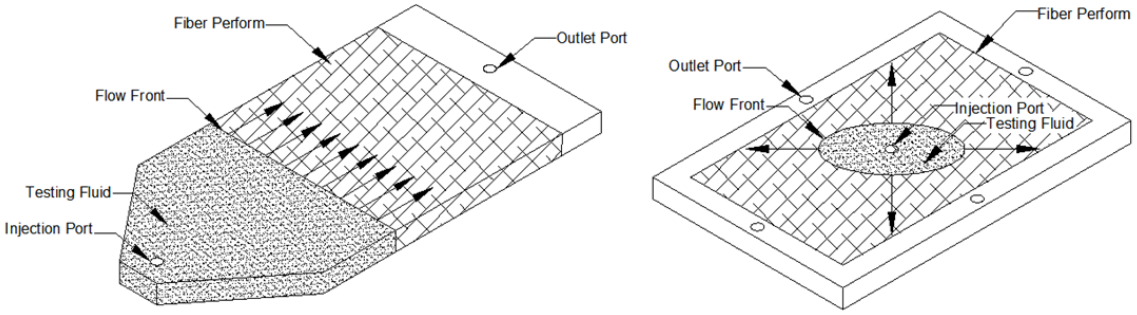

Illustration 2 Méthode de mesure linéaire et radiale

Illustration 2 montre les deux types de flux considérés lors du test de la perméabilité dans le plan; l'image de gauche décrit les expériences de flux unidirectionnel tandis que l'image de droite décrit les expériences de flux radial.

Une revue des méthodes expérimentales utilisées pour déterminer la perméabilité dans le plan est présentée. Certains articles présentent une revue plus détaillée [1, 2]. Les mesures de perméabilité basées sur les injections radiales ont été utilisées par de nombreux chercheurs. Hoes et al. [3] a utilisé une nouvelle configuration pour effectuer une injection radiale 2D à l'aide de capteurs électriques pour détecter la progression du front d'écoulement pour un tissu de verre tissé 2D pour un $V_f = 0.42$. L'écart-type de leurs données expérimentales était de 21 à 22%. Song et Youn [4] ont utilisé la méthode du flux radial pour mesurer la perméabilité dans le plan des tissus de verre à tisser simple avec une pression d'entrée constante. Comas-Cardona et al. [5] ont décrit une méthode d'injection radiale pour mesurer la perméabilité au renforcement des fibres en utilisant une configuration de test de compression après avoir déterminé le rapport d’anisotropie ;

la méthode permet le calcul de la perméabilité dans le plan et à travers l'épaisseur. Cette méthode a été appliquée sur un tissage en sergé de verre et sur des tissus de carbone NCF pour déterminer la perméabilité dans le plan.

La perméabilité saturée et non-saturée a également été discutée et étudiée. Shojaei et al. [2] ont étudié la perméabilité saturée et non saturée d'un tissu de verre à différentes pressions d'injection et des fractions de volume de fibres. Les expériences sont basées sur une injection unidirectionnelle. La différence entre la perméabilité insaturée et la saturation est également liée à la structure des pores. La perméabilité saturée est habituellement plus élevée que la perméabilité non saturée. La perméabilité insaturée a été déterminée à l'aide des mesures expérimental à flux radial à pression d'injection constante pour trois tissus 3D différents, par Endruweit et long [6], en utilisant des transducteurs de pression pour détecter la propagation du front d'écoulement

En outre, certaines études ont porté sur le développement de nouvelles techniques pour déterminer la perméabilité des tissus. Liu et al. [7]ont étudié la mesure de perméabilité dans le plan. Une nouvelle configuration est présentée, qui comprend un nouveau design de capteur et un nouveau logiciel d'analyse. La nouvelle méthode proposée a été utilisée pour mesurer la perméabilité d'un tissu sergé en basalte. Arbter et al. [8] a rendu compte de la mesure de la perméabilité dans un exercice international entre douze instituts et universités différentes. Deux tissus ont été sélectionnés 01113-1000-TF970 (tissu en verre E 2 x 2) et G0986 D 1200 (tissu de carbone 2% 2), et seize méthodes différentes ont été utilisées pour prédire la perméabilité dans le plan. Une grande dispersion des résultats a été observée entre les méthodes utilisées, qui ont été expliquées par l'incertitude expérimentale, les facteurs humains et différentes techniques expérimentales. Naik et al. [1] a présenté une discussion sur les facteurs qui influencent la mesure de la perméabilité. Il ressort de la conclusion que la perméabilité saturée est supérieure à la perméabilité insaturée sauf quelques exceptions. La perméabilité insaturée est également plus élevée pour les fibres synthétiques que pour les fibres naturelles. On constate que, pour les fluides à viscosité élevée, la perméabilité diminue. En outre, on remarque que la perméabilité transversale est inférieure aux valeurs de perméabilité dans le plan pour les tissus typiques. Les mêmes tissus ont été étudiés dans Benchmark II [9] pour résoudre les problèmes rencontrés dans le premier Benchmark [8]. L'objectif était de suivre les mêmes

directives. La dispersion entre les données expérimentales obtenues par différents groupes de recherche pour le même tissu était d'environ 20% lors de l'utilisation de la même méthode expérimentale.

À propos de la mesure de la perméabilité à travers l'épaisseur, la méthode la plus commune est l'appareil d'écoulement cylindrique unidimensionnel à débit constant. Le fluide est injecté à un débit donné, puis la pression d'injection correspondante est notée. La perméabilité est calculée en fonction d'une valeur de point unique en utilisant la loi de Darcy équation (3) pour l'écoulement unidimensionnel:

$$u = \frac{Q}{A} = \frac{K_3}{\mu} . \frac{\Delta P}{h} \tag{3}$$

où "u" représente la vitesse d'injection Darcy, "Q" le débit volumique, "A" l'aire des tissus, μ la viscosité de l'huile injectée, ΔP la perte de pression, h l'épaisseur du renfort et K_3 la perméabilité à travers l'épaisseur.

Concernant le travail au niveau de la modélisation, une revue de la littérature a révélé que la plupart des études se sont concentrées sur l'évaluation de la perméabilité pour les composites unidirectionnels. Ces études se composent de modélisations analytiques et par élément finis.

Pour les tissus 2D et 2.5D, la complexité géométrique de la cellule représentative ne permet pas d'établir une solution analytique simple, plusieurs travaux ont utilisé des méthodes numériques. Ces méthodes résolvent les équations de la mécanique des fluides en échelle mésoscopique ou à double échelle (échelle microscopique, mésoscopique). Les auteurs ont développé différentes méthodes pour prédire numériquement le tenseur de perméabilité dans le plan. Ces méthodes peuvent être regroupées en trois catégories différentes : les méthodes des éléments finis, les méthodes de différence finies et la méthode Boltzman en réseau. Chaque méthode présente ses avantages et ses inconvénients. [10-17] ont utilisé des méthodes d'élément finis. Ces méthodes sont basées sur la discrétisation de la cellule unitaire en élément, qui est représentée par des fonctions de référence définies sur chaque élément. Ces fonctions locales ont l'avantage d'être plus simples que celles qui pourraient être utilisées pour représenter la cellule unitaire totale.

Le principal inconvénient de ces méthodes est la complexité du maillage 3D, ainsi que le très grand temps de calcul.

Les méthodes de différence finie recherchent des solutions approximatives d'équations différentielles partielles en résolvant un système qui relie les valeurs de fonctions inconnues à certains points suffisamment proches les uns des autres, mais ils nécessitent une petite étape de discrétisation pour converger [18].

Les méthodes de Lattice Boltzmann ont les mêmes avantages mais l'inconvénient de ne pas converger aussi rapidement et sont également plus coûteuses en termes de temps de calcul. Ces méthodes étudient le milieu sur l'échelle mésoscopique en considérant des particules fictives dans un espace-temps discret [19-22].

Si la méthode des éléments finis est bien adaptée aux géométries complexes, son principal inconvénient est la nécessité d'un maillage 3D. L'obtention de ce maillage est parfois très difficile. La différence finie et les méthodes en réseau de Boltzmann sont utilisées pour résoudre des problèmes sur des mailles uniformes, de sorte qu'elles ne sont pas soumises à ce problème. Mais elles nécessitent un degré de discrétisation plus fine pour converger et sont donc parfois plus coûteux en termes de temps de calcul.

À l'heure actuelle, des efforts de recherche importants sont étendus au développement d'outils de simulation numérique pour évaluer la perméabilité. Cependant, les résultats sont encore loin de correspondre à la réalité [23]. En outre, la mesure expérimentale de la perméabilité fait face à beaucoup de problèmes [8]. Ceci est dû à des erreurs de manipulations, à l'inexactitude de l'équipement, aux fautes dans les techniques de mesure et à la préparation inadéquate des spécimens. Toutes ces raisons peuvent expliquer pourquoi des résultats de mesure incohérents sont obtenus qui rendent parfois l'évaluation expérimentale de la perméabilité non fiable. Cependant, de bons progrès ont été réalisés dans [9], concernant la méthodologie expérimentale, une méthode pour mesurer la perméabilité dans le plan a été convenue par 12 instituts et universités. En ce qui concerne la méthode analytique, différents chercheurs ont essayé de développer des modèles analytiques ou empiriques qui prédisent la perméabilité des tissus [24-30]. La plupart des modèles développés sont basés sur l'équation de Cozeny-Karman ou nécessitent un support externe par simulation numérique ou expérimentation pour prédire

la perméabilité macroscopique. Peu de travaux publiés sont disponibles pour prédire la perméabilité des tissus par des modèles analytiques et ceux qui existent ne sont pas généralisés et loin d'être parfaits. Les modèles analytiques prédisent bien la perméabilité des fibres unidirectionnelles. Toutefois, aucune étude comparative n'a été effectuée pour sélectionner les meilleurs modèles.

Compte tenu des différentes méthodes utilisées pour mesurer la perméabilité, les résultats obtenus ne sont pas acceptables. Des modifications mineures dans les procédures expérimentales affectent de manière significative les valeurs mesurées. Le Benchmark international II [9]a convenu d'une méthode de mesure de la perméabilité dans le plan. Cette méthode peut maintenant être adoptée comme référence.

Au niveau du troisième chapitre une étude comparative entre différent modèles analytiques avec des valeurs expérimentales et numériques est réalisée. Le but de cette étude est de sélectionner les meilleurs modèles analytiques prédisant la perméabilité des torons fibreux unidirectionnels. Pour ce faire, sept modèles analytiques prédisant la perméabilité microscopique longitudinale [31-37]et dix-sept modèles [31-36, 38-44]prédisant la perméabilité microscopique transversale sont sélectionnés de la bibliographie. À partir de la comparaison, les meilleurs modèles pour prédire la perméabilité microscopique longitudinale et transversale sont sélectionnés.

Les valeurs provenant des modèles analytiques sont comparées aux simulations numériques ou aux résultats expérimentaux de la bibliographie, mais ces résultats ont montré de grandes différences entre eux pour la même fraction de volume de fibres. Cela révèle l'importance d'effectuer une nouvelle étude numérique simulant une expérience réelle et éliminant les problèmes de l'expérience.

L'Illustration 3 montre deux tissus différents qui sont un 3D Orthogonal de la compagnie 3TEX avec une fraction de volume de fibres égale à 55,76% et un tissu à bidirectionnelles (U14EU920) de Saertex avec une fraction de volume de fibres égale à 60.59%. Notez que ces injections réelles sont effectuées afin d'affirmer que l'arrangement des fibres dans les torons est aléatoire. Ainsi, la modélisation numérique FE est effectuée sur la base d'une structure aléatoire.

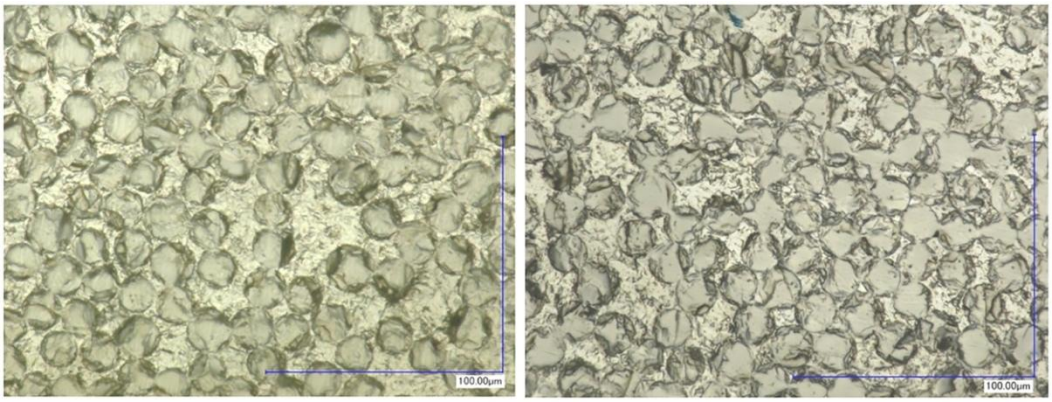

Illustration 3 Deux tissus: 3D Orthogonal de 3TEX à un taux de fibre égale à 55,76% et un tissu (U14EU920) de SAERTEX à un taux de fibre égale à 60,59%

L' Illustration 4 et l'Illustration 5 montrent simultanément les deux groupes des cellules élémentaires choisies pour les simulations transversale et longitudinale. Six valeurs de porosités ont été choisies, ces valeurs ont été sélectionnées en correspondance avec les porosités des expériences de la bibliographie.

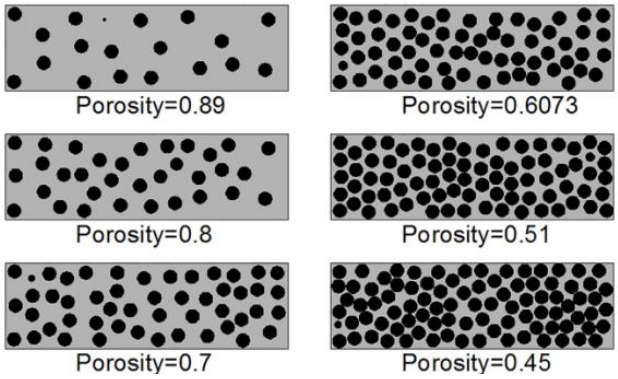

Illustration 4 Cellules élémentaires 2D

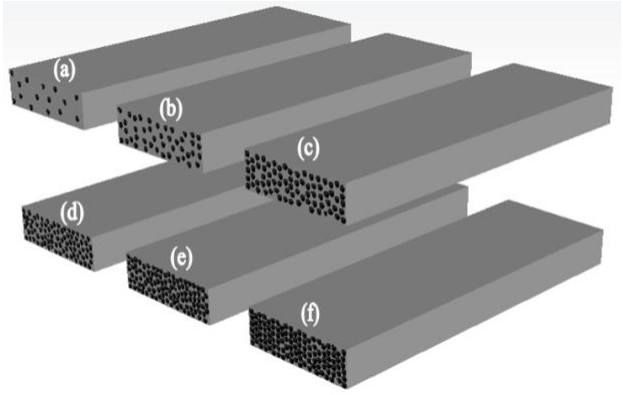

Illustration 5Cellules élémentaires 3D

Cette étude estime la vitesse moyenne de remplissage du volume sous une pression constante. En d'autres termes, c'est la valeur de perméabilité saturée. L'étude se déroule dans les directions longitudinales et transversales. Une étude plus avancée est réalisée pour la même cellule unitaire en mode transitoire, où la position du front avant du flux est détectée en fonction du temps, en tenant compte de l'effet capillaire. On déduit une perméabilité insaturée moyenne. Cette simulation a validé la cohérence de la simulation de mode statique.

Les valeurs expérimentales et numériques, avec lesquelles on va comparer ultérieurement, sont sélectionnées de la littérature à différentes fractions de volume de fibres. Lorsque deux valeurs sont à la même fraction de volume de fibres, la valeur de perméabilité qui correspond le mieux aux données numériques de l'étude réalisée est choisi pour l'étude comparative. En pratique, les expériences donnant des résultats incohérents ne sont pas utilisées dans la procédure de comparaison.

Une étude comparative à deux niveaux est réalisée entre toutes les données obtenues au cours de ce travail, avec les expériences sélectionnées et les modèles analytiques. À partir de cette comparaison, les meilleurs modèles pour prédire la perméabilité microscopique longitudinale et transversale sont sélectionnés.

Son analyse comme le montre les Illustration 6 et Illustration 7 que Bahrami et Tamayol [44], Drummond et Tahir [39], Berdichevsky et Cai ISCM et "Unified model" (arrangement carré) [31, 32] ont un bon accord avec ces données pour les composants de perméabilité microscopique longitudinale. En ce qui concerne la perméabilité microscopique transversale, les modèles Berdichevsky et Cai ISCM (arrangement hexagonal) [32], Gebart (arrangement hexagonal) [33], Drummond et Tahir (arrangement hexagonal) [39] et Kuwabara [36] ont été élus pour être les modèles les plus précis. D'autre part, les simulations de mode transitoire ont donné lieu à des résultats synchronisés avec les simulations de mode statique, ce qui a révélé la cohérence de l'étude.

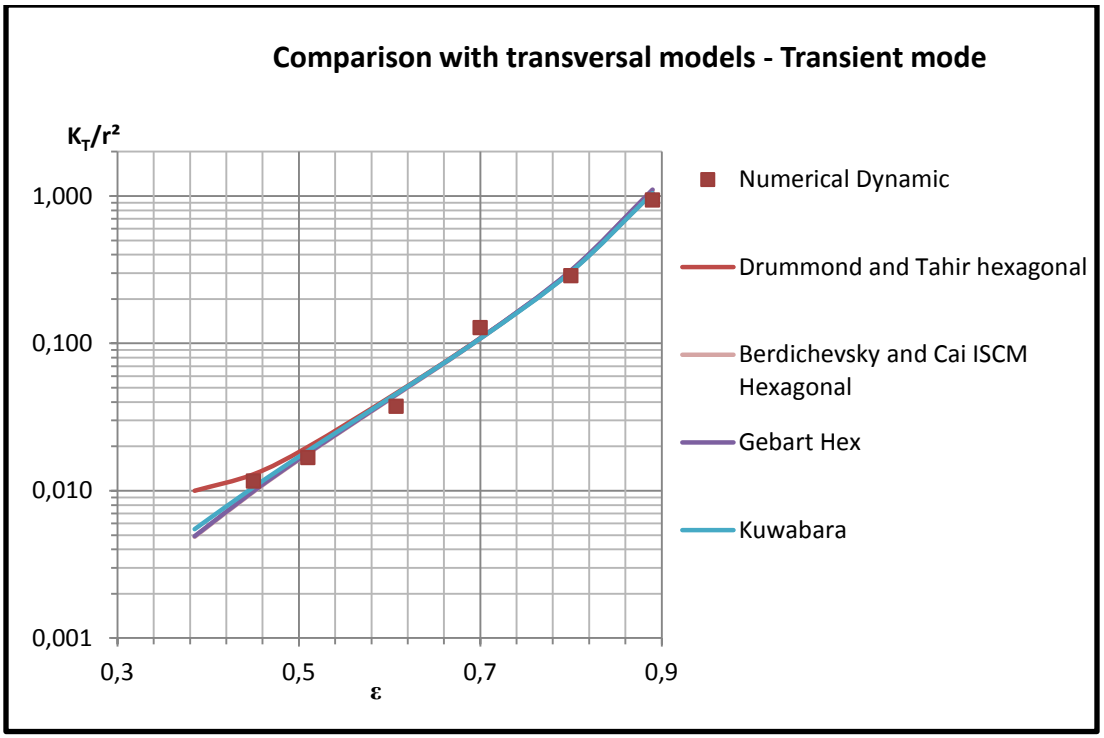

Illustration 6 Comparaison entre différent valeurs pour les simulations en direction transversal en mode transitoire

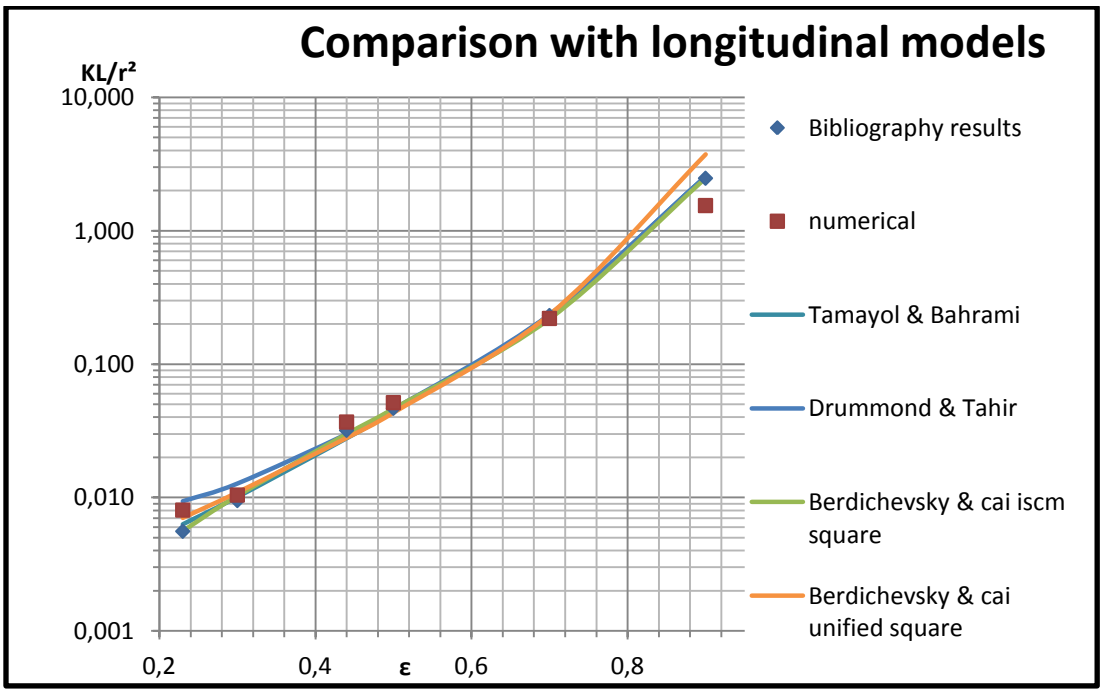

Illustration 7 Comparaison entre différent valeurs pour les simulations en direction longitudinal

Le but de cette étude est de connaître les modèles analytiques les plus pratiques pour prédire la perméabilité microscopique dans les torons de fibres unidirectionnels. En outre, pour calculer un tenseur de perméabilité précis, la valeur de la perméabilité microscopique doit être obtenue avec précision. En outre, la perméabilité microscopique pourrait être utilisée dans d'autres études telles que la pression capillaire ou les études de modélisation de la perméabilité.

Dans le chapitre 4, une méthode expérimentale pour mesurer les composants de perméabilité dans le plan est présentée. Après un une étude de la bibliographie, on constate que le calcul des composants de perméabilité par des méthodes expérimentales est toujours confronté à des problèmes majeurs. Ces problèmes sont liés à la méthode d'injection elle-même, qu'elle soit unidirectionnelle ou radiale, et reliée aux dispositifs de mesure utilisés. La méthode utilisée est basée sur une injection unidirectionnelle préformée sous pression constante. La vitesse du flux avant est mesurée, puis la perméabilité dans le sens de l'injection est calculée à partir de la loi Darcy. Pour calculer les composants de perméabilité dans le plan, trois composants de perméabilité sont calculés pour des orientations de 0 °, 45 ° et 90 °. Ensuite, les principaux composants de perméabilité K_1 et K_2 sont dérivés, l'orientation de l'axe majeur de l'ellipse est nommée "1" suivant la valeur la plus grande. Étant proches l'un de l'autre, les résultats obtenus pour une mesure de perméabilité répétée représentent une indication de la fiabilité et de l'efficacité du test ainsi que de la méthode utilisée.

En ce qui concerne la mesure de la perméabilité à travers l'épaisseur, la méthode utilisée est basée sur une injection du fluide d'essai à des vitesses alternées, la pression sera mesurée à l'aide de l'unité d'acquisition de données à chaque vitesse, la perméabilité transversale est évaluée en fonction de la loi de Darcy. Cette méthode a montré une amélioration concernant la mesure de points multiples pour chaque valeur de perméabilité au lieu de la mesure de point unique.

Le chapitre 5 présente les mesures de perméabilité dans le plan et à travers l'épaisseur en plus des données géométriques de tous les tissus. Dans le travail présenté, on étudie treize tissus différents afin d'évaluer le tenseur de perméabilité. La perméabilité dans le plan est mesurée pour les onze tissus, et la perméabilité par épaisseur est mesurée pour

sept tissus. Les tissus en carbone ou en verre sont livrés par différents fabricants. Les tissus A-G et Fabric J sont offerts par Texonic Company; d'autres tissus sont livrés par Chomarat, 3TEX et Saertex Companies. Les tissus ainsi que leurs noms et les compagnies donatrices sont nominés dans le Tableau 2.

Tissu	Nom du tissu	Compagnie	Tissu	Nom du tissu	Compagnie
Fabric A	TG-09-N-60J	Texonic	**Fabric H**	850.0445.80.0600	Tissa
Fabric B	TG-15-N		**Fabric I**	C-Ply-SP BX300	Chomarat
Fabric C	TG-33-N-50E		**Fabric J**	L14012	Texonic
Fabric D	TG-54-N-60C		**Fabric K**	C-weave 200P 3K	Chomarat
Fabric E	TG-75-N-50E		**Fabric L**	P3W-GE044	3TEX
Fabric F	TG-96-N-60I		**Fabric M**	U14EU920	Saertex
Fabric G	TC-67-N-50A				

Tableau 2 Noms des tissus

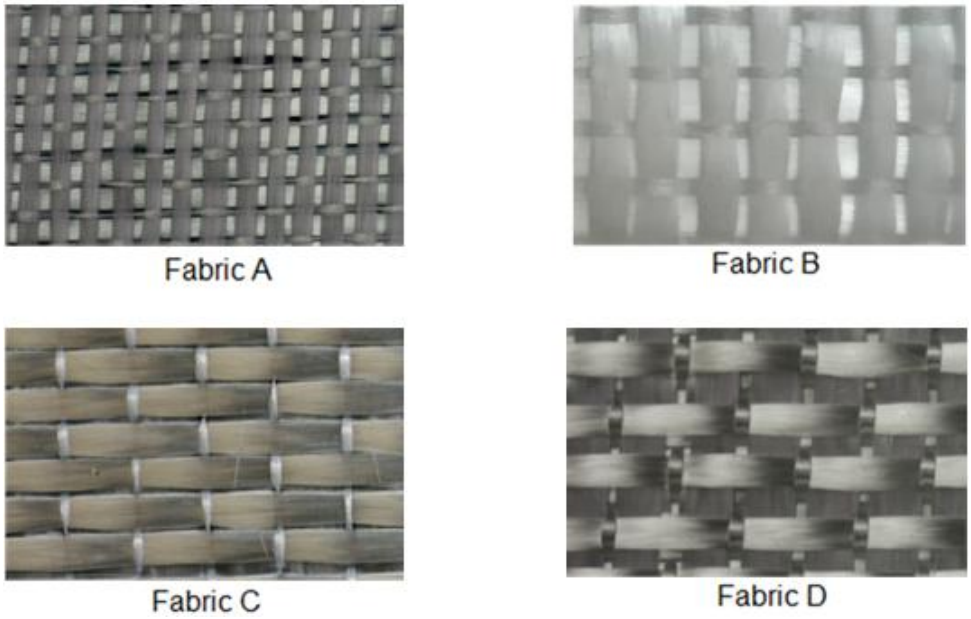

Illustration 8 Tissus A à D

Illustration 8 et Illustration 9 montrent les images des tissus. Ces images et d'autres sont prises en utilisant une caméra haute résolution, en utilisant ces photos, certaines distances comme la largeur du toron "a" et la distance entre deux torons adjacents sont mesurées. Ces mesures et celles provenant des papiers spécifiques seront utilisées dans les modélisations analytique et numérique.

Dans la section suivante, les résultats pour les mesures de perméabilité dans le plan sont présentés. Dans la première étape, les résultats bruts sont présentés à l'annexe A de la thèse. Deux ou trois mesures dans chaque direction (0 °, 45 ° et 90 °) pour chaque fraction de volume de fibre pour les valeurs de perméabilité unidirectionnelle sont établies pour les onze tissus. Dans l'étape suivante, on calcule une valeur moyenne pour les mesures de perméabilité unidirectionnelle ($K_{0\circ}$, $K_{45\circ}$ et $K_{90\circ}$) sur chaque fraction de volume de fibre ; on obtient une dispersion. La valeur de dispersion est calculée pour deux ou trois mesures successives faites pour chaque tissu sur un V_f sélectionné. La dispersion est calculée en divisant l'écart-type, nommé C_V, par rapport à la moyenne entre ces différentes mesures qui doit être inférieur à 15%. Ces résultats sont présentés au Tableau 3. K_1 représente la plus grande valeur de perméabilité et β l'angle entre K_1 et la direction chaîne.

Illustration 10 montre le diagramme d'ellipse pour le tissu A sur chaque fraction de volume de fibre. La forme de l'ellipse correspond à la forme de l'écoulement dans une injection réelle. Toutes les ellipses correspondant aux tissus A-K sont indiquées à l'Annexe 2 de la thèse.

Dans la deuxième section de ce chapitre, les mesures de perméabilité transversale sont présentées. Un essai d'injection typique pour la mesure de la perméabilité à travers l'épaisseur pour le tissu H à V_{f1} est présentée dans l' Illustration 11. Celle-ci montre la relation entre la pression et le débit, différents débits sont réglés au cours du test, en alternant les valeurs à chaque fois afin d'éviter des effets non linéaires. Selon la loi de Darcy, la relation entre la perte de pression et le débit volumique est supposée suivre un schéma linéaire comme décrit précédemment au chapitre 4. Par exemple, 0.396275 est utilisé comme rapport entre les débits et la différence de pression. R^2 montre le degré de corrélation entre les débits appliqués successivement et les pressions correspondantes. En utilisant ces données, la surface et l'épaisseur de l'échantillon, la valeur de perméabilité est calculée. Le Tableau 4 montre les valeurs de perméabilité transversale K3 pour chaque fraction de volume de fibres. Cv est noté pour les mesures répétées obtenues pour un même V_f. Cv pour les mesures répétées est inférieur à 10% pour tous les tissus, ce qui montre la cohérence des mesures. Une analyse concernant toutes les mesures est lancée, une conclusion générale est extraite.

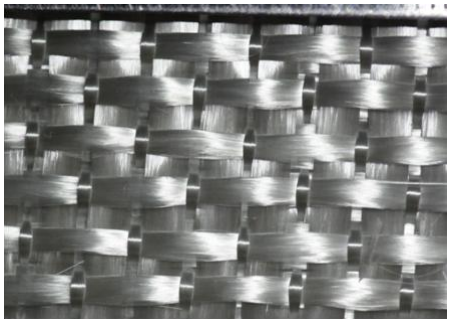

Fabric E

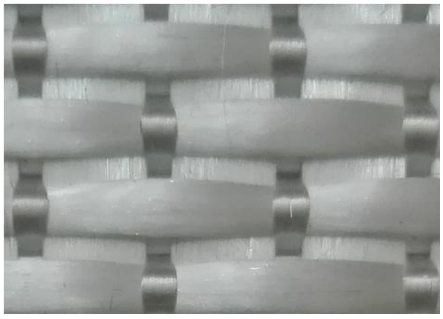

Fabric F

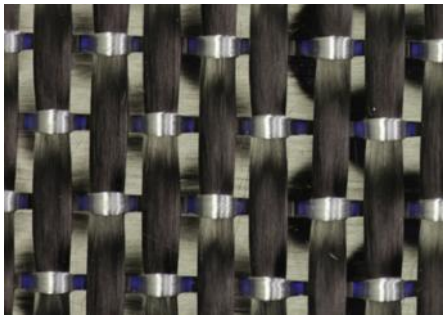

Fabric G

Fabric H

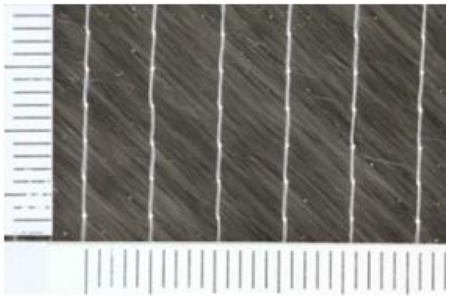

Fabric I

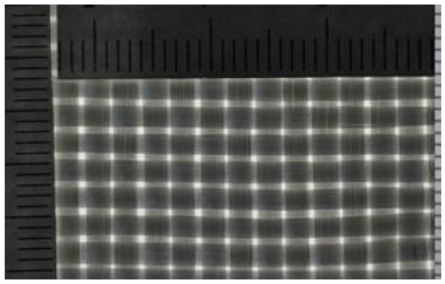

Fabric J

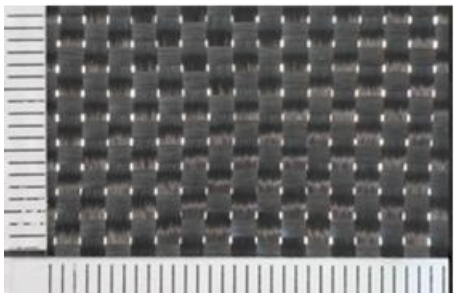

Fabric K

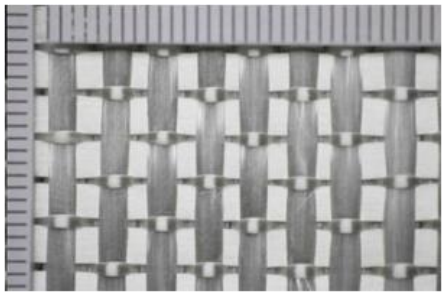

Fabric L

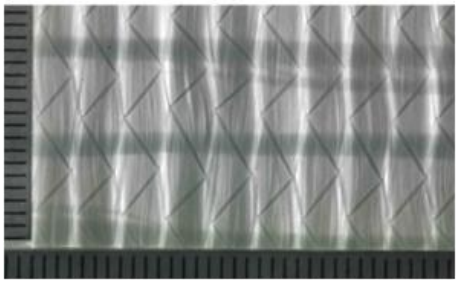

Fabric M

Illustration 9 Tissus E à M

Nom des Tissus	V_f (%)	K_1(*$10^{-11}m^2$)	K_2(*$10^{-11}m^2$)	β
Tissu A	V_{f1}= 45.99	6.32	2.94	84.6
	V_{f2}= 53.65	2.60	1.01	90.2
	V_{f3}= 61.32	1.46	0.56	97.5
Tissu B	V_{f1}= 39.83	30.311	25.493	87.5
	V_{f2}= 47.8	7.470	7.023	75.4
	V_{f3}= 55.76	1.801	1.387	78.6
Tissu C	V_{f1}= 49.48	55.960	16.096	131.1
	V_{f2}= 56.6	9.990	5.492	101.4
	V_{f3}= 63.36	5.385	2.324	112.2
Tissu D	V_{f1}= 44.94	83.875	12.984	84.9
	V_{f2}= 52.43	32.092	7.788	91.2
	V_{f3}= 59.99	13.527	3.609	99.3
Tissu E	V_{f1}= 51.26	129.518	23.887	80.2
	V_{f2}= 55.87	42.742	11.474	86.8
	V_{f3}= 64.48	8.446	3.950	82.1
Tissu F	V_{f1}= 52.83	64.662	13.600	89.9
	V_{f2}= 59.02	21.724	7.339	97.4
	V_{f3}= 67.23	1.567	0.748	93.6
Tissu G	V_{f1}= 54.08	33.662	10.360	94.8
	V_{f2}= 60.42	10.045	3.294	90.0
	V_{f3}= 68.82	3.767	0.236	118.3
Tissu H	V_{f1}= 47.93	3.486	1.388	162.3
	V_{f2}= 54.56	1.618	0.690	157.4
	V_{f3}= 61.62	0.277	0.190	179.0
Tissu I	V_{f1}= 46.21	1.500	1.193	19.1
	V_{f2}= 52.81	0.682	0.459	14.9
	V_{f3}= 65.76	0.090	0.066	18.3
Tissu J	V_{f1}= 44.51	43.059	31.176	123.9
	V_{f2}= 53.41	10.005	5.831	122.9
	V_{f3}= 62.31	2.212	0.889	127.3
Tissu K	V_{f1}= 43.4	3.046	1.571	3.9
	V_{f2}= 52.08	0.679	0.411	170.2
	V_{f3}= 60.76	0.168	0.095	179.7

Tableau 3 Valeurs principales de perméabilité dans le plan pour tissus A-K

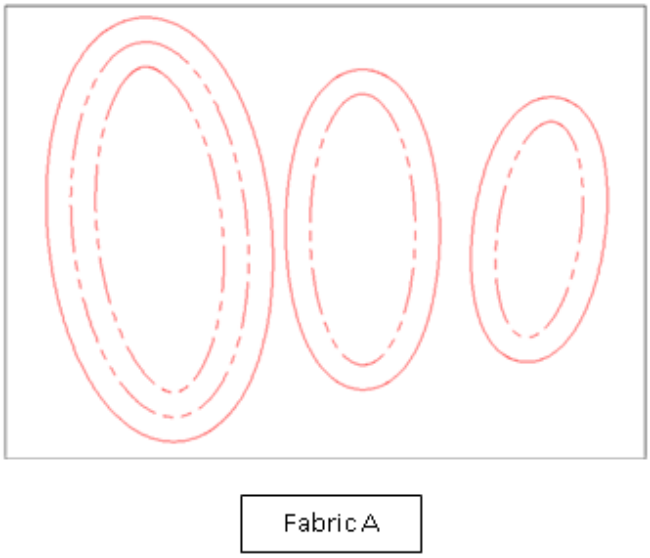

Illustration 10 diagramme d'ellipse pour le tissu A

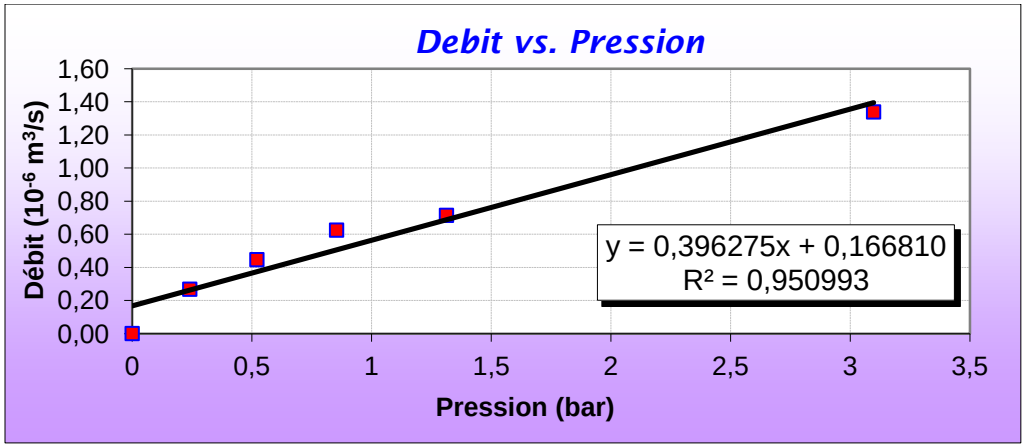

Illustration 11 Mesure de K_Z pour tissu H

Nom des Tissus	**Tissu B**			**Tissu H**		
V_f (%)	43.99	47.99	55.98	47.17	53.13	60.65
K_3(*$10^{-13}m^2$)	94.145	65.19	33.34	4.2338	2.7413	1.3090
Cv (%)	0.1	4.5	2.4	0.9	9.0	1.9
Nom des Tissus	**Tissu I**			**Tissu K**		
V_f (%)	46.39	56.33	66.27	43.74	52.49	61.24
K_3(*$10^{-13}m^2$)	1.996	1.153	0.685	6.347	4.053	2.214
Cv (%)	0.3	9.9	4.5	4.8	5.2	9.1
Nom des Tissus	**Tissu L**			**Tissu M**		
V_f (%)	49.67	55.76	63.43	40.22	50.6	58.11
K_3(*$10^{-13}m^2$)	110.197	83.972	63.860	53.037	35.227	21.463
Cv (%)	7.2	1.9	2.4	2.2	3.5	1.7

Tableau 4 Valeurs de perméabilité à travers l'épaisseur

Le chapitre 6 concerne la méthode analytique de la perméabilité. Différents chercheurs [24-30] ont essayé de développer des modèles analytiques ou empiriques qui prédisent la perméabilité des tissus. La plupart des modèles développés étaient basés sur l'équation de Cozeny-Karman ou nécessitaient un support externe par une simulation numérique ou une mesure expérimentale afin de prédire la perméabilité mésoscopique. La plupart de ces modèles ont encore besoin de développement pour être plus précis, plutôt que trop difficiles à appliquer.

L'objectif principal de ce chapitre est de présenter les développements d'un modèle analytique pour les tissus cousus NCF et les tissus 3D-orthogonaux. Ce modèle est basé sur les données géométriques architecturales des tissus offerts par l'industrie textile dans le but de prédire les valeurs de perméabilité dans le plan dans les deux directions chaine et trame $K_{0°}$ et $K_{90°}$.

Après avoir affiché les mesures géométriques, la forme des torons et d'autres informations nécessaires à la modélisation, ainsi que les résultats des mesures de perméabilité pour les cinq tissus étudiés, le modèle dans ces deux parties : modélisation géométrique et modélisation de la perméabilité est décrit. L'Illustration 12 explique brièvement les étapes suivies lors de la modélisation.

Afin de développer le modèle de perméabilité, un sous modèle analytique prédictif est choisi parmi les travaux antérieurs [45]. Ce sous-modèle utilisé pour les torons de fibres unidirectionnels est choisi dans l'étude comparative parmi les meilleurs modèles prédisant la perméabilité des torons de fibres unidirectionnels. Le modèle Bahrami et Tamayol [44] indiqué dans l'équation(4) sera utilisé pour prédire les valeurs de perméabilité.

$$K_{Sub.model} = \frac{r^2}{4(1-\varepsilon)}\left(-0.021 - \ln(1-\varepsilon) - \varepsilon - \frac{\varepsilon^2}{2} - 0.0186 * (1-\varepsilon)^4\right) \qquad (4)$$

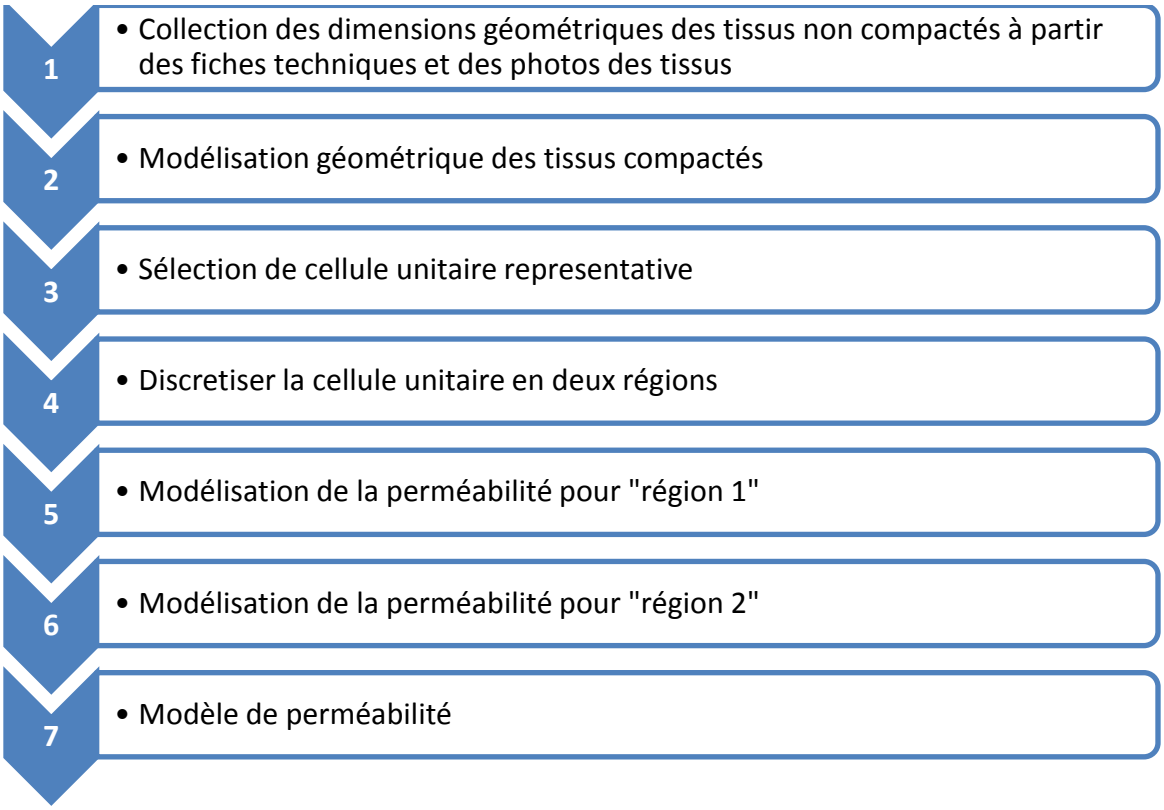

Illustration 12 étapes suivies lors de la modélisation

Les données recommandées comme entrée dans le sous modèle seront la fraction de porosité "ε" et le rayon "r". Notant que les quatre modèles élus, comme les meilleurs, dans [45] peuvent être utilisés plutôt que le modèle Bahrami et Tamayol, et des résultats similaires concernant les mesures expérimentales seront observés [32, 39, 44].

Une cellule unitaire généralisée est sélectionnée de sorte que le modèle puisse être appliqué à différents types de tissus, bien que ces derniers se situent sous trois types d'architectures différentes. La cellule unitaire choisie sera 1cm x 1cm x H_0 (épaisseur à sec avant la compaction). En choisissant cette cellule unitaire, le nombre des torons dans la direction chaîne et trame sont facilement lisibles à partir de la fiche de données du fabricant en tant que données d'entrée pour le modèle développé.

La perméabilité est régie par l'architecture des tissus, le liquide qui coule dans le tissu est divisé en deux types d'écoulement :

a. Écoulement dans les micropores
b. Écoulement dans les mésopores

La perméabilité microscopique est beaucoup plus faible que la perméabilité macroscopique. Dans un milieu bien arrangé où les mésopores sont toujours connectés entre eux, l'influence des microspores est limitée à l'effet de saturation, alors que les mésopores auront un effet dominant sur la perméabilité.

En ce qui concerne les tissus arrangés et stables lors de la compression, l'écoulement trouve son chemin toujours dans les mésopores et ne traverse jamais un micropore pour atteindre un mésopore, même si les micropores doivent être remplis en raison de la saturation. Pour prédire la perméabilité macroscopique dans le plan, le modèle évalue deux contributions du flux comme indiqué dans l'Illustration 13 :

a) Dans la région "1", l'écoulement intérieur et entre les torons de différentes couches.
b) Les déviations de l'écoulement créées par les torons cousus marqués comme région "2".

L'écoulement Q est divisé entre les deux régions comme indiqué dans l'équation (5) :

$$Q_{total} = Q_{reg1} + Q_{reg2} \tag{5}$$

La loi de Darcy a été généralisée pour tenir compte de l'équation (6) anisotropique poreuse des médias et est utilisée dans la modélisation du flux de résine des fluides.

$$\bar{u} = \frac{Q}{A} = \frac{K}{\mu} . \nabla P \tag{6}$$

Où $\bar{u}$ est la vitesse de Darcy moyennée en volume, μ est la viscosité du fluide, ∇P est le gradient de pression, et K est le tenseur de perméabilité du milieu poreux.

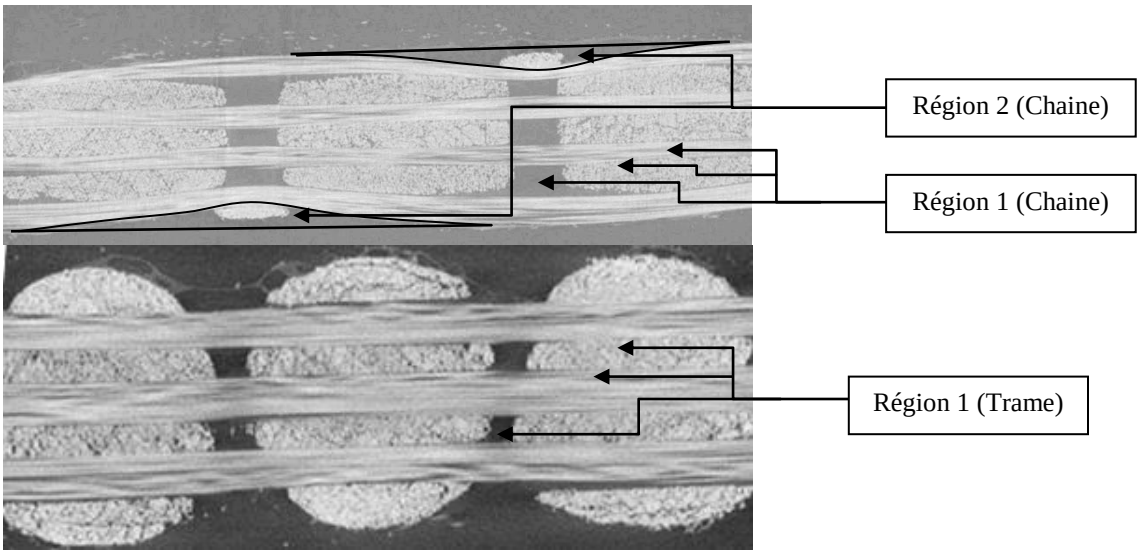

Illustration 13 contributions du flux pour TG96N

Ainsi, la perméabilité dans la direction désignée peut être écrite comme indiquée dans l'équation (7).

$$K_{0^\circ\, or\, 90^\circ} = \left[\left(1 - V_{f(reg2)}\right) * K_{reg1}\right] + \left[V_{f(reg2)} * K_{reg2}\right] \quad (7)$$

Comme décrit précédemment, la "région 2" contient les torons cousus et les mésopores autour de lui, alors $V_{f(reg2)}$ sera considéré comme la fraction volumique de la région des fils de couture.

Il nous manque la partie "*Modélisation géométrique des tissus sous compaction"* pour pouvoir appliquer le modèle. Cette partie est dédiée à la prédiction des paramètres géométriques après la compression du tissu sec à l'intérieur du moule. Après avoir été comprimés, les dimensions des torons a_w, a_f, H_w et H_f sont modifiées. Étant donné que les modifications de V_{fy} sont limitées et que la perméabilité microscopique a un effet limité sur les valeurs de perméabilité macroscopique (K_{0°, K_{90°),la modification de dimension nous considérons sera limitée à la réduction du volume du mésopore plutôt qu'à la réduction de l'aire de la section transversale des torons "*A*" pendant que le tissu est sous compaction. En tenant compte de ces hypothèses la modélisation de la géométrie est développée afin de prédire les dimensions des torons et les mésopores pour chaque V_f.

En passant à l'étape 5 du modèle "*Modélisation de la perméabilité pour (région 1)*"qui contient les torons de fibres longitudinales, transversales et les mésopores dans les deux

sens. L'écoulement dans la région 1 n'est pas discrétisé en deux écoulements séparés (un micropore et mésopore), mais le flux se trouve toujours dans le mésopore, tout en saturant les micropores dans la région partiellement saturée, comme la montre l'Illustration 14. Ainsi, l'effet des mésopores a beaucoup plus d'impact sur la perméabilité globale que l'effet des micropores; les fractions de volume des mésopores dans les deux directions chaine et trame $V_{f(ms.)}$ et $V_{f(ms.)}$ seront donc calculées après avoir considéré un toron bloqué. Lors de l'injection du fluide dans la direction de la chaîne, cette direction à un effet positif sur la perméabilité et la direction de la trame aura un effet négatif diminuant la perméabilité. Les équations (8) et (9) montrent respectivement la perméabilité dans la «région 1» lorsque l'écoulement est dans la direction chaîne ou le sens de trame.

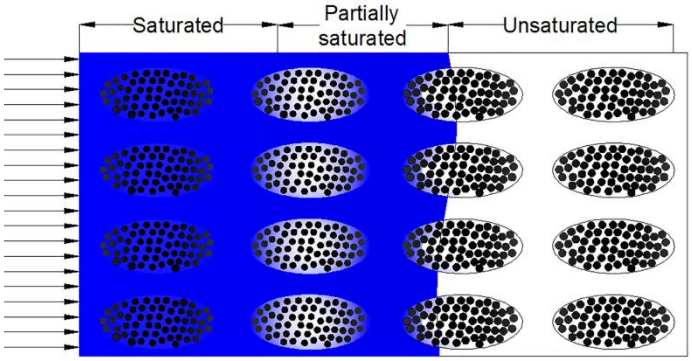

Illustration 14 progression du front

$$K_{reg1.w} = K_{submodel} * \frac{V_{f(meso.w)}}{V_{f(meso.f)}} \quad (8)$$

$$K_{reg1.f} = K_{submodel} * \frac{V_{f(meso.f)}}{V_{f(meso.w)}} \quad (9)$$

En passant à l'étape 6 du modèle « *Modélisation de la perméabilité pour (région 2)* »qui contient les torons de couture dans les couches périphériques et les mésopores qui l'entourent. Étant donné que la taille du faisceau de couture affecte le volume du mésopore autour de lui, le faisceau de couture en polyester ayant un diamètre de 25 µm est trouvé dans les tissus NCF, a un effet limité. Ainsi, la « région 2 » se trouve dans les tissus 3D-orthogonaux. Le flux dans la « région 2» est divisé en deux, l'un étant un

écoulement microscopique à l'intérieur des torons de couture et l'autre étant le flux mésoscopique autour des faisceaux de couture. Les deux équations (10) et (11) montrent la perméabilité dans la « région 2 » lorsque l'écoulement est dans la direction chaîne ou trame simultanément. Le flux se trouve toujours dans les mésopores, en outre, que la perméabilité microscopique est beaucoup plus petite que la perméabilité macroscopique telle que mentionnée dans la section précédente et la saturation de ces micropores est si rapide en raison de leur faible volume, alors l'effet de la perméabilité microscopique sera négligé.

$$K_{reg2.w} = K_{submodel} * \frac{V_{f(meso.w)}}{V_{f(meso.f)}} \tag{10}$$

$$K_{reg2.f} = K_{submodel} * \frac{V_{f(meso.f)}}{V_{f(meso.w)}} \tag{11}$$

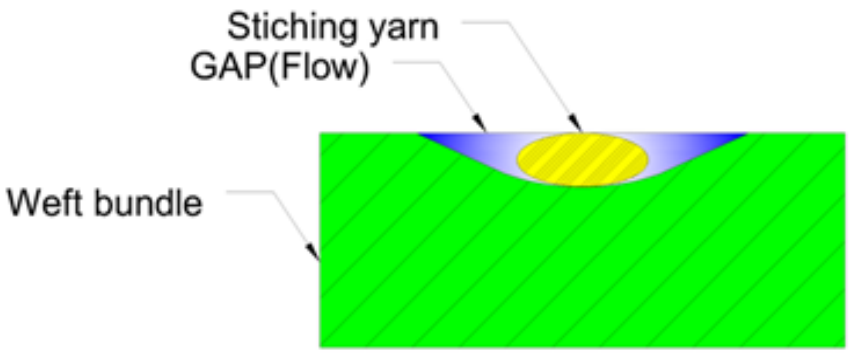

Illustration 15 Région 2

En passant à l'étape finale « modèle de perméabilité », la perméabilité de la cellule unitaire est une sommation des valeurs de perméabilité des sous-domaines soit en série, soit en parallèle, ou par une combinaison des deux selon des pourcentages définis. Puisque l'écoulement trouve toujours son chemin dans un mésopore et les micropores seront remplit plus tard lors de la saturation, alors la perméabilité moyenne est la sommation en parallèle des valeurs de perméabilité des régions à étudier comme le montre l'équation (12). Lorsque K_{avg} est la perméabilité de la cellule unitaire dans la direction désirée, V_{fi} représente la fraction volumique du domaine de la cellule unitaire avec une valeur de perméabilité K_i.

$$K_{wavg} = \sum_{i=0}^{n} (V_{fi} * K_i) \quad (12)$$

Comme indiqué précédemment, l'écoulement se trouve toujours dans un mésopore, de sorte qu'une sommation de perméabilité moyenne pondérée (parallèle) est utilisée. En sommant la perméabilité de la région "1" et la perméabilité de la région "2"; la perméabilité macroscopique est obtenue à la fois pour la direction de la chaîne "0°" (Illustration 16) et la direction trame "90°".

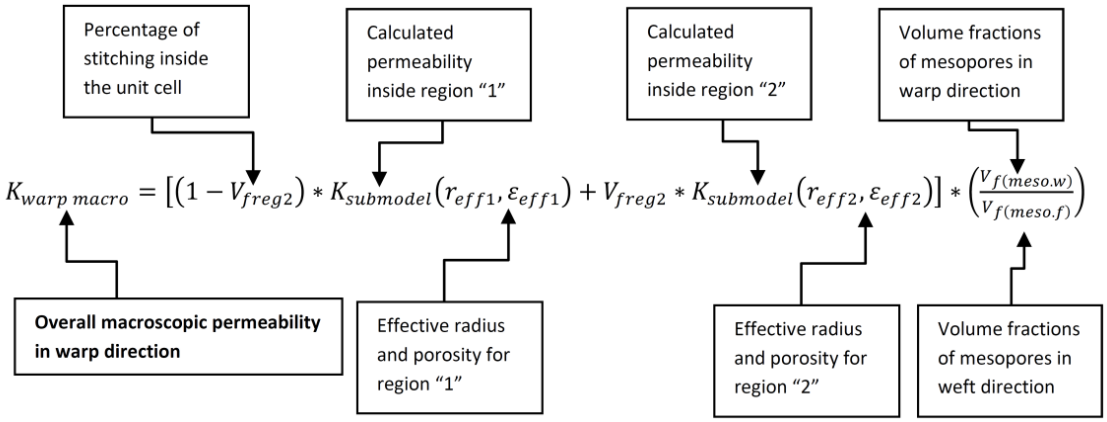

Illustration 16 modèle analytique (sens chaine)

Les valeurs de la permeabilité pour les tissus sont calculées, puis une analyse extensive est établit.

Illustration 17Illustration 18Illustration 19Illustration 20Illustration 21 montrent les valeurs mesurées de la perméabilité expérimentale (barres) et prédites (colonnes) dans la direction de la chaîne et de la trame pour les tissus TG15N- TG33N- TG54N- TG75N et TG96N respectivement. Les valeurs minimales et maximales des expériences sont représentées par des barres dans les figures indiquées. Comme le montre les figures, la perméabilité prévue est en excellente corrélation avec les données expérimentales pour le tissu 1 sans erreur observée , puisque la valeur prédite se situe entre les valeurs minimales et maximales de perméabilité mesurée. Une erreur de 33% est observée sur V_{f2} dans la direction de la chaîne. Notez que les erreurs sont calculées comme indiqué dans l'équation (13).

$$erreur = \frac{valeur\ predit - \ moyenne\ valeur\ mesuré}{moyenne\ valeur\ mesuré} * 100 \quad (13)$$

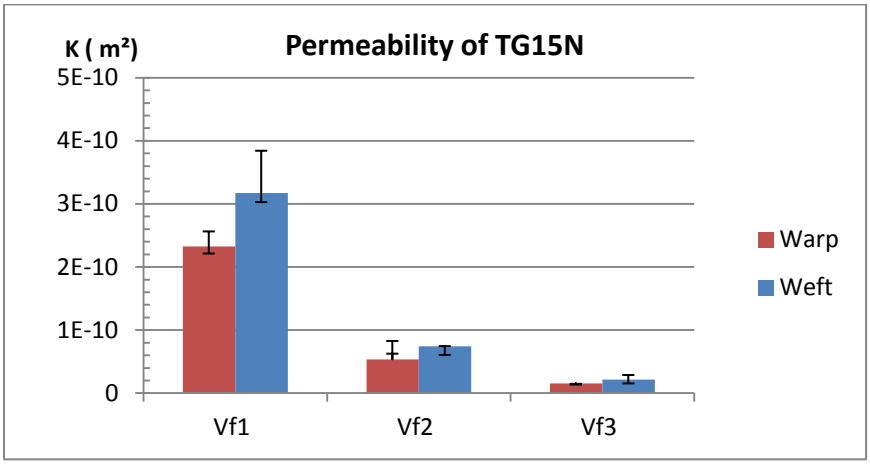

Illustration 17 Valeurs expérimentales et analytiques pour le tissus TG15N

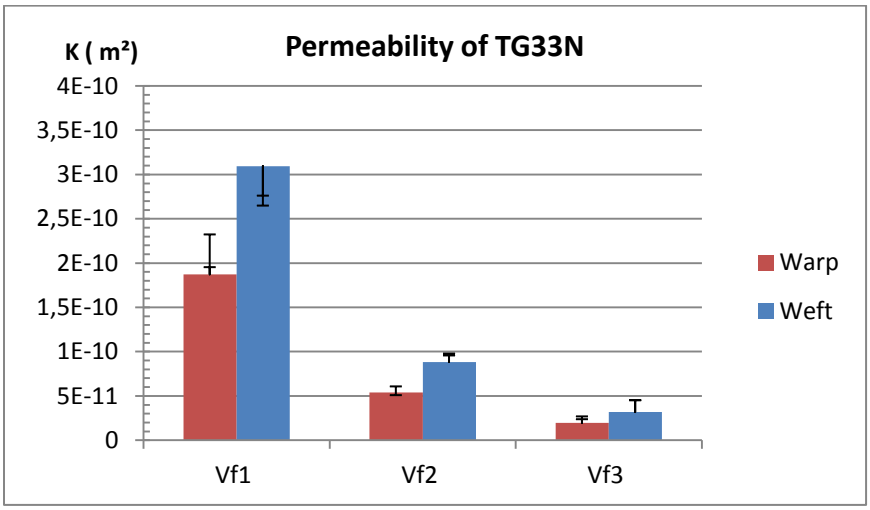

Illustration 18 Valeurs expérimentales et analytiques pour le tissus TG33N

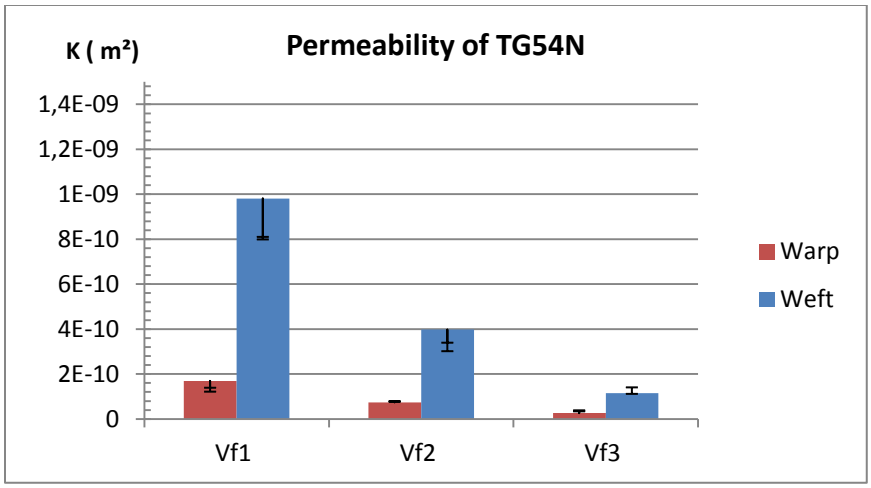

Illustration 19 Valeurs expérimentales et analytiques pour le tissus TG75N

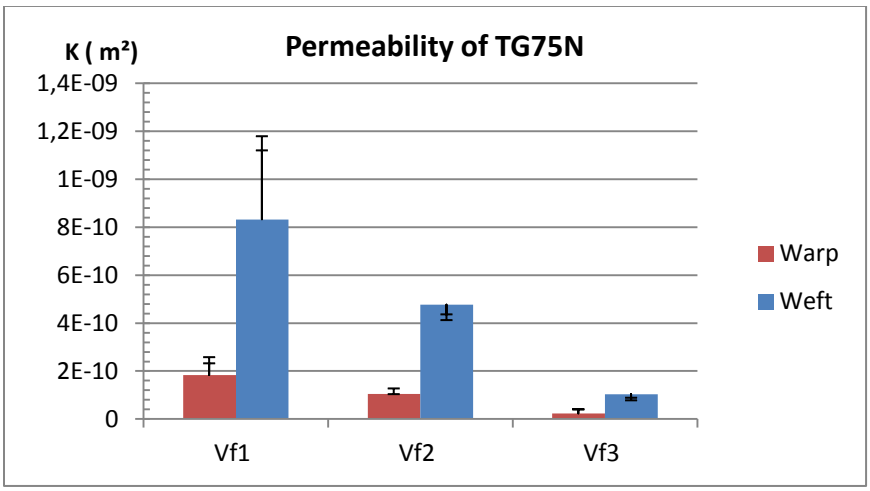

Illustration 20 Valeurs expérimentales et analytiques pour le tissus TG75N

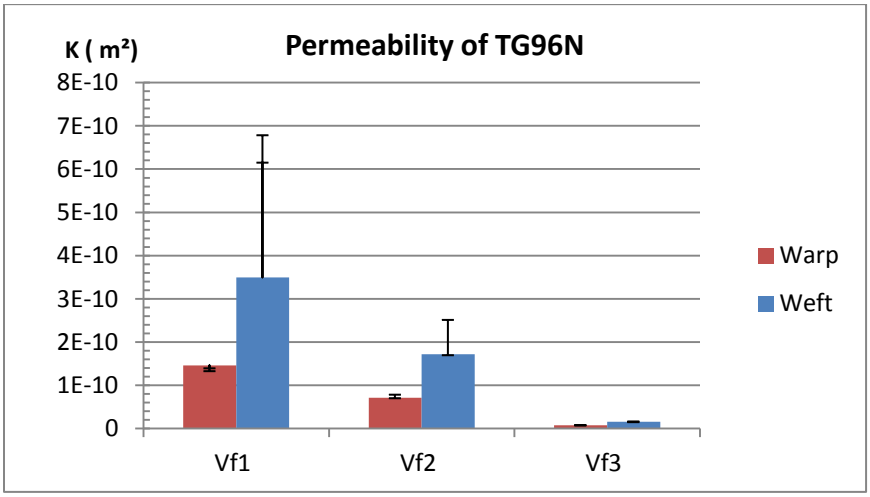

Illustration 21 Valeurs expérimentales et analytiques pour le tissus TG96N

Dans une vue globale sur toutes les 30 valeurs prédites, vingt-deux valeurs sont à l'intérieur ou très proches des valeurs dispersées expérimentales. En d'autres termes, il n'y a pas d'erreur entre ces valeurs et celles mesurées. Les autres résultats sont proches des mesures expérimentales, de sorte qu'ils représentent une représentation réelle de toute simulation ou injection réelle.

Dans la dernière partie de ce chapitre une discussion concernant la sensitivité du modèle à plusieurs paramètres est lancée. Le modèle incorpore le volume des canaux "mésopores" où leur pourcentage de volume a un fort effet sur la résistance au flux. Le modèle comprend cette influence géométrique en tenant compte de la distribution de canal entre la direction de la chaîne et de la trame, où la perméabilité augmente avec un volume croissant de mésopore selon la méthode d'injection souhaitée et vice versa. Ceci a été observé dans le rapport des «fractions volumiques des mésopores». Le modèle a pris en compte les mésopores, les micropores et l'architecture dans la région "1", où r_{eff1} prend en considération le type de matériau et ε_{eff1} représente une porosité efficace simulant les mésopores. L'effet du fil de couture est pris en compte en introduisant r_{eff2} et ε_{eff2}.

Dans le septième chapitre une méthode de modélisation élément finis (EF) est présentée dans le but de prédire la perméabilité macroscopique dans le plan.

En se référant à la revue de la littérature du chapitre 2, on peut conclure que les méthodes numériques proposées pour l'évaluation de la perméabilité macroscopique montrent des résultats insatisfaisants. Ceci est attesté par les recherches croissantes qui concentrent sur la modélisation de la perméabilité à l'échelle macroscopique.

Pour surmonter ces lacunes, cette étude met l'accent sur une modélisation numérique à l'état statique, rapide et simple des composants de la perméabilité dans le plan de NCF et du tissu Taffetas à l'aide du logiciel COMSOL Multiphysics. La simulation numérique est basée sur l'hypothèse que la perméabilité microscopique dans les torons est négligeable par rapport à celle dans les mésopores.

En supposant qu'un toron est imperméable, l'écoulement microscopique est négligé. Cela entraînera un autre problème. La modélisation de l'écoulement passant par les mésopores a donné une valeur de perméabilité surestimée, liée à une augmentation inattendue de la vitesse d'écoulement du fluide, surtout lorsque la taille du mésopore est grande. Pour

résoudre ce problème, une petite quantité de fibres a été ajoutée dans les mésopores afin de diminuer la vitesse du fluide pendant le processus de modélisation numérique en des valeurs raisonnables, d'où les prédictions de perméabilité plus fiables.

L'effet de l'ajout de fibres dans les mésopores entre les torons a montré une amélioration de la prédiction de la perméabilité pour le NCF cousu en contrôlant l'augmentation inattendue de la vitesse d'écoulement de la résine qui est causée par la vacuité totale dans les mésopores à grand volume. Les voies d'écoulement de la résine primaire sont les mésopores primaires (dans la direction d'écoulement), tandis que les voies secondaires d'écoulement de la résine sont les mésopores secondaires (perpendiculairement à la direction d'écoulement). La vacuité complète conduit à négliger l'estimation de la perméabilité des milieux poreux du textile et à négliger l'effet des voies probables d'écoulement secondaire de la résine. Pour les tissus à armure, du fait que les torons de chaîne et de trame sont entrelacés ensemble, le volume de mésopore est petit, la forme poreuse du textile est bien représentée et la perméabilité dans les voies secondaires est bien évaluée.

Afin de prédire les valeurs de perméabilité (K_{0° et K_{90°), la grandeur moyenne de la vitesse est déterminée comme une sortie des simulations. Ces valeurs sont utilisées pour calculer K_{0° et K_{90° en utilisant la loi de Darcy. Illustration 22 montre comment la vitesse à l'intérieur des mésopores primaires (mésopores le long de la direction de l'écoulement) est largement surestimée, alors que la vitesse dans les mésopores secondaires (mésopores perpendiculaires à la direction de l'écoulement) est sous-estimée.

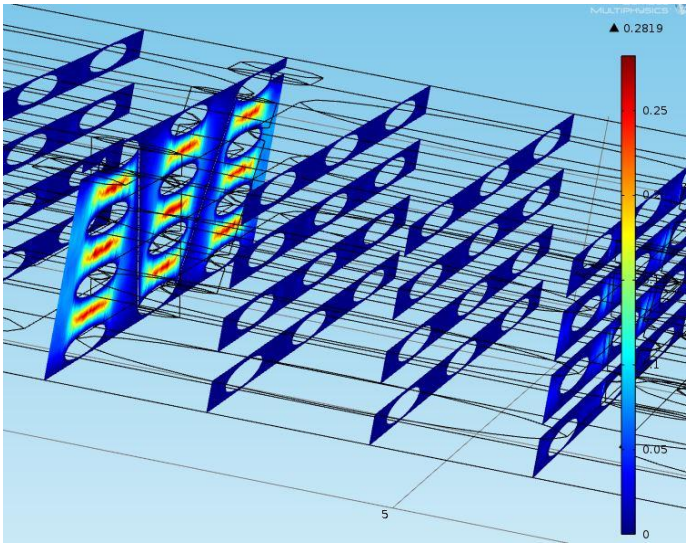

Illustration 22 Vitesse avant l'ajout des fibres

En fait, en raison du gros volume de mésopore, le mésopore est considéré comme une voie illimitée. Ainsi, afin de contrôler l'augmentation soudaine de la vitesse produite par le gros volume de mésopore, de petites fibres ont été insérées entre les torons. Cette action a résolu le problème de la modélisation numérique qui semblait ne pas comprendre le comportement de remplissage à l'intérieur du mésopore.

Le volume de fibres ajoutées est très faible par rapport au volume total du domaine. Par conséquent, il n'y a pas de changement effectif dans la fraction de volume de fibres. Le Tableau 5 montre que l'ajout de fibres à différentes dimensions ne modifie pas de manière significative les valeurs de perméabilité prédites, en effet, elle réduit considérablement l'erreur.

Fibre ajoutés	$k_{exp}(m^2)$	$k_{num}(m^2)$	**Erreur (%)**
2 Fibres (0.1*0.1 mm^2)	$1.46E^{-11}$	$8.311E^{-12}$	-43
2 Fibres (0.1*0.03 mm^2)		$8.55E^{-12}$	-41.42
4 Fibres (0.1*0.03 mm^2)		$7.977E^{-12}$	-45.36

Tableau 5 Effet du nombres de fibre ajoutés sur la permeabilité

Les résultats numériques obtenus à partir de ces simulations après l'ajout de fibres dans les mésopores ont été comparés aux données expérimentales et ils ont montré un bon accord. Pour les textiles Taffetas, les simulations numériques sont effectuées sans addition de fibres dans les mésopores en raison du petit volume de ces mésopores. Les résultats obtenus à partir de ces simulations ont été comparés aux données expérimentales

et ils ont montré un bon accord avec une moyenne des erreurs absolues de 34,48% et 33,03% dans les tissus de verre et de carbone respectivement. Enfin, la modélisation EF réalisée dans cette étude a prouvé son efficacité, où elle pourrait être utilisée pour modéliser la perméabilité à différents rapports de volume de fibre et de différents textiles dans les directions de la chaîne et de la trame de manière rapide, facile et stable. Un travail ultérieur pourrait se concentrer sur les simulations de mode transitoire.

Conclusions générales et Perspectives:

"LCM" sert à produire des pièces composites haute performance à condition de bien contrôler les conditions et toutes les étapes du procédé. L'étape la plus critique est la détermination de la perméabilité. En effet, une évaluation précise, simple et rapide de la perméabilité est une étape décisive pour effectuer des simulations de remplissage et optimiser la stratégie d'injection. Ce sont les principales raisons qui motivent ces travaux.

En conclusion générale, la valeur de perméabilité dépend d'un certain nombre de facteurs interdépendants. Chacun d'eux a sa propre influence sur le résultat final. Par exemple, deux tissus ayant la même architecture mais constitués de différents matériaux ont des tenseurs de perméabilité différents. Les principaux facteurs influençant les valeurs de perméabilité peuvent sont :

- Le type de tissu
- L'existence d'un fil liant
- Le matériau du tissu
- La densité
- Paramètres de fabrication

L'influence qualitative des paramètres mentionnés ci-dessus a été discutée au cours de ces travaux. Chaque méthode d'évaluation de la perméabilité présente ses propres avantages, inconvénients et limites. Le résumé rappelle les conclusions de ce travail sur les méthodes expérimentales, numériques et analytiques.

Les mesures expérimentales sont encore confrontées à des problèmes majeurs concernant la perméabilité dans le plan. Ces difficultés sont dues à de nombreux facteurs tels que la méthode de mesure, le dispositif de mesure, la préparation de l'échantillon et les compétences de l'opérateur. Afin de mesurer la perméabilité dans le plan, une

méthode bien connue a été adoptée dans le Benchmark II. Les composants de perméabilité dans le plan de onze tissus différents ont été déterminés dans cette thèse pour différentes fractions de volume de fibres. Le type de tissus se compose de tissu cousu unidirectionnel, NCF, tissus Taffetas et tissus 3D orthogonaux. Des résultats cohérents ont été obtenus selon la méthode utilisée. En ce qui concerne les mesures de perméabilité à travers l'épaisseur, la méthode utilisée est simple à conduire, les coûts d'outillages stables et reproductibles sont faibles. Cette méthode diffère des techniques traditionnelles dans la procédure de mesure, où une amélioration a été effectuée, dans laquelle la pression sera mesurée à l'aide de l'unité d'acquisition de données à des vitesses alternatives en remplaçant la mesure du point unique (pression-vitesse). La perméabilité transversale de sept tissus a été réalisée pour différents types de textiles (tissus unidirectionnels, bidirectionnels cousus et tissus 2D et 3D). Les mesures sont répétables et précises pour plusieurs tissus à architectures différentes.

Différentes méthodes numériques prédisent la perméabilité. Un effort continu est axé sur le développement de nouvelles méthodes numériques car aucun produit ne fournit encore de résultats cohérant avec les expériences. Cette étude a traité le problème de la prédiction de la perméabilité en résolvant l'équation de Navier-Stokes à l'intérieur des mésopores. Lors de l'évaluation de la perméabilité des torons de fibres unidirectionnels, une cellule unitaire aléatoire représentative de l'état réel du renforcement fibreux est choisie. Des simulations en mode statique ont été effectuées dans les directions longitudinale et transversale. D'autre part, les simulations de mode transitoires effectuées pour un écoulement transversal ont donné des résultats compatibles avec les simulations de mode statique. Lors de l'évaluation de la perméabilité des textiles, on utilise une méthode de simulation en mode statique en supposant que les torons sont imperméables. Cette simulation montre qu'un chemin primaire et un chemin secondaire sont disponibles. Les chemins primaires sont des mésopores dirigés le long de la direction d'écoulement, tandis que les chemins secondaires sont des mésopores dans la direction perpendiculaire. Sur le chemin primaire, pour les mésopores connectés ayant un volume élevé, la perméabilité est surestimée. De petites fibres ont été introduites dans les mésopores; ces fibres ont réduit la vitesse dans les chemins primaires, de sorte que l'erreur a été considérablement réduite par rapport aux résultats expérimentaux.

A propos des Modèles analytiques applicables aux torons de fibres unidirectionnels, beaucoup de progrès ont été réalisés dans la bibliographie sur l'évaluation analytique de la perméabilité microscopique. Plus de vingt modèles ont été trouvés dans la littérature scientifique, certains sont applicables pour les écoulements longitudinaux, d'autres pour les écoulements transversaux. Cependant, ces modèles présentent une grande dispersion par l'un rapport à l'autre. Ils peuvent être évalués en comparant la perméabilité prévue avec les résultats dérivés d'autres méthodes de prédiction. Cette analyse a montré que certains modèles ont été sélectionnés pour proposer des modèles les plus précis.

Les modèles analytiques applicables aux tissus sont peu nombreux. Cela est dû aux difficultés rencontrées dans la recherche dans ce domaine. La plupart des modèles développés sont soit loin de la cible, ou ont une gamme limitée d'applications, ou sont difficiles à appliquer. Un modèle prédictif a été développé pour estimer la perméabilité unidirectionnelle dans les directions chaîne et trame pour une famille de tissus 3D-orthogonaux et NCF. La mise en œuvre de ce modèle nécessite la connaissance des paramètres géométriques de base, de l'architecture des tissus et des informations concernant la compaction. Ces paramètres comprennent la dimension des mésopores et l'architecture des torons, qui sont déterminés à partir des images du tissu et de la fiche technique. En outre, des informations sur le volume moyen des mésopores et des faisceaux de fibres sont nécessaires et sont calculées pour différentes fractions de volume de fibres en tenant compte d'une cellule unitaire sélectionnée dans les directions chaîne et trame. Un bon accord est trouvé entre les résultats expérimentaux et les prédictions du modèle analytique proposé.

La compréhension des phénomènes physiques régissant l'écoulement d'un liquide dans les mésopores et les micropores d'un tissu représente la contribution majeure de cette thèse au domaine des composites. La dernière méthodologie expérimentale a été appliquée pour mesurer la perméabilité de treize tissus pour former une base de données de perméabilité. Des modèles analytiques ont été développés pour deux grandes familles de tissus. Leur généralisation à d'autres architectures de renforts tissés comme les tissus 2D et 2.5D interlock. Cependant, étant donné que ces tissus sont géométriquement plus complexes, en particulier en raison de l'emboitement entre les couches, il est important de développer des modèles géométriques de ces tissus à partir de rayons X à micro-

tomographie combinés à la technologie de reconstruction d'images. Des simulations numériques pourraient alors être réalisées dans des cellules unitaires représentatives du matériel réel.

Chapter 1: Introduction

Composite materials are known by the combination of two heterogeneous materials having complementary properties. The first is the fiber reinforcement and the second one is known as matrix. In general the fabric or the reinforcement supports all the necessary stiffness and strength in the composite, the matrix surrounds the fabric protecting it against chemical and environmental attack. The matrix properties have a lower modulus and greater elongation than the reinforcement, which allows benefiting from all fiber properties when transmitting the load in the composite part. Depending on the selected materials and processing, composite properties are variable in their properties and usages. Reinforcement properties depends on two main variables the material and the weaving pattern. Table 1 shows some raw material properties while compared to traditional metallic materials.

Material property	Density (Kg/m3)	Axial modulus (GPa)	Transverse modulus (GPa)	In-plane shear modulus (GPa)	Tensile strength (MPa)	Axial compressive strength (MPa)
E-glass	2600	72	72	30	2100	1500
S2-glass	2650	87	87	36	3500 – 2850	3000 - 2450
AS4carbon	1800	231	15	15	3500	3000
IM7carbon	1800	276	19	27	5180	3200
Kevlar	1400	80 - 110	7 - 10	5	3500	2900
Spectra	970	80 - 110	7 - 10	5	2400 - 3200	
Steel	7800	200	200	70	200 - 1800	200 - 1000
Aluminum	2700	70	70	40	150 - 600	100>
Epoxy LY556	1200	3.35	3.35	1.24	80	120
Polyester S-15080 L	1100	4	4	-	50	-

Table 1 Raw material mechanical properties

Fiber reinforced polymers, which are a combination of resin and fibers, are generally processed by different techniques. The methods used are Liquid Composite Molding (LCM), filament winding, pultrusion and layup processes. Depending on the application, the cost, the quantity and other criteria, a manufacturing process is selected. LCM processes is increasingly used to manufacture composites due to its repeatability, medium

cost and flexibility. Resin is injected or infused into a mold filled with dry fabric, this process is performed under different conditions (constant pressure or velocity, atmospheric or vacuum outlet ports…) with different methods (RTM, VARTM, VARI, RIF). These methods are considered as promising composite fabrication techniques because of their relatively low equipment and tooling costs, short cycle times, repeatability, and the capability to make complex parts.

1.1 Problem statement

An important problem appears in LCM due to the presence of voids and dry zones which cause different types of defects in the manufactured part. Thus, a well manufactured part after successful mold filling decreases both the macroscopic and microscopic voids, insuring optimal mechanical properties. Mechanical properties can determined experimentally, numerically or analytically [46-48]. Hallal and Younes [49] presented an analytical modeling of the mechanical behavior of textile composites, the objective of this study is to evaluate in-plane and out of plane ultimate strengths for different types of 2D and 3D fabric-reinforced polymer. Optimal mechanical properties are obtained when modeling an ideal unit cell (free voids assumption). The presence of voids has a major influence on mechanical properties. As noticed in [50-52], the tensile, flexural and inter-laminar shear strength decrease as the void content increases. It’s shown that the decreasing percentage of inter-laminar shear strength is the largest, while the flexural modulus decreased asymptotically with increasing void contents. However, the rate of decrease is lower for tensile strength. Moreover, the micro voids could affect the fatigue life of a structural component [53, 54]. In LCM process, voids appear due to faulty injection scheme, such as incorrect placement of injection ports and air vents or faulty injection and vent pressures and finally wrong filling simulations. The quality of LCM processed components depends not only on the preform and resin system, but also on the filling process itself. Parameters influencing filling behavior are the mold geometry; the resin viscosity; the mold temperature; the placement of the injection ports; and finally the most critical parameter is the permeability evaluation of the reinforcement.

Software such as PAM-RTM [55], LIMS [56] and Polyworx [57] allow one to predict the filling behavior, to obtain the filling times and flow front shapes. These software require some inputs:

- The drawing of the part
- The viscosity of the resin
- The permeability tensor

The geometry and viscosity are related to the designer and resin type respectively; while the permeability tensor depends on the type of the textile and the fiber volume fraction after compression of the fibrous reinforcement. Dry zones and voids may appear if the specifications such as positions of injection and vent gates, injection pressure, or pressure difference $P_{inlet} - P_{outlet}$ are not well defined.

Thus, the most critical step in composite manufacturing processes based on injection/infusion consists of simulating the resin flow according to injection positions and inlet flow pressure and velocity. Darcy's law [58] equation (1) was generalized to accommodate anisotropic porous media as follows, and is used in modeling the resin flow of the fluids.

$$\bar{u} = -\frac{K}{\mu}\nabla P \qquad \text{Eq.(1)}$$

where ū is the volume averaged Darcy velocity, μ the viscosity of the fluid, ∇P the pressure gradient, and *K* the permeability tensor of the porous medium. The permeability tensor will have the following form in the reference system (1, 2, 3), where (1, 2) are the in-plane directions and (3) the through-thickness direction.

$$\begin{pmatrix} K_{11} & K_{12} & K_{13} \\ K_{21} & K_{22} & K_{23} \\ K_{31} & K_{32} & K_{33} \end{pmatrix}$$

To switch from one coordinate system to another a rotation matrix must be used [59], the rotation matrix is given as follows:

$$R(\theta_1, \theta_2, \theta_3) = F \begin{pmatrix} \cos\theta_3 & -\sin\theta_3 & 0 \\ \sin\theta_3 & \cos\theta_3 & 0 \\ 0 & 0 & 1 \end{pmatrix} \begin{pmatrix} \cos\theta_2 & 0 & -\sin\theta_2 \\ 0 & 1 & 0 \\ \sin\theta_2 & 0 & \cos\theta_2 \end{pmatrix} \begin{pmatrix} 1 & 0 & 0 \\ 0 & \cos\theta_1 & -\sin\theta_1 \\ 0 & \sin\theta_1 & \cos\theta_1 \end{pmatrix}$$

where (Θ_1,Θ_2,Θ_3) are respectively the rotations about the axis (1,2,3). If the permeability tensor is orthotropic, as per general cases for laminates, 2D textiles and 3D preforms, so $K_{12}=K_{21}=K_{23}=K_{32}=K_{13}=K_{31}=0$, and thus the permeability tensor in the principal coordinate system (1,2,3) will be simplified to:

$$\begin{pmatrix} K_1 & 0 & 0 \\ 0 & K_2 & 0 \\ 0 & 0 & K_3 \end{pmatrix}$$

In the general case, the thickness of the manufactured part is much smaller than the in-plane dimensions; hence the through-thickness permeability K_3 can be neglected in most injection processes, while K_1 and K_2 are essential to model the in-plane flow. However K_3, the transversal permeability is important for thick parts and in some particular 3

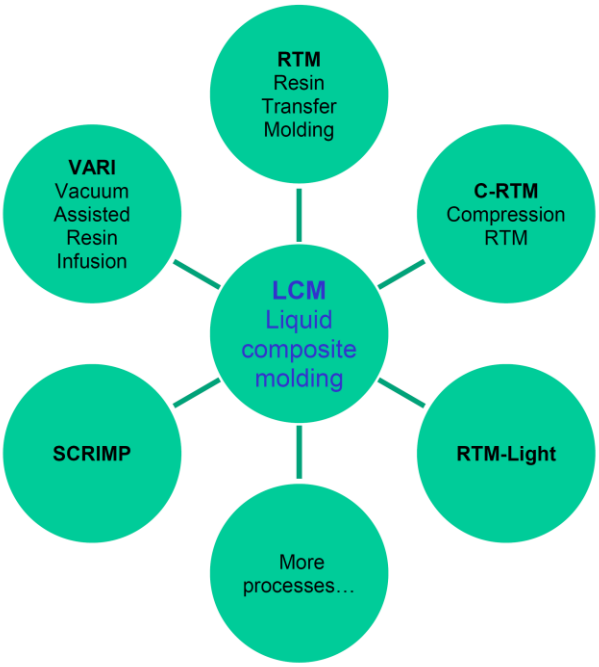

Figure 1 Liquid Composite Molding Examples of processes

Figure 2 [60] describes briefly different liquid molding techniques, showing the reinforcements architecture and main polymers that can be used in each process. In the next section, a brief review on most used injection processes, RTM (Resin Transfer Molding) and VARTM (Vacuum-Assisted RTM) is presented. Other processes such as VARI (Vacuum-Assisted Resin Infusion) and RFI (Resin Film Infusion) are widely used as infusion processes.

Processing techniques	*Brief description*	*Main reinforcements*	*Main polymers*
Injection molding	Thermoset or thermoplastic resins are heated into the barrel and transformed into a liquid before the injection into a mold	None, short fibers	Numerous thermoplastics, unsatured polyesters, phenolics
Vacuum injection molding	Vacuum is used as the sole force for the impregnation by a preformulated resin	Mats, fabrics, core materials for sandwich	Thermoset resins
Resin transfer molding (RTM)	Liquid resin is transferred with low pressure into the closed mold to impregnate the preplaced reinforcement	Mats, fabrics, foam or other cores, inserts, etc. 3-D fabrics	Thermoset resins
Reactive injection molding (RIM)	Monomer and initiator reactive solutions are mixed just prior the injection to offer fast polymerization	None	Polyurethanes, polyamides 6 (NyRIM), thermoset resins
Reinforced reactive injection molding (RRIM)	Reinforcement is added to one of the resin component before mixing	Short fibers, glass flakes	Polyamides, polyurethanes, cyclic polyesters, thermoset resins
Structural reaction injection molding (SRIM)	Combination of RTM with RIM	Mats, fabrics	Polyamides, polyurethanes, cyclic polyesters, thermose resins
Reaction injection pultrusion (RIP)	Reinforcement is pulled continuously through a die where a reactive resin	Rovings, mats, fabrics	Thermoset resins, Polyamide, polystyrene

Figure 2 Description of the different liquid molding techniques

RTM and VARTM

RTM and VARTM are injection processes, where the mold is loaded with the fibrous reinforcement, the mold is closed, and resin is injected (Figure 3). As previously described, one of the most critical steps is predicting the fabric's permeability. Since they are injection processes, in-plane permeability predicted values (K_1, K_2) are an input for filling simulating software. In their turn these software will describe the filling behavior and filling time. Good prediction of permeability values will reduce the drawbacks, increase part quality, and lower injection time. The mold is often put under vacuum; it must be designed so that resin can reach all areas of the part. In general molds are made of composites, but metallic materials can be used. Table 2 shows some advantages and drawbacks of RTM process.

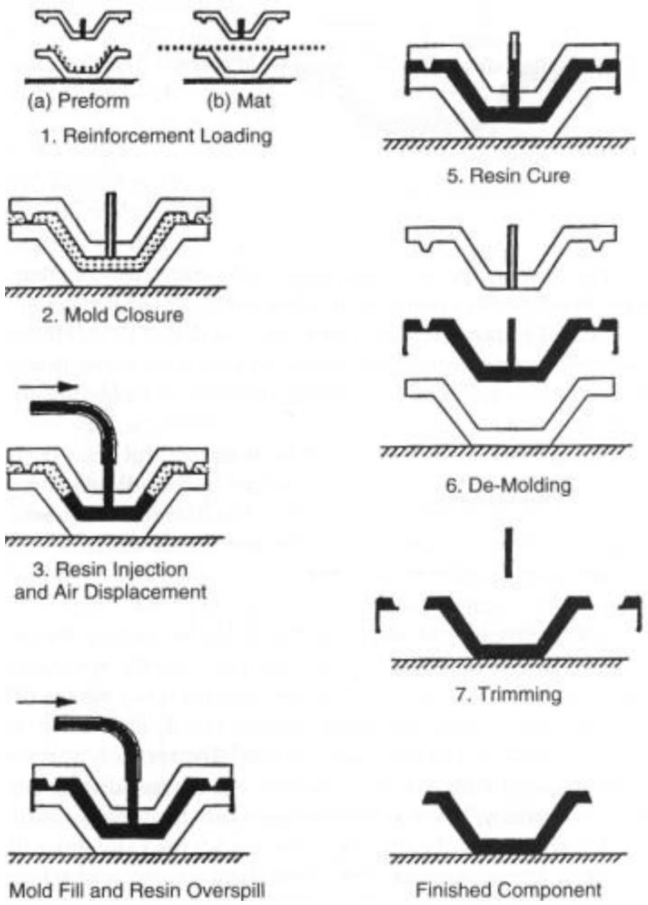

Figure 3 RTM schematic

Advantages	Disadvantages
Very complex shapes can be made	Moulds and presses can be very expensive
Production times shorter than lay-up	Mould design is critical and difficult
Surface finish is better than lay-up	Control of resin uniformity is difficult
Many mould materials are available	May have resin-rich corners and edges
Better reproducibility than lay-up	Used to fabricate small to medium parts
Better health and safety conditions than lay-up	Reinforcement movement during resin injection in low clamping pressure
Amenable to automation	

Table 2 Advantages and disadvantages of RTM process

Advantages	Disadvantages
Can be used to fabricate very large parts	Inlet and outlet design is critical and difficult
Single-sided mould means low tooling costs	V_f usually lower than prepreg or RTM
Much better properties than wet lay-up	Control of resin uniformity is difficult, with resin-rich corners and edges
Better health and safety conditions than lay-up	Reinforcement movement during resin injection is potentially a problem
Amenable to automation	Susceptible to problems with vacuum leaks

Table 3 Advantages and disadvantages of VARTM process

VARTM is quite similar to RTM, but one part mold substitutes the two parts mold, a vacuum bag is used instead of the second part and vacuum is connected to the outlet port. This change permits fabricating large parts. Table 3 shows some advantages and drawbacks of RTM process.

Overview about fabrics' architectures and their qualitative influence on permeability

Different types of fabrics are found in the market. Their material as well as the weaving pattern has a big influence on mechanical properties. Figure 4 shows five different types of fabrics generally used in LCM processes.

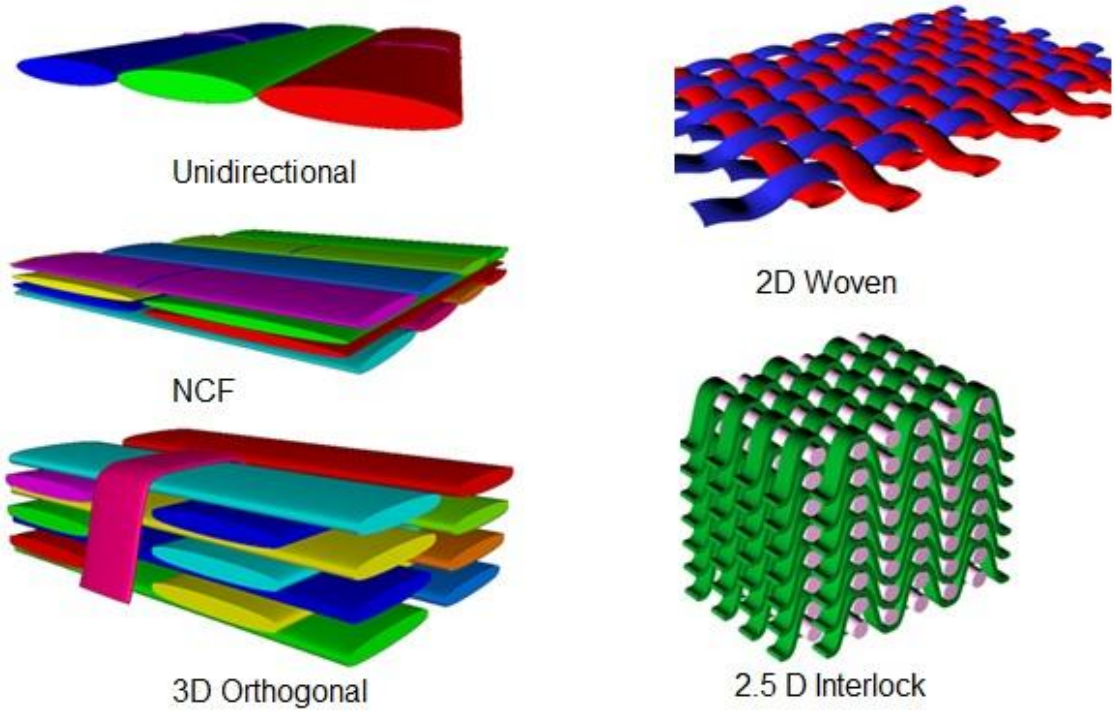

Figure 4 Different fabric architectures

In the NCF the mesopores, namely the gap between the tows, are much larger than the open elongated spaces inside the tow, micropores and these large gaps are connected. So the flow path can be treated as if the mesopore and micropores were connected together in parallel. The liquid will flow mainly through the mesopores and the permeability is determined predominately by the flow resistance in the mesopores.

In unidirectional textiles, its structure is similar to that of the NCF except for two issues:

- The mesopores are smaller than those in the NCF.
- The flow paths are different along the warp and weft directions.

So the flow in the unidirectional fabric can be modeled as a mesopore and a micropore connected together; this connection is in series for a flow in the weft direction (crossing the bundles) and considered in parallel for the flow in the warp direction (along the bundles). Thus the permeability is dominated by the mesopore permeability in the warp direction flow and this value drops significantly when the flow is forced to pass across the bundles in the weft direction.

The 3D orthogonal fabrics are quite similar to NCF with larger mesopore size, and large through-thickness bundles. The mesopore size being larger, this represents an increase in the permeability in this region, while the through-thickness bundles are at the same time obstacles and gains for permeability:

- These bundles increase the resistance to the flow.
- These bundles create mesopores of significant size while interlacing over the weft bundles.

Concerning 2D woven reinforcements, although there are many mesopores in the fibrous reinforcement, these pores are generally not connected to each other. To flow from a mesopore to another, the liquid has to go through some smaller mesopores or through micropores, depending on the nesting factor. So the flow in these fabrics can be described as passing through a large mesopore and a medium pore or a micropore connected together in series. The permeability of this kind of fabrics is mainly determined by the flow resistance in the small mesopores and micropores.

The 2.5D Interlock fabrics are similar to the 2D woven fabrics, but these textiles are more stable under compaction, since their permeability is less disturbed by the nesting factor.

Different methods have been used to predict the permeability tensor: experimental, numerical, and analytical methods. Significant research effort have been directed on the development of numerical prediction methods, indeed these methods are far from

predicting improper permeability, although a lot of computer time is needed to converge, which make it impractical.

However, the prediction of the permeability tensor, even experimentally, is still facing a series of problems [8]. Experimental errors, used equipment, measurement techniques, and faulty preparation of specimens provide inconsistent results which make unreliable the experimental evaluation of the permeability tensor. Fortunately much progress was achieved to agree on a measurement method in the second international permeability benchmark [9].

Analytical research results non for predict the microscopic longitudinal and transverse permeability of unidirectional fiber beds. Indeed, no comparative study was conducted to select the best models from experimental results. On the other hand, few models were developed to predict the permeability tensor of engineering textiles. The few models proposed suffer from one of the following drawbacks:

1. Show a large scatter when compared to experimental values.
2. The models are based on empirical considerations that limit their range of applicability to specific fabrics.
3. Some models are difficult to apply, due to the difficulty of obtaining required its input data.
4. Others are only verified for a single value of fiber volume fraction.

In general, the few models found in the scientific literature are specific and do not cover a wide range of fiber volume fractions or textiles.

1.2 Objectives and Methodology

Objectives

In this study, the main goal is to obtain the in-plane permeability values in the most accurate, simple, and robust way. To do so, a series of secondary objectives are enumerated below:

1. A comparative study is conducted to select the best models to predict the permeability of unidirectional fiber beds.

2. The in-plane permeability is measured for eleven different fabrics of different architectures. These measurements are carried out using a well known, internationally agreed on, reliable and efficient experimental method.
3. Because of a lack of data on fabric specifications and permeability, detailed geometrical parameters are provided for each fabric, as input for analytical or finite element FE numerical models
4. Develop a simple, accurate and easy to apply analytical model to predict the in-plane permeability.
5. Develop a simple and rapid numerical simulation method to predict the in-plane permeability.

In addition to the mentioned objectives, note that the through-thickness permeability was also measured for seven textiles.

Methodology

In order to achieve these goals, two new methodologies were developed under the following acronyms.

- Methodology “1” to predict the in-plane permeability by an analytical model.
- Methodology “2” to predict numerically the in-plane permeability.

In a first step, before explaining these approaches, it was necessary to preform a series of measurements to gather necessary information on which this work is based.

Methodology “1”

In a comparative study, a series of convenient analytical models allowed evaluating the analytical permeability of unidirectional fibrous media in normal and parallel flows. In a first step, analytical models reviewed were compared with numerical simulations and experimental results obtained in the scientific literature. However these results showed big differences between each other for the same fiber volume fraction. This reveals the importance of performing a numerical study to simulate a real experiment and find a way to validate the experiments. This numerical FE analysis is applied for a random fiber packing structure. The average volume filling speed evaluated under constant pressure, namely the saturated permeability value. The numerical

investigation was conducted in both the longitudinal and transversal directions. A more advanced study carried out for the same unit cell in transient mode, in which the flow front position is detected as a function of time, taking into consideration capillary effect. The average unsaturated permeability is derived from the numerical results. This simulation approved the consistency of static mode simulation. The values were selected from the scientific literature at different fiber volume fractions. When two values exist for the same fiber volume fraction, the permeability value that best matches with the numerical data is chosen for the comparative study. This selection between different experimental values is necessary, because experiments are far from being perfect. This is probably due to the inconsistency of the measuring procedures used by different investigators. A two-level comparative study is performed between all the data provided by the selected experiments and the analytical models. ***From this comparison, the best models to predict the microscopic longitudinal and transversal permeability for unidirectional fiber beds are selected.***

Based on the selected microscopic permeability analytical model of unidirectional fiber bundles, ***a predictive model is developed to estimate the unidirectional permeability in both, the warp and weft directions, for a family of non-crimped and 3D orthogonal fabrics.*** The implementation of this model requires basic geometrical parameters of the fabric architecture and information concerning the compaction of the preform. Those parameters include the dimension of the mesopores and the architecture of the fiber bundles, which are determined from pictures of the fabric, and from the textile data sheets. In addition, the average volume of mesopores and fiber bundles are required and are calculated for different fiber volume fractions by considering a unit cell in the warp and weft directions. As a matter of fact, the model evaluates two contributions: the first one deals with the flow inside and in between the tows, while the second one figures out the flow deviations arising from the stitching yarns. The model uses the effective average radius of the fibers and the fiber volume fraction to evaluate the permeability for the two flow contributions mentioned from the analytical previously selected unidirectional microscopic permeability models. The permeability values of the two regions are summed in parallel. The macroscopic permeability is calculated by multiplying the permeability of the two regions by a factor representing the ratio of the

mesopore volumes in one direction with respect to the other. A comparison is done between experimental results and the predictions of the proposed analytical model.

Methodology "2"

This methodology is used to develop a steady-state fast and easy numerical study of the in-plane permeability components for unidirectional, NCF, and plain weave fabrics using COMSOL Multiphysics software. The modeling is based on a unit cell that uses solid bundles and takes into account only the mesoscopic flow, and neglects microscopic flow inside the bundles. The equivalent permeability of the mesopores is shown to be very high. Adding fibers in the mesopores between bundles showed a significant improvement in permeability prediction for stitched NCF and 3D orthogonal textiles. For plain weave or angle interlock textiles, since the warp and weft bundles are interlaced together, the mesopore volume is small, the porous shape of textile is well represented and the secondary flow channels are considered. A comparison between the errors before and after adding fibers in the mesopores is shown. The results obtained will be compared to experimental measurements of in-plane permeability components.

1.3 Thesis outline

This thesis is divided into eight chapters including this one. The second chapter presents a review on permeability prediction methods. In Chapter 3 a comparative analytical, numerical and experimental analysis of the microscopic permeability of fiber bundles is achieved. Chapter 4 show a description of the selected methodologies for both the in-plane and through-thickness measurements, and describe the fabric specifications and the permeability measurements. Chapter 5 develops the analytical model predicting the in-plane permeability for different NCF and 3D orthogonal fabrics. Chapter 6 presents a numerical analysis of permeability for unidirectional, NCF and plain weave fabrics. Finally, chapter 7 draws the conclusions of this work and sketches future perspectives.

2 Chapter 2: Review of Permeability Evaluation Methods

Different methods have been used to evaluate the permeability tensor: experimental, numerical and analytical methods. At the present time, significant research effort is extended on the development of numerical simulation tools to evaluate the permeability. However the results are still far from matching reality [23]. In addition, the experimental measurement of permeability faces also a lot of problems [8]. This is due to personal errors, equipment inaccuracy, faults in measurement techniques, and inadequate preparation of specimens. All these reasons may explain why inconsistent measurements results are obtained that make the experimental evaluation of permeability unreliable. However good progress was done in [9], concerning the experimental methodology, a method to measure the in-plane permeability was agreed on by 12 institutes and universities. As for the analytical method, different researchers tried to develop analytical or empirical models that predict the permeability for fabrics [24-30]. Most of the models developed were based on Cozeny-Karman equation or need an external support by numerical simulation or experiment to predict the macroscopic permeability. Most of these models still need require improvement to be more accurate. On another hand, more work was done on analytical models predicting the permeability of unidirectional fiber beds, but it remains limited to a specific family of fibrous reinforcements.

In an overview over the literature, no review was done regarding the different methods predicting the permeability tensor of fibrous reinforcements. Otherwise some reviews were dedicated on the prediction of permeability of other materials. These reviews are found applicable in petroleum, soil mechanics, nano-composites and other domains. Per example Babadagli and Al-Salmi [61], involved in petroleum field, reviewed the prediction of permeability in heterogeneous carbonates. The use of porosity and other petrophysical properties of rock in permeability prediction is discussed for carbonaceous rocks. This discussion also covers the usefulness of a wide variety of correlations developed using pore-scale. Lai et al. [62] overviewed the relationship between pore throat size distribution and permeability of tight sandstones. Renard et De Marsily [63] reviewed various methods used to calculate the equivalent permeability of a

heterogeneous porous medium. Water or petrol were the target flowing fluids. The review was limited to saturated regime and single phase medium.

Regarding fibrous reinforcements permeability, some efforts were done. Otherwise reviewed work was not extended to cover the essential predicting methods. Patino et al. [64] focused in their review on parameters affecting the permeability such as capillary pressure and injection port positions; leaving behind a huge family of analytical models predicting fiber bed permeability and other models predicting engineering textile permeability. Also they missed mentioning numerical prediction methods.

2.1 Analytical models

After several years trying to predict without much success, the permeability of fibrous reinforcements, considering only a single porosity scale, research has naturally turned towards taking into account the dual-scale architecture of engineering textiles. In fact, the presence of micropores between the fibers reduces permeability compared to a single scale prediction. The amount of reduction depends on the arrangement of micropores and mesopores; in other words, it is related to the architecture of woven fabrics.

Analytical models are generally based on single scale theory. Thus dual-scale permeability is not well predicted. Some models incorporate the effect of micropores by using an empirical factor. Because of these limitations and of the complicated interactions between the flowing resin and the fiber bed, previous work focuses on deriving analytical models predicting the permeability values of unidirectional fiber beds, typically known as microscopic permeability values.

A major progress occurred in development of models predicting permeability of unidirectional fiber beds. No general comparative study was found in the bibliography focusing on all the approaches used to characterize the microscopic permeability. Researchers who predicted permeability using different approaches used to validate their results by comparison with a selected experiment, a given model, or specific numerical simulations from the bibliography. We can note here a lack of generalized comparison. Chen and Papathanasiou [65] compared their finite element simulation results with the model of Drummond and Tahir [39]. Choi et al. [25] compared their finite element simulations to the analytical models of Gebart [33] and Berdichevsky and Cai [31, 32].

Tamayol and Bahrami [44] compared their analytical model to experiments from the literature. Wang and Hwang [66] compared the results of a finite element simulation to Gebart analytical model [33]. Sadiq et al. [54] compared their experimental results with the asymptotic model developed by Brushke and Advani [38].

2.1.1 Fiber bundle permeability

Analytically, researchers have studied the microscopic permeability for unidirectional fibers, and then derived different analytical models based on four various modeling approaches:

- lubrication theory,
- capillary model,
- analytic cell calculation,
- mixed models based on previous approaches.

Studies on the permeability of porous media date back to the experimental work of Carman [67] and Sullivan [68] in 1940s, and the theoretical analyses of Kuwabara [36], Happel [35] and Brenner [69]. ($Appendix\ 1\ Eq.1$).

Authors considered different types of unit cells, depending on fiber stacking pattern. Figure 5 [44] shows four types of fiber stacking. Square and hexagonal arrays are the most widely used arrangements in this area.

Kuwabara [36] solved the vorticity transport and stream function equations and employed a boundary layer approach to predict permeability for flows normal to randomly arranged fibers for materials of high porosity ($Appendix\ 1\ Eq.2{,}3$). Happel [35] and Brenner [69] solved analytically the Stokes equation for parallel and normal flows around a single cylinder with a free surface model (limited boundary layer). The boundary conditions used by Happel and Brenner [69] were different from Kuwabara's study [36]. They supposed that the flow resistance of a random 3D fibrous structure is equal to one third of the parallel plus two thirds of the normal flow resistance of a 1D array of cylinders. Later, Sangani and Acrivos [43] performed analytical and numerical studies on viscous permeability of square and staggered arrays of cylinders for the entire range of porosity values, when their axes were perpendicular to the flow direction. Their analytical models were accurate for the lower and higher limits of porosity. ($Appendix\ 1\ Eq.4$)

Drummond and Tahir [39] solved Stokes equations for normal and parallel flow towards different types of ordered structures. They used a distributed singularity method to find the flow-field in square, triangular, hexagonal, and rectangular arrays. They compared their results with the numerical values of Sangani and Acrivos [43] for normal flows. The model of Drummond and Tahir [39] for transversal flow was very close to the analytical model of Sangani and Acrivos [43], but it is accurate only for highly porous materials. ($Appendix\ 1\ Eq.5,6,7$)

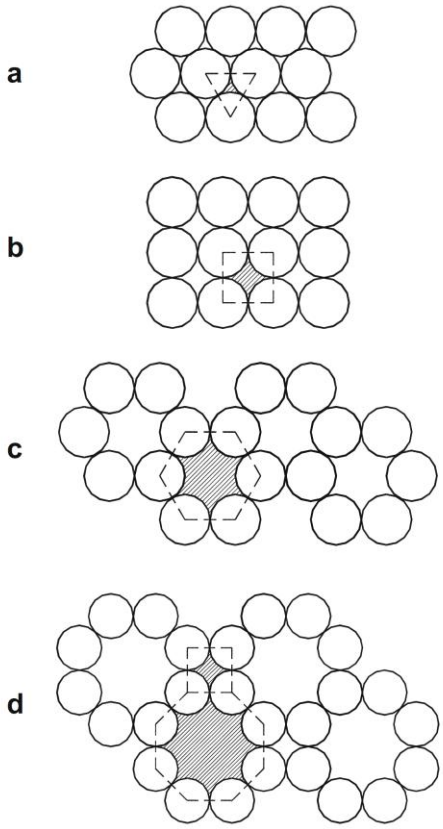

Figure 5 Triangular, square and hexagonal unit cells and combination of octagonal and square array of cylinders.

Sahraoui and Kaviani [42] included inertial effects and determined numerically the permeability of cylinders for normal flow. They also proposed a correlation which turned out to be accurate for a limited range of porosity values, i.e., 0.4 < 0.7. ($Appendix\ 1\ Eq.8$)

A general mathematical model derived by Gutowski [34] assumed that the fibers make up a deformable, nonlinear elastic network. The resin flow is modeled using Darcy's Law for anisotropic porous medium. ($Appendix\ 1\ Eq.9$). Gebart [33] derived an analytical model to predict the unidirectional permeability from Navier-Stokes equation, ($Appendix\ 1\ Eq.10,11$). In 1993 Berdichevsky and Cai [32], after performing numerical simulations, considered that permeability depends on the actual and ultimate fiber volume fractions. Then they derived a unified empirical model. ($Appendix\ 1\ Eq.12,13$). In the same year, they developed a "self-consistent model" [32], where Stokes flow and Darcy flow are respectively considered in each region. The boundary and interface conditions as well as two consistency conditions including the total amount of flow and energy dissipations, are implemented simultaneously. The permeability is calculated based on these considerations. The improved permeability model captures the flow characteristics in a given fiber bundle. In the transverse case, the gaps between neighboring fibers govern the flow resistance. The expression derived for the transverse permeability contains two variables: the averaged fiber volume fraction and the maximum packing efficiency, which turned out to describe correctly the status of a fiber bundle. ($Appendix\ 1\ Eq.14,15$).

Phelan and Wise [41] studied the transverse flow through rectangular arrays of porous elliptical cylinders and derived a semi-analytical model based on lubrication theory. The Brinkman equation is used to model the flow inside porous structures, and the Stokes equation to model the flow in the open media between the structures. ($Appendix\ 1\ Eq.16$). Lee and Yang [40] considered the flow as a non-Darcy flow through a porous medium. The continuity and momentum equations are solved at the pore scale on a Cartesian grid. To circumvent the numerical difficulties resulting from a flow domain of irregular shape, weighting functions based on the APPLE algorithm and the SIS solver are employed. The Darcy-Forchheimer drag (pressure drag) is then determined from the resulting volumetric flow rate under a prescribed pressure drop to derive their permeability model. ($Appendix\ 1\ Eq.17$). Brushke and Advani [38] considered the flow across regular arrays of cylinders. The analytic solutions are matched to produce a closed form solution. This is done by employing the lubrication approach at low porosity and the analytic cell model solution at high porosity. ($Appendix\ 1\ Eq.18$).

Using numerical simulations, Van der Westhuizen and Du Plessis [37] proposed a correlation for the normal permeability of 1D fibers. ($Appendix\ 1\ Eq.19{,}20$). Tamayol and Bahrami [44] studied ordered fibrous media normal and parallel flows in ordered fibrous media and derived an analytical permeability model. To predict permeability, a compact relationship is suggested by modeling 1D fibers in contact as a combination of channel-like conduits. Moreover, analytical relationships are developed for pressure drop and permeability of rectangular arrangements. This is performed by using an "integral technique" and simulating a parabolic velocity profile in the unit cells. The experimental results collected by others for square arrangements confirm the models developed. ($Appendix\ 1\ Eq.21{,}22$).

Tamayol and Bahrami [70] studied the transverse permeability of fibrous porous media both experimentally and theoretically. A scale analysis technique is used to derive the transverse permeability of fibrous media with a variety of fibrous matrices including square, staggered, and hexagonal unidirectional fiber arrangements. In this field, a relationship is established between permeability and porosity, fiber diameter, and the tortuosity of the fibrous medium. The pressure drop through different fiber arrangements and metal foams is measured in creeping flow regime. The results obtained are then used to calculate the permeability of the samples. Compact relationships can be obtained by performing comparisons with the present experimental results and the data given by others. ($Appendix\ 1\ Eq.23{,}24$).

The models listed in this section predict the longitudinal and transversal microscopic permeability "K_L" and "K_T". For most models, the permeability is a function of the fiber radius "r" and fiber volume fraction "V_f". However, some models links the permeability with other parameters like the maximum fiber packing factor "V_{fmax}", geometrical constants, and information on the packing structure (hexagonal or square or other structures) "V_a". These models will be compared in Chapter 4, where best models predicting the permeability will be selected.

2.1.2 Prediction of the fabric permeability

This part focuses on presenting the analytical models available to predict permeability. Carman [71] suggested the first to predict the permeability K of granular spheres. This

approach was applies later to composites. This model relates the permeability to the fiber volume fraction V_f, the fiber radius r_f together with an empirical parameter k called Kozeny constant:

$$K = \frac{r_f}{4k}\frac{(1 - V_f)^3}{V_f^2} \qquad \text{Eq.(2)}$$

Kozeny-Carman equation (2) was initially developed in Soil Mechanics. It was used later in order to predict the permeability of unidirectional fiber beds (microscopic permeability) [33], as well as fabrics' permeability values (macroscopic permeability) [25] and [72]. To predict the permeability of a woven fabric, Simacek and Advani [11] simplified the case-study by considering the 3D reinforcement as a 2D problem. They developed a model that can be resolved numerically. The flow is described by Darcy's equation within the yams and Stokes equation between the yarns and the mold. Using lubrication theory the flow is modeled in the mesopores located between the fabric and the mold. The mesopores inside the fabric are neglected. The longitudinal and transversal microscopic permeability values were considered equal. In order to validate the model, the effect of shear on pre-estimated values of permeability was investigated. It was observed that the trends for change in permeability with the angle of shearing are weaker in the model. The model is evaluated using some qualitative factors.

Choi et al. [25] studied the unit cell as a dual-scale fibrous medium. A coupled flow model was developed in this study by combining sequential and parallel flows in the micropores and mesopores. Carman-Kozeny model was used in order to predict the microscopic and mesoscopic permeability values. Carman-Kozeny constants are evaluated from finite element analysis. This model may be used in obtaining a more quantitative estimation of the permeability of fibrous media. The results were compared with the experimental measurements of Skartsis et al. on Hercules AS-4 graphite aligned fibers beds [73]. For perpendicular flow, the model is limited in predicting the permeability at relatively low fiber volume fraction. Although the agreement is yet far from the perfect, but the model showed an improvement when compared to previous models.

Shih and Lee [72] developed an empirical model in which they studied the flow in micropores, mesopores, and the relation between them. Berdichevsky and Cai model [31] was used to estimate the permeability in the micropores. Based on curve fitting with experimental measurements, the permeability of mesopores was predicted by Carman-Kozeny equation. The total permeability was summed up as a percentage of sequential and parallel permeability values. The results were qualitatively compared with experimental data.

Yu and Lee [30] considered a dual-scale flow problem; they employed Stokes equation for the flow in the mesopores, and applied Berdichevsky and Cai model in the micropores. The parameters of fabric architecture were measured prior to compaction. Based on experimentally measured permeability values, factors serving to predict the geometry of the compacted fabric were introduced. The model was validated for three different fabrics. Then Yu et al. [74] developed a fractal in-plane permeability model for the same fabrics; the pore size is calculated as function of the total fiber volume fraction. The flow rate through a single pore is given by modifying Hagen-Poiseuille equation. The finally proposed fractal in-plane permeability model is a function of the pore area fractal dimension, the tortuosity fractal dimension, and the parameters of fabric architecture. Results were then compared with previous data [75]. Nordlund et al. [26] developed a combined CFD unit cell/Network technique applied to NCF fabrics. The local permeability tensor is predicted by CFD, and by using a network modeling technique, the local permeability values are summed up in order to predict in-plane permeability values. More data of the geometrical dimensions were required be able to accurately validate the model, but the model values seem to follow the trend of experimental data.

Chen et al. [24] predicted the permeability in mesopores by numerical simulation and the permeability in micropores using Gebart analytical model [33]. Then under specified boundary conditions, they deduced the in-plane permeability based on Darcy's law. Satisfactory agreement is observed for three plain-weave fabrics with experimental data available in the literature [76]. Dong et al. [75] constructed a model in order to predict the permeability of non-crimped stitched fabric. The model deals with the unit cell with two essential regions; in the tows, Gebart model [33] was applied to predict the

permeability in the micropores. Based on Bahrami et al. [77], the permeability in the second region is predicted based on the pressure drop that can be related to geometric parameters of the cross-section. Finally, for a single fiber volume fraction, the calculated permeability is compared with finite element simulations [78] and experimental measurements [79]. A fiber volume fraction range of acceptability is noticed.

Shou et al. [27] developed an analytical model to predict the transversal permeability of aligned fibrous beds in a dual-scale medium. Their model correlated fairly well with experimental and numerical results in literature [41, 54, 80].

An analytical model was developed by Vernet and Trochu [28, 29] to predict the permeability of 2.5 D interlock fabrics. The model calculates the pressure drop inside the fabric after predicting the size and distribution of the mesopores. The model was validated by comparison with experimental values of principal permeability measured for five different 2.5 D interlock fabrics at a selected fiber volume fraction for each fabric.

2.2 Numerical simulations

In some cases, the geometrical complexity of the unit cell prevents from deriving an analytical solution. It is then necessary to resort to numerical methods and solve the equations of Fluid Mechanics at the mesoscopic level or dual-scale fibrous medium (microscopic and mesoscopic scales). Authors developed different methods to predict the in-plane permeability tensor numerically. These methods are based under three families of numerical techniques: finite element, finite difference, and Lattice-Boltzmann. Each method presents advantages and drawbacks.

Finite element methods are used in a large number of articles [10, 12-14, 16, 17, 81]. The approach consists of discritizing the unit cell into elements, inside which reference elements are defined. These local functions have the advantage of being simpler than those which could possibly be used to represent the total unit cell. [14] compared the derived results with a developed analytical model; the comparison shows good agreement for permeability values larger than 10^{-4} m^2. The main disadvantage of this method is its limitation to be applied to engineering textiles since finite element simulations did not converge on this permeability order.

Hoareau developed an analytical model based on lubrication theory and finite element simulations which were carried out on unidirectional lenticular impermeable fiber bundles [10]. Due to lack of experimental data no comparison was made between experimental and numerical results, indeed acceptable agreement is observed between permeability values derived from analytical and numerical modeling.

Laine performed numerical simulations in order to predict the permeability of two Hexcel fabrics: 2X2 twill weaved (G986) and a 2.5D interlock (G1151) [17, 81]. Nesting factor as well as the number of plies effects are considered on the permeability of the reinforcements. The permeability without taking into account nesting factor is compared to the permeability with nesting factor for both Stokes flow and Stokes-Brinkmann flow. Higher permeability values are observed for fabrics where the nesting factor is neglected. The limited amount of experimental results published on woven reinforcements, did not allow them to carry out a deep numerical-experimental prediction comparison.

Loix developed a methodology allowing to determine numerically the permeability when considering slow saturated flows through previously deformed woven fabrics [16]. Loix considered that the in-plane permeability magnitude order (10^{-9} m^2) is realistic as compared with experimental results obtained using similar fabrics. His comparison was more likely to be qualitative than quantitative.

Ngo and Tamma [12] applied stokes equation to model the flow in the mesopores and brinkman's equation in the micropores. The simulations were carried on a woven fabric. Due to the lack of experimental measurements in the literature, the simulation was compared to experimental results of Adams et al. [76] with a lower fiber volume fraction.

With the help of the FEM Takano et al. presented a new evaluation method of the permeability of different fabrics from the multi-scale viewpoints by the asymptotic homogenization theory. They tried to study the relation between microscopic and macroscopic permeability for woven fabrics. The verification of the proposed method was given only for UD composites.

The main drawbacks of these methods are the 3D meshing complexity as well as the very large computing time. Note that some authors compared their results qualitatively with

published data, this reveals to the lack of published permeability measurements or to the inconsistency of the modeling.

Finite difference methods seek approximate solutions of partial differential equations by solving a system linking the values of unknown functions at certain points sufficiently close to each other.

Verleye et al. [18] employed a three-dimensional finite difference solver. The solver works on a regular grid likewise lattice Boltzmann method (LBM); however it works with more acceleration techniques for the resulting partial differential system of equations. The fabrics were drawn in WiseTex, in the second step FlowTex software is used in order to predict the permeability. Figure 6 and Figure 7 show the modeling technique, where the homogenization of the Stokes equations is applied within the periodic domain of a textile and yields Darcy's law on the macro-level. The validation of this method on three kinds of fabrics is done with respect to experimental data from literature; a maximum scattering of 50 % is observed. This error was revealed to the sensitivity of the mesopores size measurement. The main drawback of this approach is the very fine discretization required to converge.

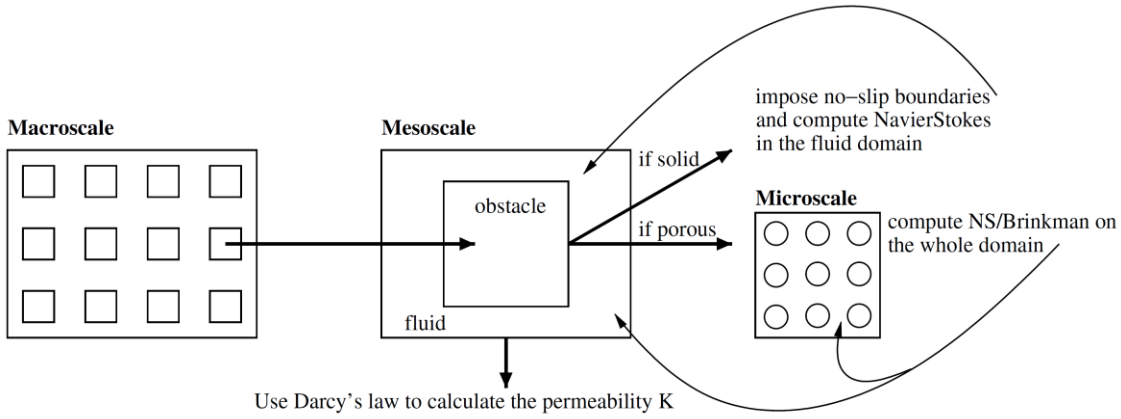

Figure 6 The different scales and mathematical equations

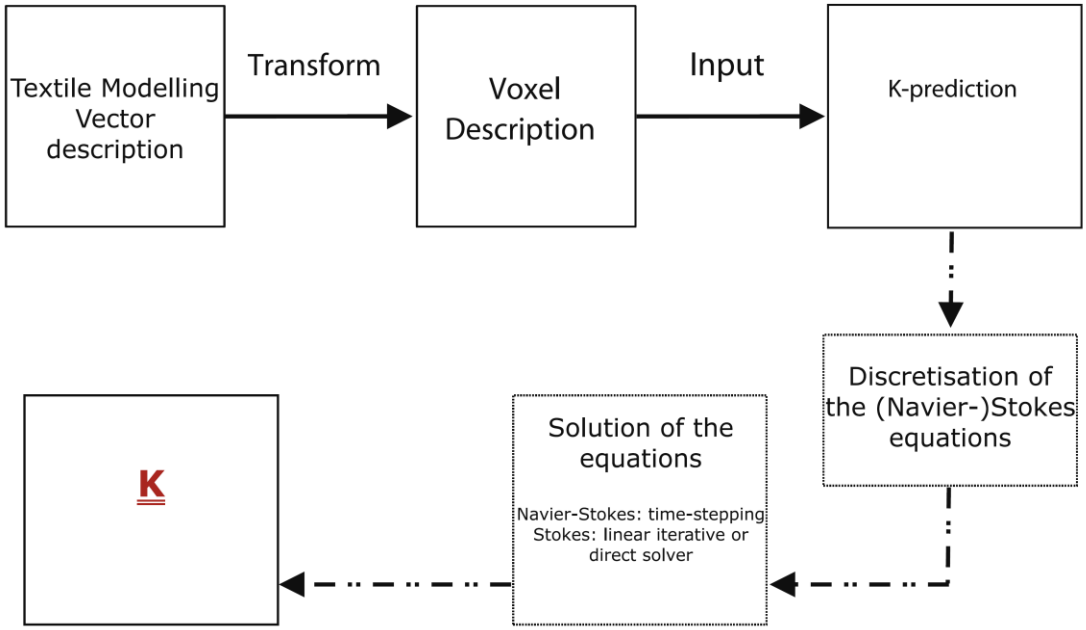

Figure 7 Flow chart of the numerical procedure

The Lattice-Boltzmann methods have the same advantages with the disadvantage of not converging as rapidly as a function of the discretization pitch and are also more expensive in terms of computational time. These methods study the fibrous medium at mesoscopic scale and consider fictitious particles in a discrete space-time grid [19-22].

If the finite element method is well adapted to complex geometries, its main disadvantage is the need of a 3D mesh. Obtaining this mesh is sometimes very difficult because of the complex 3D architecture of fibrous reinforcements. Finite differences and Boltzmann's lattice methods solve problems on uniform meshes, hence they do not present this type of problem, but they require a discretization pitch sufficiently low to ensure convergence and are therefore sometimes more expensive in terms of calculation time.

2.3 Experimental measurements

We present here different types of permeability measurements by distinguishing between measurements in the in-plane and through-thickness directions. In a manufacturing process the resin is generally injected in a dry preform in a radial or longitudinal injection; under constant pressures unless or at constant flow rate.

The permeability is measured experimentally in different ways. The methods can be classified by the measurement procedure, the measuring device, and the fluid used:

- radial or longitudinal, depending on the position of the inlet gate see Figure 8 for the in-plane permeability,
- saturated or unsaturated, depending if the preform is saturated with resin or dry when measuring permeability,
- constant pressure at the inlet or constant velocity during the injection,
- type of injected fluid,
- measuring device.

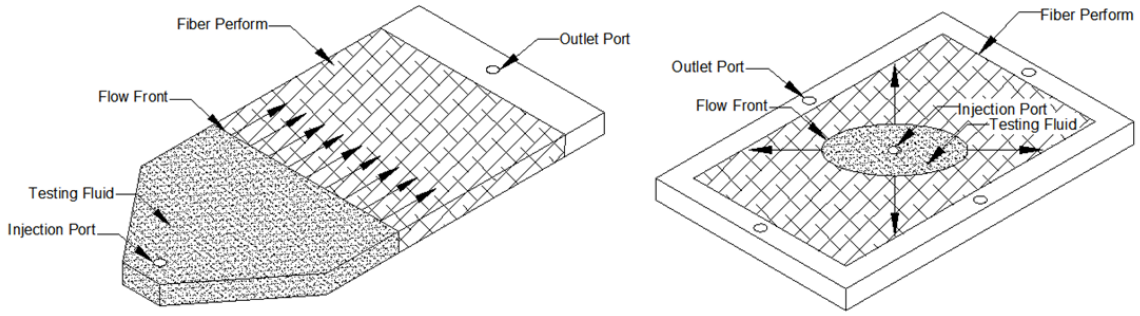

Figure 8 Schematic of two types of flow geometries considered in the testing of the in-plane permeability; the left picture describes unidirectional flow experiments, and the right picture radial flow experiments.

2.3.1 Bibliography on measuring in-plane permeability

A review of experimental methods used to determine the in-plane permeability is presented. Some papers present a more detailed review [1, 2]. Permeability measurements based on radial injections were used by many researchers. Kris Hoes et al. [3] used a new set-up for performing 2D radial injection using electrical sensors to detect the progression of the flow front for a 2D woven glass fabric at V_f = 0.42. The standard deviation of their experimental data was 21 -22%. Song and Youn [4] used the radial flow method to measure the in-plane permeability of plain weave glass fabrics with a constant inlet pressure. Comas-Cardona et al. [5] described a radial injection methodology to measure fiber reinforcement permeability using a compression test setup after determining the anisotropy ratio; the method allows the calculation of the in-plane and through-thickness permeability. This method was applied on a glass twill weave and on NCF carbon fabrics to determine the in-plane permeability.

The saturated and unsaturated permeability were also discussed and investigated. Shojaei et al. [2] studied the saturated and unsaturated permeability of a glass-woven fabric at different injection pressure and fiber volume fractions. The experiments are based on a unidirectional injection. The difference between the unsaturated and the saturated permeability is also related to the pore structure. The saturated permeability is usually higher than the unsaturated permeability. The unsaturated in-plane permeability of three different 3D woven fabrics was determined using radial flow experiments at constant injection pressure, using pressure transducers to detect the flow front propagation by Endruweit and long [6, 82].

In addition, some studies have focused on developing new techniques to determine the permeability of engineering textiles. Liu and al. [7] have investigated the in-plane permeability measurement. A new set-up is presented, which consists of a new sensor design and new analysis software. The proposed new method was used to measure the permeability of a basalt woven twill fabric. Arbter et al. [8] reported on the measurement of permeability in an international benchmark exercise between twelve different institutes and universities. Two fabrics were selected 01113-1000-TF970 (twill 2x2 E-glass fabric) and G0986 D 1200 (twill 2x2 carbon fabric), and sixteen different methods were used to predict the in-plane permeability. A big scatter in the results was observed between the methods used, which were explained by experimental uncertainty, human factors, and different experimental techniques. Naik et al. [1] presented a discussion of the factors that influence the measurement of permeability. It is shown from the conclusion that the steady-state permeability is higher than the transient permeability with few exceptions. The unsaturated permeability is also higher for synthetic fibers than for natural fibers. It is found that for high viscosity fluids the transient and steady-state permeability decrease. However, for lower values of viscosity no significant effect is shown. In addition, it is noticed that transversal transient permeability is lower than in-plane transient permeability values for typical fabrics. The same fabrics were studied in Benchmark II [9] to solve the problems encountered in the first Benchmark [8]. The objective was to follow the same guidelines. The scatter between experimental data obtained by different research groups for the same fabric was about 20% when using the same experimental method.

2.3.2 Bibliography on measuring through-thickness permeability

The most common method to measure the through-thickness permeability is the one-dimensional cylindrical flow apparatus at constant flow rate. The fluid is injected at a flow rate, and then the corresponding injection pressure is noted. The through-thickness permeability is calculated based on a single point value using Darcy‘s law for one-dimensional flow:

$$u = \frac{Q}{A} = \frac{K_3}{\mu} . \frac{\Delta P}{h} \qquad \text{Eq.(3)}$$

where u stands for the Darcy injection speed, Q for the volumetric flow rate, A for the area of the fabrics, μ for the viscosity of the injected oil, ΔP for the pressure loss, h for the thickness of the reinforcement and K_3 for through-thickness permeability.

Chae et al. [83, 84] measured the transversal permeability using silicone oil (200F/100CS) as test fluid for five different preforms by measuring the pressure difference between two points, with pressure transducers, for each experiment at the inlet and outlet after injecting the resin through a permeable wall under constant pressure.

Trevino and al. [85] and Weiztenbock and al. [86] used specially designed apparatus for transverse permeability measurements based on steady state unidirectional experiment. They measured the pressure at the inlet and used a one-dimensional permeability equation derived from Darcy’s law to calculate permeability.

Wu and al. [87] measured the transversal permeability for three different fabrics by measuring the pressure at the inlet under constant velocity; they used DOP or water as testing fluid. The transverse permeability is shown to be independent of the flow rate only for low pressure injections.

Sadik and al. [54] measured the flow rate and the pressure drop to deduce the transverse permeability of aligned fibers. In their study they performed a set of three different investigations: in the first one corn syrup was used as testing fluid and solid rods for fiber arrays; in the second set of experiments, Carbopol solutions were used instead of the corn syrup, and in the third parts of experiments they used fiber bundles with corn syrup. The effects of shear thinning fluid and Newtonian fluid on measured results were compared.

Pavel et al. [88] presented an improved non-intrusive method of the SMART weave sensor system [89]. That method is based only on visualization, where the 3D permeability of fibrous composites could be determined without using any embedded sensors. Elbouazzaoui et al. [90] calculated the transverse permeability of three non-crimped fabrics using an apparatus developed by Drapier et al. [91] .Once the pressures of the injected test fluid are calculated at the inlet and outlet of the specimen, the transverse permeability of the fabrics is determined using Darcy's law.

Ouagne and Bréard [92] proposed a new technique to measure continuously permeability, for different fiber volume fractions. It presents the advantage of giving automatically the permeability curve as a function of the volume fraction of fibers in a single experiment. The results obtained are comparable to these of conventional methods.

Scholz et al. [93] attempted to preform transverse permeability measurements with a gas and compared the results with water measurements. Taking into account air compressibility, 8% gap was reported between water and air.

2.4 Conclusion

Considering the different methods used to measure permeability, the results obtained do not generally agree. Minor changes in the experimental procedures affect significantly the measured values. The international benchmark II [9] agreed on a measurement method of the in-plane permeability. This method can now be adopted as a reference.

Some progress appeared in numerical modeling, but computational limitations remain an obstacle.

The analytical models predict well the permeability of unidirectional fiber bed. However; no comparative study was carried out to select the best models. Few published works are available to predict permeability by analytical models and the few one that exist are not generalized and far from being perfect. Although the general trend as a function of fiber volume fraction is reproduced, the predicted permeability values do not match measurement results.

3 Chapter 3: A Comparative Analytical, Numerical and Experimental Analysis of the Microscopic Permeability of Fiber Bundles in Composite Materials

3.1 Introduction

In this chapter a comparative study is launched, where convenient analytical models evaluating the permeability of unidirectional fibrous media towards normal and parallel flow are selected. These models are compared with respect to available data early published. Static and transient mode simulations are launched in order to filter out the consistent bibliography values; analytical models are later compared with respect to the selected data. The analysis of the comparative study presents that Bahrami and Tamayol, Drummond and Tahir, Berdichevsky and Cai ISCM, and unified (square) models have good agreement with these data for longitudinal microscopic permeability components. Concerning transverse microscopic permeability, Berdichevsky and Cai ISCM (hexagonal), Gebart (hexagonal), Drummond and Tahir (hexagonal), and Kuwabara models are elected to be the most accurate models.

In order to simulate the resin injection and to predict the filling time of any structure, the permeability of the fabric is required. A dry fabric is considered as a dual-scale medium, Figure 9. Researchers classify the flow inside the bundles as “microscopic flow”, between the bundles as “mesoscopic flow”, and as “macroscopic flow” at piece level. In other words, the permeability of bundles or unidirectional yarns is called microscopic permeability while that for a fabric is called macroscopic permeability. Microscopic permeability is an important parameter to discover resin flow through the fiber bed and understand the mechanisms of air entrapment which governs the quality of composite parts made by LCM. Moreover, it is an essential step towards macroscopic permeability modeling.

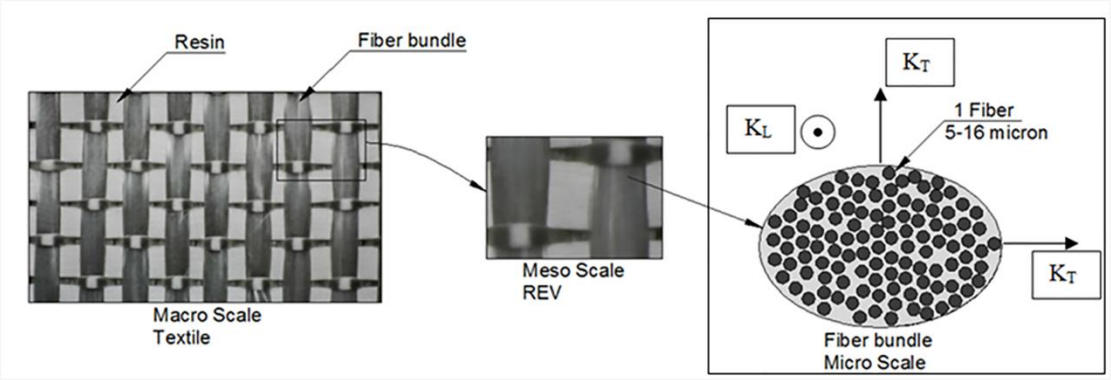

Figure 9 P3W-GE044 from 3TEX Company

3.1.1 Problem statement

This part deals with microscopic permeability of unidirectional yarns; longitudinal permeability K_L and transverse permeability K_T. In general, the evaluation of these permeability values is done by experimental measurements, analytical models, or finite Element (FE) numerical simulations. While analyzing the previously stated prediction methods, wide scattering is observed. In addition, many analytical models exist, while there is no clear comparative study that evaluates all these models.

The main objective of this chapter is to evaluate the available analytical models, by comparing their results to the available bibliography data. However, because of the wide scattering found in bibliography results, this data is to be refined. Thus a finite element modeling is done, in which a more realistic unit cell is used where the fibers are arranged in a random manner; neither square nor hexagonal. Static mode and transient mode simulations are launched. The values of transient simulations approved the consistency of static mode simulations. The bibliography results that better fit the FE modeling results are selected. Then a comparative study is performed and the best analytical models for K_L and K_T are presented.

3.1.1.1 Bibliographic experimental and numerical scattering

Researchers [31, 34, 40, 54, 66, 68, 94-99] predicted the permeability values either by numerical simulations or experimental measurements. This section aims to show the scattering found for both experimental measurements and numerical predictions for aligned fiber beds with the same fiber volume fraction. Permeability measurements

depend on many parameters including the method, the apparatus, the techniques and operator skills, as well as the injection method which could be either radial or unidirectional. On the other hand, numerical simulations depend on many parameters such as the used code, the used method, the boundary conditions, and the most important and influencing parameter which is the unit cell selection. Table 4, Table 5, and Table 6 show different experimental measurements and numerical simulations of the dimensionless permeability components K_L/r^2 and K_T/r^2 values, where "r" is the fiber radius.

Longitudinal	ε	K_L/r^2
Sullivan[68]	0.23	0.0056
Sangani and Yao [94]	0.3	0.00952
	0.44	0.032
	0.5	0.0468
	0.7	0.232
Skartsis and Kardos[95]	0.9	2.48

Table 4 Measurements for longitudinal microscopic permeability

Reference	ε	K_T/r^2	Reference	ε	K_T/r^2
Kirsch and Fuchs [96]	0.7	0.1292	Chmielewsik and Jayaraman [97]	0.7	0.10636
	0.8	0.3		0.967	11.2
	0.85	0.5997	Sadiq et al. [54]	0.385	0.00288
	0.89	1		0.416	0.00508
	0.935	2.597403		0.51	0.016
	0.955	4.36		0.59	0.038
	0.982	17.36	Lee and Yang [40]	0.4345	0.005076
	0.99	40		0.6073	0.039139
	0.9945	83.2		0.8076	0.337553
Coulaud et al. [98]	0.4345	0.00791171	Zhong et al. [100]	0.95	4
	0.6073	0.04489842		0.976	12

Table 5 Measurements for transversal microscopic permeability

Sullivan [68] measured the permeability for different fiber types like glass wool, goat wool, and copper wire, with cross-sectional diameter ranging from 7.6µm up to 150.5µm. Sangani and Yao [94] predicted the permeability of aligned cylinders in different array structures. Skartsis and Kardos [95] measured the permeability and consolidation of oriented carbon fiber beds. Concerning transversal permeability, Kirsch and Fuchs [96] performed a permeability study on fibrous parallel cylinders of aerosol filters which

consist of Kapron fibers of diameters 0.15, 0.225 and 0.4mm. Chmielewsik and Jayaraman [97] measured experimentally the transversal permeability for acrylic circular cylinders array having a diameter of 4.76 mm and 38 mm long. Coulaud et al. [98] chose a numerical method where the medium has been modeled by cylinders of either equal or unequal diameters arranged in a regular pattern with a square or triangular base. Sadiq et al. [54] measured the transversal permeability of unidirectional cylinders consisting of solid circular nylon fibers, whose diameter is equal 711.2 µm. Lee and Yang [40] predicted the transversal permeability by considering a non-Darcy flow through a porous medium. Zhong et al. [100] measured the transversal permeability of square arrayed rods of diameter 3.18 mm.

ε	K_T/r^2	Reference	Difference %
0.4345	0.007912	Coulaud	55%
0.4345	0.005076	Lee and yang	
0.5	0.0488	Sangani and Yao	300%
0.5	0.012	Sadiq et Al	
0.7	0.1292	Kirsch and Fuchs	240%
0.7	0.24	Sangani and Yao	

Table 6 Permeability values with corresponding scattering

Reference	Geometry	ε=0.3	ε=0.7	ε=0.3		ε=0.7	
		K_T/r^2		Average	Scatter	Average	Scatter
Dave et Al.[99]	-	1.25E-03	8.66E-01	1.04E-03	75.85%	1.86E-01	130.59%
Gutowski [34]	Squ. Packing	1.92E-04	8.65E-02				
Gutowski [34]	Hex. Packing	1.31E-03	1.23E-01				
Berd. and Cai[32]	-	2.57E-03	1.54E-01				
Berd.and Cai [32]	Hex. Packing	1.62E-03	1.08E-01				
Berd. and Cai[32]	Squ. Packing	3.32E-04	1.02E-01				
Wang et Al. [66]	Squ.Packing	4.26E-04	1.10E-01				
Choi et Al. [25]	Hex. Packing	1.57E-03	9.84E-02				
Choi et Al. [25]	Squ. Packing	8.18E-05	2.44E-02				

Table 7 Effect of the packing structure on the scattering between the numerically predicted permeability values for two selected porosities

As shown in Table 6, on the same porosities different studies measured the permeability with a scattering going from 55% to 300%. Table 7 shows that the permeability is not only related to the fiber volume fraction and porosity, but is also greatly influenced by the packing structure. This effect has been shown clearly in the

scatter between the predicted permeability values for two selected porosities, where for a porosity of 30% the scatter is more than 70% and for a porosity of 50% the scatter is more than 130%. The scattering is calculated by equation (4).

$$scattering = \frac{standard\ deviation}{mean} * 100 \qquad \text{Eq.(4)}$$

3.1.1.2 Analytical scattering

Analytically, researchers have studied the microscopic permeability for unidirectional fibers, and then derived various analytical models based on four different modeling approaches:

- Lubrication approach
- Capillary approach
- Analytic Cell modeling
- Mixed models based on previous models.

Model Name/(ε= 0.5)	K_L/r^2	K_T/r^2
Kuwabara [36]	0.0342	0.017
Gutowski (for Va=0.83) [34]	-	0.0131
Gutowski (for Va=0.78) [34]	0.1786	0.0086
Gebart (Square) [33]	0.0702	0.0129
Gebart (Hexagonal) [33]	0.0755	0.0164
Berdichevsky and Cai ISCM (Square) [32]	0.0464	0.0097
Berdichevsky and Cai ISCM (Hexagonal) [32]	0.0354	0.0116
Tamayol and Bahrami (Square) [70]	-	0.0117
Scattering	67.7%	217.6%

Table 8 Comparison between analytical models from the bibliography on a selected porosity

Table 8 shows a comparison between some analytical models from the bibliography on a selected porosity ($\boldsymbol{\varepsilon} = 0.5$). It's well noticed that for the same fiber volume fraction, different models give rise to values of permeability with a scatter more than 60% for longitudinal permeability and more than 200% for transversal permeability models.

Although compared at the same fiber volume fractions, a wide scattering between permeability values derived from analytical models, numerical simulations, and

experimental measurements was observed. That scattering reveals the importance of this study that aims to investigate and compare the different analytical models to numerical and experimental results.

No generalized comparative study was found in the bibliography focusing on all approaches to characterize the microscopic permeability. It is noticed that researchers who predicted the permeability values using different approaches used to approve their results by comparing them with a selected experiment, a selected model, or a selected numerical simulation from the bibliography instead of doing a generalized comparison. Chen and Papathanasiou [65] compared their finite element simulation results to Drummond and Tahir model [39]. Same for Choi et al. [25] who compared their finite element simulation to Gebart [33] and Berdichevsky and Cai [31, 32] analytical models. Tamayol and Bahrami [44] compared their analytical model to experiments from literature. Wang and Hwang [66] compared the results of a finite element simulation to Gebart [33] analytical model. Sadiq et al. [54] compared their experimental results with the asymptotic model developed by Brushke and Advani [38].

3.1.2 Objectives

The main objective of this work is to select the best available analytical models predicting the permeability values for unidirectional fiber beds. To do so, seven analytical models predicting the longitudinal microscopic permeability [31-37] and seventeen models [31-36, 38-44] predicting the transversal microscopic permeability is selected from bibliography. From the comparison, the best models for predicting microscopic longitudinal and transversal permeability are selected.

3.1.3 Methodology

Reviewed analytical models' calculations are compared with numerical simulations or experimental results from bibliography; but these results showed big differences between each other for the same fiber volume fraction as previously explained in the first part. This reveals the importance of performing a new numerical study simulating a real experiment and eliminating experiment's problems.

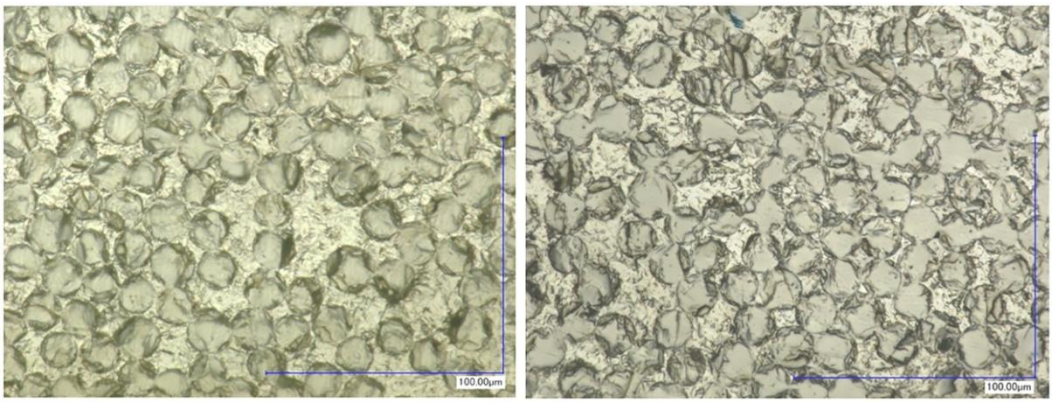

Figure 10 Two fabrics: 3D Orthogonal from 3TEX at a fiber volume fraction equal to 55.76% and unidirectional stitched fabric (U14EU920) from SAERTEX at a fiber volume fraction equal to 60.59%

Figure 10 shows two different fabrics which are 3D Orthogonal from 3TEX with fiber volume fraction equal to 55.76%, and a unidirectional stitched fabric (U14EU920) from SAERTEX with fiber volume fraction equal to 60.59%. Note that these real injections are done in order to affirm that the fiber arrangement is random. Thus the numerical FE modeling is performed based on a random fiber packing structure. This study measures averaged volume filling speed under a constant pressure. In other words, it is the saturated permeability value. The study is done in both longitudinal and transversal directions. A more advanced study is done for the same unit cell in a transient mode; where the flow front position is detected as function of time, taking into consideration capillary effect. Averaged unsaturated permeability is deduced. This simulation approved the consistency of static mode simulation.

Values are selected from the literature at different fiber volume fractions. When two values are at the same fiber volume fraction, the permeability value which best matches with the numerical data is chosen for the comparative study. The selection between different values is convenient, taking into consideration that the unselected experiments are far from being perfect due to the inconsistency in the measuring process.

A two-level comparative study is done between all data derived from present work with the selected experiments and analytical models. From this comparison, the best models for predicting microscopic longitudinal and transversal permeability are selected.

3.1.4 Organization

A review of the available analytical models in the literature is established. In the second section, a numerical study is launched in order to simulate the longitudinal and transversal flow in aligned fiber beds at different fiber volume fractions in a steady state mode "saturated permeability". In the third section, the experiments are selected based on the numerical simulations and a comparative study is launched in order to select the best analytical models based on the previous numerical simulations and selected experiments. Then, a numerical simulation in a transient free boundary problem mode is done and consequently the best analytical models will be filtered from the selection made in the third part. At the end of this study, a conclusion is deduced.

3.2 Analytical Models

Section 2.1.1 lists the available analytical models in the bibliography. These models are to be compared with the permeability values in section 3.3.2.

3.3 Numerical steady state method and results (Saturated permeability)

In this section, a FE modeling, using COMSOL MULTIPHYSICS software which consists of a CFD analysis is performed to estimate the microscopic saturated permeability value of multiple cases involving porous media. Two cases were studied, which involve a longitudinal and a transversal flow through certain porous media in order to predict the saturated permeability value of the media. A finite element (FE) based model for viscous, incompressible flow through random packing of fibers is employed for predicting the permeability associated in the porous media.

3.3.1 Methodology

In this study, random arrangement of fiber is considered, which is shown to be as most representative for a real fiber stacking. Figure 11 shows the 2D unit cell dimensions for transverse permeability predictions having a length of 0.33mm and a width of 0.1mm. However, the 3D unit cell dimensions for longitudinal permeability are length = 0.33mm, width = 0.1mm, and depth=1mm. Different fiber contents are selected to cover a wide

range of porosities (0.3 to 0.9) for both transversal and longitudinal simulations Figure 12 and Figure 13. Porosities are selected with respect to available data from the bibliography; refer to the introduction.

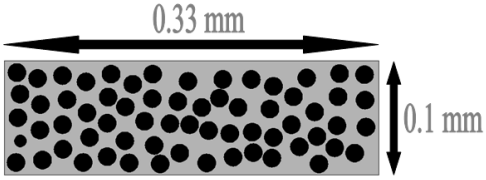

Figure 11 Unit cell Dimensions

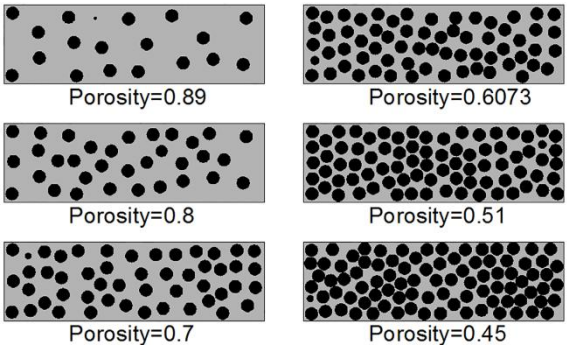

Figure 12 Selected porosities for transversal flow simulation

The model used is based on Navier-Stokes equation, where the fluid is subjected to the action of a body force F, the Navier-Stokes equation can be written as follow in equation (5).

$$\rho.\left[\frac{d\vec{v}}{dt}+\vec{v}.\nabla\vec{v}\right]=\rho\vec{F}+\nabla.\sigma \qquad \textit{Eq. 5}$$

Where ρ is the density, v is the velocity of the fluid, t is time, P is the pressure, and F is the volumetric force. Permeability in fluid mechanics is a measure of the ability of a porous material to allow fluid to pass through it. The most widely used equation for describing flow is Darcy's equation for flow through porous media. Fluids modeled by Darcy's law, equation (6) must obey the assumptions used to formulate the Navier-Stokes equation. Namely, fluids must have a constant density and viscosity and must obey Newtonian behavior [101].

$$K = \frac{\mu . H . U_D}{\Delta P} \qquad Eq.\ 6$$

μ is the viscosity of the fluid, ΔP is the pressure drop, K is the permeability tensor of the porous medium, U_D is the velocity of the fluid, and H is the depth of the unit cell.

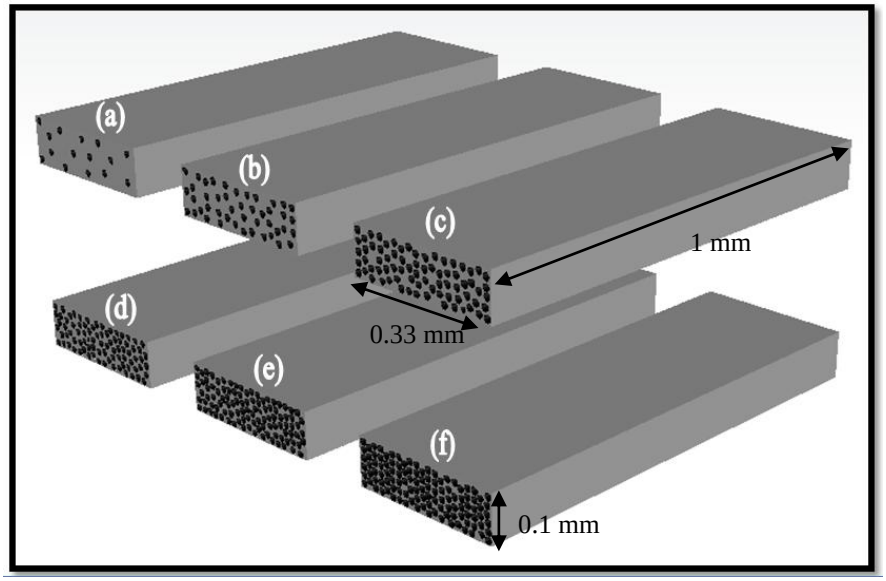

Figure 13 Selected porosities for transversal flow simulation
(a): 0.9, (b): 0.7, (c):0.5, (d): 0.44, (e): 0.3, and (f):0.23

The flow Reynolds number should be kept sufficiently low to ensure negligible effects of inertial terms. Reynolds number equation (7) is ranged between 1 and 10 ($1 < Re < 10$) [102], Where D_e is the equivalent pore diameter.

$$Re = \frac{\rho . U_D . D_e}{\mu} \qquad Eq.\ 7$$

The porosity of a porous medium is the ratio of the pore volume to the total volume of a representative sample of the medium; it can be calculated using this equation (8).

$$\varepsilon = 1 - \frac{N . \pi . d^2}{4 . S_t} \qquad Eq.\ 8$$

Where N is the number of fibers, d is the fiber diameter and S_t is the total surface of the unit cell. So for a selected fluid "selected viscosity", on a selected porosity and on a predefined inlet and outlet pressures the filling time is obtained from the simulation. Using equation (6) the saturated permeability is calculated.

3.3.1.1 Selected porosities

Based on the available data from literature, different porosities were selected Table 9, in order to predict the microscopic permeability values on these porosities.

ε (longitudinal flow)	0.23	0.3	0.44	0.5	0.7	0.9	-
ε (transversal flow)	0.385	0.45	0.51	0.6073	0.7	0.8	0.89

Table 9 Porosity values for performing the study

3.3.1.2 Flow type and Fluid properties

In fluid transients, laminar flow occurs when a fluid flows in parallel layers, with no disruption between the layers. At low velocities, the fluid tends to flow without lateral mixing, and adjacent layers slide past one another like playing cards. Neither cross-currents perpendicular to the direction of flow, nor eddies or swirls of fluid exist. In laminar flow, the motion of the particles of the fluid is very orderly with all particles moving in straight lines parallel to the walls. The fluid used in simulations is epoxy resin which has the properties shown in Table 10.

Fluid properties	
Temperature	293 K
Density	1120 kg/m^3
Transient viscosity	0.195 Pa.s

Table 10 Fluid properties of epoxy resin

3.3.1.3 Meshing Technique

CFD simulation requires that the computational domain gets divided into small cells where the flow is modeled and the flow equations are solved. COMSOL MULTIPHYSICS software is used to generate the mesh that will be used in simulations involving random form. The generated mesh for longitudinal and transversal unit cells and meshing controls are shown respectively in Figure 6 and Table 11. For example for a longitudinal permeability unit cell for a V_f of 0.5, the complete mesh consists of 1603619 domain elements, 461336 boundary elements, and 57153 edge elements.

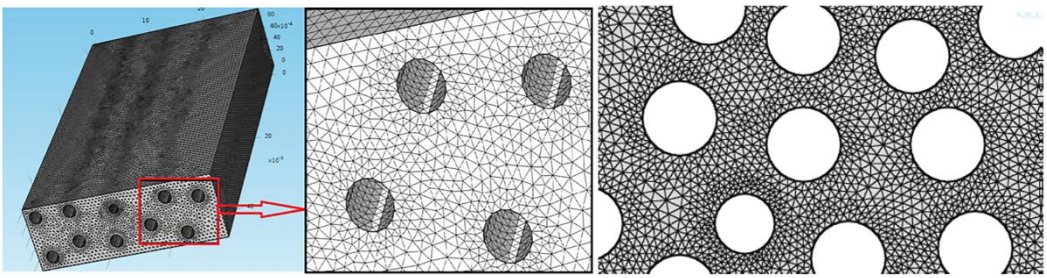

Figure 14 Generated mesh for longitudinal and transversal unit cells

Control	Longitudinal	Transversal
Mesh type	Free Tetrahedral	Free Triangle
Maximum element size	0.055 mm	0.055 mm
Minimum element size	0.044 mm	0.044 mm
Max element growth rate	1.4	1.4
Calibrated for	Fluid Transients	Fluid Transients

Table 11 Meshing Conditions

3.3.1.4 Boundary conditions

After the mesh process is completed, the next step is to specify the boundary conditions. Similar boundary conditions were used in all the simulations, which are shown in Table 12. Type of boundary condition: constant pressure with no viscous stress.

Surface	**Boundary conditions**
Left surface	Inlet pressure =1.5 bar
Right Surface	Outlet pressure =1 bar
Other surfaces	No slip wall

Table 12 Boundary Conditions

3.3.1.5 Solver Settings

Since the flow in the simulations that were performed is supposed to be Laminar (low velocity flow), the Laminar model that solves the Navier-Stokes equations was used Table 13.

Solver Setting	**Solver Type: Longitudinal**	**Solver Type: Transversal**
Direct	MUMPS	PARADISO
Fully coupled	Iterative	DIRECT
Iterative	GMRES	GMRES

Table 13 Solver Settings for stationary solver

Where MUMPS: Multifrontal Massively Parallel Sparse (direct Solver), GMRES: Generalized Minimum Residual (iterative method).

3.3.2 Results and comparison for numerical simulations in steady state mode

The results of the calculated permeability values are shown in the Table 14. In the next section, two comparative studies are launched for both longitudinal and transversal microscopic permeability values; where in the results derived from numerical steady state mode simulations and experimental measured results will be compared with results derived from available analytical models.

ε (longitudinal flow)	0.23	0.3	0.44	0.5	0.7	0.9	-
Numerical Steady state mode K_L/r^2	0.0081	0.0105	0.0369	0.0516	0.2206	1.5482	-
Bibliography results K_L/r^2	0.0056	0.0095	0.0320	0.0468	0.2320	2.4800	-
ε (transversal flow)	0.385	0.45	0.51	0.6073	0.7	0.8	0.89
Numerical Steady state mode K_T/r^2	0.00156	0.0058	0.0124	0.03394	0.09	0.26	0.672
Bibliography results K_T/r^2	0.00288	0.012	0.016	0.03914	0.1292	0.3	1

Table 14 Permeability results of the numerical simulation in steady state mode for longitudinal and transversal flow with the selected measurements

A comparison is launched between analytical models on one hand and the bibliography results and numerical results on the other hand. This comparison aims to choose the analytical models which best matches with these results.

3.3.2.1 Comparison for longitudinal flow (steady state mode)

As shown in Table 15 and Chart 1, Gutowski model values compared with the bibliography results show big scatter at most of the selected porosities such as 34.8% at porosity ε = 0.3, and keeps rising till 70.9% at porosity ε = 0.7. Similarly, the comparison of these models' values with the simulation reveals almost same scattering ranging between 30.6% and 72.1%.

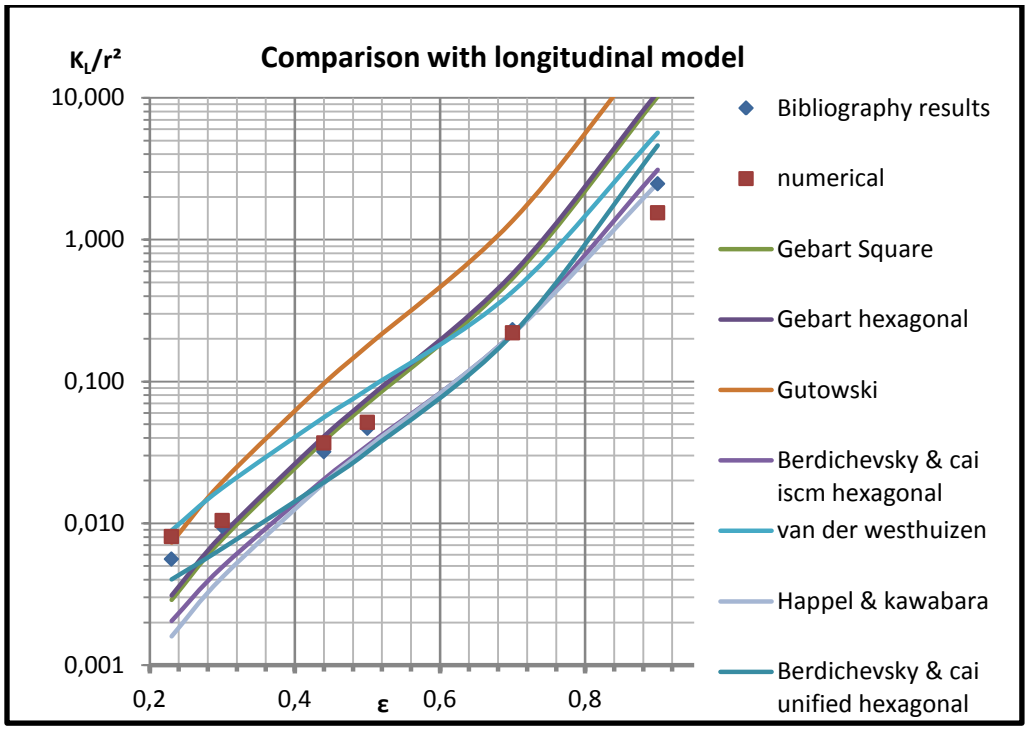

Chart 1 Comparison between longitudinal models

Van der Westhuizen model results reveal large scattering when compared to bibliography and numerical results. This scatter starts from 22.9% and rises up till 39.1%. Gebart (square and hexagonal) models' results exhibit low scattering only on the porosities 0.3 and 0.44 such as 6.7% and 8.7% with the bibliography results, and 1.6% and 5.3% when compared with the numerical ones. But the scattering increases sharply at porosities less or greater than 0.3 and 0.44, ranging between 23.4% and 47.4% when compared to bibliography and numerical results. Analogously, the models Berdichevsky and Cai ISCM (hexagonal), Berdichevsky and Cai unified (hexagonal), and Happel and Kuwabara show an intersection with the bibliography and numerical results at a single porosity which is 0.7 (scatter around 3% and 1% when compared with the bibliography and numerical results respectively), while it seems to be high on the other porosities for the entire three models. The models Gutowski, Van der Westhuizen, Gebart (square and hexagonal), Happel and Kuwabara, Berdichevsky and Cai ISCM (hexagonal), and Berdichevsky and Cai unified (hexagonal) are excluded due to the big scatter between the results of these models when compared to the bibliography and numerical values on almost all of the selected porosities.

Analytical models / ε		0.23	0.3	0.44	0.5	0.7	0.9
Happel and Kuwabara	scatter with bibliography	55.6%	39.1%	25.0%	15.7%	3.6%	0.3%
	scatter with numerical	67.0%	43.0%	31.5%	20.4%	1.1%	23.4%
Gebart Square	scatter with bibliography	32.1%	10.4%	8.7%	20.0%	39.5%	61.0%
	scatter with numerical	47.4%	15.0%	1.6%	15.3%	41.6%	73.7%
Gebart Hexagonal	scatter with bibliography	28.8%	6.7%	12.3%	23.4%	42.5%	63.2%
	scatter with numerical	44.5%	11.4%	5.3%	18.8%	44.6%	75.3%
Gutowski	scatter with bibliography	13.4%	34.8%	50.4%	58.5%	70.9%	82.6%
	scatter with numerical	4.8%	30.6%	44.9%	55.2%	72.1%	88.8%
	scatter with numerical	17.9%	0.8%	10.3%	5.3%	0.4%	23.3%
Berdichevsky and Cai ISCM hexagonal	scatter with bibliography	46.4%	31.6%	21.9%	13.9%	3.1%	11.2%
	scatter with numerical	59.5%	35.8%	28.6%	18.7%	0.6%	33.5%
Van der westhuizen	scatter with bibliography	22.9%	30.3%	27.2%	30.5%	29.9%	39.1%
	scatter with numerical	5.0%	25.9%	20.5%	26.0%	32.2%	57.1%
Berdichevsky and cai unified hexagonal	scatter with bibliography	16.4%	17.7%	24.4%	19.0%	3.8%	30.0%
	scatter with numerical	33.5%	22.3%	31.0%	23.6%	1.3%	49.7%

Table 15 Scattering values derived from the comparison with the bibliography results and numerical simulation results

Analytical models / ε		0.23	0.3	0.44	0.5	0.7	0.9
Tam. and Bahrami	scatter with bibliography	5.8%	2.8%	7.1%	3.1%	0.3%	1.3%
	scatter with numerical	12.4%	1.9%	14.1%	7.9%	2.8%	24.4%
Drum. and Tahir	scatter with bibliography	25.3%	14.5%	3.4%	0.8%	0.8%	1.5%
	scatter with numerical	7.5%	9.8%	10.4%	5.6%	3.3%	24.5%
Berd. and Cai ISCM square	scatter with bibliography	0.2%	4.0%	3.3%	0.4%	2.9%	0.1%
	scatter with numerical	17.9%	0.8%	10.3%	5.3%	0.4%	23.3%
Berd. and Cai unified square	scatter with bibliography	11.3%	6.9%	6.7%	3.9%	0.7%	20.3%
	scatter with numerical	6.9%	2.1%	13.7%	8.8%	3.2%	41.5%

Table 16 Scattering results derived from the comparison with the bibliography results and numerical simulation results

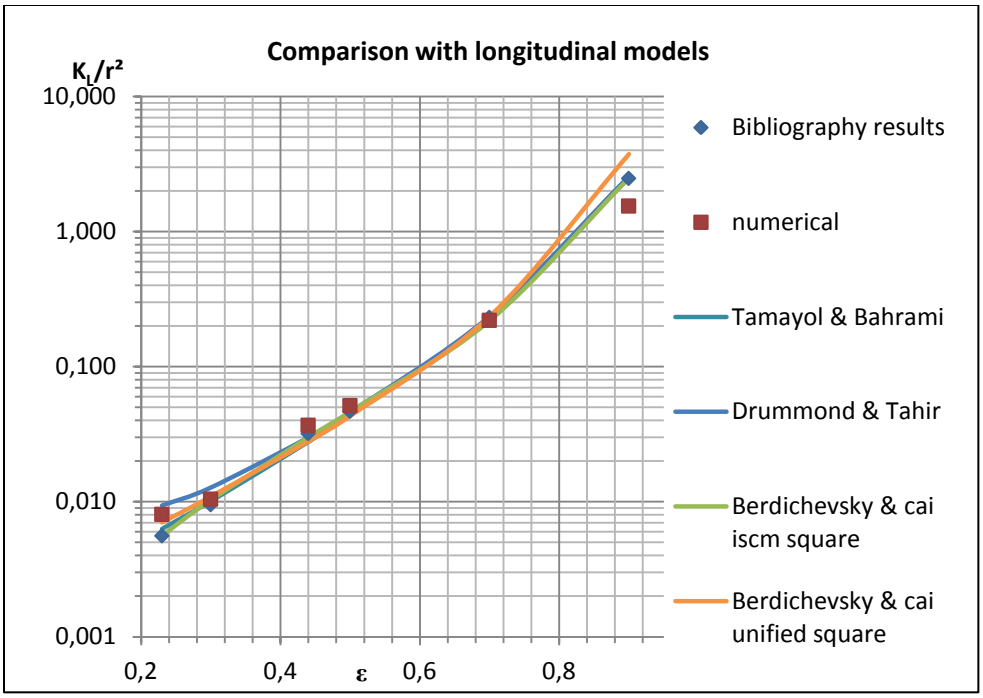

Chart 2 Comparison between longitudinal models

On the other side of the coin by referring to Table 16 and Chart 2, it is obviously realized that there are four models that give values which are very close to the bibliography and numerical values, evidenced by the low scattering between the values at most of the selected porosities. One of these models is Tamayol and Bahrami which when compared with bibliography values has a range of scatter lying between 0.3% at porosity ε = 0.7, and 7.1% at porosity ε = 0.44. And compared to the numerical results, it also shows very low scattering, as shown in the table; 1.9% at porosity 0.3 and 7.9% at porosity 0.5. Drummond and Tahir is also one of the models that have results close to the bibliography and numerical results. Examples are 3.4% scatter with the bibliography result at porosity 0.44 and 3.3% scatter with numerical value at porosity 0.7. But the scatter is relatively high (25.3%) compared to the bibliography result on porosity 0.23.

The other two models which show very low scatter in comparison with the bibliography and numerical results are Berdichevsky and Cai ISCM square and Berdichevsky and Cai unified square. The scattering with the bibliography results ranges between 0.4% and 4.0% for the first model and between 0.7% and 11.3% for the second one. Similarly, the comparison with the numerical study results also reveals very low ranges of scattering,

being between 0.4% and 17.9% for the first model and between 2.1% and 13.7% for the second.

3.3.2.2 Comparison for transversal flow (steady state mode)

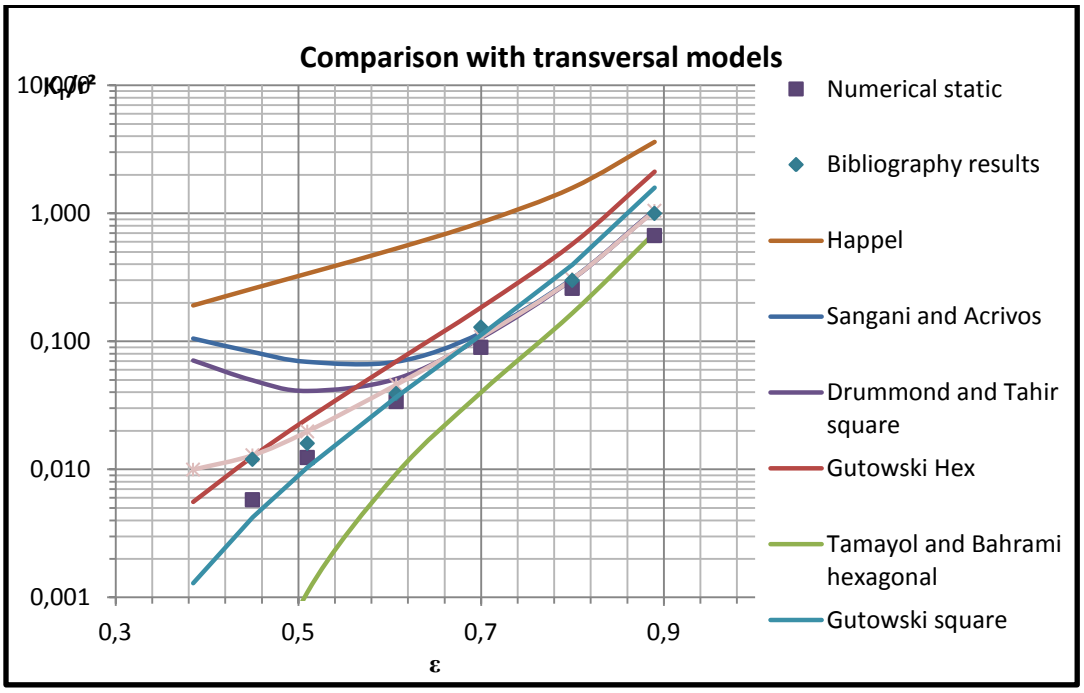

Chart 3 Comparison between transversal models

By referring to Table 17 and Chart 3, Happel shows very high scattering with bibliography results on all selected porosities, with the least scattering equal to 56.7% at porosity 0.89 and greatest one equal to 91.1% at porosity 0.45. The scattering is similarly high with numerical results ranging between 68.7% and 95.6%.Gutowski (hexagonal) reveals distinct scattering values but the overwhelming majority lies between 21.6% and 51.8%.Tamayol and Bahrami (hexagonal) displays great scattering values with the bibliography results on one hand and with the numerical results on the other hand, which range between 17.4% and 98.3%. The models having great scatter with the bibliography and numerical results are excluded from the study. Those are Happel, Gutowski (hexagonal), and Tamayol and Bahrami (hexagonal) models. Both models Sangani and Acrivos and Drummond and Tahir (square) when compared with both bibliography and numerical results show big scattering at lower porosities and smaller scattering values at higher porosities, which reveals the ineffectiveness of these models in our study. The comparison of Sangani and Acrivos results with the bibliography results show scattering

values 8.7%, 2.2% and 5.0% at porosities 0.7, 0.8, and 0.89 respectively; while the scattering is high at lower porosities (19.3%, 46.3%, 23.2%). Similarly, when compared to the numerical results, the scattering values are divided into two halves, some are high and the others are relatively low. Drummond and Tahir scattering values with numerical and bibliography values are mostly greater than 20% at the first three porosities, and lower than 20% at the next three ones.

Analytical models / ε		0.45	0.51	0.6073	0.7	0.8	0.89
Happel	scatter with bibliography	91.1%	91.0%	86.3%	73.6%	68.1%	56.7%
	scatter with numerical	95.6%	92.9%	88.0%	80.8%	71.8%	68.7%
Sangani and Acrivos	scatter with bibliography	19.3%	46.3%	23.2%	8.7%	2.2%	5.0%
	scatter with numerical	49.2%	37.6%	17.6%	10.0%	9.9%	27.4%
Drummond and Tahir square	scatter with bibliography	61.1%	43.9%	13.2%	9.7%	1.0%	3.0%
	scatter with numerical	79.1%	53.6%	20.1%	8.3%	8.1%	22.5%
Gutowski Hexagonal	scatter with bibliography	2.2%	21.6%	28.0%	17.5%	31.5%	35.8%
	scatter with numerical	36.8%	33.3%	34.4%	34.3%	37.8%	51.8%
Tam. and Bahrami hexagonal	scatter with bibliography	98.3%	87.2%	61.8%	52.9%	28.8%	17.4%
	scatter with numerical	96.5%	83.7%	57.2%	38.7%	22.1%	2.3%

Table 17 Scattering results derived from the comparison with the bibliography results and the numerical simulation results

As shown in the Table 18 and Chart 4, Bruschke and Advani model shows mostly scattering values greater than 15%. For example, compared with bibliography values, some of the scattering values are 13.6%, 15.5%, and 24.5%. And the comparison with the numerical results shows scattering values 29.8% at porosity 0.45, 23.0% at porosity 0.51, 22.4% at porosity 0.8. Gebart (square), Gutowski (square), and Van der Westhuizen intersect with the bibliography and numerical results at a single porosity each. That's to say, Gebart (square) showed low scattering with both bibliography and numerical values (4.5% and 8.2%) at porosity 0.51, but the scattering is higher at the entire other porosities. Similarly, Gutowski has a single intersection with the bibliography and numerical results, and that's at porosity 0.6073 with scattering 3.1% compared to bibliography result and 4.0% compared to numerical result, while the scatter increases at the other porosities. In addition, Van Der Westhuizen values intersect with the bibliography and numerical results at porosity 0.8 and the other scattering values take place between 2.9% and 26.5%. Bruschke and Advani, Gebart (square), and Gutowski (square) are the most likely to be eliminated from the study.

Analytical models / ε		0.45	0.51	0.6073	0.7	0.8	0.89
Gebart Square	scatter with bibliography	28.2%	4.5%	6.1%	3.6%	12.0%	18.3%
	scatter with numerical	7.3%	8.2%	13.1%	14.3%	19.0%	36.6%
Drummond and Tahir hexagonal	scatter with bibliography	3.7%	10.7%	7.9%	8.7%	1.2%	2.4%
	scatter with numerical	38.0%	23.0%	15.0%	9.3%	8.4%	22.0%
Gutowski Square	scatter with bibliography	47.9%	21.3%	3.1%	6.8%	13.9%	22.8%
	scatter with numerical	15.7%	8.8%	4.0%	11.2%	20.8%	40.6%
Sahraoui and Kaviany	scatter with bibliography	34.0%	12.0%	1.2%	11.2%	1.0%	2.1%
	scatter with numerical	1.0%	0.7%	5.9%	6.9%	8.1%	17.6%
Berdichevsky and Cai ISCM square	scatter with bibliography	40.9%	18.7%	8.3%	17.9%	2.3%	4.0%
	scatter with numerical	7.1%	6.2%	1.2%	0.0%	4.8%	23.5%
Phelan and Wise	scatter with bibliography	28.2%	4.5%	6.1%	3.6%	12.0%	18.3%
	scatter with numerical	7.3%	8.2%	13.1%	14.3%	19.0%	36.6%
Lee and yang	scatter with bibliography	33.2%	11.2%	1.1%	11.4%	2.2%	4.0%
	scatter with numerical	1.9%	1.5%	6.0%	6.6%	9.3%	23.4%
Bruschke and Advani	scatter with bibliography	5.7%	10.7%	13.6%	0.5%	15.5%	24.5%
	scatter with numerical	29.8%	23.0%	20.5%	18.4%	22.4%	2.1%
Berdichevsky and Cai unified model Square	scatter with bibliography	31.5%	9.1%	0.2%	12.0%	0.4%	2.0%
	scatter with numerical	3.7%	3.7%	6.9%	6.0%	7.5%	21.5%
Berdichevsky and Cai unified model Hex	scatter with bibliography	9.2%	5.6%	5.4%	11.6%	2.8%	2.9%
	scatter with numerical	26.5%	18.1%	12.5%	6.4%	4.4%	16.8%
Van Der Westhuizen and Du Plessis	scatter with bibliography	16.2%	4.5%	7.0%	6.2%	8.8%	17.6%
	scatter with numerical	19.8%	17.1%	14.0%	11.8%	15.8%	36.0%

Table 18 Scattering results derived from the comparison with the bibliography results and numerical simulation results

The models Drummond and Tahir (hexagonal), Sahraoui and Kaviany, Berdichevsky and Cai ISCM (square), Phelan and Wise, Lee and Yang, Berdichevsky and Cai unified Model Square, and Berdichevsky and Cai unified model Hex exhibit in most of the comparisons with both bibliography and numerical results scattering values less than 15%.

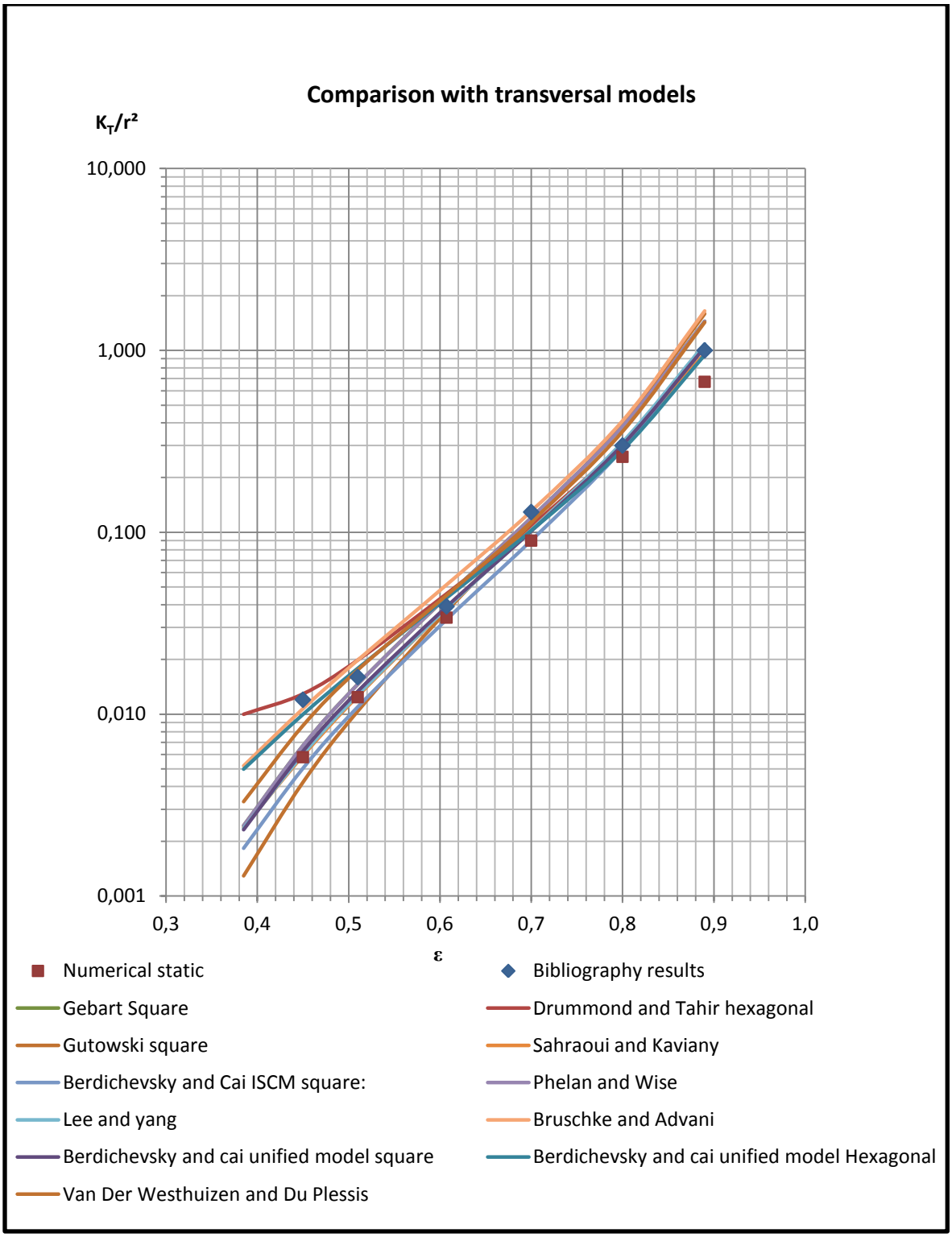

Chart 4 Comparison between transversal models

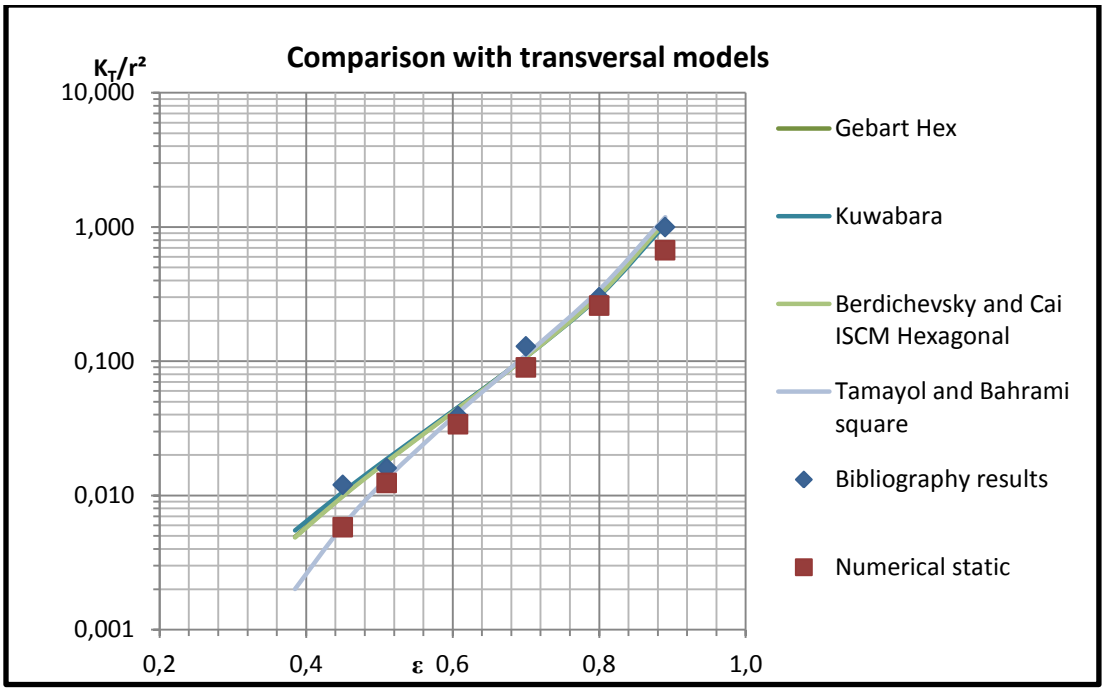

Chart 5 Comparison with transversal models

Analytical models / ε		0.45	0.51	0.6073	0.7	0.8	0.89
Gebart (hexagonal)	scatter with bibliography	9.4%	5.9%	6.9%	8.8%	2.2%	5.1%
	scatter with numerical	26.3%	18.5%	14.0%	9.2%	9.3%	24.4%
Kuwabara	scatter with bibliography	6.3%	7.8%	7.5%	9.0%	1.0%	2.3%
	scatter with numerical	29.2%	20.3%	14.6%	9.0%	8.1%	21.8%
Berdichevsky and Cai ISCM (hexagonal)	scatter with bibliography	9.8%	5.5%	6.5%	9.2%	1.7%	4.6%
	scatter with numerical	25.9%	18.1%	13.6%	8.8%	8.9%	24.0%
Tamayol and Bahrami (square)	scatter with bibliography	33.9%	9.1%	2.6%	7.3%	6.5%	8.5%
	scatter with numerical	2.0%	6.9%	17.0%	16.6%	19.2%	37.4%

Table 19 Scattering results derived from the comparison with the bibliography results and numerical simulation results

Each one of the models mentioned in the Table 19 and Chart 5 shows results which have very low scattering when compared with the bibliography and numerical results, which is in most of the cases less than 15%.All models having a scattering less than 15% are selected to be discussed in the next section.

3.4 Numerical simulation in a transient free boundary problem mode

In the previous section the transversal numerical simulation was performed in a steady state mode in which a single phase problem was solved, where the studied fluid is located in the saturated region Figure 15. The capillary pressure and surface tension were neglected; thus the measured microscopic permeability value was the transversal saturated microscopic permeability.

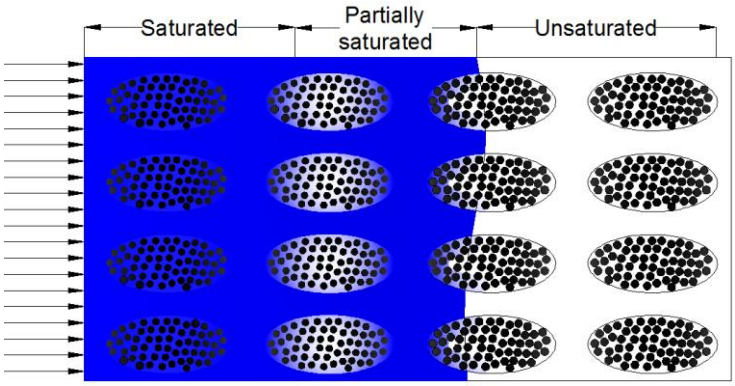

Figure 15 Flow front progression

In this part, a numerical simulation in a transient mode is done; where capillary pressure and surface tension are taken into account. The flow front progression is registered in function of time, and corresponding velocity values for selected flow front positions are recorded. Average permeability is then derived from local permeability values. Due to computational limitations, only the transversal microscopic unsaturated permeability will be predicted. The selected models from the previous comparative study between the numerical results (steady state mode), analytical models, and bibliography measurements will be compared with results derived from the new simulations (transient mode).

3.4.1 Simulation parameters in transient mode

The two fluids selected in this simulation are: Air and Epoxy Resin. Same meshing technique and boundary conditions are used when simulating in a transient mode, whereas, different parameters are took into consideration when the transient simulation is performed, which are the surface tension, mobility, and relative tolerance.

3.4.1.1 Surface Tension

The COMSOL MULTIPHYSICS allows the calculation of capillary pressure between each two fibers. Capillary pressure is the necessary pressure to force "non-wetting fluid" to displace the "wetting fluid" in a capillary. Capillary pressure [103] can be mathematically expressed as P_c, equation (9); where P_{nw} and P_w are the pressures of the non-wetting phase and wetting phase across the interface

$$P_c = P_{nw} - P_w \qquad \textit{Eq 9}$$

In other words, capillary pressure is defined by the capillary forces divided by the surface between the two fibers or between the fiber and the plane. Young-Laplace equation [104] Eq 10 is of fundamental importance in order to understand the capillary forces; where *r1* and *r2* are two principal radii of curvature, γ is the surface tension between air and fluid Figure 16 for Epoxy Resin ($\gamma=44*10^{-3}$ N/m), σ_{SA} is the surface tension between the solid and air, σ_{SW} is the surface tension between solid and fluid and Ψ is the wetting angle.

$$\Delta P = \gamma\left(\frac{1}{r_1}+\frac{1}{r_2}\right) \qquad \textit{Eq 10}$$

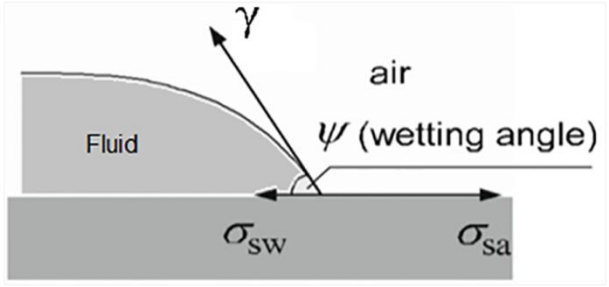

Figure 16 Wetting angle between fluid and surface

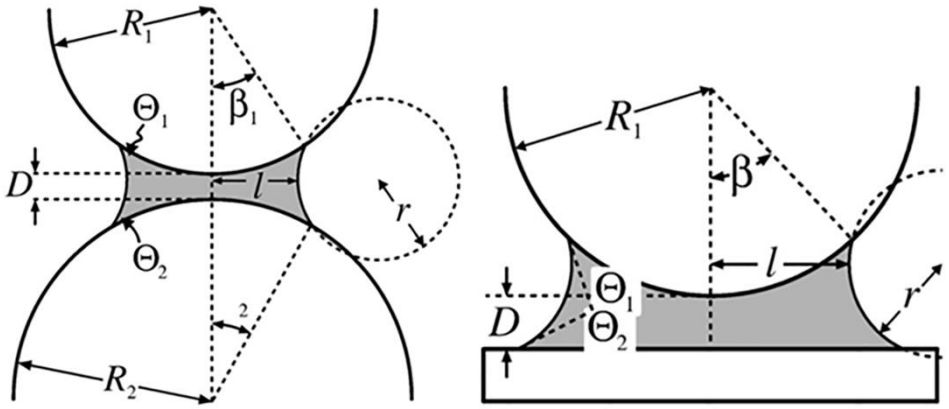

Figure 17 Fluid subjected to capillary forces in sphere-sphere or sphere-plane geometries [104]

Figure 17 and Table 20 show the capillary forces in sphere-sphere & sphere-plane geometries, where D is the distance between two interacting solid surfaces, F is the capillary force, l is the Azimuthal radius of a meniscus, R1 and R2 are the radii of two spherical particles, r is the meridional radius, β is the angle characterizing position of three phase contact line on sphere, γ is the surface or interfacial tension and θ1, θ2 contact angles on the two interacting surfaces.

Contact type	Calculated dependences
Sphere-sphere	$F = \pi\gamma R_1 \sin\beta_1 \left[2\sin(\theta_1+\beta_1) + R_1 \sin\beta_1 . \left(\frac{1}{r}-\frac{1}{l}\right)\right]$ $r = \frac{R_1(1-\cos\beta_1) + R_2(1-\cos\beta_2) + D}{\cos(\theta_1+\beta_1)+\cos(\theta_2+\beta_2)}$ $l = R_1\sin\beta_1 - r[1-\sin(\theta_1+\beta_1)] = R_2\sin\beta_2 - r[1-\sin(\theta_2+\beta_2)]$
Sphere-plane	$F = \pi\gamma R_1 \sin\beta \left[2\sin(\theta_1+\beta) + R_1 \sin\beta . \left(\frac{1}{r}-\frac{1}{l}\right)\right]$ $r = \frac{R_1(1-\cos\beta) + D}{\cos(\theta_1+\beta)+\cos\theta_2}$ $l = R_1\sin\beta - r[1-\sin(\theta_1+\beta)]$

Table 20 Contact type and calculated dependences [104]

3.4.1.2 Mobility and Relative Tolerance

The mobility is related to the time-scale of the Cahn-Hiliard diffusion and therefore governs the diffusion-related time scale of the interface. The χ parameter should be optimized to maintain a constant interface thickness and avoid damping the convective motion. A very high mobility can also lead to excessive diffusion of droplets [95].

Relative tolerance is the permitted variation in some measures and characteristics of an object or work piece. It indicates the precision of reading flow time results.

3.4.2 Results for transient simulation

The flow front position is recorded at different selected filling time intervals, after extracting the set of results of filling time and correspondent flow front position. The elementary permeability is calculated using Darcy's law. Then the total permeability is calculated by interpolating these results. Figure 18 shows the flow front observed at two different positions. The local permeability values at successive positions are calculated based on equation (6); then an average permeability value is calculated using equation (11).

$$K_Z = \frac{\sum_{i=0}^{i=n} K_{Zi}}{n} \qquad \textit{Eq 11}$$

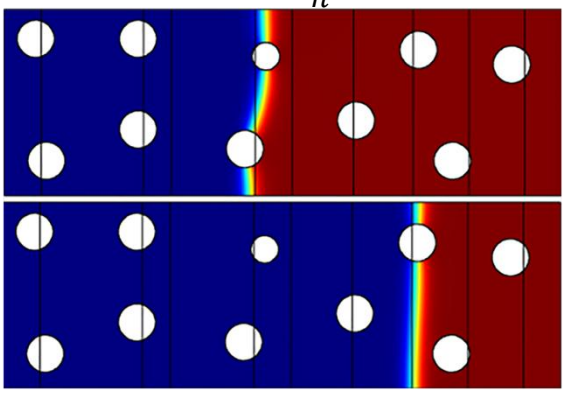

Figure 18 Flow front observed at two different positions for 0.89 porosity unit cell.

The following Table 21 shows the results of the simulation in a transient mode which gives rise to unsaturated microscopic permeability values.

ε	0.45	0.51	0.6073	0.7	0.8	0.89
Numerical / Transient mode (K_Z/r^2)	0.01164	0.0168	0.03744	0.128	0.288	0.94

Table 21 Results of the numerical simulation in transient mode

3.4.3 Comparative study (transient mode)

The models previously selected from the comparative study with steady state mode numerical simulation are subjected to sorting, in which the models with relatively lowest scattering in comparison with numerical simulation in transient mode are considered to

be the most suitable for obtaining the transversal microscopic permeability. In this comparative study the chosen models are those having a scattering less than 10%.

Table 22 indicates that Berdichevsky and Cai unified model (square) shows three scattering values 2%, 2.4%, and 5.1% which are less than 10%, at porosities 0.6073, 0.8, and 0.89 respectively. On the other hand, the other three values are greater than 10% (30.10% at porosity 0.45, 11.20% at porosity 0.51, and 11.60% at porosity 0.7).

Similarly, Berdichevsky and Cai ISCM square, Gebart Square, Tamayol and Bahrami square, Van Der Westhuizen and Du Plessis, Sahraoui and Kaviany, Phelan and Wise, and Lee and yang exhibit in each one of them three values of scattering less than 10% and other three values greater than 10%. Whereas, Berdichevsky and Cai ISCM hexagonal, Gebart hexagonal, Drummond and Tahir hexagonal, and Kuwabara are better relatively, due to the scattering values that are less than 10% at all selected porosities as shown in Table 22.

Analytical models / ε	0.45	0.51	0.6073	0.7	0.8	0.89
Berdichevsky and Cai unified model Square	30.1%	11.5%	2.0%	11.6%	2.4%	5.1%
Berdichevsky and Cai unified model Hexagonal	7.7%	3.1%	7.7%	11.2%	0.7%	0.2%
Berdichevsky and Cai ISCM square	39.6%	21.1%	6.1%	17.4%	0.3%	7.1%
Berdichevsky and Cai ISCM Hexagonal	8.3%	3.1%	8.7%	8.7%	3.8%	7.7%
Gebart Hexagonal	7.9%	3.5%	9.1%	8.3%	4.2%	8.1%
Gebart Square	26.8%	7.0%	8.3%	3.2%	14.0%	21.2%
Drummond and Tahir hexagonal	5.2%	8.2%	10.1%	8.2%	3.3%	5.5%
Tamayol and Bahrami square	32.6%	11.5%	4.9%	6.8%	8.5%	11.6%
Van Der Westhuizen and Du Plessis	14.7%	2.1%	9.2%	5.8%	10.8%	20.6%
Kuwabara	4.7%	5.3%	9.7%	8.5%	3.0%	5.4%
Sahraoui and Kaviany	32.6%	14.4%	1.0%	10.7%	3.0%	1.0%
Phelan and Wise	26.8%	7.0%	8.3%	3.2%	14.0%	21.2%
Lee and yang	31.8%	13.6%	1.1%	10.9%	4.2%	7.1%

Table 22 Scattering derived from the comparison with the numerical simulation in transient mode results

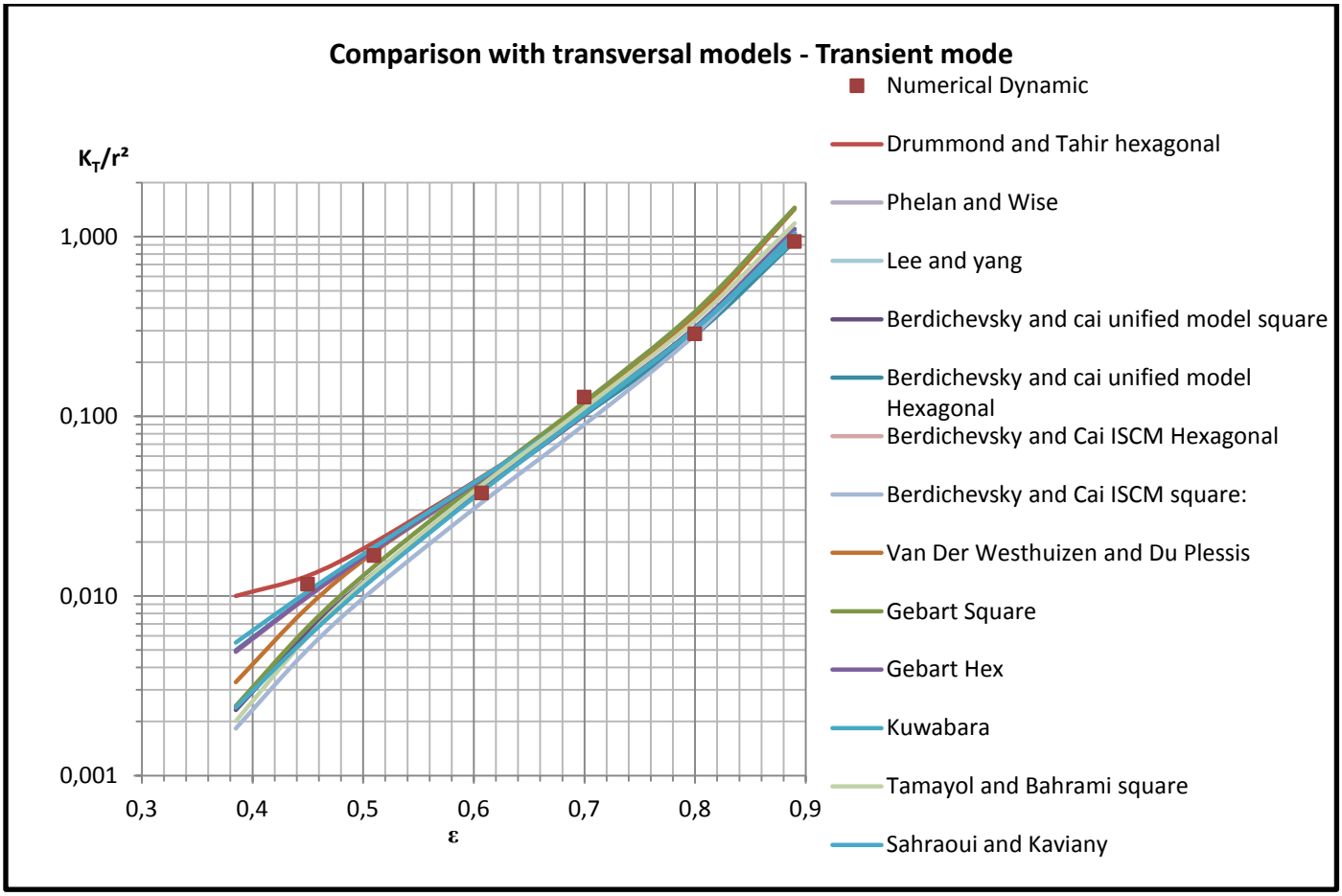

Chart 6 Comparison with transversal results

3.5 Discussion and analysis

The comparative studies listed in the previous part of the article are done in order to choose the best models which serve in predicting the microscopic permeability.

After performing the comparison between the longitudinal models and the results of the bibliography and numerical simulations in steady state mode, the models Bahrami and Tamayol, Drummond and Tahir, Berdichevsky and Cai ISCM square, and Berdichevsky and Cai unified square are elected to be the most accurate in predicting longitudinal microscopic permeability. This selection was done based on the low scattering values in these comparisons.

Regarding the comparative study between the transversal models and the results of the bibliography and numerical simulations in steady state mode, a primary selection was

done which highlighted the models that show lower scattering values in comparison with the other models. The selected models are Berdichevsky and Cai unified model Square, Berdichevsky and Cai unified model Hexagonal, Berdichevsky and Cai ISCM Square, Berdichevsky and Cai ISCM Hexagonal, Gebart Hexagonal, Gebart Square, Drummond and Tahir Hexagonal, Tamayol and Bahrami Square, Van Der Westhuizen and Du Plessis, Kuwabara, Sahraoui and Kaviany, Phelan and Wise, and Lee and Yang.

Those models are subjected to a secondary selection process which aims to ensure choosing the most convenient models able to fulfill the prediction of transversal microscopic permeability when recommended in any study. This selection process is spread on two steps. First, a numerical simulation in transient mode is done at the same given unit cells previously. This simulation solves a dual phase problem and thus gives permeability value which is more realistic and resembling a real experiment. Second, a comparative study is done between the analytical results of the models and the obtained results from the numerical simulation in transient mode. The models which show the least scattering in this comparison are Berdichevsky and Cai ISCM (hexagonal), Gebart (hexagonal), Drummond and Tahir (hexagonal), and Kuwabara. These selections are the most convenient models for predicting transversal microscopic permeability which is involved in obtaining the permeability tensor value.

3.6 Conclusion

The microscopic permeability analytical models were subjected to sorting by comparing their permeability outputs to results derived from other prediction methods. A numerical study was performed, distinguished by utilizing a unit cell with random fiber arrangement which was most representative for real experiment. A comparative study was done between analytical modeling, bibliography, and numerical results. Its analysis presents that Bahrami and Tamayol, Drummond and Tahir, Berdichevsky and Cai ISCM and unified (square) models have good agreement with this data for longitudinal microscopic permeability components. Concerning transverse microscopic permeability, Berdichevsky and Cai ISCM (hexagonal), Gebart (hexagonal), Drummond and Tahir (hexagonal), and Kuwabara models were elected to be the most accurate models. On the

other hand, transient mode simulations gave rise to results synchronized with the static mode simulations, which revealed the consistency of the study.

The profit of this study is to know the most convenient analytical models to predict the microscopic permeability in unidirectional fiber bundles. Furthermore, in order to calculate an accurate permeability tensor, the value of the microscopic permeability should be obtained precisely. Moreover, the microscopic permeability could be employed in some other studies such as capillary pressure or permeability modeling studies.

4 Chapter 4: Experimental measurement

4.1 Introduction

In a manufacturing process the resin is generally injected or infused in an unsaturated dry preform in a radial or longitudinal injection; under constant pressure unless a constant injecting velocity device is used.

The method for measuring the in-plane permeability adopted in Benchmark II [9] is used in this study. The objective was to work on standardizing experimental permeability measurements. The scatter between experimental data obtained by different research groups for the same fabric was less than 25% using this experimental method. That method with its guidelines was adopted in this work.

Concerning through-thickness permeability measurement, some improvements on measuring techniques, which were developed in "Ecole de Polytéchnique de Montréal" are presented. In the next sections, the experimental methods adopted will be explained as well as the materials preparation and specifications.

This chapter also presents the in-plane and through-thickness permeability measurements, in addition to all fabrics' geometrical data. In its last section a discussion concerning the results is launched. In the presented work thirteen different fabrics are investigated in order to evaluate the permeability tensor. In-plane permeability is measured for the eleven fabrics, and through-thickness permeability is measured for seven fabrics. Carbon or glass fabrics are delivered by different manufacturers. Fabrics A-G and Fabric J are afforded by Texonic Company; other fabrics are delivered by Chomarat, 3TEX, and Saertex Companies.

4.2 Materials Preparation

4.2.1 Properties of testing fluid

The test fluid used is silicon oil "PMX-200" with a selected viscosity of (0.05 or 0.1Pa.s) with perfect Newtonian behavior. Although it is more expensive than some alternatives such as corn oil for example, this test fluid was preferred over the years for permeability measurements because of the stability of its properties with respect to time.

It is important to know the behavior of this liquid and in particular the evolution of the viscosity as a function of the temperature in order to be able to calculate the permeability to the most just. Indeed, the room in which the tests were carried out is not temperature-controlled. Depending on the days, the temperature could vary by several degrees. Since the viscosity depends on the temperature, this has been noted at the beginning of each experiment to adjust the viscosity value. Figure 19 shows the results of a rheological analysis with a verification of the Newtonian behavior and the evolution of viscosity as a function of temperature.

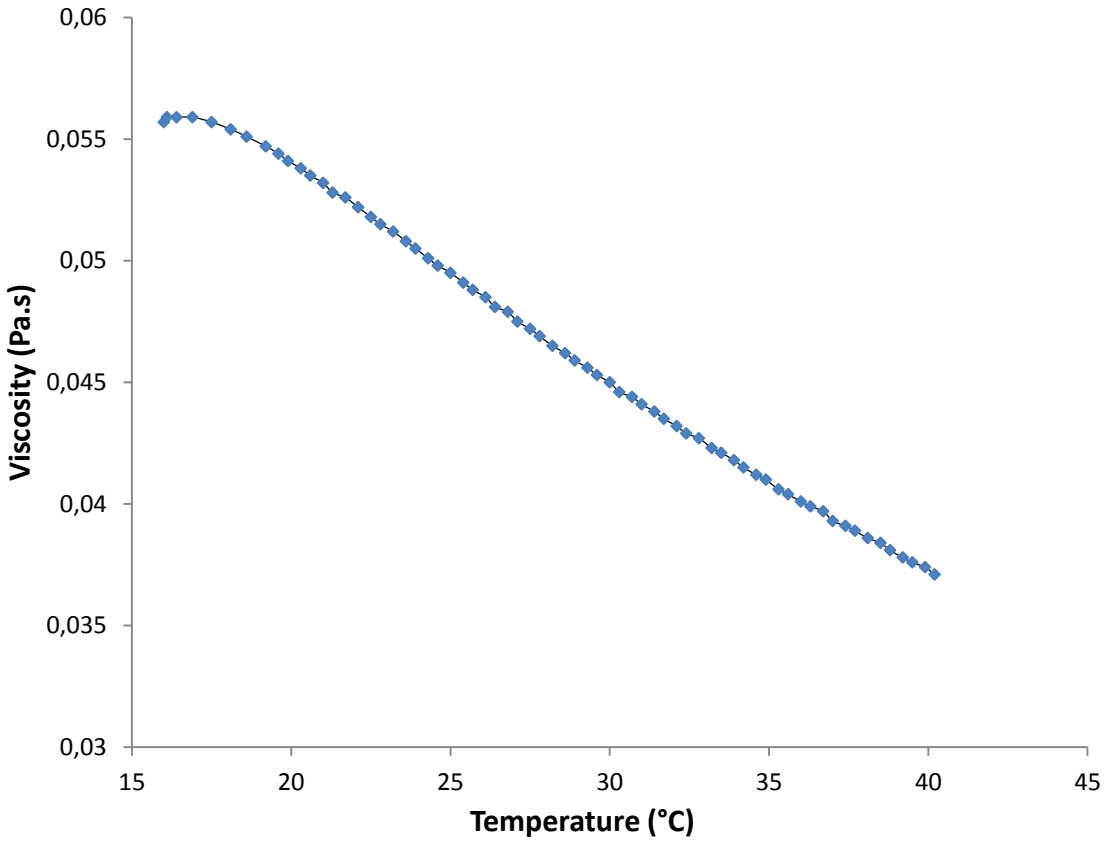

Figure 19 Rheological behavior of silicone oil "PMX-200" 50CS

4.2.2 Reinforcement cutting procedure

The layers of the fibrous reinforcement have to be cut in three directions defined after the weaving pattern of the fibers. As shown in Figure 20, the warp direction is taken as the 0° orientation. The two other orientations of the samples are at angles of 45° and 90° with respect to the warp direction, the latter orientation being along the weft direction of

the fabric. The orientations used in the sequel of this chapter always refer to the directions defined in Figure 20. It is important to cut the fibrous reinforcement in an accurate and precise way in order to reduce the variability of the measurements. Usually two approaches can be followed:

- Cutting with a press using a die rectangular samples
- Using an automated cutting machine.

(a) For the first option the reinforcements are cut using rectangular die with precise dimensions (100*400 mm), then stacked on a flat holding pieces.

(b) With an automatic cutting machine. With appropriate blades any shape drew in AutoCAD software format can be cut with a good efficiency.

Figure 21 shows the cutting pattern used to obtain samples of 100 x 400 mm² for the in-plane permeability measurements. Note that the same equipment can be used to cut the circular samples for transverse permeability measurements.

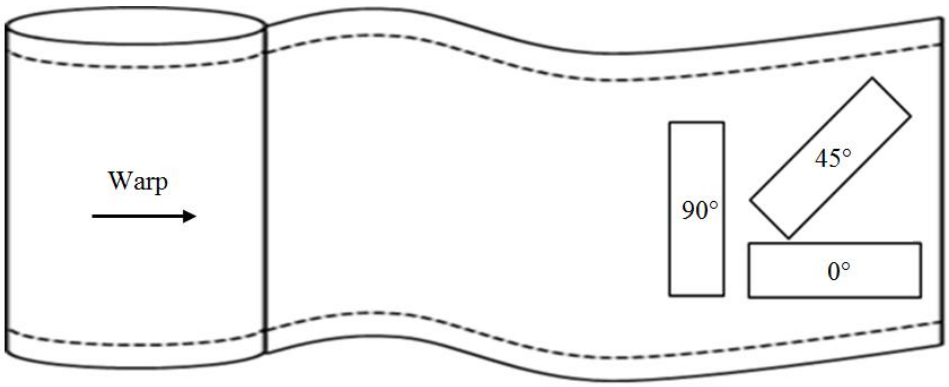

Figure 20 Fiber orientation in the roll

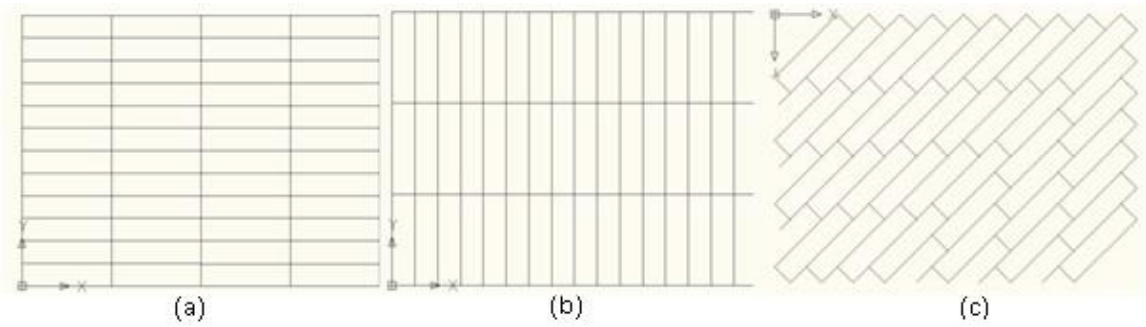

Figure 21 Cutting patterns: (a) at 0°, (b) at 90°, (c) at 45°.

4.3 In-plane Permeability Measurement Method

In order to obtain the principal components of the in-plane permeability of a fabric, three unidirectional injections are required. Indeed, as shown in Figure 22, the in-plane flow front pattern is elliptic. Thus, three directions of measurement (three points) are needed to determine the characteristics of that ellipse [9, 105]. However, unidirectional experiments consisting of filling a rectangular mold were found not only to be simpler to conduct, but also more robust. Unidirectional tests turned out to give the best results in terms of repeatability and accuracy. For many reasons, it is less prone to errors, which makes it the preferred choice over other methods reported in the scientific literature.

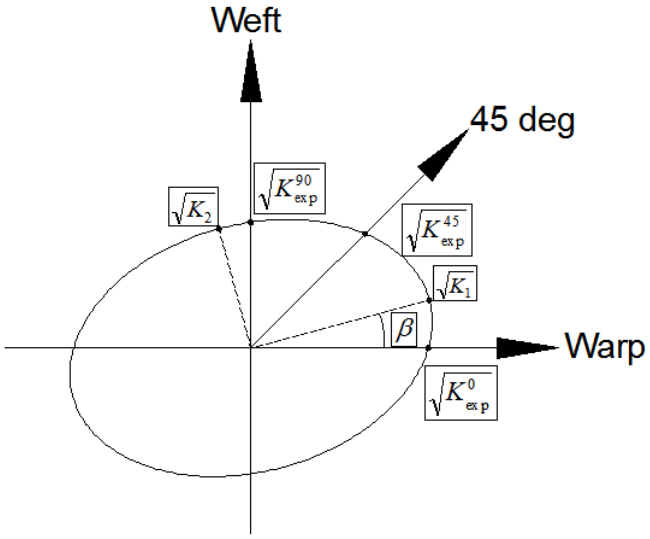

Figure 22 Elliptic pattern of the flow front for an anisotropic fibrous reinforcement.

4.3.1 Permeability mold setup

The experimental setup for unidirectional in-plane permeability measurements is shown in Figure 23 and Figure 24. The mold is composed of three principal parts: a lower metallic base, a cover plate in tempered glass, and an upper metallic frame, Figure 23. The reinforcement is positioned in the cavity between the inferior and superior plates. In order to ensure the right cavity thickness and provide the desired fiber volume fraction, a metallic frame is placed between the lower and upper parts of the mold. The cavity thickness is pre-determined using a special paste made from argil. A sealing rubber is then inserted in the cavity along the sides of the frame. To prevent peripheral flows on the lateral sides of the mold, also called “edge effects”, silicone caulking is applied along

the sides of the reinforcement to fill up the space left between the sealing rubber and the fibers. Note that this new mold concept for in-plane permeability measurements was designed and built by ERFT Composites.

As shown in Figure 24, the mold is held in place by a supporting structure, on which two hydraulic pistons are installed. These pistons provide a way for automatic closing of the mold at a pressure around 1500 psi applied directly on the compression frame. Figure 24 also shows the injection pot, from which the test fluid is injected, and the acquisition box and laptop which record the pressure and flow front positions in time.

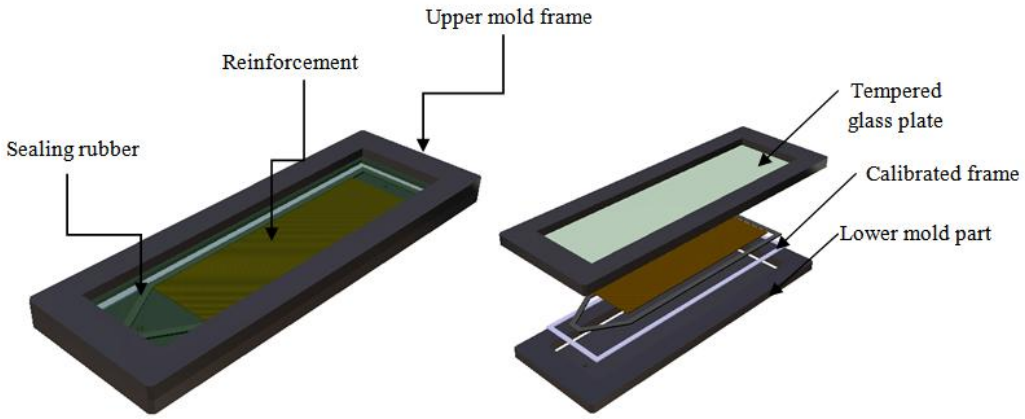

Figure 23 Rectangular mold for in-plane permeability measurements.

Figure 24 In-plane permeability mold setup.

This method of permeability characterization is based on recording the progression of the fluid front as the resin flows through the fiber bed. The more regular is the flow front, the more accurate is the measurement. Figure 25 illustrates the desired straight shape of the flow front in a unidirectional injection. Pictures of real injections for a 3Dorthogonal fabric are shown in the Figure 26. These figures correspond to injections at 0°,45° and 90° on a $V_f = 55.35\%$. No race tracking is observed due to the insulation insured by the silicon rubber (black color) and the silicon mastic (white color). A straight flow front is observed in the Figure 26 (a) and Figure 26 (c), and a 45° straight flow front is observed in the Figure 26 (b); reflecting a good sign concerning the quality of the experiments.

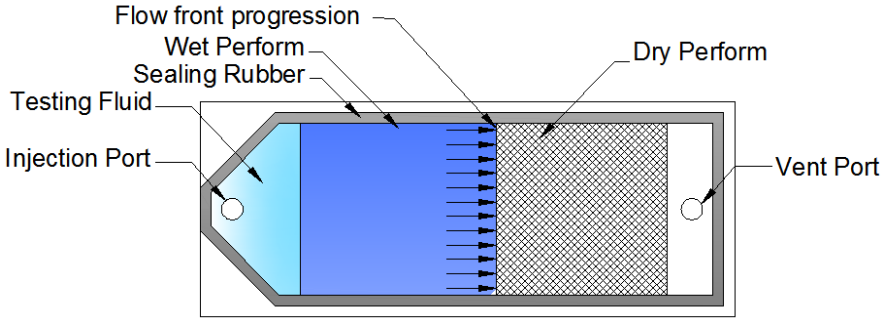

Figure 25 Principle of unidirectional in-plane permeability measurements.

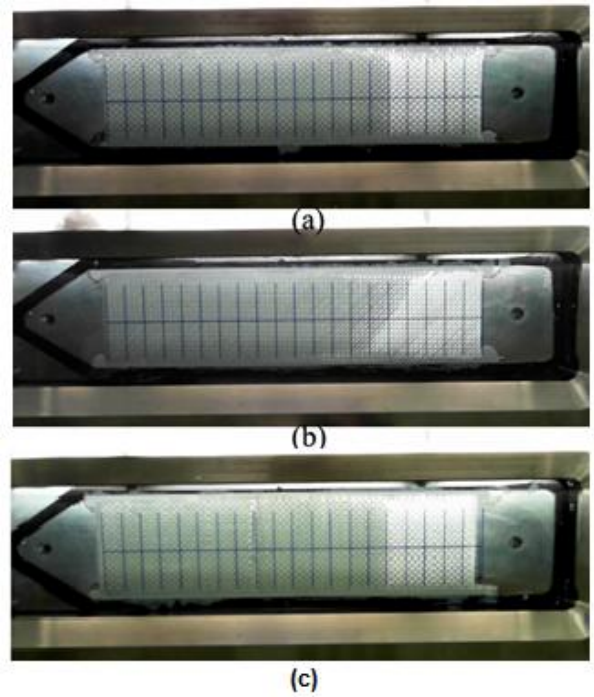

Figure 26 (a) Flow front for 0° injection, (b) flow front for 45°injection, (c) flow front for 90° injection.

4.3.2 Software description

The existing software module used for permeability characterization was developed by ERFT Composites. It allows measuring unidirectional permeability by PermLab and calculating the permeability ellipse using PrinPer.

4.3.2.1 PermLab data acquisition software

PermLab is a real-time data acquisition interface for unidirectional permeability measurement and calculation. Permeability measurements can be performed on-line in both rigid "Resin Transfer Molding" (RTM) configuration and flexible "Vacuum Assisted Resin Infusion" (VARI) configuration. During a permeability test, the values of pressure inside the mold and the positions of the flow front are acquired in time. Figure 27 shows an example of the injection pressure evolution in function of time during a test in a sample cut along the warp (0° orientation). The evolutions of the flow front and of its velocity appear in Figure 28 and Figure 29 respectively. Finally, Figure 30 shows a graph of permeability calculated at each position in the mold during resin injection. The dots represent the experimental values recorded during an injection experiment at a constant pressure, while the red line is obtained using Darcy's law. In the permeability graph, the estimated permeability represented by a dotted line is calculated by a least square method. Usually, a slight difference between the experimental results and the interpolated line is tolerated, but major spreads indicate an anomaly in the measure. These graphs provide a detailed log of the experiment and allow verifying if Darcy's law can be used to evaluate the "process permeability" or if it should be discarded because of too high "edge effect", for example, or any other possible experimental perturbation.

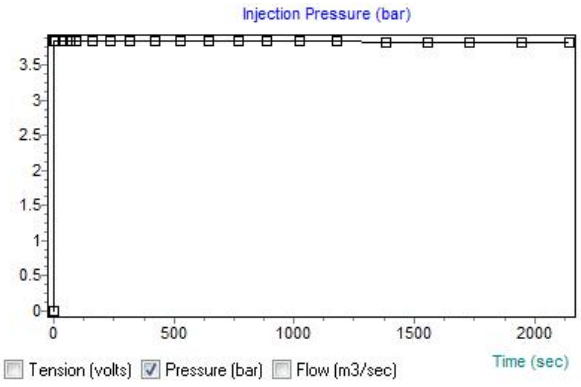

Figure 27 Injection pressure at the injection gate as a function of time in a test at 0°.

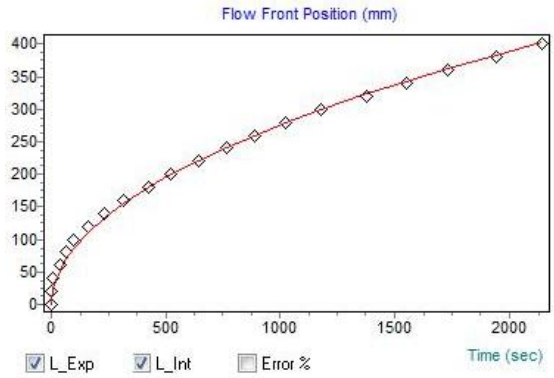

Figure 28 Flow front position as a function of time in a test at 0°.

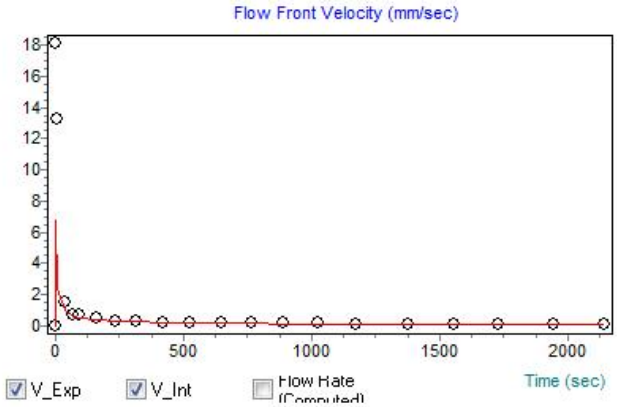

Figure 29 Flow front velocity as a function of time during a test at 0°

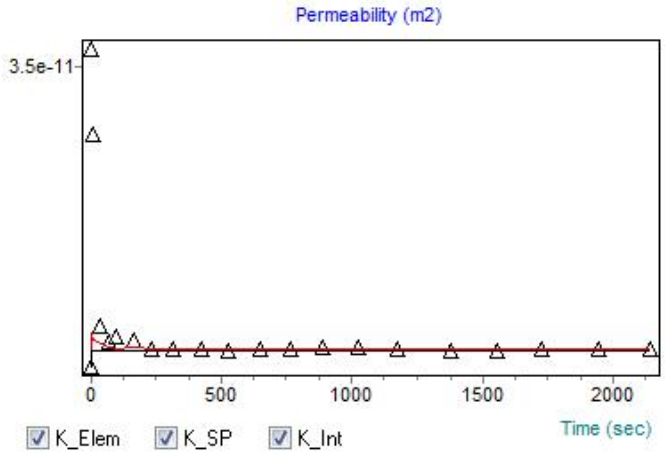

Figure 30 Permeability as a function of time during a test at 0°

Figure 27 shows an unusually perfect pressure build-up right at beginning of injection. The graph shown in Figure 28 shows that Darcy's law is well respected in this experiment, where the experimental data points follow the theoretical curve of the flow front position obtained by Darcy's law. Note that a small discrepancy is usually observed

at the beginning of injection until Darcy flow regime becomes established. The velocity decreases rapidly before the Darcy flow regime is established at the beginning of injection, and then slows in time as expected in a constant pressure injection experiment Figure 27. The triangles denote the point wise permeability evaluated from the local velocity of the flow front. This permeability is always higher at the beginning of injection before the Darcy flow regime is established. The straight line least square fit represents the "process permeability" evaluated in the characterization experiments Figure 27.

4.3.2.2 PrinPer principal permeability analysis software

PrinPer is a program that estimates the elliptic flow front pattern of anisotropic fabrics from a series of unidirectional measurements. It allows calculating the principal permeability values, the highest (K_1) and lowest (K_2), and their orientations β in anisotropic fabrics, from the effective permeability measured in three different directions by unidirectional injections. The calculations are done as shown in equations (12-16).

In this report the effective permeability is the unidirectional permeability measured along one of the specified direction (0°, 45° and 90°), as opposed to principal permeability values given by the two components K_1 and K_2 of the permeability tensor together with the angle β of the highest permeability direction K_1 with a reference taken on the reinforcement. Figure 9 displays a result of PrinPer.

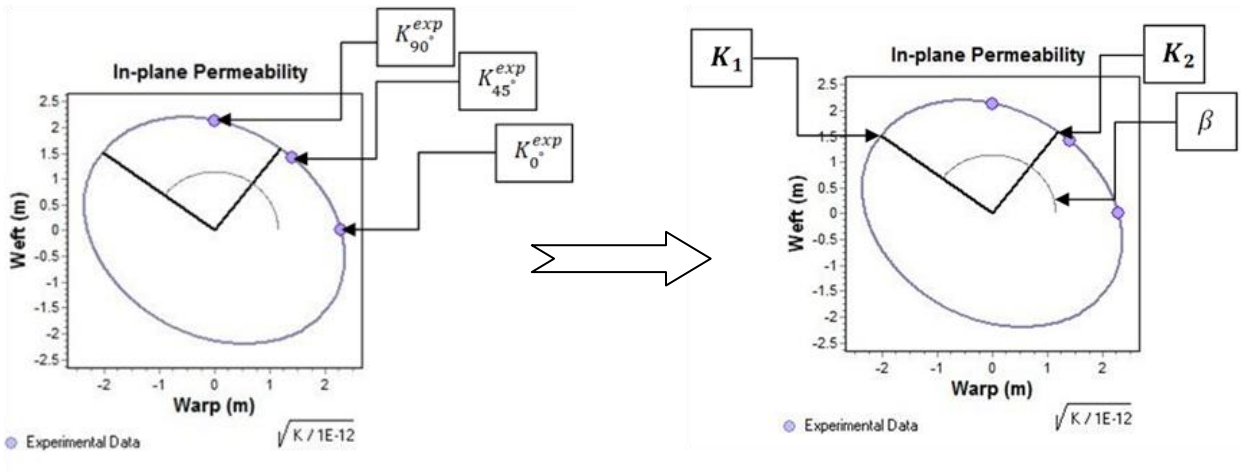

Figure 31 Permeability ellipse for a fabric at V_f= 50.7%.

$$K_1 = K_{0^\circ}^{exp} \frac{(\alpha - \gamma)}{\left(\alpha - \frac{\gamma}{cos(2\beta)}\right)} \quad \text{Eq.(12)}$$

$$K_2 = K_{90^\circ}^{exp} \frac{(\alpha + \gamma)}{\left(\alpha + \frac{\gamma}{cos(2\beta)}\right)} \quad \text{Eq.(13)}$$

$$\beta = \frac{1}{2}\tan^{-1}\left(\frac{\alpha}{\gamma} - \frac{\alpha^2 - \gamma^2}{\gamma * K_{45^\circ}^{exp}}\right) \quad \text{Eq.(14)}$$

$$\alpha = \frac{\left(K_{0^\circ}^{exp} + K_{90^\circ}^{exp}\right)}{2} \quad \text{Eq.(15)}$$

$$\gamma = \frac{\left(K_{0^\circ}^{exp} - K_{90^\circ}^{exp}\right)}{2} \quad \text{Eq.(16)}$$

The Ellipse drawing, for a 3D Orthogonal, is shown in the figure 10 for a stack at a fiber volume fraction of 55.35%. The Figure 32 shows the three permeability values K_{0° , K_{45° *and* K_{90° then in the results the principal permeability values K_1, K_2, β and the ellipse drawing.

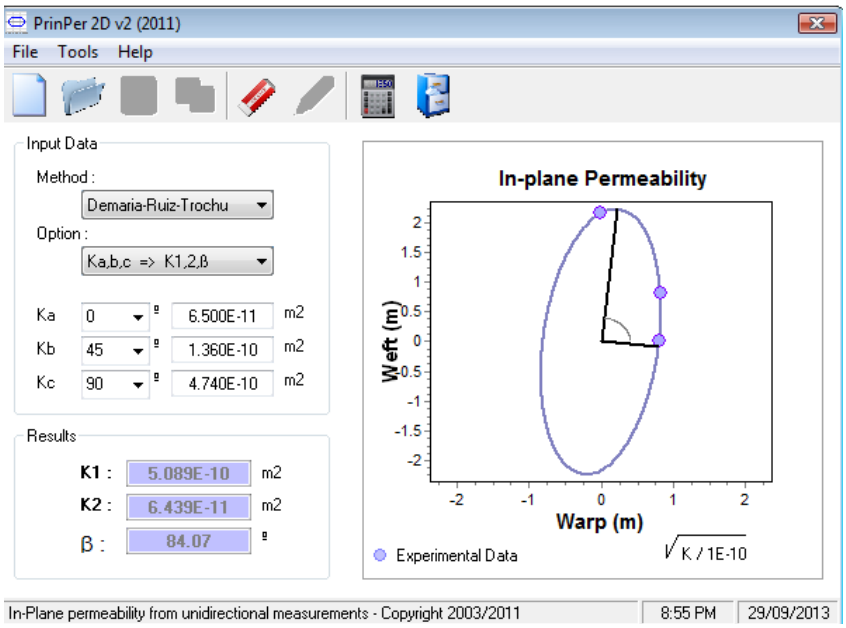

Figure 32 The ellipse shape extracted from PrinPer at V_f =55.35%.

4.4 Through-thickness permeability measurement method

In through-thickness permeability measurements; the flow rate is measured as a function of the injection pressure. The value of the transverse permeability K_3 is determined by using Darcy's law in its unidirectional form as shown in equation (17).

$$u = \frac{Q}{A} = \frac{K_3}{\mu} \cdot \frac{\Delta P}{h} \qquad \text{Eq.(17)}$$

Where u stands for the Darcy injection speed, Q for the volumetric flow rate, A for the area of the fabrics, μ for the viscosity of the injected oil, ΔP for the pressure loss, and h for the thickness of the reinforcement.

The principle of the transverse permeability measurement is to obtain a linear relationship between the pressure loss and the volumetric flow rate (i.e., a linear fit), by fixing different levels of Q and measuring the corresponding ΔP as shown in equation (18).

$$\frac{Q}{\Delta P} = m = \frac{K_z}{\mu} \cdot \frac{A}{h} \qquad \text{Eq.(18)}$$

"*m"* is the slope of the curve in the flow rate-pressure loss graph. In this way, the only unknown variable in Darcy's law is the transverse permeability K_3, which is derived from the slope *m* and the other constant parameters *A*, *h* and *μ:*

$$K_3 = \frac{m \cdot \mu \cdot h}{A} \qquad \text{Eq.(19)}$$

Figure 33 shows the injection system. When injecting the silicon oil inside a mold as seen in Figure 34, the oil can't be followed visually. The used method is injecting the oil in a radial way into a wet saturated preform under constant velocity. At each injection velocity, a while is waited until a steady pressure at the inlet of the textile is obtained. A curve relating the pressure to the corresponding oil flow will give the slope used to calculate K_3 as explained in equation (19). The transverse permeability mold is made out of two hollow concentric cylinders, inside which the reinforcement is positioned horizontally. The fibers are placed between two circular metallic plates pierced with numerous holes so as to ensure at the same time a uniform compaction of the preform and

a homogeneous flow of the oil injected in the mold. A set of shims is used to set the fiber volume content (determined from the thickness of the fabric sample). The mold is closed by three nuts tightened manually. Figure 34 illustrates the geometry of the transverse permeability mold.

Figure 33 Oil injection System

Using a hydraulic cylinder, the oil is injected at constant speed (i.e. constant volumetric flow rate) in the bottom cavity of the mold (under the reinforcement), where a pressure sensor connected to a data acquisition system is installed. In this way, the values of pressure in the oil can be recorded as function of time on a graph displayed on a computer Figure 35; where for each injection flow rate the injection pressure stabilize on a constant pressure after a certain time. These values are noted as (P1, Flow1), (P2, Flow2), (P3, Flow3) and so on.

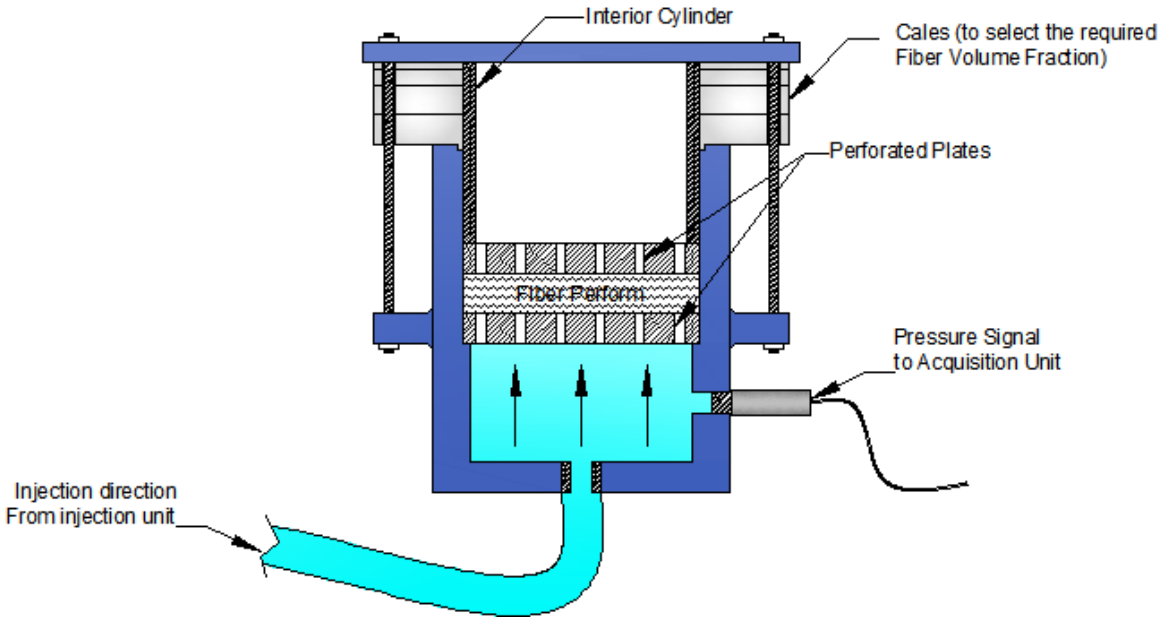

Figure 34 Schematic of the mold used for the measurement of the transversal permeability.

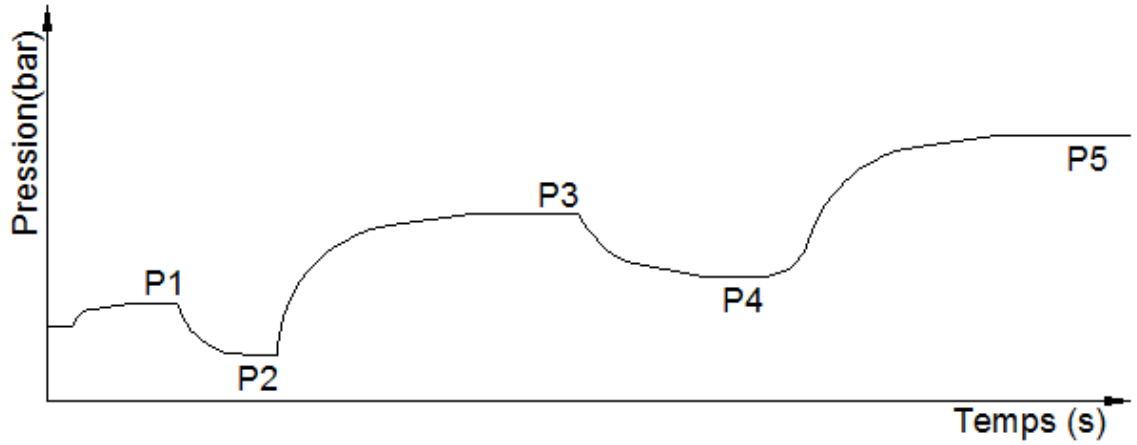

Figure 35 Evaluated pressures function of time and flow rate

In order to obtain a relation between the pressure loss and the volumetric flow, several different injection flows are set during the test, alternating from higher to lower values each time in order to avoid nonlinear effects. According to Darcy's law, the relationship between pressure loss and volume flow rate is supposed to follow a linear pattern. A

typical injection test sequence for transverse permeability is presented in

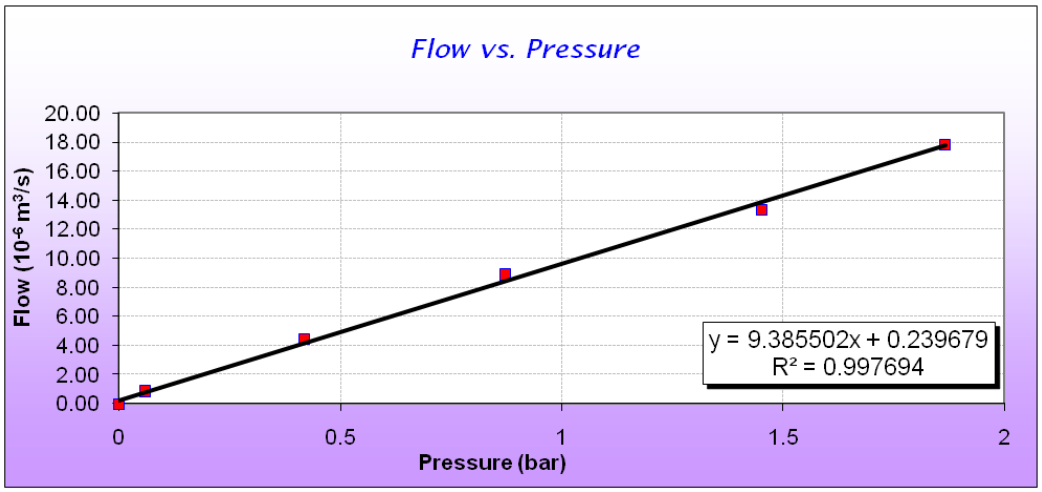

Figure 36 (for V_F = 49.67%). R^2 shows the degree of correlation between successive applied flow and corresponding pressures, a higher R^2 value means a more reliable experiment.

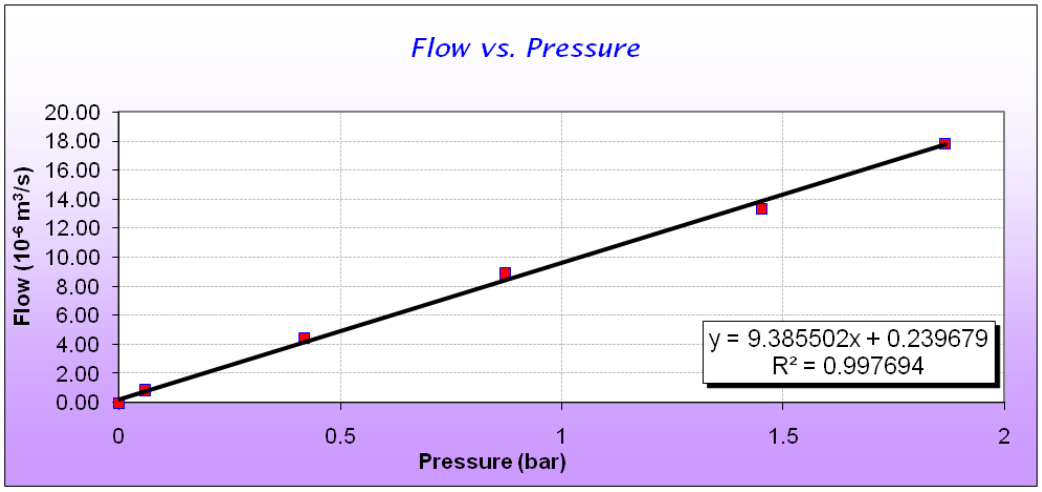

Figure 36 Flow function of pressure

4.5 Fabric specifications

Fabrics A-F fabrics are either non-crimped stitched fabrics NCF or 3D orthogonal fabrics. Table 23 and Table 24 show properties for fabrics A-F, these properties include the used materials, counts number, surface density ρ_s, initial thickness H_0, and warp weft bundle properties, in addition to the fabric identity.

Fabric	Fabric Name	Fabric type	Primary material	Secondary material	Counts/cm	
					Warp	Weft

Fabric A	TG-09-N-60J	NCF	E-Glass	Polyester	5.5	5.2
Fabric B	TG-15-N		E-Glass	Polyester	3.1	10.4
Fabric C	TG-33-N-50E		E-Glass	Polyester	4.6	8.4
Fabric D	TG-54-N-60C	3D orthogonal	E-Glass	E-Glass	8	11.4
Fabric E	TG-75-N-50E		E-Glass	E-Glass	11.4	12.6
Fabric F	TG-96-N-60I		E-Glass	E-Glass	6.9	14.8
Fabric G	TC-67-N-50A		Carbon	E-Glass	6.9	13.6

Table 23 Fabrics (A-G) properties

Fabric A is a two layer e-glass NCF with a surface density equal 320 g/m^2 stitched in both directions by a polyester binder. The warp/weft volume ratio, 51/49, shows that this fabric is balanced with approximately equal bundle width, counts and volume for both directions. Fabric B is a three layer e-glass NCF with a surface density equal 518 g/m^2 stitched in the warp direction by a polyester binder. The warp/weft volume ratio is 55/45, with a warp bundle 2.6 times bigger than the weft bundles. Fabric C is a four layer e-glass NCF with a surface density equal 1125 g/m^2 stitched in warp direction by a polyester binder. The warp/weft volume ratio is 55/45.

Fabric	**Surface density ρ_S (g/m^2)**	**Thickness H_0(mm)**	**Warp/ Weft Volume %**	**Number of layers**		**a (mm)**	
				Warp nbw	**Weft nbf**	**Warp**	**Weft**
Fabric A	320	0.36	51/49	1	1	1	1.1
Fabric B	518	0.5	45/55	1	2	2.35	1.47
Fabric C	1125	0.9	45/55	2	2	3.9	2.1
Fabric D	1800	1.52	48/52	3	4	3.15	1.9
Fabric E	2542	2.29	46/54	3	4	2.15	1.65
Fabric F	3250	2.79	50/50	3	4	3.4	1.9
Fabric G	2275	2.54	51/49	3	4	3.3	1.1

Table 24 Fabrics (A-G) properties

The four 3D orthogonal fabrics "D-G" are all seven layers fabrics. Two fabrics are E-glass 3D orthogonal fabrics with an E-glass through-thickness along the warp direction (Fabrics D and F) with a surface density 1800 and 3250 g/m^2 respectively, one 3D orthogonal fabric with an E-glass binding yarn along the warp direction and two different Tex in the weft direction (Fabric E) with a surface density 2542 g/m^2. The forth, fabric G, is a carbon fabric with an E-glass binding yarn along the warp direction with a surface density 2275 g/m^2. Table 25 shows bundle properties for the above mentioned fabrics,

where the Tex represents the linear density of the used bundles in g/Km and the filament radius in µm.

Fabric	Material (Tex)				Filament radius (µm)			
	Warp		Weft		Warp		Weft	
	Pri.	Sec.	Pri.	Sec.	Pri.	Sec.	Pri.	Sec.
Fabric A	275	16.7	275	16.7	16	25	16	25
Fabric B	735	16.7	275	-	13	25	16	-
Fabric C	1100	16.7	735	-	17	25	13	-
Fabric D	1100	134	735	-	17	9	13	-
Fabric E	1100	275	1100	735	17	16	17	
Fabric F	2*1100	275	1100	-	17	16	17	-
Fabric G	2*775	275	800	-	8	16	8	

Table 25 Fabrics (A-G) bundle properties

A UD-Glass roving fabric stitched by HS glass bundles is provided by Tissa Company, Fabric H. Chomarat Company provided a carbon fabric, Fabric I where ±45° bidirectional layers are stuck to each other, then sewed by a polyester binder in the warp direction. The distance between two polyester binders is 5.2 mm. Two different plain weave fabrics are studied, the first is a carbon fiber plain weave fabric supplied by Chomarat Company, Fabric K, and the second is an E-glass plain weave provided by Texonic, Fabric J. Fabric L is a 3D orthogonal fabric having architecture similar to Fabric F, with approximate same surface density. Fabric M is a ±90° bidirectional fabric layers are stuck to each other and knitted with a polyester yarn. This fabric is not balanced; the small quantity of weft bundles (~8% from the total volume) ensures easy manipulation of the fabric for manufacturing purposes. Table 26, Table 27, and Table 28 show the identity, fabric properties and fabrics bundle properties for the above mentioned fabrics (H-M).

Fabric	Company	Fabric Name	Type	Material
Fabric H	Tissa	850.0445.80.0600	Unidirectional	E-Glass
Fabric I	Chomarat	C-Ply-SP BX300	Bidirectional	Carbon
Fabric J	Texonic	L14012	Plain weave	E-Glass
Fabric K	Chomarat	C-weave 200P 3K	Plain weave	Carbon
Fabric L	3TEX	P3W-GE044	3D orthogonal	E-Glass
Fabric M	Saertex	U14EU920	Bidirectional	E-Glass

Table 26 Fabrics (H-M) identity

Fabric	ρ_S (g/m^2)	H_0 (mm)	Number of layers		a (mm)		Counts/cm	
			Warp nb_w	Weft nb_f	Warp	Weft	Warp	Weft
Fabric H	445	0.39	1	1	2.53	0.325	3.6	1

Fabric I	303	0.37	1	1	-	-	-	-
Fabric J	597	0.53	1	1	2.1	2	4	3.9
Fabric K	200	0.28	1	1	1.52	1.8	4.9	4.9
Fabric L	3280	2.54	3	4	2.35	2.93	7.5	10.5
Fabric M	995	1	1	1	3.15	1.76	-	-

Table 27 Fabrics (H-M) properties

Fabric	**Material (Tex)**				**Filament radius (μm)**				**Warp/ Weft Volume %**
	Warp		**Weft**		**Warp**		**Weft**		
	Pri.	**Sec.**	**Pri.**	**Sec.**	**Pri.**	**Sec.**	**Pri.**	**Sec.**	
Fabric H	1100	275	1100	735	17	16	17		98.8/1.2
Fabric I	200	-	200	-	3.5	-	3.5	-	N/A
Fabric J	750	-	750	-	13	-	13	-	50.5/49.5
Fabric K	200	-	200	-	3.5	-	3.5	-	50/50
Fabric L	N/A	N/A	N/A	N/A	16	16	16	-	51.5/48.5
Fabric M	N/A	N/A	N/A	N/A	16	-	16	-	91.6/8.4

Table 28 Fabrics (H-M) bundle properties

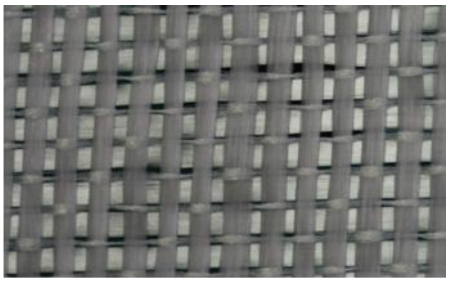

Fabric A

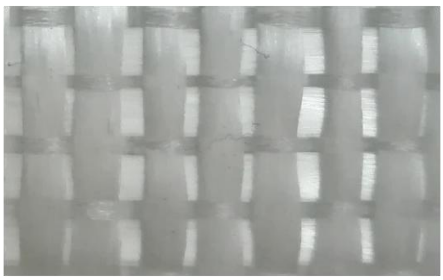

Fabric B

Fabric C

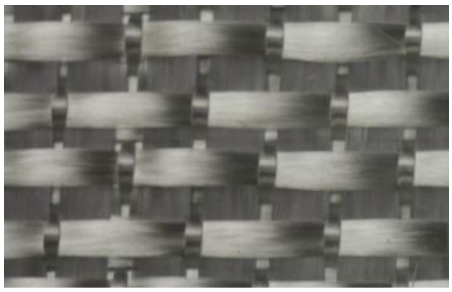

Fabric D

Figure 37 Fabrics E-H pictures

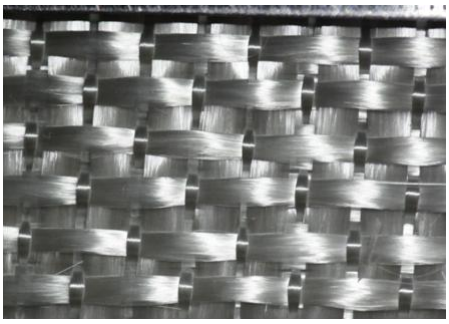

Fabric E

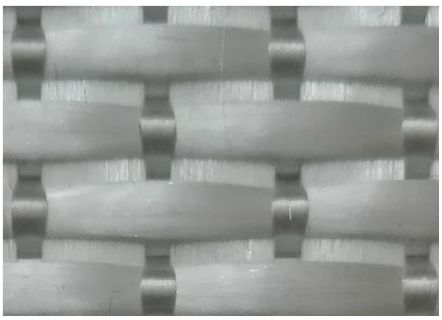

Fabric F

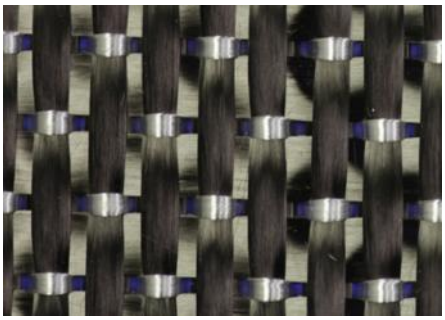

Fabric G

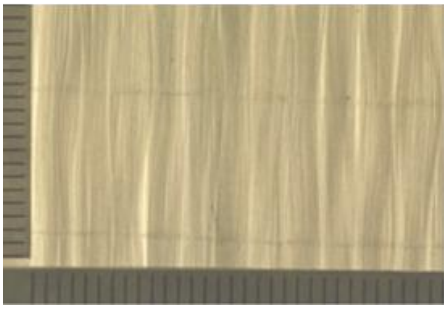

Fabric H

Figure 38 Fabrics A-D pictures

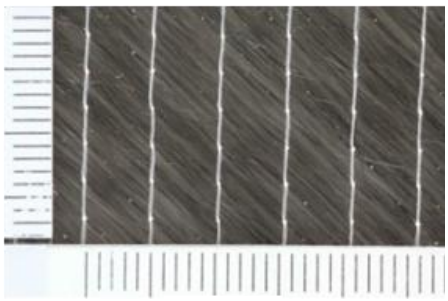

Fabric I

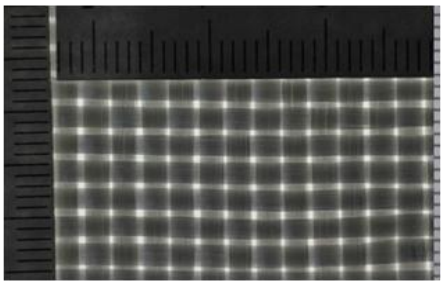

Fabric J

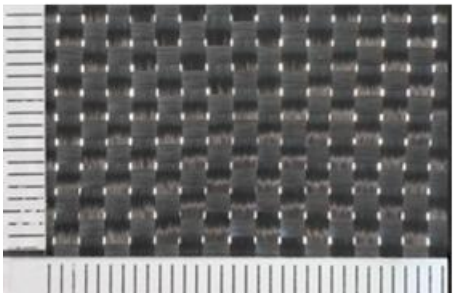

Fabric K

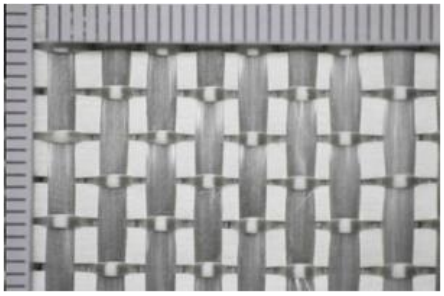

Fabric L

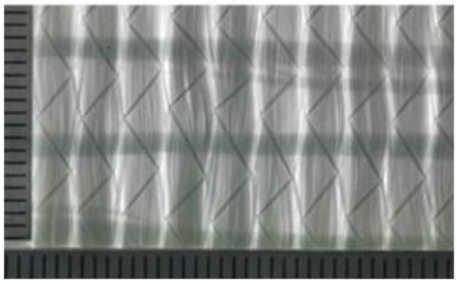

Fabric M

Figure 39 Fabrics I-M pictures

Figure 37, Figure 38, and Figure 39 show fabrics' pictures. These pictures and others are took using a high resolution camera, using these photos some distances like the bundle width "a" the gap size between two adjacent bundles are measured.

4.6 Permeability measurements

4.6.1 In-plane permeability measurements

In this section the results for in-plane permeability measurements are presented. In the first step the raw results are presented in Appendix A. Two or three measurements in each direction (0°, 45°, and 90°) for each fiber volume fraction for the unidirectional

permeability values are established for the eleven fabrics. In the next step a mean value for the unidirectional permeability measurements is calculated ($K_{0°}$, $K_{45°}$, and $K_{90°}$) on each fiber volume fraction; a corresponding scattering is obtained. Scattering value is calculated for two or three successive measurements done for each fabric on a selected V_f. The observed deviation C_V, namely the standard deviation, over the mean between those different measurements must be less than 15% as previously mentioned in Chapter 4. These results are shown in Table 29, Table 30, Table 31, and Table 32.

Fabric Name	**Fabric A**			**Fabric B**			**Fabric C**		
V_f (%)	45.99	53.65	61.32	39.83	47.8	55.76	49.48	56.6	63.36
$K_{0°}$ (*$10^{-11}m^2$)	2.96	1.01	0.57	25.5	7.05	1.4	23.24	5.59	2.53
$K_{45°}$ (*$10^{-11}m^2$)	4.31	1.45	0.73	27.9	7.35	1.65	16.15	6.37	2.54
$K_{90°}$ (*$10^{-11}m^2$)	6.26	2.60	1.42	30.3	7.44	1.78	27.05	9.68	4.53
C_V at 0° (%)	7.8	4.1	3.2	0.1	11.4	4.2	8.6	8.8	6.2
C_V at 45° (%)	1.7	3.8	1.0	2	0.1	9.6	0.6	8.6	0.1
C_V at 90° (%)	9.8	4.1	4.7	0.1	0.1	14.08	2.1	1.1	0.1

Table 29 Unidirectional permeability values for fabrics A-C

Fabric Name	**Fabric D**			**Fabric E**			**Fabric F**		
V_f (%)	44.94	52.43	59.99	51.26	55.87	64.48	52.83	59.02	67.23
$K_{0°}$ (*$10^{-11}m^2$)	13.07	7.79	3.68	24.46	11.50	3.99	13.60	7.42	0.75
$K_{45°}$ (*$10^{-11}m^2$)	25.81	12.23	4.81	52.38	19.32	5.97	22.55	9.74	0.97
$K_{90°}$ (*$10^{-11}m^2$)	80.45	32.05	12.62	114.93	42.39	8.27	64.66	21.04	1.56
C_V at 0° (%)	5.5	1.8	5.4	5.2	0.1	0.3	2.4	5.5	4.4
C_V at 45° (%)	1.6	1.4	8.4	0.3	0.5	6.8	2.7	12.2	1.6
C_V at 90° (%)	0.7	11.4	10.6	2.6	2.8	11.6	4.9	19.4	5.2

Table 30 Unidirectional permeability values for fabrics D-F

Fabric Name	**Fabric G**			**Fabric H**			**Fabric I**		
V_f (%)	54.08	60.42	68.82	47.93	54.56	61.62	46.21	52.81	65.76
$K_{0°}$ (*$10^{-11}m^2$)	10.410	3.294	0.299	3.060	1.350	0.277	1.46	0.661	0.087
$K_{45°}$ (*$10^{-11}m^2$)	14.562	4.958	0.256	1.590	0.753	0.224	1.43	0.608	0.084
$K_{90°}$ (*$10^{-11}m^2$)	33.143	10.045	0.865	1.470	0.754	0.190	1.22	0.469	0.068
C_V at 0° (%)	4.9	11.3	1.1	3.1	1.35	0.28	10.9	6.4	13.3
C_V at 45° (%)	10.1	6.8	18.2	1.7	0.97	0.1	5.1	3.6	14.1
C_V at 90° (%)	10.0	0.1	10.5	6.28	0.1	0.1	1.1	3.2	3.4

Table 31 Unidirectional permeability values for fabrics G-I

Thirdly, the main in-plane permeability values (K_1 and K_2) and the deviation angle are derived. The equations relating the unidirectional permeability values ($K_{0°}$, $K_{45°}$, and $K_{90°}$)

to the principal permeability values (K_1 and K_2) and the deviation angle β are previously described in chapter 4.

Fabric Name	Fabric J			Fabric K		
V_f (%)	44.51	53.41	62.31	43.4	52.08	60.76
$K_{0°}$ (*$10^{-11}m^2$)	34.1	6.65	1.14	3.033	0.666	0.168
$K_{45°}$ (*$10^{-11}m^2$)	31.5	5.94	0.899	2.167	0.473	0.121
$K_{90°}$ (*$10^{-11}m^2$)	38.5	8.26	1.43	1.575	0.416	0.095
C_V at 0° (%)	10.35	1.5	3.1	13..48	0.1	16.11
C_V at 45° (%)	4.3	2.8	0.1	6.8	5.6	10.9
C_V at 90° (%)	5.76	9.3	5	7.9	13.7	2.3

Table 32 Unidirectional permeability values for fabrics J-K

As an example, Table 33 shows the principal in-plane permeability values for Fabric A. this table shows the selected fiber volume fractions and corresponding in-plane principal permeability values (K_1 and K_2). K_1 represents the bigger value and β the angle between K_1 and warp direction. Figure 40 shows the ellipse diagram for Fabric A on each fiber volume fraction. Ellipse shape corresponds to flow shape in a real injection. All principal permeability values and injection schematics for Fabrics B-K are shown in Appendix 2.

Fabric name	V_f (%)	K_1 (*$10^{-11}m^2$)	K_2 (*$10^{-11}m^2$)	β°
Fabric A	V_{f1}= 45.99	6.32	2.94	84.6
	V_{f2}= 53.65	2.60	1.01	90.2
	V_{f3}= 61.32	1.46	0.56	97.5

Table 33

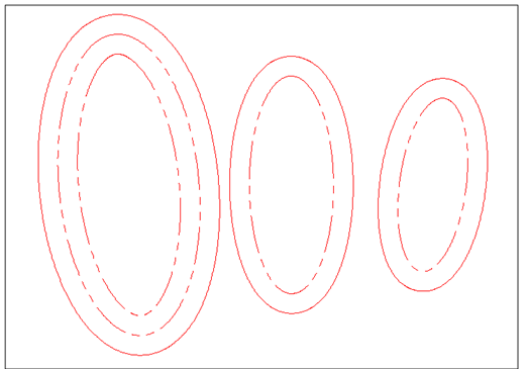

Fabric A

Figure 40 Ellipse shape for an imposed injection, the right ellipse corresponds for the lower V_f "Fabric A"

4.7 Through-thickness permeability measurements

In this section the transversal permeability measurements are presented. A typical injection test sequence for through-thickness permeability measurement for Fabric H at V_{f1} is presented in Figure 41; it shows the relation between the pressure and the volumetric flow, different injection flows are set during the test, alternating from higher to lower values each time in order to avoid nonlinear effects. According to Darcy's law, the relationship between pressure loss and volume flow rate is supposed to follow a linear pattern as previously described in chapter 4. Per example 0.396275 is used as the ratio between differential flows to the pressure. R^2 shows the degree of correlation between successive applied flow and corresponding pressures. Using these data the sample area and thickness, the permeability value is calculated. Figure 42 shows a second injection on same condition. According to repeated measurements a scattering value is then calculated. Table 34, Table 35, and Table 36 show the transversal permeability values K_3 for every fiber volume fraction. The scattering Cv, is noted for repeated measurements performed at each V_f. An average scattering for repeated measurements is below 10% for all fabrics, showing the consistency of the measurements.

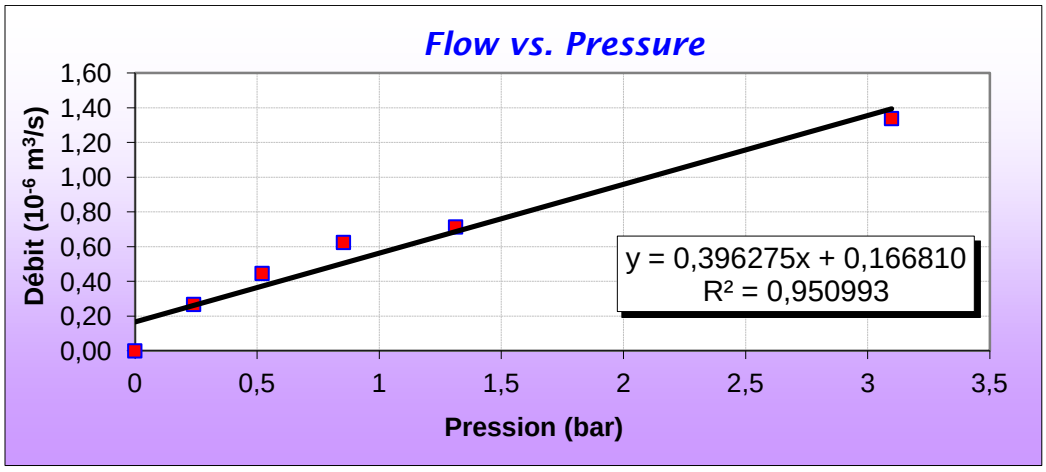

Figure 41 Fabric H through-thickness permeability measurement (V_{f1}, exp_1)

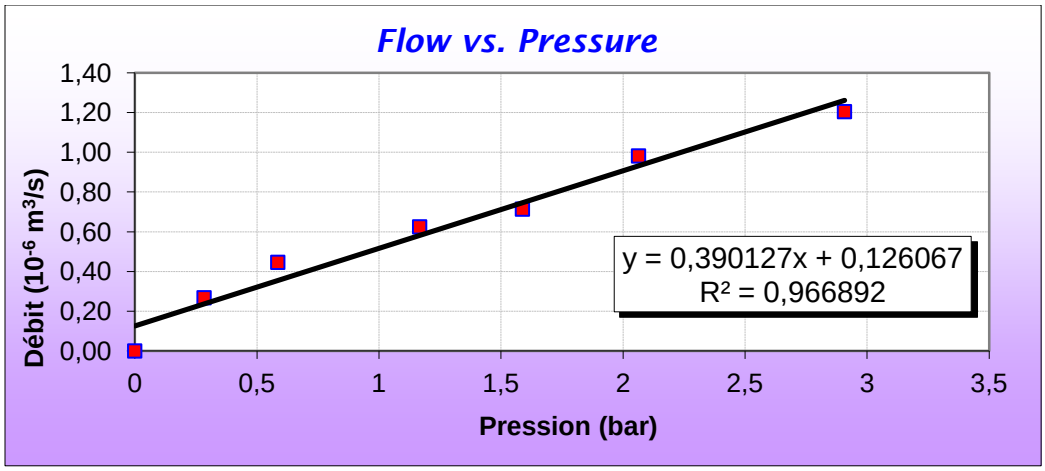

Figure 42 Fabric H through-thickness permeability measurement (Vf_1, exp_2)

Fabric Name	Fabric B			Fabric H		
V_f (%)	43.99	47.99	55.98	47.17	53.13	60.65
K_3 (*10^{-13} m^2)	94.145	65.19	33.34	4.2338	2.7413	1.3090
Cv (%)	0.1	4.5	2.4	0.9	9.0	1.9

Table 34 Through-thickness permeability values for Fabrics (B, H)

Fabric Name	Fabric I			Fabric K		
V_f (%)	46.39	56.33	66.27	43.74	52.49	61.24
K_3 (*10^{-13} m^2)	1.996	1.153	0.685	6.347	4.053	2.214
Cv (%)	0.3	9.9	4.5	4.8	5.2	9.1

Table 35 Through-thickness permeability values for Fabrics (I, K)

Fabric Name	Fabric L			Fabric M		
V_f (%)	49.67	55.76	63.43	40.22	50.6	58.11
K_3 (*10^{-13} m^2)	110.197	83.972	63.860	53.037	35.227	21.463
Cv (%)	7.2	1.9	2.4	2.2	3.5	1.7

Table 36 Through-thickness permeability values for Fabrics (L, M)

4.8 Analysis and conclusion

In this chapter, an experimental method to measure the in-plane permeability components is presented. After a state of art it is found that the calculation of permeability components by experimental methods is still facing major problems. These problems are related to the injection method by itself, whether it is unidirectional or radial, and related to the setup and measuring devices used. The used method is based on a unidirectional injection performed under a constant pressure. The velocity of the front flow is measured, and then the permeability in the injection direction is calculated from

the Darcy law. In order to calculate the in-plane permeability components, three permeability components are calculated for 0°, 45° and 90° orientations. Then, principle permeability components K_1 and K_2 are derived with; the orientation of the major axis of the ellipse. Being close to each other, the obtained results for a repeated permeability measurement represents an indication of the reliability and efficiency of the test as well as of the used method. Concerning through-thickness permeability measurement, the used method is based on an injection of the test fluid at alternating velocities, the pressure will be measured using the data acquisition unit at each velocity; the transversal permeability is evaluated based on Darcy's law. This method showed an improvement concerning the multiple point measurement for each permeability value instead of single point measurement.

4.8.1 In-plane permeability

The principal permeability is showed with respect to the fiber volume fraction variation based on Appendix 2 Tables 12 and 13. A decrease of both principal permeability components (K_1, K_2) with respect to an increasing V_f is observed in all studied fabrics.

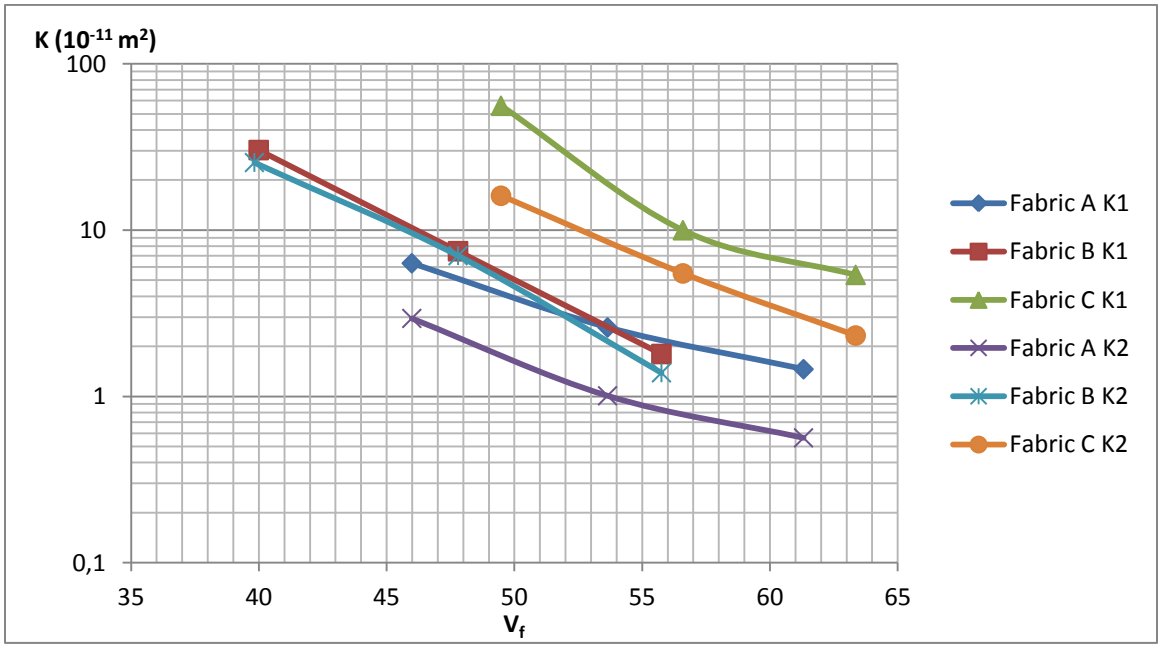

Figure 43 Principal permeability Vs fiber volume fraction for Non-crimped fabrics (A-C)

Based on Figure 43, Appendix2 Table 13, and Appendix2 Figure 1; it's remarked that fabric C has biggest permeability values among all the V_f values. When $V_f < 51\%$, Fabric B has bigger (K_1, K_2) than Fabric A. Noting that the surface density of the above mentioned fabrics are arranged as follows (ρ_S Fabric A< ρ_S Fabric B< ρ_S Fabric C), the permeability values are increasing with increasing surface density of similar architecture fabrics. Also a deviation angle $\beta=90\pm30°$ is observed for these fabrics, this means that $K_{0°}$ is always smaller than $K_{90°}$, this is revealed to the presence of stitching yarns in the warp direction, playing the role of obstacles in front of the 0° flow. The results shown for the NCF, Fabric A, indicate a decrease of (K_1, K_2) with increase with a ratio constant K_1/K_2 around 2.2, and the predicted β is around 90°. Fabric B, indicate a decrease of (K_1, K_2) with increase with a constant ratio K_1/K_2 around 1.2, and the predicted β is around 80°. Fabric C has a large K_1/K_2 ratio= 3.2 for V_{f1} where K_1 directed along 78° direction; this ratio decreases for V_{f2} and V_{f3} to around 2, while β increases.

Based on Figure 44, Appendix2 Table 12 and 13, and Appendix2 Figure 1 and 2 the 3D orthogonal fabrics are discussed. β value is almost stable around 90°, for all fabrics and almost on all fiber volume fractions except for Fabric G, on a very high fiber volume fraction V_{f3}=69% (where β=120°) the weft mesopores seems to be equal in size for both direction 0° and 90°.

Fabrics D and F have close structure, same material "E-glass" but with 2 main differences, the first is the mesopores volumes (mesopore size* number), the second is size of the mesopore created around the stitching yarn (this effect will be discussed in Chapter 6. In addition to the factor of surface density previously discussed for NCFs. This leaded to a higher permeability values (K_1, K_2) for Fabric F. Noting that the ratio K_1/K_2 is larger for Fabric D (6.5→3.7) than Fabric E (4.8→2.1).

Fabric E shows high permeability (K_2) values in 90° direction while smaller values are shown for K_1. Fabrics F and G have same structure, near mesopores, and same stitching yarn material and size. These fabrics have different warp and weft material (e-glass and carbon) and Fabric F have thickness H_0=2.79mm while H_0=2.54mm for Fabric G. (K_1, K_2) are larger for the e-glass fabric, Fabric F; except for a $V_f > 62\%$ where K_1 for Fabric G > K_1 Fabric F which decreased intensively on high fiber volume fraction.

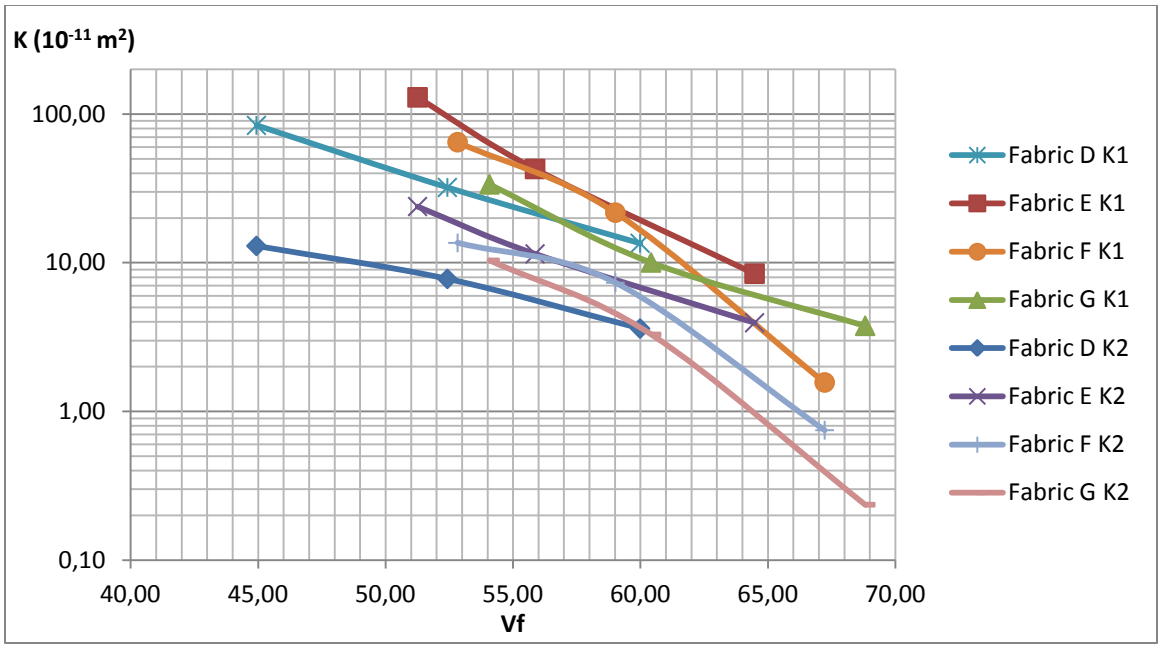

Figure 44 Principal permeability Vs fiber volume fraction for 3D orthogonal fabrics (D-G)

Based on Figure 45, Appendix2 Table 13, and Appendix2 Figure 2, the following discussion is presented. Concerning the unidirectional Fabric H has shown a decrease in K_1 with increasing V_f from 48% to 61 % from 3.486 x 10^{-11} m^2 to 0.277 x 10^{-11} m^2. The same decrease in permeability is also shown for the second component K_2 from 1.388 x 10^{-11} m^2 to 0.19 x 10^{-11} m^2. The ratio K_1/ K_2 is almost constant for the first two volume fractions (48% and 54%), while it decreases to 1.46 for V_f = 61%. This is due to the reduced size of the channel that has the direction of warp yarns for higher V_f, which reduces the principle permeability component K_1 the most.

For the bidirectional textile, Fabric I, the influence of V_f is well noticed. A decrease of both principal permeability components is shown. The permeability predicted for V_f =46% is twice and about seventeen times those for V_f 56% and 66% respectively. The ratio K_1/ K_2 is almost stable and around 1.4. In addition the predicted β for all V_f are almost the same, around 20°. This deviation in the ellipse shape indicates that the influence of stitched yarns that creates the channels and gaps is similar for both warp and weft directions; that's come back to the 45° direction of the stitching yarn (which is along 0° direction) with both ±45° carbon yarns.

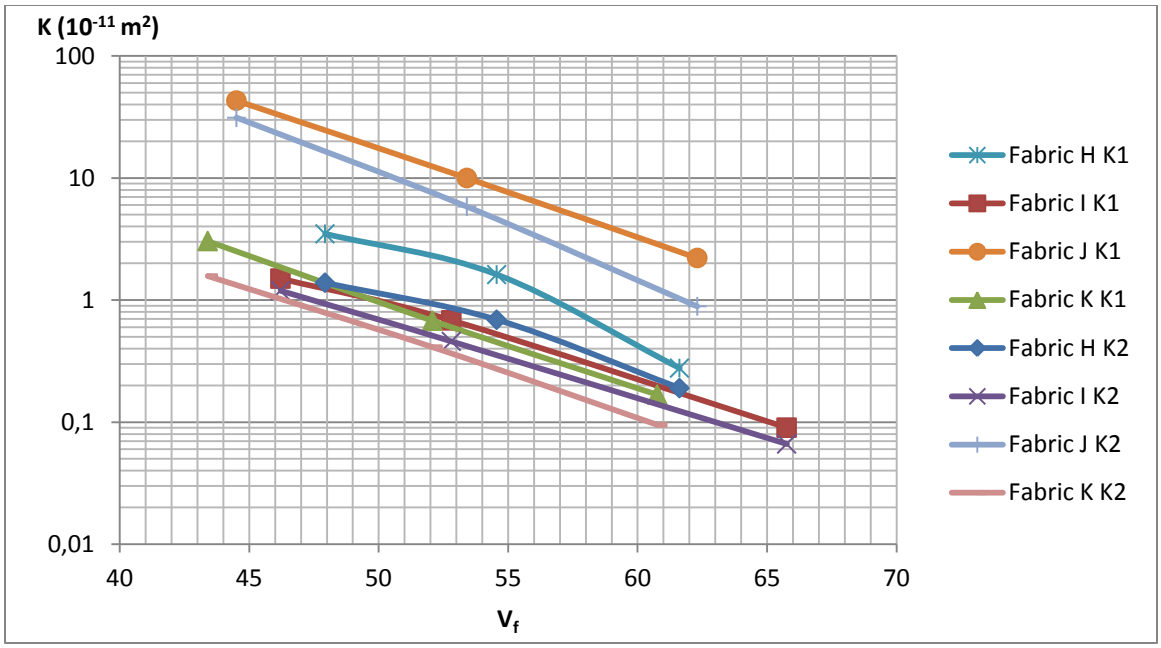

Figure 45 Principal permeability Vs fiber volume fraction for fabrics (H-K)

Concerning the plain weave fabric, Fabric K, the predicted (K_1, K_2) for V_f=43.4%, which are 3.04 x 10^{-11} m^2 for K_1 and 1.571 x 10^{-11} m^2 for K_2, are 4 times and 18 times bigger than the permeability for V_f =52.08% and 60.76% respectively. The ratio K_1/K_2 is almost stable and around 1.8. In addition the predicted β for all V_f are almost the same; around 0°. The fabric is designed to be almost balanced; however, the measurement of geometrical parameters indicates a higher gap between warp yarns in comparison with weft yarns. This leads to a higher permeability in the warp direction, $K_{0°}$ is much bigger than $K_{90°}$. Consequently, K_1 is directed along 0° direction.

Regarding the second plain weave fabric, Fabric J, the ratio K_1/K_2 is increasing from 1.4 to 1.7 to 2.5 for V_f ranging from 44% to 62%. In addition the predicted β for all V_f are almost the same; around 125°. It should be noticed that for this fabric, K_{90} is higher than K_0, so that the ratio K_1/K_2 isn't equal to 1, due to the higher gap found for weft yarns in comparison with that for warp yarns.

4.8.2 Through-thickness permeability

The permeability K_3 has the biggest values for Fabric L ranging from 1.1*10^{-11} m^2 at V_{f1} to 0.63*10^{-11} m^2 at V_{f3}. This fabric has high width gap (0.6mm in the warp direction and 1.6mm in the weft direction), these mesopores, well organized, helps the flow to flood

easily. Fabric B and Fabric M has moderate permeability values. These two fabrics are bidirectional E-glass fabrics. Smaller mesopores (0.8mm in the warp direction and 0.4 mm in the weft direction) than Fabric L, and thinner stitching yarn (polyester instead of glass) caused a reduction in permeation.

Fabric H, Fabric I, and Fabric K has very low permeability values "K_3". The values are in an order of magnitude of 10^{-13} m^2; this is explained by their architectures, which are respectively a unidirectional, bidirectional with no noticeable mesopore, and a plain weave, where no noticeable gap is measured for these fabrics; thus the fluid encounters difficulty to permeate through the thickness. In these three fabrics the permeability is at the same order of magnitude of microscopic permeability. In this part the effect of compaction on permeability values "K_3" is studied. The ratio of permeability value for the lowest V_f on the highest V_f is shown in Figure 46.

It is remarked that the calculated ratio for all fabrics is around 2.5; the highest ratio is shown for Fabric H (Unidirectional) with a value of 3.2, however the lowest ratio is for Fabric L (3D orthogonal) with 1.7.

This observation meats the logic since in a 3D orthogonal fabric, an E-glass stitching yarn keeps the mesopores open while being compacted, while in a unidirectional fabric K_3, the small mesopores in the one layer fabric is directly closed due to nesting effect while being compacted.

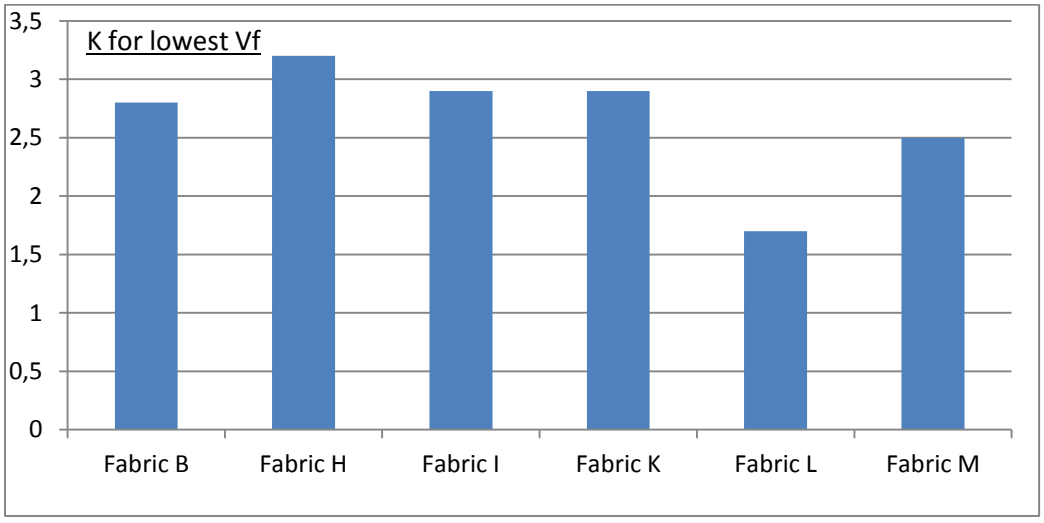

Figure 46 Through-thickness permeability ratios for extreme Vf

While most composite parts are manufactured with a V_f ranging between 40% and 60%, the calculated ratio indicates that the V_f have less influence on through-thickness permeability values than in-plane permeability values. It means that fabrication of structural parts using infusion process for high V_f could be achievable easily depending on a good prediction of the magnitude order of K_3. It is clear that the gap size has a big influence on through-thickness permeability "K_3". Thick layer fabrics are less influenced by the nesting factor, especially 3D orthogonal fabrics.

5 Chapter 5: In-Plane Permeability Prediction Model for Non-Crimp and 3D Orthogonal Fabrics

5.1 Introduction

Permeability represents a measure of the ability of a composite fabric to allow fluids to pass through it. A predictive model has been developed to estimate the unidirectional permeability in both, the warp and weft directions, for a family of non-crimped and 3D orthogonal fabrics. The model is based on an analytical solution derived from previous studies, in which the microscopic permeability of unidirectional fiber bundles is estimated. The implementation of this model requires basic geometrical parameters of the fabric architecture and information concerning the compaction of the preform. Those parameters include the dimension of the mesopores and architecture of the fiber bundles, which are determined from pictures taken for the fabric and from the textile data sheet. In addition, the average volume of mesopores and fiber bundles are required and are calculated for different fiber volume fractions taking into account a selected unit cell in the warp and weft directions. As a matter of fact, the model evaluates two contributions; the first one deals with the flow inside and in between the tows while the second one figures out the flow deviations arising from the stitching yarns. The model uses effective radius and fiber volume fraction to evaluate permeability for the two flow contributions mentioned above. An experimental investigation validates the predictive model for five different fabrics and three different fiber volume fractions. A good agreement of is found between experimental results and those predicted by the proposed analytical model.

A well manufactured part which is required and crucially demanded by the industries is characterized by a successful filling of the mold that decreases both macroscopic and microscopic voids. In order to simulate the resin injection and to predict the filling time of any structure, accurate permeability values of the fabric is required. Any fabric could be considered as a dual scale medium, where the flowing resin is modeled as a dual scale flow. Researchers classify the flow inside the bundles as “microscopic flow” and between the bundles as “mesoscopic flow”; however at the piece level the scale is named

"macroscopic flow", as shown in Figure 47 . In other words, the permeability of bundles or unidirectional yarns is called microscopic permeability while that for a fabric is called macroscopic permeability. $K_{0°}$ and $K_{90°}$ represent the permeability values in both warp and weft directions respectively.

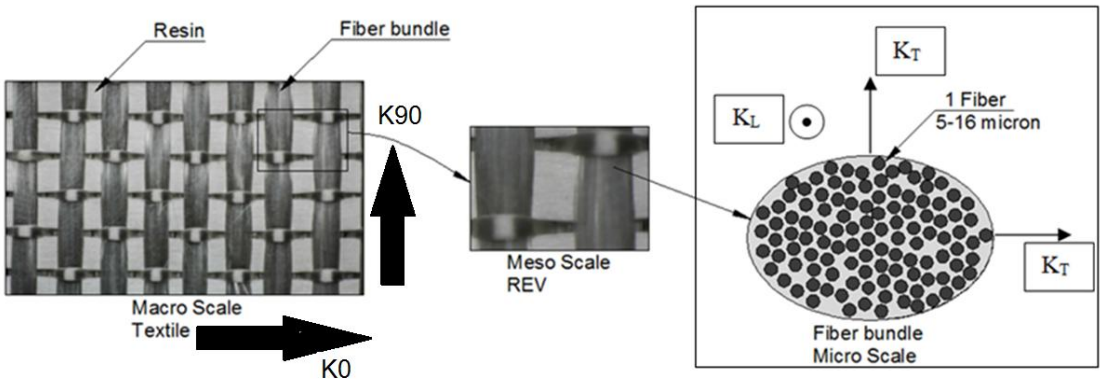

Figure 47 P3W-GE044 fabric scales "3TEX Company"

Different methods have been used to evaluate the permeability tensor: experimental, numerical and analytical methods. At present, significant research effort is being expended on the development of numerical simulations of the permeability values, even though numerical simulations dissipate time, still they are far from matching reality [23]. In addition, experimental measurement of the permeability values is also still facing a lot of problems [8]. This is due to personal errors, equipment inaccuracy, faults in measurement techniques, and repeated preparation of specimens which altogether could provide inconsistent results that make the experimental evaluation of permeability unreliable. But it cannot ignored that a good advance was done in [9]; concerning experimental methodology; in which a method for measuring the in-plane permeability was agreed on by 12 institutes and universities. As for the analytical method, different researchers [24-30] tried to develop analytical or empirical models that predict the permeability for fabrics. Most of the developed models were based on Cozeny-Karman equation or needs external support by a numerical simulation or an experimental measurement in order to predict the mesoscopic permeability. Most of these models still need development in order to be more accurate, rather than that are too much difficult to be applied.

Consequently, the main objective of this study is to develop an analytical model for non-crimped stitched fabrics (NCF) and 3D orthogonal fabrics. This model is based on the architectural geometrical data of the fabrics afforded by textile industry in order to predict the in plane permeability values in both directions $K_{0°}$ and $K_{90°}$.

In order to develop the model, five NCF and 3D orthogonal fabrics are selected; fabrics' architectural geometry is collected from manufacturer data sheet and camera pictures. Using these dimensions and bundle shapes, the bundles' volumes in warp and weft directions are calculated; and the mesopores' volumes are deduced. The model evaluates two contributions of the flow which adopt the flow inside and in between the bundles of different layers (inter and intra two regions) on one side and the flow deviations created by stitched yarns on the other. The permeability of each contribution is predicted by using unidirectional permeability analytical models, using effective radius and fiber volume fraction as input data. The permeability values of the two regions are summed in parallel. The macroscopic permeability is calculated by multiplying the permeability of the two regions by a factor representing the ratio of the mesopores' volume for one direction to the other.

In the first part of the chapter a bibliographic study is displayed, then the selected fabrics are described and the experimental measurements are shown. In the third part the new predictive model is presented. The model is then validated by a comparison with measured experimental data. A conclusion is presented.

5.2 State of art on available models

A state of art is presented in section 2.1.2, where the analytical models predicting fabric permeability are stated.

In a conclusion for the state art, several permeability models have been proposed in the bibliography for both single and dual scale mediums. Kozeny-Carman model, a widely used model, defined permeability as a material parameter depending only on the specific surface which was manifested in Kozeny constant and porosity of the porous medium. Kozeny constant must be predicted numerically, where each textile has its own Kozeny constant values for each V_f and direction. In addition to all that, Kozeny-Carman model

was initially developed for granular beds and does not take anisotropy into account, thus several limitations appeared when it was applied to engineering textiles.

Newly developed analytical models can be classified into two general categories:

1. empirical or semi-analytical models
2. pure analytical models

"Empirical and semi-analytical models" are based on a sub-model, same as Kozeny-Carman model or backed up with an experimental measurement or a numerical simulation. Kozeny-Carman constants are also predicted using finite element software package [25, 27, 72]. In order to predict the compacted fabric architectural parameters, [30] selected the permeability values matching with the experimental data. Some of the models like [27], predicted the permeability of a dual scale medium but their model is applicable only to unidirectional fiber beds and cannot be applied to engineering textiles. Some models, due to the big scatter found with experiments or due to lack of data, compared qualitatively their results with experimental data [72]. Really few models are classified as "pure analytical models" predicting the permeability of engineering textiles [28, 29]. Their model is function of weaving parameters, tortuosity and length of the mesopores a related pressure drop is estimated; thus it is complicated to be applied. It was applied on a single type of architecture "3D interlock fabric", and validated on a single fiber volume fraction.

The goal of this work is to develop a model applicable to NCF and 3D orthogonal fabrics, and can be extended to other type of fabrics. It counts on the geometrical parameters available in the fabrics' data sheet, camera pictures and a target fiber volume fraction. Also it must afford reliable results while compared to experimental work.

5.3 Experimental measurements

5.3.1 Fabric specifications

Five Texonic fabrics were selected which comprises two non-crimped stitched fabrics (NCF) and three 3D orthogonal fabrics. Figure 48 and Figure 49 show Fabrics' schematics of the 3D orthogonal and NCF respectively.

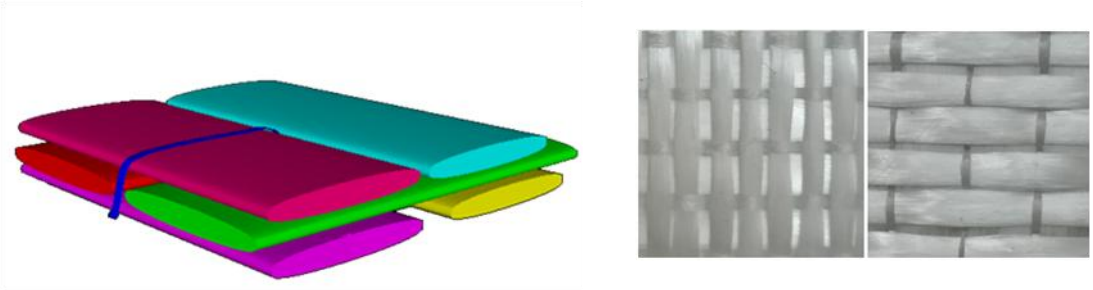

Figure 48 NCF fabrics: TG15N and TG33N

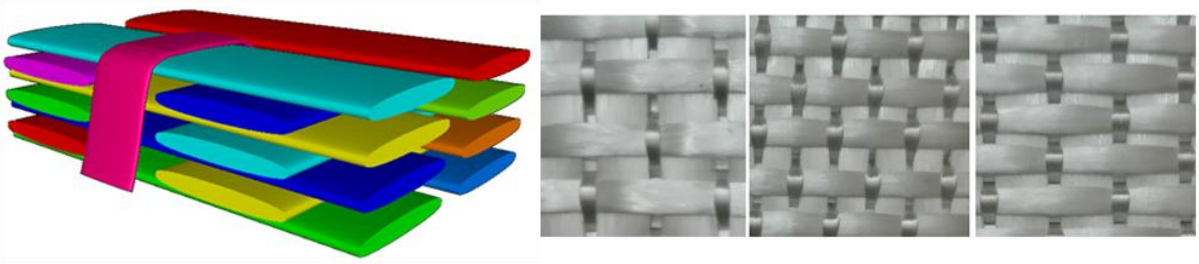

Figure 49 3D orthogonal fabrics: TG54N, TG75N and TG96N

5.3.1.1 Bundles shape

The transversal section of yarns could be represented in different shapes: rectangular, circular, lenticular, elliptical and racetrack shapes, Figure 50 [106]; yarns section depends mainly on fabrics' architecture.

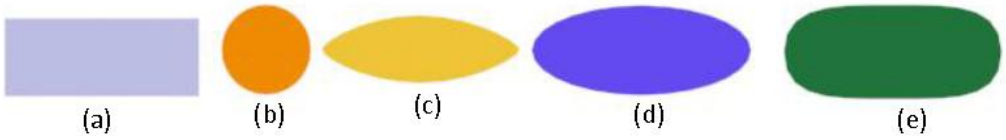

Figure 50 Geometrical parameters and different yarn cross-sections: a) rectangular, b) circular, c) lenticular, d) elliptical, e) racetrack

However in this study, fabrics' architectures are mainly divided into two types, 3D orthogonal and NCF. It's remarked from the X-ray micro tomography of fabricated composite parts that yarns belonging to NCF have elliptical shapes Figure 51, where others classified as 3D orthogonal has rectangular, and mixed shapes (average of rectangular and elliptical) Figure 52.

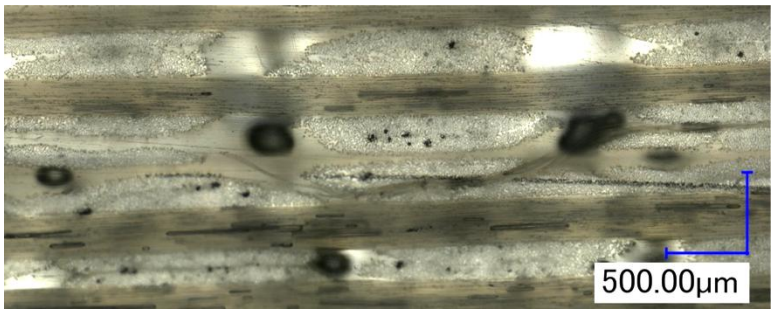

Figure 51 Cross sectional view of composite part, TG-15-N fabric at V_f=40.15

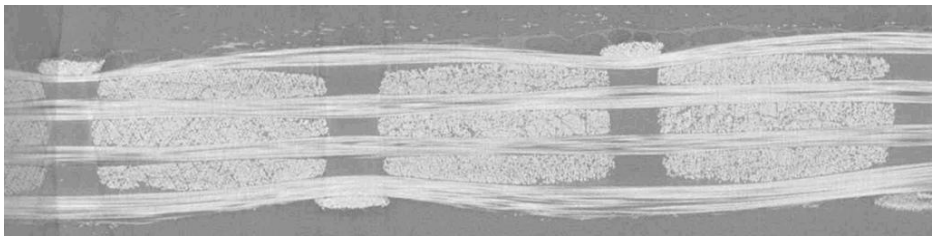

Figure 52 X-Ray cross-sections for TG96N dry fabric

5.3.1.2 Geometrical parameters

In this section fabrics' specifications will be mentioned. Figure 53 shows the notations that will be used in this work to describe the geometrical parameters.

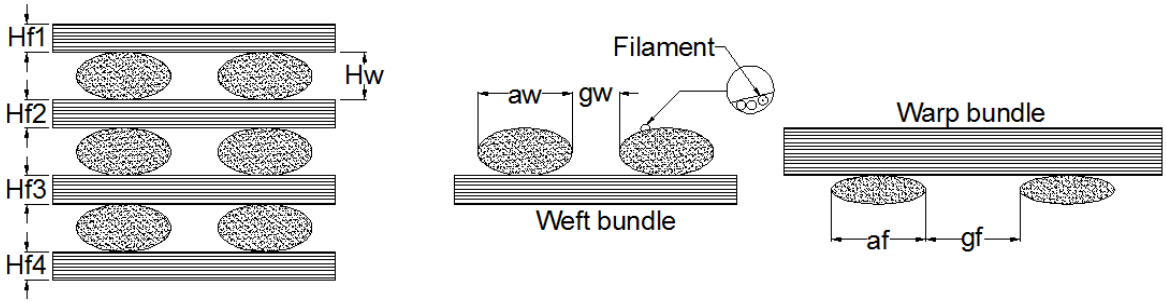

Figure 53 Notations

Table 37, Table 38, Table 39 and Table 40 show fabrics' specifications according to data sheets and captured pictures. Where Table 37 shows fabrics' names, types, number of layers and counts number in both directions, and Table 38 represent fabrics' surface density, initial thickness and fiber volume fractions "V_{f0}", and bundles' widths "a" in both directions. Table 39 represents fabrics' materials with corresponding volume percentage in both directions, while Table 40 shows bundles' TEX and corresponding filament diameter.

Fabric	Fabric Name	Fabric type	Number of layers		Count/cm	
			Warp "nb_w"	Weft "nb_f"	Warp	Weft
Fabric 1	TG-15-N	NCF	1	2	3.1	10.4
Fabric 2	TG-33-N	NCF	2	2	4.6	8.4
Fabric 3	TG-54-N	3D orthogonal	3	4	8	11.4
Fabric 4	TG-75-N	3D orthogonal	3	4	11.4	12.6
Fabric 5	TG-96-N	3D orthogonal	3	4	6.9	14.8

Table 37 Fabric name, type, number of layers and counts

Fabric	Surface density ρ_S (g/m^2)	Thickness H_0(mm)	V_{f0}	"a" (mm)	
				Warp	Weft
Fabric 1	518	0.5	0.406	2.35	1.47
Fabric 2	1125	0.9	0.496	3.9	2.1
Fabric 3	1800	1.52	0.464	3.15	1.9
Fabric 4	2542	2.29	0.435	2.15	1.65
Fabric 5	3250	2.79	0.457	3.4	1.9

Table 38 Fabrics' surface density and initial parameters

Fabric	Warp material (E-glass)			Weft material (E-glass)		
	Primary	Secondary	Volume %	Primary	Secondary	Volume %
Fabric 1	735 Tex	16.7 Tex	45	275 Tex	-	55
Fabric 2	1100 Tex	16.7 Tex	45	735 Tex	-	55
Fabric 3	1100 Tex	134 Tex	52	735 Tex	-	48
Fabric 4	1100 Tex	275 Tex	54	1100 Tex	735 Tex	46
Fabric 5	2*1100 Tex	275 Tex	50	1100 Tex	-	50

Table 39 Fabrics' materials with corresponding volume percentages

Material	Linear density (Tex)	Filament diameter (µm)
Polyester	16.7	25
E-glass	134	9
E-glass	275	16
E-glass	735	13
E-glass	1100	17

Table 40 Bundles' TEX and corresponding filament diameter

5.3.2 Permeability measurements results

Three measurements are done for each fabric in each direction as previously mentioned. The result that does not satisfy the experimental recommendation previously described is omitted. Scattering values represent the standard deviation over the mean value of the repeated measurements. The scattering between the accepted measurements is around 10 percent. Table 41 shows the permeability measurements for NCF and Table 42 shows the permeability measurements for 3D orthogonal fabrics.

Fabric Name	**Fabric 1**			**Fabric 2**		
Fabric Type	NCF			NCF		
V_f	0.4015	0.4817	0.562	0.5144	0.5884	0.6587
$K_{0°}$ $(*\ 10^{-11}m^2)$	23.9	7.05	1.4	21.4	5.59	2.53
Scattering for 0°	0.1	11.4	4.2	8.6	8.8	6.2
$K_{90°}$ $(*\ 10^{-11}m^2)$	34.3	6.74	2.45	27.05	9.68	4.53
Scattering for 0°	0.1	0.1	14.08	2.1	1.1	0.1

Table 41 Unidirectional permeability for non-crimped stitched fabrics.

Fabric Name	**Fabric 3**			**Fabric 4**			**Fabric 5**		
Fabric Type	**3D orthogonal**			**3D orthogonal**			**3D orthogonal**		
V_f	0.4494	0.5117	0.5838	0.4984	0.5432	0.627	0.5458	0.6098	0.6946
$K_{0°}$ $(*\ 10^{-11}m^2)$	13.1	7.79	3.68	24.46	11.5	3.98925	13.6	7.42	0.753
Scattering for 0°	5.5	1.8	5.4	5.2	0.1	0.3	2.4	5.5	4.4
$K_{90°}$ $(*\ 10^{-11}m^2)$	80.5	32.1	12.6	115	42.4	8.27	64.7	21	1.56
Scattering for 90°	0.7	11.4	10.6	2.6	2.8	11.6	4.9	19.4	5.2

Table 42 Unidirectional permeability for 3D orthogonal fabrics

5.4 Predictive analytical model

5.4.1 Introduction

In this part, the developed analytical model is described, which is used in order to predict the in plane macroscopic permeability values $K_{0°}$ and $K_{90°}$.The non-compacted fabrics are built up of straight fiber bundles in both warp and weft directions, while through thickness fiber yarns or stitching yarns fixe the in plane bundles in positions Figure 52; thus an ideal unit cell is took in consideration.

While the fabrics are being compacted, the new dimensions must be predicted in order to calculate the new areas of bundles as well as thickness of layers and inter bundle distance. The model will be divided as follows:

1. Geometrical modeling
2. Permeability modeling

Figure 54 shows the modeling methodology. After measuring the bundle width "a" and collecting all the non-compacted fabrics' geometrical data from fabrics' data sheet and calculations, the second step is to predict these data for different fiber volume fraction. A generalized unit cell is selected. This unit cell is divided into two regions based on flow contributions. A model is developed in order to predict permeability of each region. Finally, the analytical model is presented in the last part.

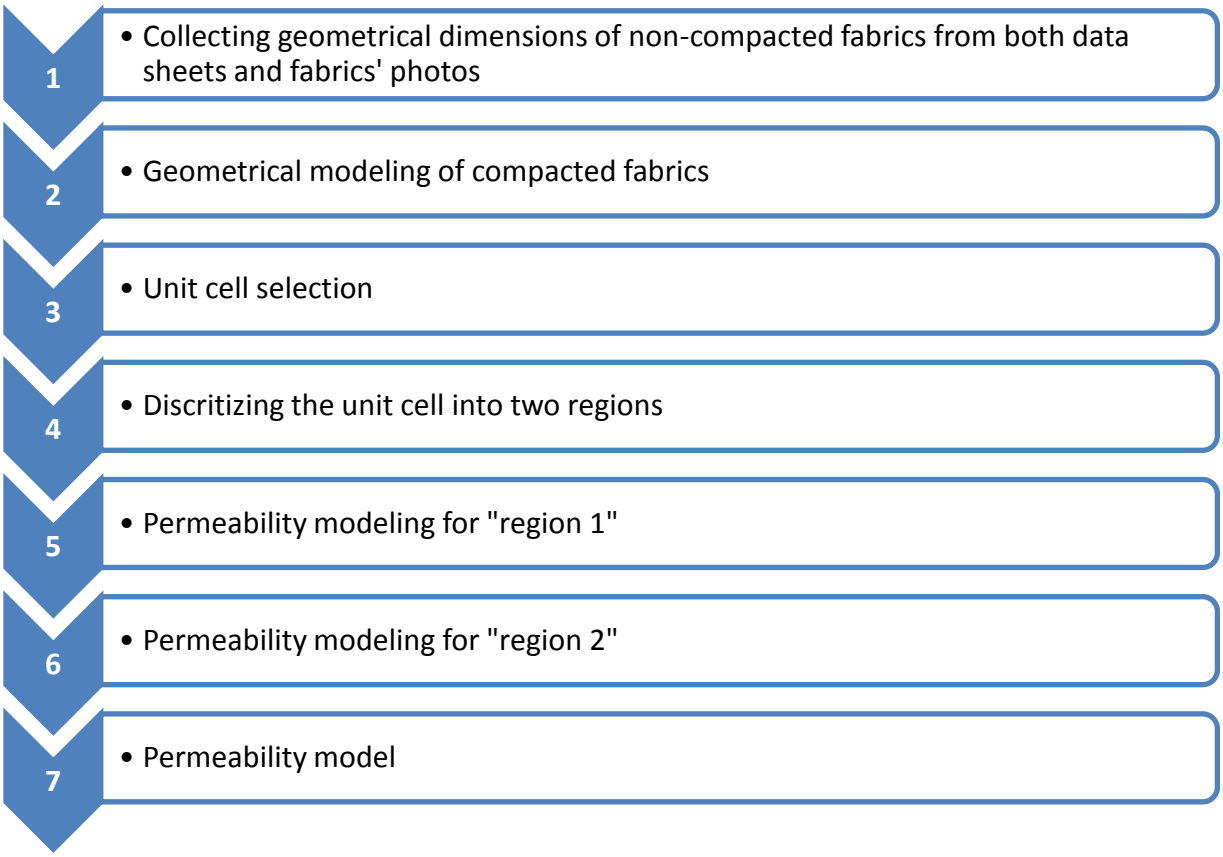

Figure 54 methodology of modeling

In order to develop the permeability model, a predictive analytical sub model is selected from previous work. This sub model used for aligned fiber beds, is selected from in the

comparative study [45] from the best models predicting the permeability of unidirectional fiber beds, Figure 55 [45] . Bahrami and Tamayol model [44] stated in equation (20) will be used in order to predict the permeability values. The recommended data as input to the sub model will be the porosity fraction "ε" and the radius "r". Note that all elected models in [45] can be used rather than Bahrami and Tamayol model, and similar results regarding experimental measurements is observed [32, 39, 44]

$$K_{Sub.model} = \frac{r^2}{4(1-\varepsilon)}\left(-0.021 - \ln(1-\varepsilon) - \varepsilon - \frac{\varepsilon^2}{2} - 0.0186 * (1-\varepsilon)^4\right) \quad \text{Eq.(20)}$$

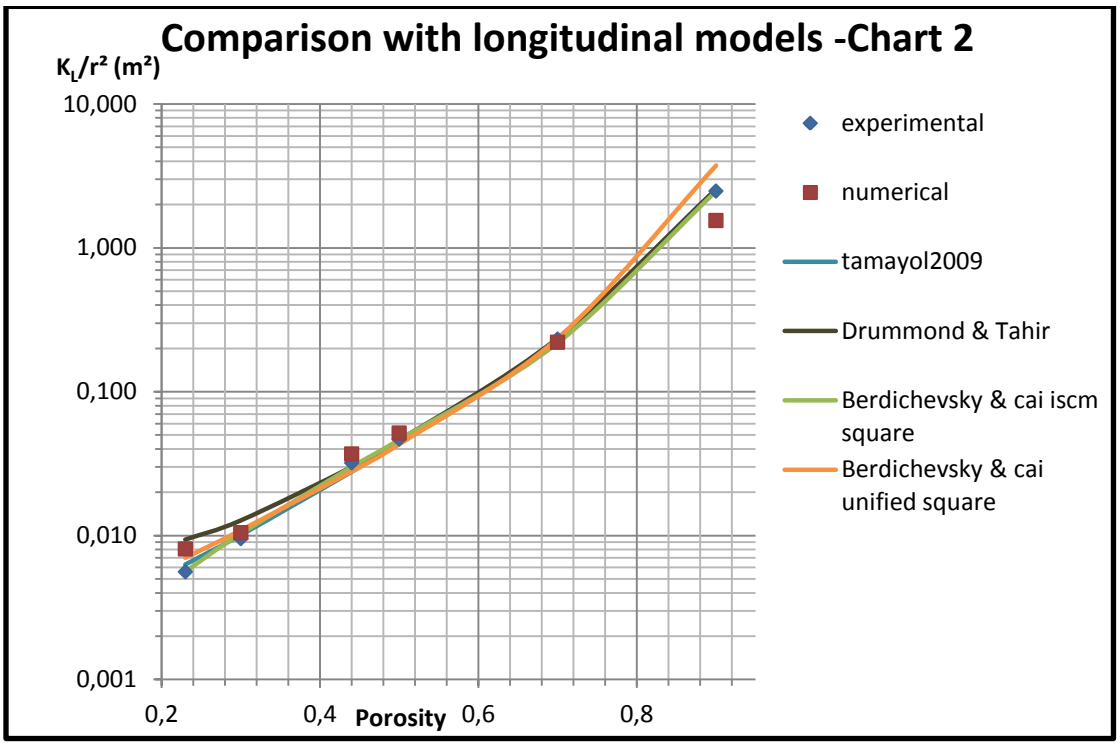

Figure 55 Comparison of elected sub models with experimental and numerical values [45]

5.4.2 Unit cell

The developed model will be applied on five different fabrics previously described in Fabric's specification section Table 37, Table 38, Table 39 and Table 40.These fabrics have different Tex for the bundles and lay under three different architecture properties:

1. Two non crimped stitched fabrics with a polyester stitching yarn (Fabric 1 and fabric 2).

2. Two 3D orthogonal fabrics with an E-glass through thickness along the warp direction (Fabric 3 and fabric 5).
3. One 3D orthogonal fabric with an E-glass binding yarn along the warp direction and 2 different Tex in the weft direction (Fabric 4).

A generalized unit cell should be selected so that the model could be applied to different types of fabrics, the chosen unit cell will be 1cm x 1cm x H_0. By choosing this unit cell the counts in the warp and in the weft directions are easily readable from the manufacturing data sheet as an input data for the developed model.

5.4.2.1 Flow contributions

The permeability is governed by the fabric architecture; the flowing liquid in the fabric is divided into two flow types:

c. Flow in micropores
d. Flow in mesopores

5.4.2.1.1 Flow in micropores

Table 43 shows for "fabric 1", at two different fiber volume fractions, the macroscopic permeability measured in the warp direction $K_{0°}$, and also shows the microscopic longitudinal permeability K_L predicted by analytical modeling [44] for aligned fiber beds. As the results show, the microscopic permeability is 39 times smaller than the macroscopic permeability even though the samples have the same fiber volume fraction, and 22 times smaller at the second one. Table 44 shows $K_{90°}$, the macroscopic permeability measured in the weft direction for fabric 1 and K_T. The microscopic permeability is predicted by analytical modeling [32] at two different fiber volume fractions where the microscopic permeability is 130 times and 54 times smaller than the macroscopic permeability.

Fiber volume fraction (%)	$K_{0°}$ (m^2) (Longitudinal macroscopic permeability)	K_L (m^2) (Longitudinal microscopic permeability)
40.15	23.9 E-11	6.2 E-12
48.17	7.05 E-11	3.25 E-12

Table 43 Comparison between longitudinal permeability values between a fabric « macroscopic level » and unidirectional fiber beds « microscopic level » at the same fiber volume fraction

Fiber volume fraction (%)	$K_{90°}$ (m^2) (Transversal macroscopic permeability)	K_T (m^2) (Transversal microscopic permeability)
40.15	34.3 E-11	2.629 E-12
48.17	6.74 E-11	1.238 E-12

Table 44 Comparison between transversal permeability values between a fabric « macroscopic level » and unidirectional fiber beds « microscopic level » at the same fiber volume fraction

As a conclusion the microscopic permeability is much smaller than the macroscopic permeability. In a well arranged repeatable medium where the mesopores are always connected between each other, the microspores' influence is limited to the saturation effect, while mesopores will have the dominant effect on the permeability.

5.4.2.1.2 Flow in mesopores and saturation effect

As for arranged and stable fabrics, the flow always finds its way in the mesopores and is never forced to cross through a micropore to reach a mesopore, although the micropores must be filled in due to saturation matters. To predict the macroscopic in-plane permeability, the model evaluates two contributions of the flow as shown in Figure 56 and Figure 57:

c) In the region "1" the flow inside and in between the bundles of different layers (inter and intra two regions).
d) Flow deviations created by stitched yarns marked as region "2".

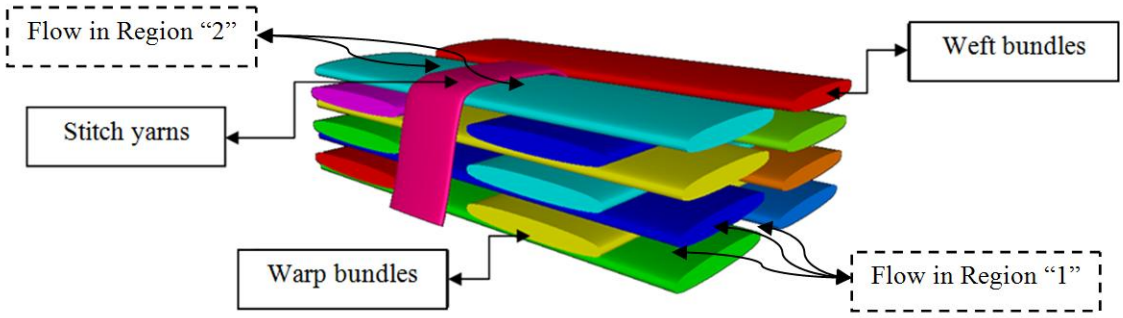

Figure 56: Flow contributions schematic

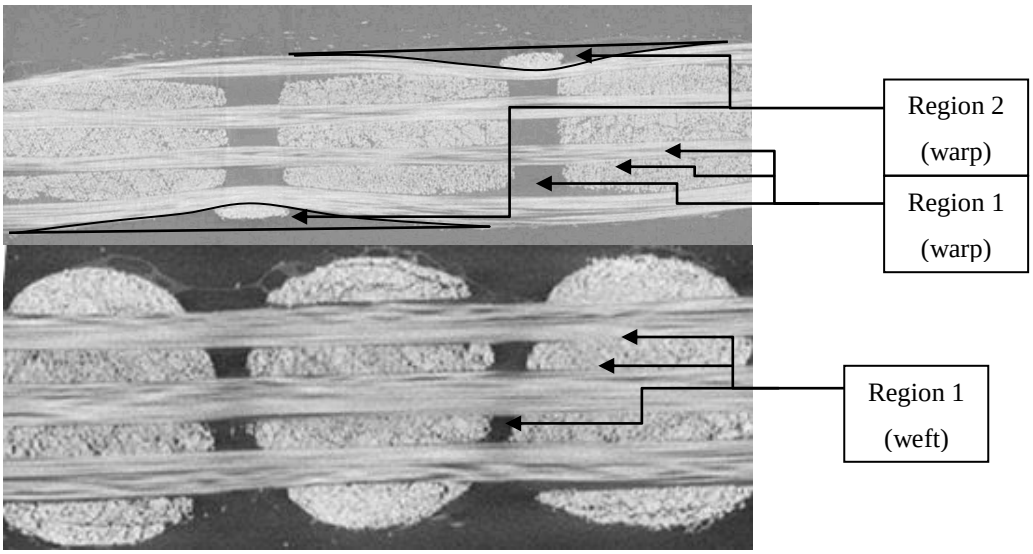

Figure 57 Flow contributions in X-Ray cross-sections of "TG96N"

The flow Q is divided between the two regions as stated in eq. (21), refer to Figure 57. Darcy's law was generalized to accommodate anisotropic porous media eq. (22), and is used in modeling the resin flow of the fluids. Thus the permeability in the designated direction can be written as shown in eq. (23).

$$Q_{total} = Q_{reg1} + Q_{reg2} \qquad \text{Eq.(21)}$$

$$\bar{u} = \frac{Q}{A} = \frac{K}{\mu} . \nabla P \qquad \text{Eq.(22)}$$

Where ū is the volume averaged Darcy velocity, μ is the viscosity of the fluid, ∇P is the pressure gradient, and K is the permeability of the porous medium.

$$K_{0° \, or \, 90°} = \left[\left(1 - V_{f(reg2)}\right) * K_{reg1}\right] + \left[V_{f(reg2)} * K_{reg2}\right] \qquad \text{Eq.(23)}$$

As previously described, "region 2" contains the stitched yarns and the mesopores around it, then $V_{f(reg2)}$ will be considered as the volume fraction of the stitching yarns region.

5.4.3 Geometry predictions under compaction

This part is dedicated for predicting the geometrical parameters after compressing the dry fabric inside the mold. After being compressed, the bundles' dimensions a_w, a_f, H_w and H_f are subjected to change. Since V_{fy} changing and consequently microscopic permeability effect have limited effect, while the fabric is being compacted, when compared to V_f and macroscopic permeability values. Then the dimension modification is considered to be restricted to the reduction of mesopore size rather than reducing bundles cross section area "A".

Figure 58 shows the used notations for the fabric before and after being compressed; the distance L between two bundles remains the same after compression. Equations (12), (25) and (26) are dedicated for calculating the fabric thickness, warp and weft bundle thickness. h_{wi} and h_{fi} , the warp and weft bundles thickness at different compaction factors, are considered to change in the same ratio of their initial volume percentages $\propto_w$ and $\propto_f$. *nbw* and nb_f represents the number of layers in the warp and weft directions respectively, while H_0 and H_i are the fabric thicknesses prior and under compaction.

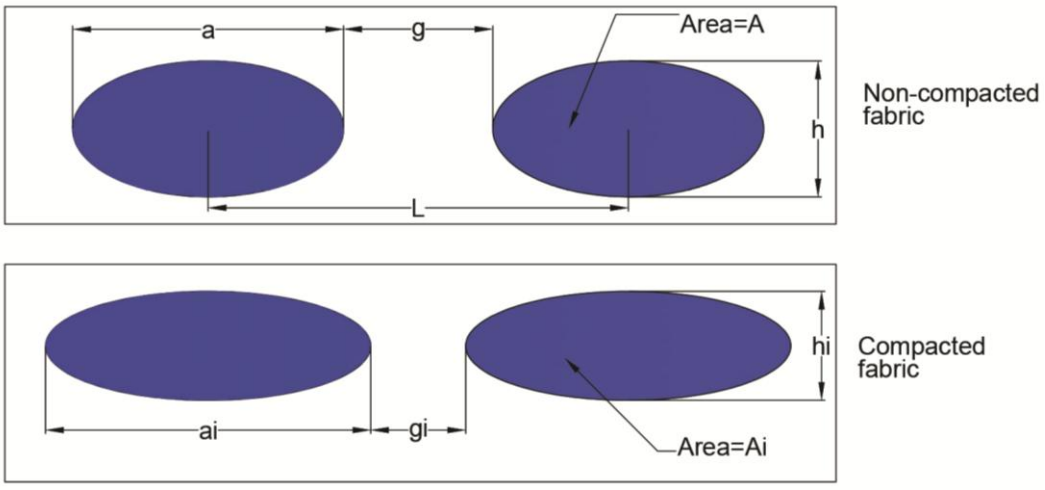

Figure 58 Bundles notations

$$H_i = \frac{\rho_s}{V_{fi}.\rho} \qquad \text{Eq.(24)}$$

$$h_{wi} = H_i * \frac{\propto_w}{nb_w} \qquad \text{Eq.(25)}$$

$$h_{fi} = H_i * \frac{\propto_f}{nb_f} \quad \text{Eq.(26)}$$

The new gap width g_i equation (28) is predicted based on the compaction factor C_{fac} equation (27). The in-between bundle distance "*L*" is a constant value independent of the fiber volume fraction. Then the bundle width a_{wi} and a_{fi} are deduced, equation (29).

$$C_f = \frac{H_i}{H_o} \quad \text{Eq.(27)}$$

$$g_{wi} = g_{w0} * C_f \; and \; g_{fi} = g_{f0} * C_f \quad \text{Eq.(28)}$$

$$a_{wi} = L_w - g_{wi} \; and \; a_{fi} = L_f - g_{fi} \quad \text{Eq.(29)}$$

Based on the calculated values of dimensions "a", "h" and bundles' shape, "A" is calculated for both elliptical cross sections equation (30) and racetrack cross sections equation (31); where the extremities of racetrack shape are considered as half circles and its middle is rectangular.

$$A_{ellipse} = \frac{a * h * pi}{4} \quad \text{Eq.(30)}$$

$$A_{racetrack} = \left[\frac{h^2 * pi}{4} + \left((a - h) * a\right)\right] \quad \text{Eq.(31)}$$

In order to observe the change of V_{fy} in intra bundle region, two fabrics "TG-15-N" are injected at different fiber volume fractions with Vinyl ester resin "Derakane 411-350".Figure 59 shows cross sections at the bundles of the injected parts. By referring to microstructures sections, the fiber volume fraction inside the bundles is calculated based on a fiber radius r_f=13µm, Table 40. Table 45 shows the change of fiber volume fraction V_{fy} inside the bundles while the overall V_f changed by more than 8%. As previously described in Table 43 and Table 44, this means that no noticeable effect of micropores on the overall macroscopic permeability will be observed while the microscopic permeability effect is limited on these V_{fy} values.

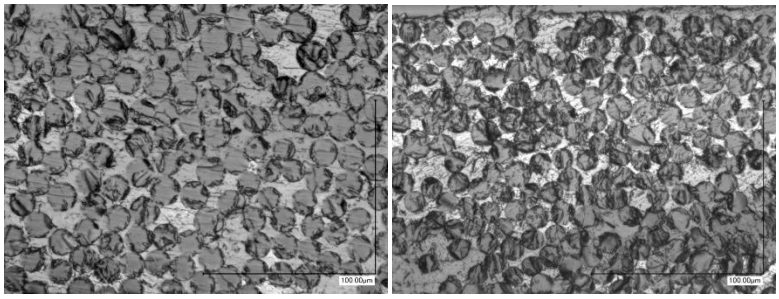

Figure 59 Bundle microstructure at different fiber volume fraction (0.4015 and 0.4817)

Target V_f	Measured V_{fy}
0.4015	0.51
0.4817	0.55

Table 45 V_{fy} changes while compaction

5.4.4 Permeability of "Region 1"

"Region 1" contains longitudinal fiber bundles, transversal fiber bundles and mesopores in both directions. The flow in the region 1 is not discretized into two separate flows (a micropore flow and a mesopore flow), but instead the flow always finds its way in the mesopore, while saturating the micropores in the partially saturated region. Thus mesopores effect has much more effect on the overall permeability than micropores effect; volume fractions of the mesopores $V_{f(meso.w)}$ and $V_{f(meso.f)}$ will be calculated after considering a blocked bundle Figure 61, equations (34 and 35). When injecting the fluid in the warp direction then this direction has an enhancing effect on the permeability and the weft direction will have a negative effect decreasing the permeability. Equations (32) and (33) shows both the permeability in the "region 1" when the flow is in the warp or the weft direction simultaneously.

$$K_{reg1.w} = K_{submodel} * \frac{V_{f(meso.w)}}{V_{f(meso.f)}} \quad \text{Eq.(32)}$$

$$K_{reg1.f} = K_{submodel} * \frac{V_{f(meso.f)}}{V_{f(meso.w)}} \quad \text{Eq.(33)}$$

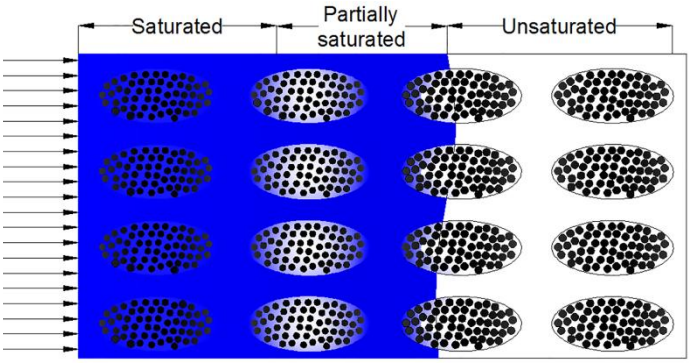

Figure 60 Flow front progression

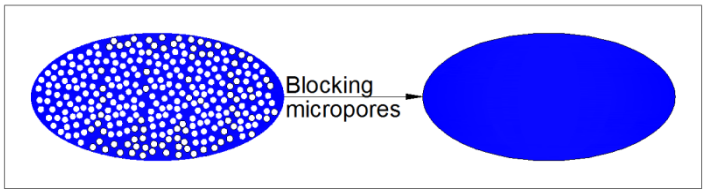

Figure 61 Blocked micropores

$$V_{f(meso.w)} = \frac{Vol_{(meso.w)}}{Vol_{(unitcell)}} = \frac{(nbl_w * l_w * l_f * H_{wi}) - (counts_w * l_w * A_{bundle.w})}{H_i * l_f * l_w} \quad \text{Eq.(34)}$$

$$V_{f(meso.f)} = \frac{Vol_{(meso.f)}}{Vol_{(unitcell)}} = \frac{(nbl_f * l_w * l_f * H_{fi}) - (counts_f * l_f * A_{bundle.f})}{H_i * l_f * l_w} \quad \text{Eq.(35)}$$

Moreover since different filament radii might be found in the same fabric, and the fabric is a dual scale porous medium, then, instead of using filament radius ”r” and porosity “ε”, the following data is required in order to calculate $K_{submodel}$:

- Effective radius of the filaments inside the bundles “r_{eff}” function of “r”
- Effective porosity “ε_{eff}” function “ε”

$$K_{submodel} = \frac{r_{eff1}^2}{4(1-\varepsilon_{eff1}^2)}\left(-0.021 - \ln(1-\varepsilon_{eff1}) - \varepsilon_{eff1} - \frac{\varepsilon_{eff1}^2}{2} - 0.0186 * (1-\varepsilon_{eff1})^4\right) \quad \text{Eq.(36)}$$

Fabric	Warp material (E-glass)			Weft material (E-glass)		
	Primary	Volume percentage	Diameter (µm)	Primary	Volume percentage	Diameter (µm)
Fabric 1	735 Tex	45	13	275 Tex	55	16
Fabric 5	2*1100 Tex	50	17	1100 Tex	50	17

Table 46 “Fabric 1” and “Fabric 5” filament radius

Filament radius depends on the type of the fabric, and is especially related to the TEX. "r" can be found in Table 40. As an example, "fabric 1" has an effective radius "r_{eff1}" equal to 7.325 µm equation (37), and for "fabric 5" r_{eff1} = 8.5 µm. Where volume percentage of the warp and weft bundles "$\%Vol_{warp}$" and "$\%Vol_{weft}$" can be found in

$$r_{eff1} = (r_{warp} * \%Vol_{warp}) + (r_{weft} * \%Vol_{weft}) \quad \text{Eq.(37)}$$

The effective porosity ε_{eff1} is assumed to be equal to the compaction factor "H_i/H_0". Where the compaction factor is an indicator to the porosity, and inversely proportional to it. This assumption is considered after selecting different approximations after which this approximation fitted the experimental data for one fabric, and then it was validated on the other four fabrics.

Fabric	Fabric 1	Fabric 2	Fabric 3	Fabric 4	Fabric 5
V_{f1} target	0.4095	0.5144	0.4719	0.4984	0.5449
ε_{1eff1}	0.920	0.920	0.920	0.873	0.837
V_{f2} target	0.4914	0.5884	0.5276	0.5432	0.6088
ε_{2eff1}	0.827	0.843	0.880	0.801	0.749
V_{f3} target	0.5733	0.6587	0.5999	0.627	0.6934
ε_{3eff1}	0.709	0.753	0.774	0.694	0.658

Table 47 Effective porosity "ε_{eff1}"

Table 47 shows the target fiber volume fraction of the five studied fabrics and the corresponding effective porosity εeff1. Noting that ε_{eff1} will be limited to 0.92 because the used models equation (20) and (36) are not applicable in higher porosities.

5.4.5 Permeability of "Region 2"

"Region 2" contains stitching bundles in the peripheral layers and mesopores around it, refer to Figure 56 and Figure 57. Since stitching bundle size affects the volume of the mesopore around it, then the polyester stitching bundle having a diameter of 25µm Table 39 and Table 40 which is found in fabrics "1" and "2", has a limited effect. So "region 2" is found in fabrics "3-5". The flow in the "region 2" is divided into two , one being a microscopic flow inside the stitching bundles and the other being the mesoscopic flow around the stitching bundles. Both equations (38) and (39) show the permeability in "region 2" when the flow is in the warp or the weft direction simultaneously. $V_{f(meso.w)}$

and $V_{f\ (meso.f)}$ are calculated in the section 4.4. Appropriate effective radius and porosity r_{eff2} and ε_{eff2} must be predicted in this section for $K_{submodel}$.

$$K_{reg2.w} = K_{submodel} * \frac{V_{f(meso.w)}}{V_{f(meso.f)}} \quad \text{Eq.(38)}$$

$$K_{reg2.f} = K_{submodel} * \frac{V_{f(meso.f)}}{V_{f(meso.w)}} \quad \text{Eq.(39)}$$

The flow finds always its way in mesopores moreover that the microscopic permeability is much smaller than the macroscopic permeability as mentioned in section "Unit cell" and the saturation of these micropores is so quick because of their small volume then the effect of microscopic permeability will be neglected. Thus the bundle will be considered as a pre-saturated region Figure 61, with an approximate fiber volume fraction V_{fy}=0.5. The equivalent radius "r_{eff2}" of the bundle will be calculated using equations (40, 41 and 42) assuming an ellipsoid shape. No noticeable change was observed in cross-sectional area of the bundles while compacting, thus "r_{eff2}" is constant after compaction, Table 48.

$$A_{s.0} = \frac{Tex_s}{V_{fy} * \rho_s} = \frac{Tex_s}{0.5 * 2550} = \frac{Tex_s}{1275} \quad \text{Eq.(40)}$$

$$h_{s.0} = \frac{4 * A_s}{a_{s.0} * \pi} \quad \text{Eq.(41)}$$

$$r_{equivalent} = r_{eff2} = \frac{0.775 * A_s^{0.625} * 10^{-3}}{\left(2\pi * \left(\left(\frac{w_s}{2}\right)^2 * 0.5 + \left(\frac{h_s}{2}\right)^2\right)^{0.5}\right)^{0.25}} \quad \text{Eq.(42)}$$

Fabric	r_{eff2} (m)
Fabric 3	$0.169*10^{-4}$
Fabric 4	$0.205*10^{-4}$
Fabric 5	$0.240*10^{-4}$

Table 48 Effective radius "region 2"

In order to calculate ε_{eff2} a computer analysis is launched, studying the relationship with compaction factor. As previously demonstrated the bundle cross sectional area is considered as constant with an internal fiber volume fraction V_{fy} equal to 0.5. Equation (43) shows the effective porosity of region 2, where A_{SY} is the cross

sectional area of stitching fiber bundle and A_{GAPSY} is previously mentioned area in addition to the mesopore area surrounding it. Figure 62 shows a cross sectional view of region "2" prior to compaction where ε_{0eff2} is measured for different fabrics (per example Figure 57) and found to be near 0.6.

$$\varepsilon_{eff2} = 1 - \frac{A_{SY}}{A_{GapSY}} \qquad \text{Eq.(43)}$$

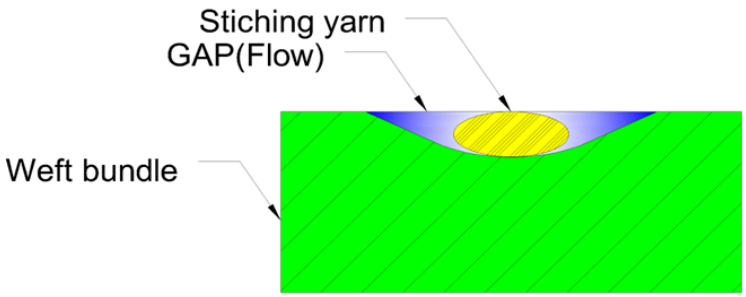

Figure 62 Region 2

Figure 63 shows the computational analysis of "region 2" from V_{f0} to V_{f3} where ε_{eff2} is predicted. This analysis shows that ε_{eff2} followed up equation (45), where $V_{feff2.0}$ is the initial fiber volume fraction prior to compaction.

$$\varepsilon_{0eff2} = 1 - V_{0feff2} \qquad \text{Eq.(44)}$$

$$\varepsilon_{eff2} = 1 - V_{feff2} = 1 - V_{f0eff2}\left(\frac{H_0}{H_i}\right)^{1.35} \qquad \text{Eq.(45)}$$

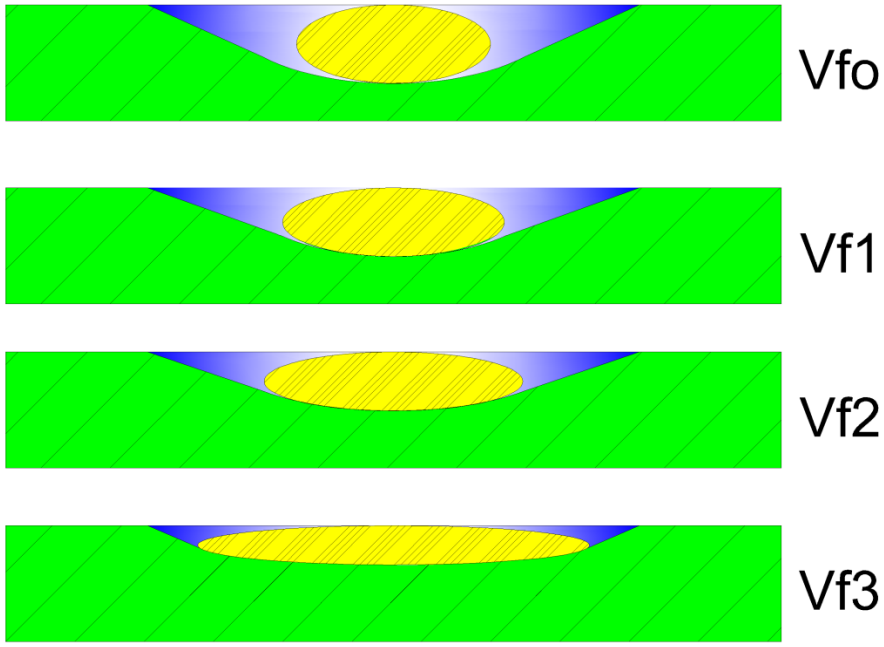

Figure 63 Region 2 under compaction

Fabric	Fabric 3	Fabric 4	Fabric 5
V_{f1} target	0.4719	0.4984	0.5449
ε_{1eff2}	0.6	0.52	0.49
V_{f2} target	0.5276	0.5432	0.6088
ε_{2eff2}	0.524	0.461	0.409
V_{f3} target	0.5999	0.627	0.6934
ε_{3eff2}	0.435	0.345	0.3

Table 49 Effective porosity "ε_{eff2}"

Based on equation (45), the effective porosity ε_{eff2} is calculated, the results are shown in Table 49. Note that the maximum packing factor in a square fiber array is 0.785 [107]. Near this level the medium is considered as a microscopic porous medium, where no mesopores are present. At this level the effect of the "region 2" on the permeability is neglected. This case is observed for fabric 5 at the third compaction "V_{f3}" where the effective fiber volume fraction is 0.7 (ε_{3eff2}=0.3), thus this value is omitted.

5.4.6 General model

The permeability of the unit cell is a summation of the permeability values of sub domains either by series, or by parallel Figure 64, or by a combination of both according

to defined percentages. The equation (46) shows Weighted-Average Permeability-Parallel summation method and equation (47) shows Harmonic-Average Permeability-Series summation method. Where K_{avg} is the permeability of the unit cell in the desired direction and V_{fi} represents the volume fraction of the domain of the unit cell with a permeability value K_i.

$$K_{wavg} = \sum_{i=0}^{n} (V_{fi} * K_i) \quad \text{Eq.(46)}$$

$$K_{havg} = \frac{\sum_{i=0}^{n} (L_i)}{\sum_{i=0}^{n} (\frac{L_i}{K_i})} \quad \text{Eq.(47)}$$

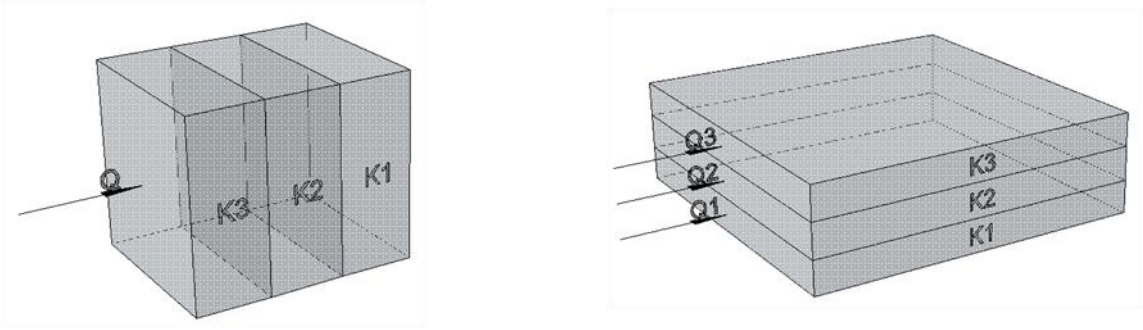

Figure 64 Harmonic and weighed average permeability

As previously stated in section 4.2 the flow always finds its way in a mesopore, thus a weighted average permeability summation is used equation (23). By summing up the permeability of region "1" equations (32) or (33) and the permeability of region"2" equations (38) or (39); the macroscopic permeability is obtained for both warp direction "0°" Figure 65and weft direction "90°" Figure 66.

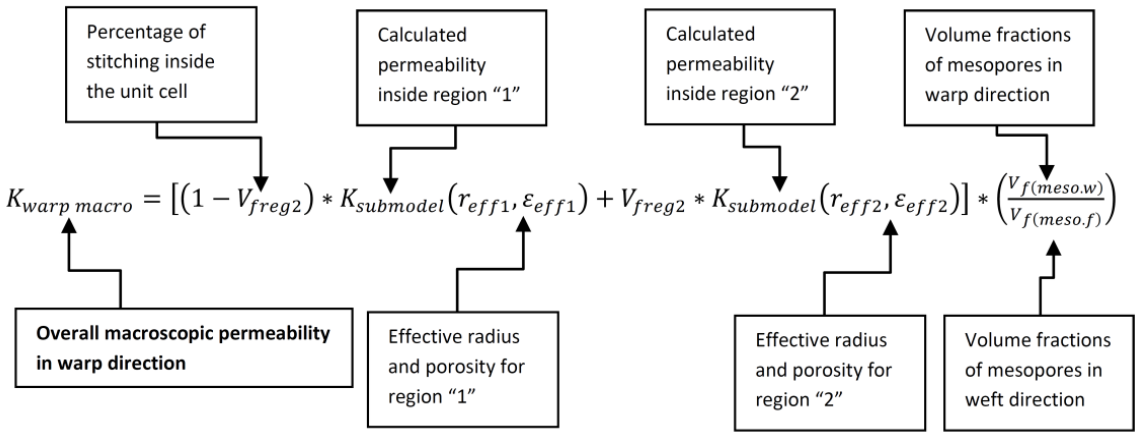

Figure 65 Macroscopic permeability for warp direction

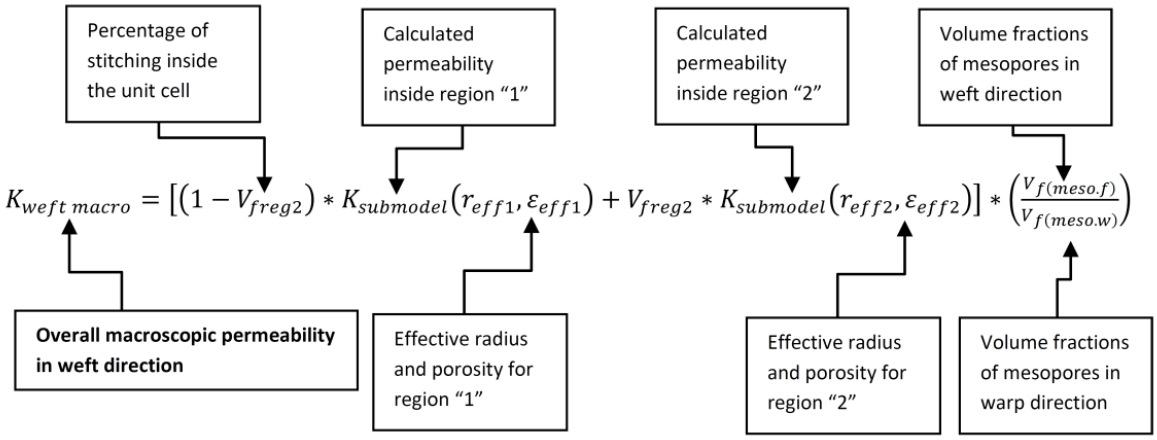

Figure 66 Macroscopic permeability for weft direction

5.5 Model predictions and discussion

5.5.1 Comparison of analytical and experimental results

Figure 67 to Figure 71 shows the measured experimental (bars) and predicted (columns) permeability values in both warp and weft direction for Fabrics 1 to 5, respectively. As previously stated in section 3, the experiments are repeated for the same fabric at a selected V_f two or three times, the minimum and maximum values are represented as bars in the stated figures. As shown in Figure 67, the predicted permeability is in excellent correlation with experimental data for fabric 1 with no observed error; since the predicted value lies between the minimum and maximum measured permeability values. An error

of 33% is observed on V_{f2} in the warp direction. Note that the errors are calculated as stated in equation (48).

$$error = \frac{predicted\ value - mean\ measured\ value}{mean\ measured\ value} * 100 \qquad \text{Eq.(48)}$$

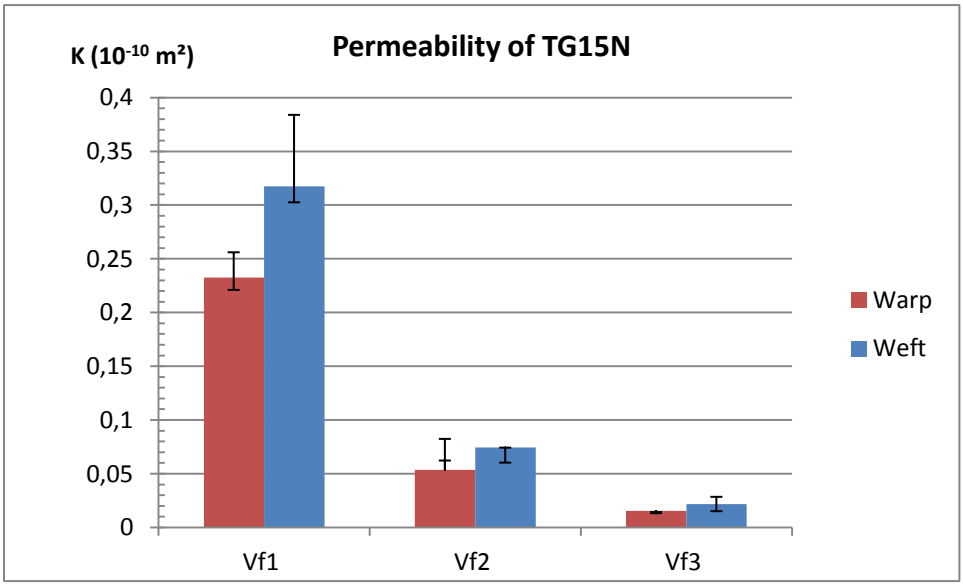

Figure 67 Experimental (error bars) and predicted (columns) warp and weft permeability values for Fabric 1

The displayed figures for fabrics 2 to 5 show a correlation between the calculated and measured permeability values, which lie inside or very close to the standard scatter of measurements of the major variety of the predicted values. Figure 68 shows the results for fabric "2" where an error less than 15% is observed, unless for V_{f3} where an error of 23% and 30% are observed in both warp and weft directions respectively. Figure 69 shows the results for fabric "3", where three predictions on "V_{f2} warp, V_{f3} warp and V_{f3} weft" lie inside the experimental value range; and an error less than 30% is observed on other fiber volume fractions. Figure 70 shows the results for fabric "4" where 3 predictions, on "V_{f2} warp, V_{f3} warp and V_{f3} weft" lie very close to the experimental value range; an error less than 30% is observed for other compaction ratios. Figure 71 shows the results for fabric "5" where all permeability predictions lie inside the experimental scatter range. An error near 40% is observed for V_{f3} weft direction.

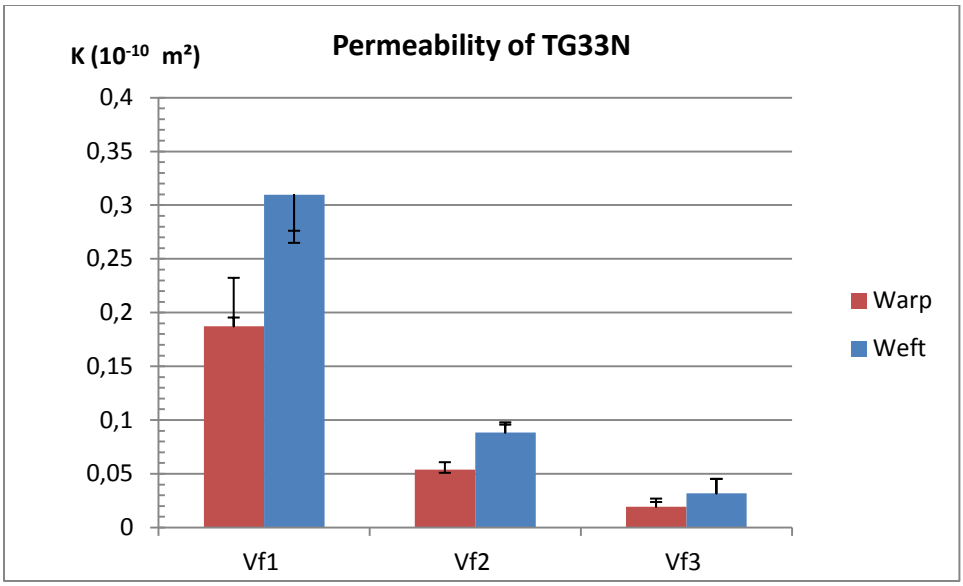

Figure 68 Experimental (error bars) and predicted (columns) warp and weft permeability values for Fabric 2

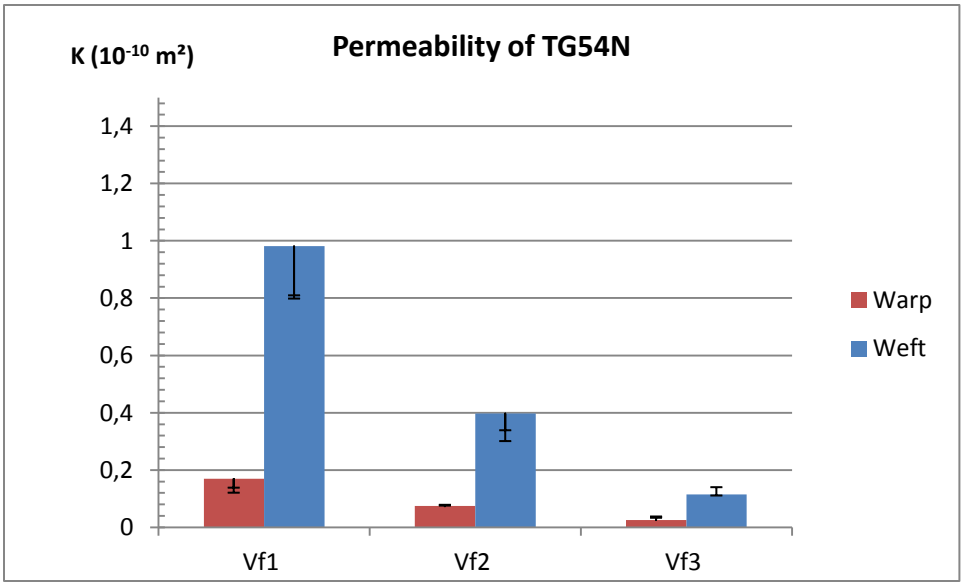

Figure 69 Experimental (error bars) and predicted (columns) warp and weft permeability values for Fabric 3

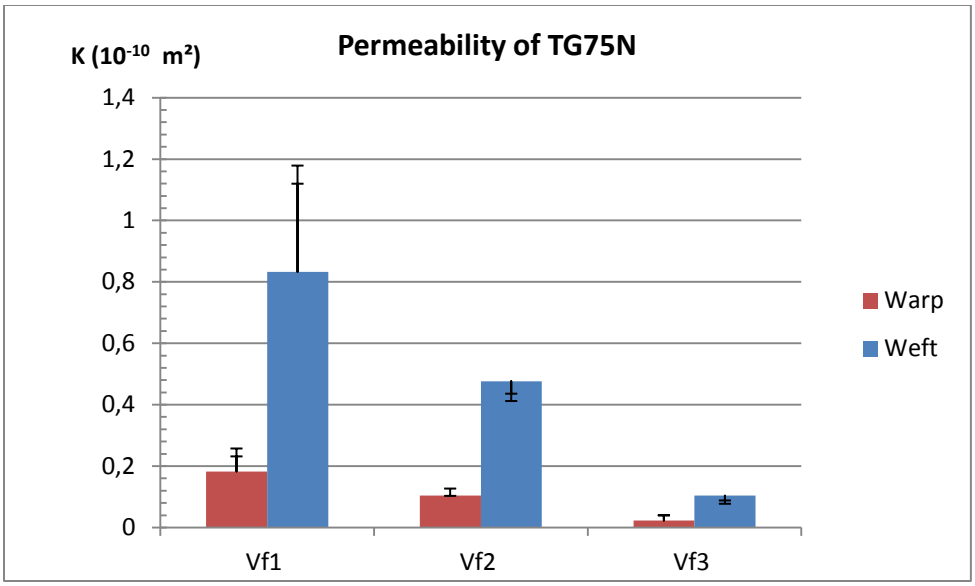

Figure 70 Experimental (error bars) and predicted (columns) warp and weft permeability values for Fabric 4

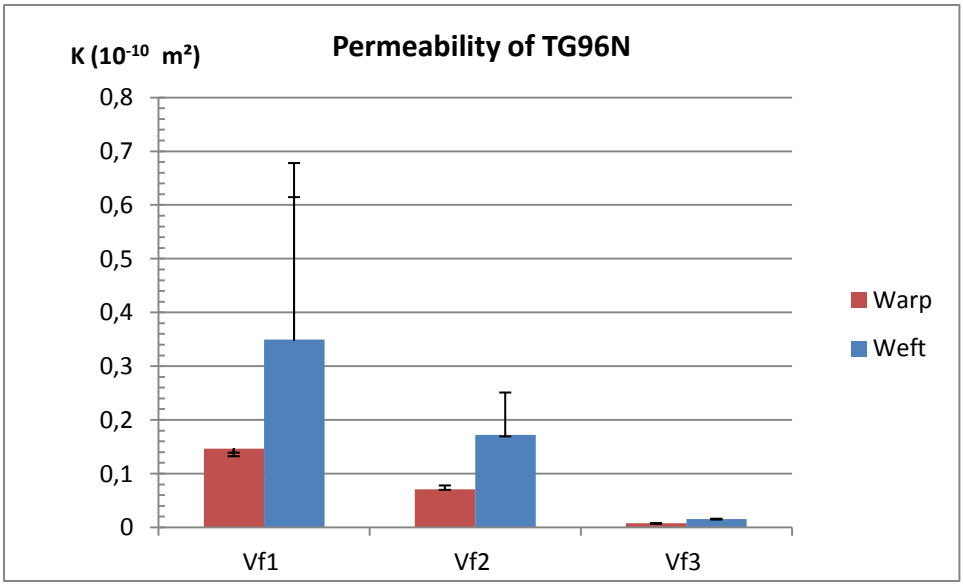

Figure 71 Experimental (error bars) and predicted (columns) warp and weft permeability values for Fabric 5

In an overall view on all the 30 predicted values, twenty two values are inside or very close to the experimental scattered values. In other words, there is no error between these values and the measured ones. The other results are close to the experimental measurements, so that they are a real representation in any simulation or real injection.

5.5.2 Sensitivity of permeability model

The model involved the volume of the channels "mesopores" where their volume percentage has a strong effect on the flow resistance. The model includes this geometric influence by taking into account the channel distribution between warp and weft direction, where the permeability increased with an increasing mesopore size in the desired injection way and vice versa. This was observed in the ratio of "volume fractions of mesopores". The model took into consideration mesopores, micropores and architecture inside the region "1", where r_{eff1} takes into consideration the type of material and ε_{eff1} represents an effective porosity simulating the mesopores. The effect of stitching yarn is taken into account by introducing r_{eff2} and ε_{eff2}.

5.5.2.1 Sensitivity to selected sub model

The targets of this part are to prove the possibility of usage of a permeability sub model instead of that one selected in equation (36), in addition it aims to demonstrate the sensitivity of the sub model to the minor change in porosity. These are demonstrated in Table 50 where Tamayol and Bahrami model [44], Drumond model [39], and Berdichevsky and Cai model [32] are compared between each other on similar porosities where the scattering equation(48) is calculated and a very small scattering less than 3.2% between these models prove the possibility of switching between it with no noticed change in macroscopic permeability predictions.

ε	**Tamayol and Bahrami** [44]	**Drummond and Tahir** [39]	**Berdichevsky and cai** [32]	**Scattering**
0.5	2.82E-12	2.95E-12	2.97E-12	2.3%
0.7	1.49E-11	1.51E-11	1.40E-11	3.2%
0.9	1.63E-10	1.63E-10	1.59E-10	1.2%
0.91	1.96E-10	1.97E-10	1.96E-10	0.3%
0.92	2.41E-10	2.41E-10	2.46E-10	0.9%

Table 50 Submodels predictions on selected porosities

Also it can be deduced from this table that a minor change in the porosity in a 0.1 increment may increase the permeability from $1.6e^{-10}$ to $1.96e^{-10}$ to $2.4e^{-10}$. This shows how much this factor is sensitive and may influence, if wrongly estimated, the final result in a catastrophic way.

5.5.2.2 Sensitivity to filament diameter

Filament diameter, stated in Table 40, was introduced in the model while predicting the permeability of region "1". This parameter has an influence on the saturation speed of micropores. Table 51 represents longitudinal permeability prediction for different filament diameters on V_{fy}=0.5 using Bahrami and Tamayol model equation (36). The predicted values are increasing by a factor of 3 or 4 times, while the filament diameter is doubling.

Linear density (Tex)	Filament diameter (µm)	Permeability on V_{fy}=0.5 (m^2)
134	9	8.908*10-13
275	16	2.815*10-12
735	13	1.858*10-12
1100	17	3.178*10-12

Table 51 Permeability prediction for different filament diameters using Bahrami and Tamayol model

5.5.2.3 Sensitivity to fabric architecture

The model took into consideration ideal fabric architecture, , which conserve the positions, sequence and shapes of pores while being compressed, and that is due to yarn stacking and weaving pattern. Also this model took into account the effect of stitching yarn in region "2" with two points of view:

1. No effect for stitching yarn was introduced for NCF, fabric "1" and "2", where a small polyester stitching yarn does not create a mesopore around it.
2. The effect of the mesopore created by stitching yarn for 3D orthogonal fabrics, fabrics "3", "4" and "5", where a significant e-glass through thickness yarn is used; this effect was eliminated in case of very high fiber volume fraction was a target; ε_{eff2} was too small, case of V_{f3} of fabric 5.

5.5.2.4 Sensitivity to mesopore volume and direction

Mesopores volume was predicted in warp and weft directions, and then volume ratios were calculated. This ratio has a big influence in enhancing or reducing the permeability in flow direction. Increasing ratios of the volume fraction of weft mesopores on the volume fraction of warp mesopores, equation (34, 35), will increase the weft permeability $K_{90°}$ and vice versa.

5.6 Conclusion

Five different NCF and 3D orthogonal fabrics were investigated. The key to permeability prediction is the architecture of the media. The mesopores and their distribution have the biggest influence on permeability values. The parameters investigated such as mesopores volumes, their ratios, and the mesopore created around the stitching depend on the weaving parameters and on the compaction of the fabric at the given fiber volume fraction. These parameters are either collected from simple figures and data sheets or predicted using simple geometrical modeling. This model was created in order to predict the permeability measurement.

A slight difference is observed for Fabric “1” ,”2” and “3” while measuring the permeability in the weft direction on the first fiber volume fraction, V_{f1}. This scattering does not have a negative effect while it’s less than a scattering between two successive experiments. Thus this scattering is referred to the fabric itself.

The model affirmed its sensitivity to architecture, filament radius as well as mesopores size and direction. The model is useful for industries and can be applied for a further study. A very good correlation was observed for all considered fabrics while comparing the results with measured experimental permeability values.

In a future work, the model is to be generalized to cover a wider range of fabrics’ architectures. The aim is to implement the model inside CAD and CAM software.

6 Chapter 6: Numerical Analysis of Composite Fabrics Permeability

6.1 Introduction

6.1.1 Problem Description

The evaluation of permeability is of great importance to manufacture composites by *Liquid Composite Molding* (LCM) processes, in which the resin is injected through the fiber bed contained in a closed and rigid mold like in *Resin Transfer Molding* (RTM). Knowing the permeability of a certain fabric will allow calibrating the filling time, the injection parameters, as well as reducing manufacturing costs and improving the quality of the product. In engineering fabrics, the three-dimensional permeability tensor is divided into in-plane and through-thickness components. These components are evaluated either by experimental, analytical or numerical methods.

The evaluation of permeability faces different obstacles:

- A relatively high standard deviation is observed in experimental results. Depending on the method used to measure permeability, a scatter over 1000 % for has been observed in some cases [8, 9, 108], especially if different ways of performing the experiments are compared as in the benchmark exercise I in 2011[8]. In addition, performing the measurements remains time consuming. In fact, the.
- The lack of a reliable analytical method to evaluate permeability is also a concern. A large number of mathematical models have been described in the scientific literature, but none of them gives satisfactory results for the whole range of existing textiles [64].
- An inadequate prediction capability by numerical simulation was also observed. Previous investigations show significant errors between numerical and experimental results. For example, Endruweit [23] simulations for a fiber volume fraction V_f = 55% are off by 600 % in the case of a 3D orthogonal fabric.

The aim of this chapter is to present a Finite Element (FE) model to predict the in-plane permeability based on a unit cell geometry of solid fiber bundles. Only the mesoscopic

flow between the bundles is taken into account. The proposed model attempts to improve numerical predictions by comparison with experimental data. This investigation can be possibly used as a reference for future analytical work since numerical calculations are perfectly repeatable, which is not the case of experimental measurements.

The *Resin Transfer Molding* (RTM) is one of the most popular LCM processes. To improve the quality of RTM parts, the formation of voids must be controlled. Figure 72 [109] shows a series of microscopic and mesoscopic air entrapments. Voids play a key role on quality as starting points for the propagation of cracks and delaminations.

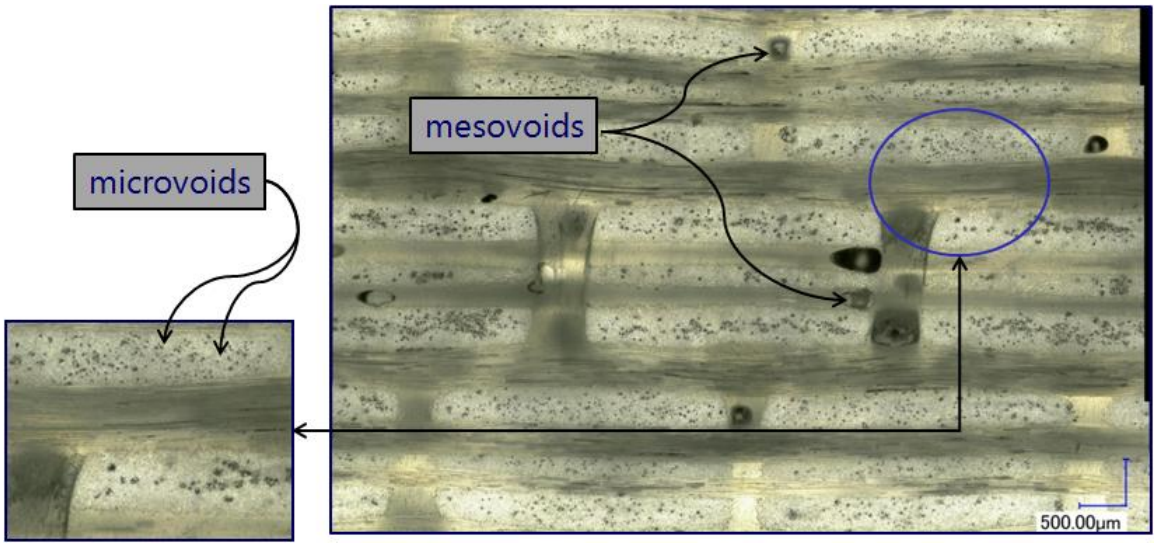

Figure 72 Picture taken from a microtomographic scan showing microscopic and mesoscopic voids

The main parameters that are needed to simulate the isothermal RTM flow are the permeability components, the required fiber volume fraction, the thickness of the part, the injection parameters (injection pressure or flow rate), and the location of inlet and outlet gates. To prevent void formation, the filling time and flow pattern, including the shape of the evolving flow front in time must be predicted. Simulation packages such as PAM-RTM [55], LIMS [56] and Polyworks [57] all use three kinds of inputs to predict isothermal mold filling: (i) the geometry of the part, (ii) the viscosity of the resin at the injection temperature, and (iii) the permeability of the fibrous reinforcement.

6.1.2 Literature Review

Several studies have focused on the evaluation of longitudinal and transverse permeability for unidirectional fiber bundles. These investigations included experimental work, analytical calculations and FE simulations. A comparative study published earlier show a review on permeability evaluating methods of unidirectional fiber beds [45]. However less work was published on the evaluation of permeability of engineering textiles. The permeability of fibrous reinforcement was firstly studied experimentally by Carman [67] and Sullivan [68] in the 1940s.Kuwabara [36], Happel and Brenner [69] and Sparrow and Loeffler [110] in the 1950s. Happel and Brenner [69]solved Stokes equation analytically for parallel and normal flows to a single cylinder for the free surface problem. Later, Sangani and Acrivos [43] performed analytical and numerical studies on the permeability of square and hexagonal staggered arrays of cylinders for the entire range porosity values between 0.2 and 0.8. Recently, Sobera and Kleijn [111] studied analytically and numerically the permeability of random 1D and 2D fibrous media.

For 2D and 2.5D woven fabrics, the geometrical complexity of the unit cell prevents from deriving a simple analytical solution. Therefore, it is then necessary to use numerical methods. The equations of fluid mechanics are solved in the mesoscopic flow channels of the dual-scale porous medium (microscopic scale inside the fiber bundles, mesoscopic scale when considering the open spaces between the bundles). Authors developed different methods to predict the in-plane permeability tensor numerically. These methods belong to three different categories: finite elements, finite differences, and Lattice Boltzmann. As described below, for each group of numerical methods considered to predict permeability, there are advantages and drawbacks:

a) The finite element method used in references [10-17] is based on the discretization of the unit cell into elements. These local functions have the advantage of being simpler than those which could possibly be used to represent analytically the flow in the total unit cell. The main limitation remains the complexity of creating a 3D mesh of the flow channels, namely the meso porous network, together with the significant computing time. [14] compared the derived results with a developed analytical model; the comparison shows good agreement for permeability values larger than 10^{-4} m^2. The main disadvantage of this method is its limitation to be applied to engineering textiles since finite element

simulations did not converge on this permeability order. Laine performed numerical simulations in order to predict the permeability of two Hexcel fabrics: 2X2 twill weaved (G986) and a 2.5D interlock (G1151) [17, 81]. The limited amount of experimental results published on woven reinforcements, did not allow them to carry out a deep numerical-experimental comparison. Loix developed a methodology allowing to determine numerically the permeability when considering slow saturated flows through previously deformed woven fabrics [16]. His comparison was more likely to be qualitative than quantitative.

b) Finite difference methods seek approximate solutions of partial differential equations by solving a system which links the values of unknown functions at certain points sufficiently close to each other to ensure convergence [18]. This approach is also limited by the computer time required to simulate the flow through complex 3D textile architectures. Verleye et al. [18] employed a three-dimensional finite difference solver. The validation of this method on three kinds of fabrics is done with respect to experimental data from literature; a maximum scattering of 50 % is observed. This error was revealed to the sensitivity of the mesopores size measurement. The main drawback of this approach is the very fine discretization required to converge.

c) Lattice Boltzmann methods study the flow through the porous medium at the mesoscopic scale by considering fictitious particles in a discrete space-time continuum [19-22].Convergence of the calculations is not as rapid as the other methods. They are also more expensive in terms of computer time.

If the finite element method is generally well adapted to complex geometries, its main disadvantage is the need of constructing a complex 3D mesh. Most of the time obtaining such a mesh is not an easy task. Finite differences and Lattice Boltzmann's methods are used to solve problems on uniform meshes, so no complex mesh is needed. However, a refined discretization is needed to ensure convergence, which makes these two approaches finally more expensive in terms of calculation time. Hence, numerical methods give unsatisfactory results. Note that some authors compared their results qualitatively with published data, this reveals to the lack of published permeability measurements or to the inconsistency of the model. Others developed numerical models that are not applicable to engineering textiles.

In this study a steady state simulation considering a theoretical unit cell is launched. The micropores are assumed to be blocked. Bundles shape and dimensions as well as mesopores sizes are respected in each simulation. This simulation is easy to implement. The meshing and simulating time are short when compared to a simulation in a transient

mode without closing the micropores. The predicted permeability results are far from being perfect, especially for fabrics having an open mesopore path. A mutation to the unit cell is assumed, where a single fiber is inserted inside each mesopore along the flow path and in the same direction. This fiber is small enough so that its addition does not affect the total fiber volume fraction. This addition corrected the predicted saturated permeability value.

6.1.3 Methodology

This study focuses on steady-state as well as faster numerical modeling of the in-plane permeability components ($K_{0°}$ and $K_{90°}$) for NCF and plain weave fabrics using COMSOL Multiphysics software. The numerical simulation assumes that the microscopic permeability in the bundles is negligible compared to the mesoscopic flow through the channels between the bundles. This is mainly due to the large size of mesopores between the bundles compared to the bundle width, Figure 73. Thus the liquid will easily flow through the mesopores rather than filling the bundles.

It will be shown that the predicted macroscopic in-plane unsaturated permeability values are significantly larger than the microscopic permeability values inside the fiber bundles.

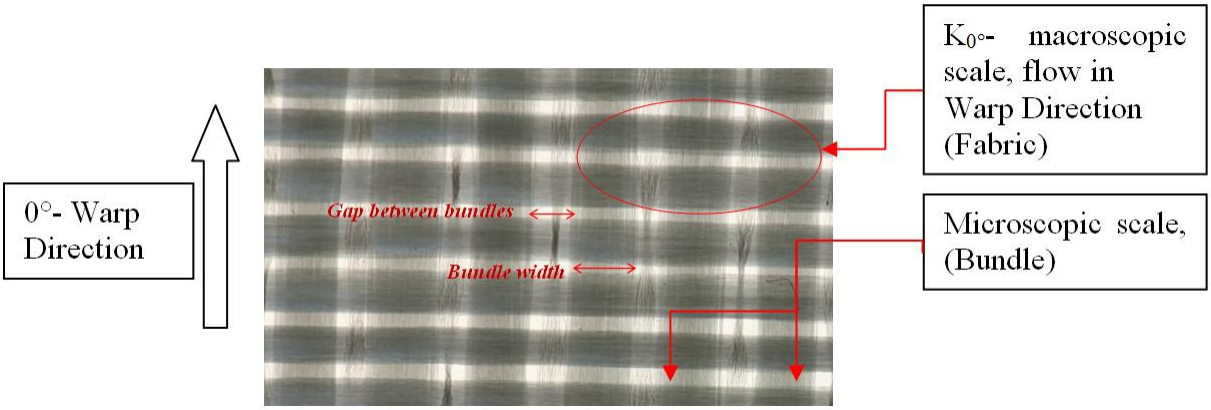

Figure 73 Picture of the NCF TG-15-N fabric from Texonic

Figure 74 Unidirectional stitched fabric - Tissa

In order to validate that assumption, the permeability predicted by a well-known analytical model (Gebart microscopic model [33]) was compared to experiments for the unidirectional stitched fabric. Tissa fabric is shown in Figure 74. Table 52 shows that the experimental results are 10 times higher for the lower fiber volume fraction V_f of 54.6%, and around 4.5 times for higher values of V_f. It is significant to show that an increase of V_f by 13% (from 54.6% to 61.6%) decreases the ratio from 10 to 4.5, while the next increase by 11% (from 61.6% to 68.2%) shows that the ratio remains almost unchanged. This is explained by the decrease of the mesopore size for larger values of V_f, which attenuates the effect of mesoscopic flow and favors that of microscopic flow. It is believed that when such fabric attains a maximum compaction, for the maximum possible V_f, the mesopore size will be almost zero. Then the microscopic flow is the major flow, and the prediction of permeability using analytical microscopic-models will converge to those experimental.

V_f	Permeability Gebart model (m^2)	Permeability Experimental $k_{0°}$(m^2)	Experimental / Analytical
54.56%	$1.24E^{-12}$	$1.24E^{-11}$	10
61.62%	$6.1E^{-13}$	$2.77E^{-12}$	4.5
68.2%	$2.92E^{-13}$	$1.34E^{-12}$	4.6

Table 52Comparison of mcroscopic and macroscopic permeability

The calculation using the analytical model used the composite V_f instead of that of the bundles. For more precision, the V_f of the bundles should have been used, which of course is higher and would have led to much lower permeability values and hence larger macroscopic to microscopic permeability ratios. The microscopic flow is neglected in the numerical simulations by assuming that a fiber bundle is impermeable.

In this study a steady state simulation considering a theoretical unit cell is launched. The micropores are assumed to be blocked so a single phase problem is solved. Bundles' shape and dimensions as well as mesopores sizes are respected in each simulation. The meshing and simulating time are short when compared to a simulation in a dual scale transient mode (without blocking the micropores). The predicted permeability results are **saturated permeability values inside a theoretical REV**, Figure 75. But the reality is that the mesopores' dimensions are not ideal and some of them could be closed or reduced thus a pressure drop ΔP_1 is considered in order to compensate this issue. A **saturated permeability value inside a real REV** is gathered A second pressure drop ΔP_2 should be considered in order to take the saturation effect including capillary pressure. This leads to the **unsaturated permeability value inside a real REV** as shown in Figure 75, which will be compared with measured permeability values.

In order to take the two pressure drop effects into consideration , a single mutation to the theoretical unit cell is assumed, where a single fiber is inserted inside each mesopore along the flow path and in the same direction. This fiber is small enough so that its addition does not affect the total fiber volume fraction. This addition corrected the predicted permeability value .

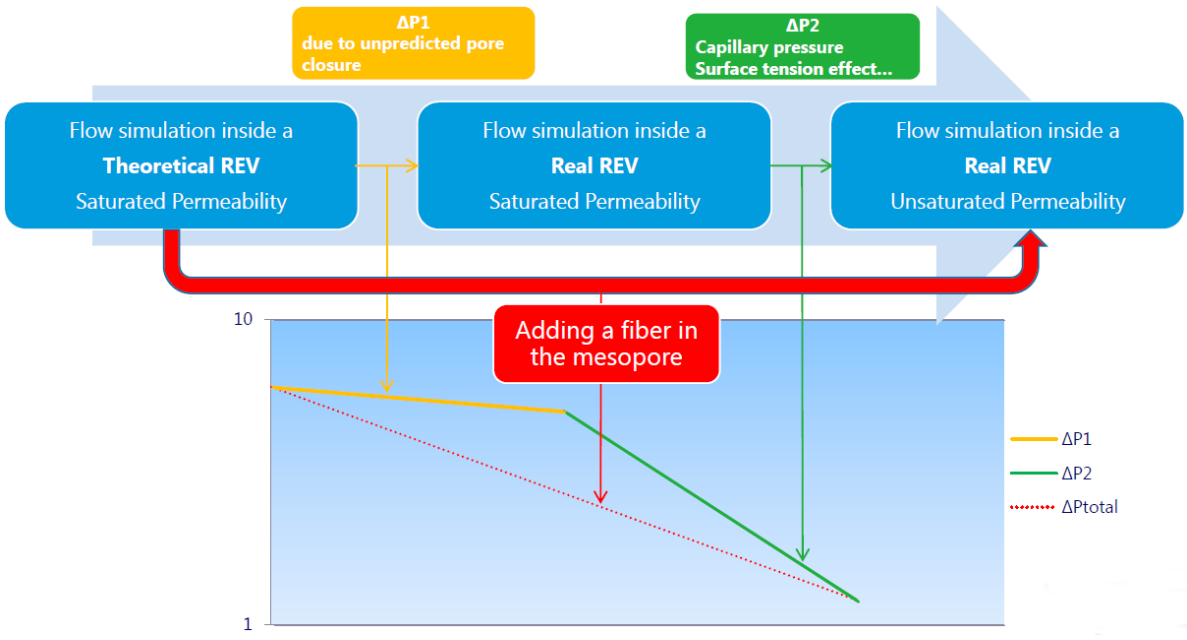

Figure 75 Work flow

This addition is inspired from the presence of these fibers in a real injection as shown in Figure 76. Primary resin flow paths are the mesopores along the flow direction, while secondary resin flows occur in the mesopores perpendicular to the flow direction. The assumption of empty mesopores without adding fibers leads to an overestimation in the macroscopic permeability of the textile. For plain weave or angle interlock textiles, since the warp and weft bundles are interlaced together, the mesopore volume is smaller, thus the porous shape of the textile is well represented, and the permeability in the secondary pathways can be better evaluated.

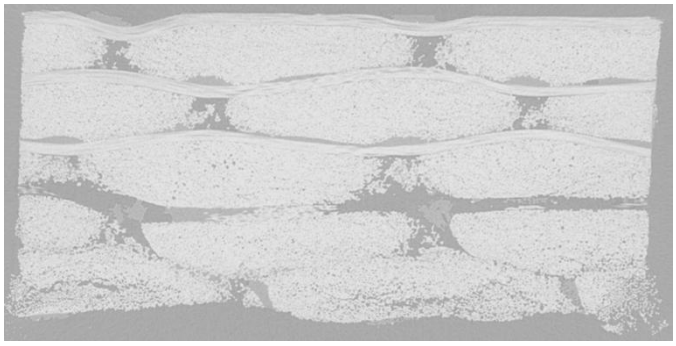

Figure 76 Impregnated fabric showing the dispersed fibers in the mesopores

Figure 77 shows the modeling methodology. As a first step, the bundle width “a” and all the non-compacted fabrics’ geometrical data are collected from the fabrics’ data sheets and camera pictures such as Figure 73 and Figure 74. The second step is to predict these data for different fiber volume fraction. A theoretical unit cell is selected. This unit cell is drawn using TexGen software. The permeability correction factor is inserted to the drawings. In the sixth step, the numerical simulations predicting permeability before and after the insertion of the fiber are launched. Finally, the results are compared with respect to measured experimental results.

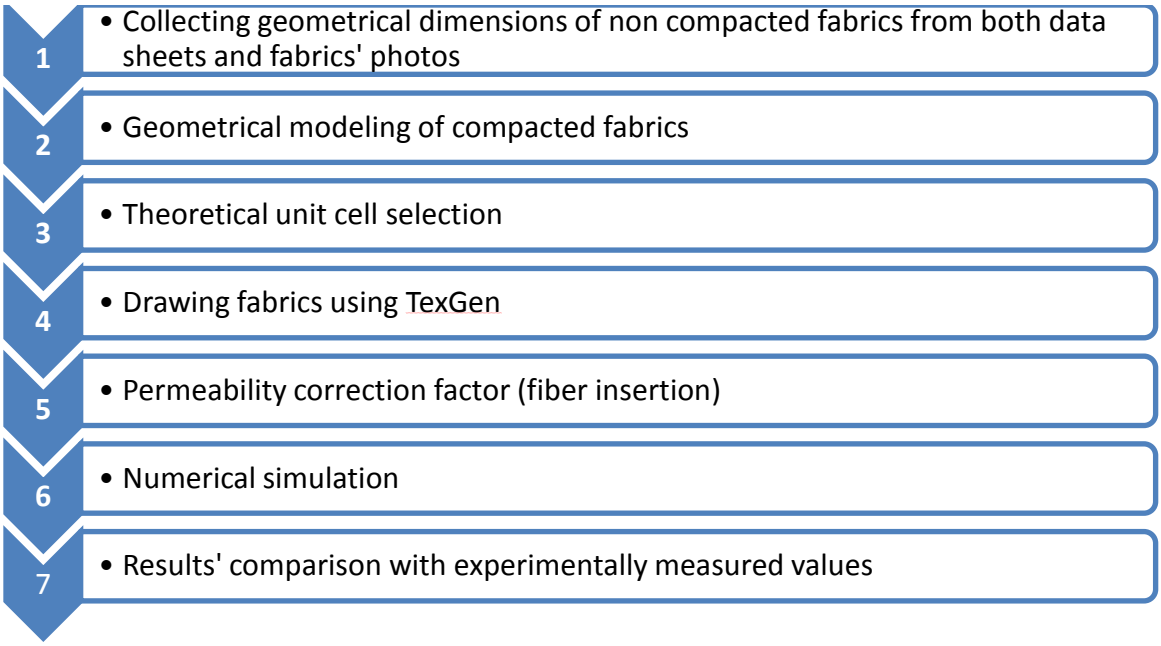

Figure 77 Working flow chart

6.2 Textile geometry and experimental measurement

In this study, the in-plane permeability components of different textiles are evaluated by Finite Element analysis. The results are compared to available experimental data. The fabrics consist of NCFs and 2D plain weave fabrics. The geometric models of these textiles are constructed with TexGen software [112] for different fiber volume fractions (V_f), where V_f is the ratio of the fiber volume with respect to the total volume of the unit cell. It can be calculated as follows:

$$V_f = \frac{n.s}{\rho.h} \qquad \text{Eq.(49)}$$

where s is the surface density of the textile, n the number of layers, ρ the density of the fibers, and h the height of the unit cell.

6.2.1 Specifications of the fabrics

The fibrous reinforcement “850.0445.80.0600”shown in Figure 77 is a unidirectional E-Glass roving fabric stitched by HS glass bundles, is provided by Tissa Company.

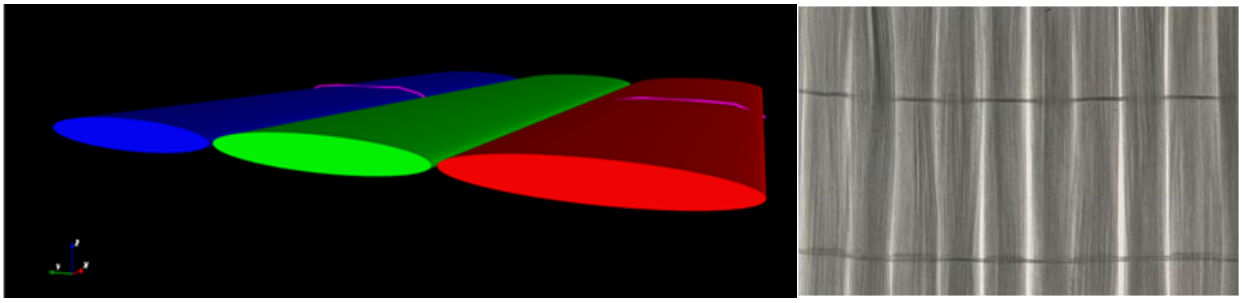

Figure 78 Geometry of the unidirectional textile from Tissa

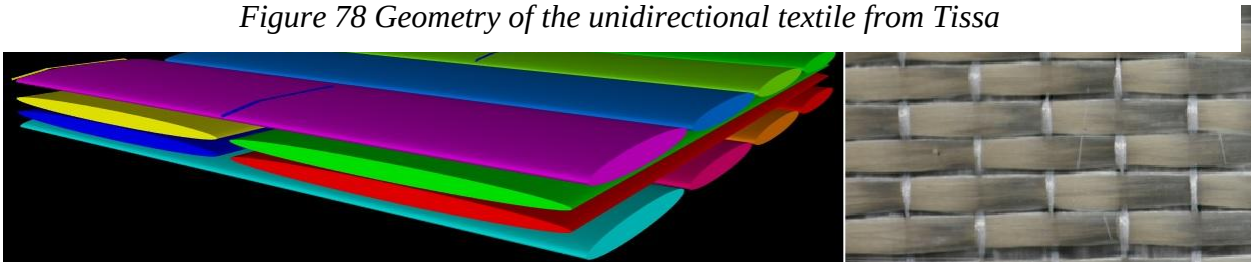

Figure 79 Geometry of TG-33-N textile from Texonic

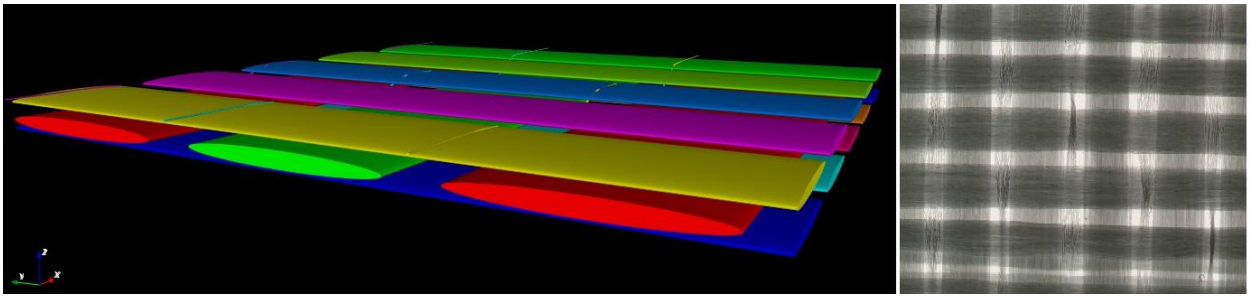

Figure 80 Geometry of the TG-15-N textile from Texonic

The architecture of textiles TG-33-N and TG-15-N are shown in Figure 79 and Figure 80 respectively. TG-15-N is a three layer E-glass NCF with a surface density equal to 518 g/m^2, stitched in the warp direction by a polyester binder. The warp/weft volume ratio is 55/45, with a warp bundle 2.6 times larger than the weft bundles. TG-33-N is a four layer E-glass NCF with a surface density equal to 1125 g/m^2, stitched in warp direction by a polyester binder. The warp/weft fiber volume ratio is 55/45.

Two different plain weave fabrics are studied, a carbon fiber textile supplied by Chomarat (C-WEAVE 200P 3K), and an E-glass fibrous reinforcement provided by Texonic (L14012). Both textilesare formed from one layer each. Figure 81 shows the unit cell of carbon plain weave fabric. L14012 fabric has the same architecture as the C-weave, but with different dimensions. Figure 82 introduces the geometrical parameters of

the fabric. The subscripts "*w*" and "*f* "denote the warp and weft bundles; the addition of 0 to the subscript stands for the non-compacted fabric. Table 53 and Table 54 give the parameters taken from the supplier data sheets and the experimentally obtained geometrical parameters of the textiles.

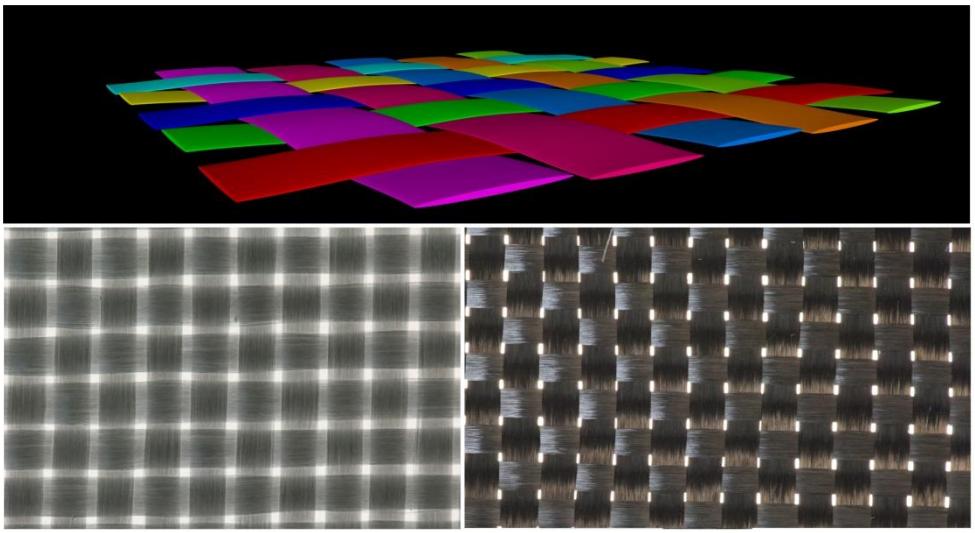

Figure 81 Fabric 7 « L14012 » and fabric 8 « C-WEAVE 200P » left and right fabrics respectively

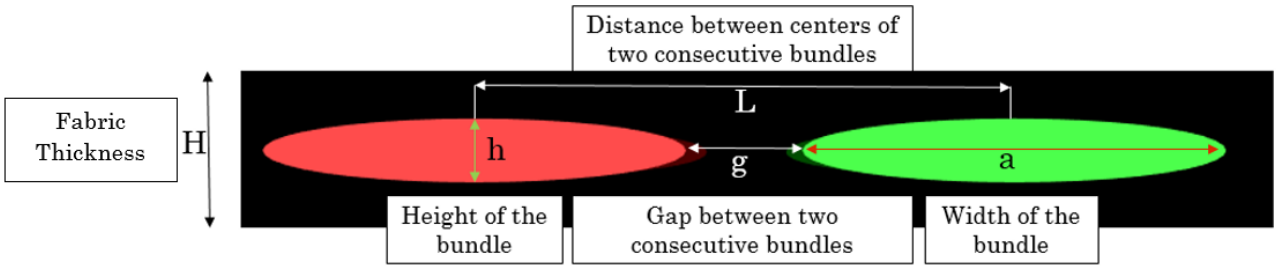

Figure 82 Textiles dimensions.

Fabric	Fabric Name	Company Name	Fabric type	Number of layers		Count/cm	
				Warp	Weft	Warp	Weft
Fabric 1	TG-15-N	Texonic	NCF	1	2	3.1	10.4
Fabric 2	TG-33-N	Texonic	NCF	2	2	4.6	8.4
Fabric 6	850.0445.80.0600	Tissa	Unidirectional	1	1	3.6	1
Fabric 7	L14012	Texonic	Plain weave	1	1	4	3.9
Fabric 8	Cweave200P 3K	Chamarat	Plain weave	1	1	4.9	4.9

Table 53 Initial dimensions for Textiles-1

Table 55 depicts the geometrical data after compaction predicted by a simple analytical model [113].

Fabric	a_{w0}(mm)	g_{w0} (mm)	a_{f0}(mm)	g_{f0}(mm)	H_0(mm)	ρ_S (g/m2)	Material
Fabric 1	2.35	0.88	1.47	0.44	0.52	518	E-glass
Fabric 2	3.9	0.45	2.1	0.28	0.9	1125	E-glass
Fabric 6	2.53	0.25	0.325	9.675	0.39	445	E-glass
Fabric 7	2.1	0.4	2.1	0.464	0.53	597	E-glass
Fabric 8	1.52	0.52	1.8	0.239	0.28	200	Carbon

Table 54 Initial Dimensions for Textiles-2

Fabric	Fabric 1			Fabric 2			Fabric 6		
V_f(1,2,3)	0.4	0.48	0.56	0.5	0.57	0.64	0.55	0.6162	0.682
H (mm)	0.5	0.4249	0.364	0.89	0.78	0.697	0.32	0.28	0.25
h_w(mm)	0.2	0.17	0.13	0.18	0.17	0.15	0.31	0.27	0.24
a_w(mm)	2.585	2.73	3	4.12	4.15	4.17	2.646	2.716	2.724
g_w(mm)	0.87	0.72	0.62	0.44	0.39	0.32	0.132	0.062	0.054
h_f(mm)	0.13	0.105	0.08	0.235	0.2	0.18	-	-	-
a_f(mm)	1.583	1.74	1.8	2.1	2.13	2.16	-	-	-
g_f(mm)	0.43	0.36	0.31	0.27	0.24	0.21	-	-	-

Fabric	Fabric 7			Fabric 8		
V_f(1,2,3)	0.4451	0.5341	0.6231	0.434	0.5208	0.6076
H (mm)	0.53	0.4383	0.3757	0.2584	0.2133	0.1829
h_w(mm)	0.265	0.219	0.175	0.1292	0.1	0.087
a_w(mm)	2.1	2.17	2.38	1.561	1.755	1.788
g_w(mm)	0.4	0.33	0.12	0.48	0.286	0.253
h_f(mm)	0.265	0.219	0.175	0.1292	0.1	0.087
a_f(mm)	2.1	2.1802	2.38	1.8204	1.983	1.981
g_f(mm)	0.464	0.384	0.184	0.22	0.06	0.06

Table 55 Predicted geometrical dimensions of the compacted fabrics

6.2.2 Computational fluid dynamics simulation

This section presents the experimentally measured in-plane permeability components. A brief summary on the experimental methodology is given in Chapter 4. More detailed information is available in [9, 105]. The results of the experimental work are shown Section 5.2.1.

Various Computational Fluid Dynamics (CFD) methods are used in order to simulate the flow through porous media based on Navier-Stokes or Brinkman equations, an extension of Darcy's law. Brinkman equation is considered as a practical way to deal with the coupled problem of flows in a porous medium and in the open spaces between the fiber bundles (mesopores). When studying the separate flow paths, namely the mesoscopic and microscopic flows (respectively between and inside fiber bundles), Naviers-Stokes equation models the flow inside the mesopores, whereas equations derived from or compatible with Darcy's law model the flow inside the micropores. Since the two flows (microscopic and mesopscopic) are either in series, in parallel, or a combination of the two, thus the permeability must be averaged from the microscopic and mesoscopic values because it is difficult to model the interaction between the two flows, which depends on the microstructure of the composite and on the boundary conditions (capillary versus viscous flow depending if an injection pressure is specified or not). Hence, the way to proceed and combine the two flows remains indeterminate. In order to simplify the analysis, an assumption is considered, namely hereto neglect the microscopic permeability. This assumption may be justified by considering that the mesopores play a determinant role on the flow.

The steady flow in the mesopores is modeled by Navier-Stokes equation (51) [12, 114, 115], which is solved by the finite element method with COMSOL Multiphysics software. The velocity and pressure calculated in the analysis are used to evaluate the saturated permeability of the fibrous reinforcement in m^2 based on Darcy's law [116]. The permeability k, is given by equation (22), where μ is the dynamic viscosity of the resin (Pa.s), L the length covered by the resin (m), U the averaged volume velocity (m/s), and ΔP the pressure drop (Pa).The fluid obeys the standard assumptions of Navier-Stokes equation (51) with a constant density, viscosity, and Newtonian behavior [117]. When a numerical solution of the steady-state Navier-Stokes is required then the time-dependent derivative in equation (51) is set to zero.

$$k = \frac{\mu L U}{\Delta P} \qquad \text{Eq.(50)}$$

$$\rho\left({}^{\partial v}/_{\partial t} + (v.\nabla)v\right) = -\nabla p + \mu\nabla^2 v + f \qquad \text{Eq.(51)}$$

6.2.3 Flow Type

Since the flow in the numerical simulations is supposed to be laminar (low velocity flow), the laminar model was used to solve the Navier-Stokes equation.

- Study type: steady state flow
- Compressibility: incompressible flow (Ma<0.3)

The fluid used in the simulations is a typical epoxy Resin (X238), whose properties are shown in Table 56.

Temperature	293 K
Density	1670 Kg/m^3
Dynamic Viscosity	0.195 Pa.s

Table 56 Properties of Epoxy Resin X238

6.2.4 Finite Element Mesh

CFD simulations require that the computational domain gets divided into small cells where the flow is modeled. The unit cells for the two plain weave fabrics are shown in Figure 81. Figure 83shows the unit cell of the TISSA unidirectional reinforcement after adding fibers in the mesopores, where 2 layers of the fabric form the unit cell. Figure 84 and Figure 85 show the unit cells with one layer of each fabric and the fibers of materials TG-33-N and TG-15-N respectively added in the mesopores.

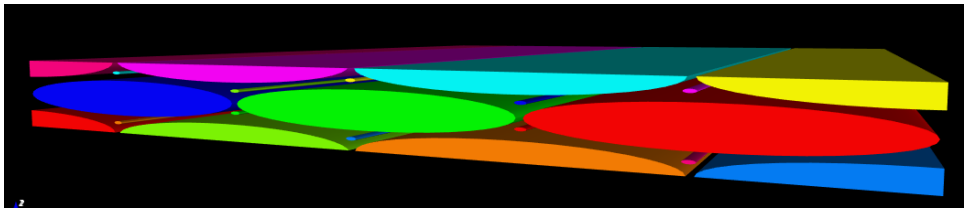

Figure 83 Unit Cell of Tissa fabric at Vf = 0.4793

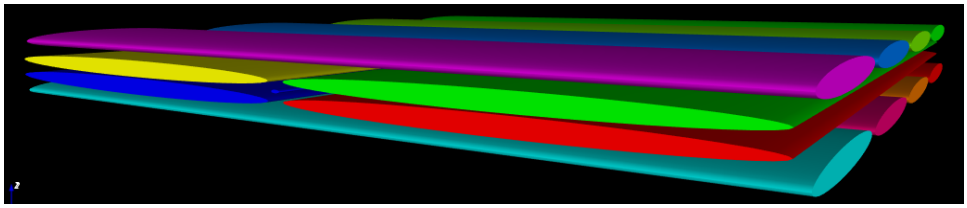

Figure 84 Unit Cell of TG-33-N at V_f=0.4948

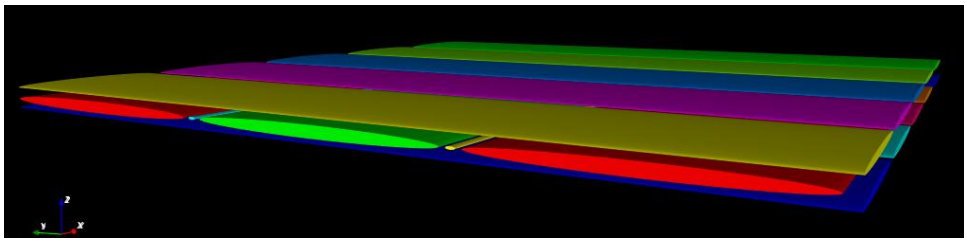

Figure 85 Unit Cell of TG-15-N at V_f=0.4063

Table 57 shows the meshing characteristics of the selected unit cells. For example, the bidirectional TG-15-N fabric has been meshed with 294535 elements. Figure 86 shows an example of the mesh generated for the L14012 unit cell.

Mesh type	Mesh size	Max element size(mm)	Min element size(mm)	Max element growth rate
Free Tetrahedral	Fine	0.816	0.102	1.45

Table 57 Meshing Properties

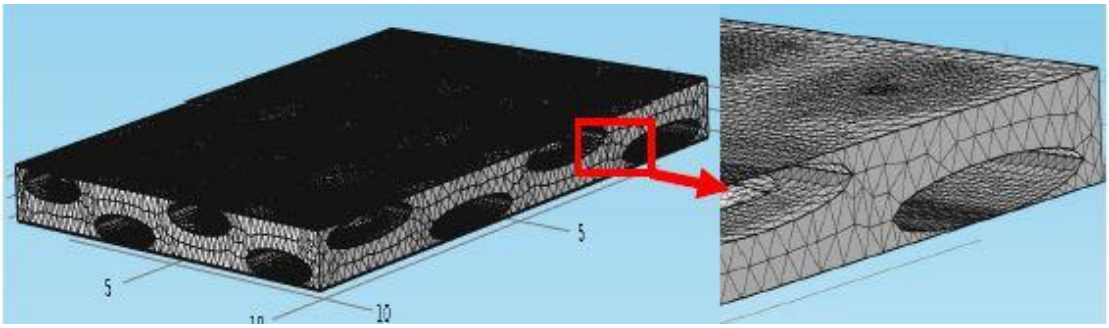

Figure 86 Plain-Weave L14012 Generated Mesh

6.2.5 Boundary Conditions

After the mesh has been constructed, the next step consists of specifying the boundary conditions. Similar boundary conditions were used in all the numerical simulations performed in this study. Two types of boundary conditions were considered: specification of the inlet and outlet pressures, and non-viscous stress on the other edges of the unit cell. Table 58 displays the boundary conditions of the unit cell studied.

Edge	Boundary Conditions
Inlet edge	Pressure = 1.5 bar
Outlet edge	Pressure = 1 bar
Remaining edges	No Slip Wall

Table 58 Boundary Conditions

6.3 Effect of adding fibers in mesopores

In order to predict permeability values ($K_{0°}$ and $K_{90°}$), the average velocity magnitude is determined as an output of numerical simulations. These values allow calculating $K_{0°}$ and $K_{90°}$based on Darcy's law. Figure 87 shows how the velocity inside the primary mesopores (mesopores along the flow direction) tends to be overestimated, whereas the velocity inside the secondary mesopores (mesopores perpendicular to the flow direction) seems underestimated.

In fact, due to the large mesopore volume, the mesopores are considered as unlimited pathways. So, in order to control the sudden increase in velocity magnitude caused by the large mesopore volume, small fibers were inserted between bundles. This action solved the problem of the numerical modeling which appeared to misunderstand the filling behavior inside the mesopore.

The volume of added fibers is very small compared to the total volume of the domain. Therefore, this does not really affect the overall fiber volume fraction. However, because of the location of these added fibers, it will have a significant effect on the flow, and hence on permeability. The following example will show how adding fibers in mesopores does not affect V_f. For a selected fabric on (V_f =0.52), the radius of an added fiber is 0.04 mm. This radius was chosen as small as possible while respecting meshing requirements. The total volume of fibers added is the number of fibers multiplied by the volume of each fiber.

$V_{addedfibers}$ = 9*π*0.042*10.5263 = 0.4762 mm^3

V_{domain} = 10.5263*11.25*1.353 = 160.218 mm^3

Fibers	$k_{exp}(m^2)$	$k_{num}(m^2)$	Error (%)
2 Fibers (0.1*0.1 mm^2)	$1.46E^{-11}$	$8.311E^{-12}$	-43
2 Fibers (0.1*0.03 mm^2)		$8.55E^{-12}$	-41.42
4 Fibers (0.1*0.03 mm^2)		$7.977E^{-12}$	-45.36

Table 59 Effect of the number and dimensions of added fibers

The added volume fraction is 0.00297, which does not affect the overall fiber volume fraction. Table 59 shows that the change of dimensions and the number of fibers does not influence the warp permeability predictions for TG-15-N at V_f = 0.56.

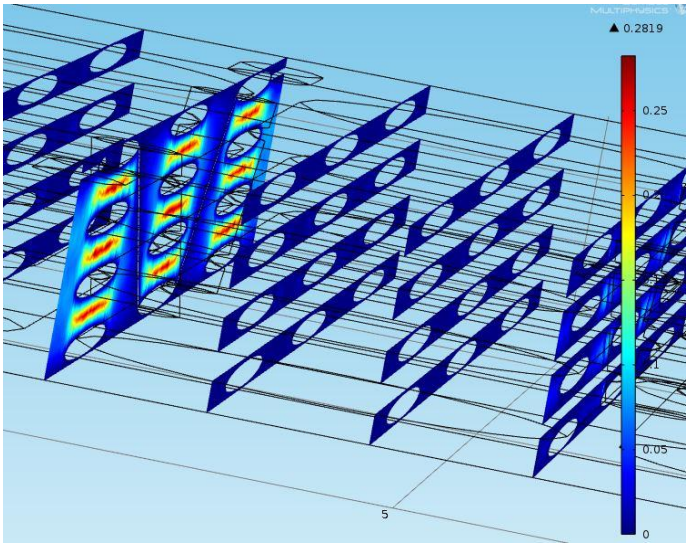

Figure 87 Velocity magnitude before adding fibers

In order not to distort the real material, the dimensions and number of fibers used in this study are the smallest possible while respecting meshing requirements (one fiber "$0.03*0.1mm^2$" in each mesopore).

6.4 Results and Analysis

The results obtained from different simulations are used to calculate the permeability of various textiles. The permeability is calculated from numerical simulations at different fiber volume fractions. The numerical and experimental values of permeability ($K_{0°}$ and $K_{90°}$) before and after adding fibers in mesopores will be shown in the warp and weft directions at different fiber volume fractions. Then, a comparison between numerical and experimental values is carried out to show the effect of the added fibers in the mesopores. Finally, a graphical comparison between the experimentally measured and predicted permeability after adding fibers is presented.

6.4.1 Fabric 2 "TG-33-N" Results

Table 60 shows a comparison between experimental and numerical permeability values before and after adding fibers in mesopores for TG-33-N. For the third largest fiber volume fraction of TG-33-N, the gap between bundles is very small, and the results without adding fibers fit well the experimental measurements. As shown, the permeability values predicted before and after adding fibers in mesopores are both close

to experimental values. This is due to the low volume of the mesopore in TG-33-N textile in which the gap width in the warp direction "g_w" is small with respect to the bundles' dimensions; where g_w ranges from 0.44 mm for the V_{f1} to 0.32 mm for the highest compaction value. Table 61 shows a comparison between experimental and numerical permeability values, before and after adding fibers in the mesopores of TG-33-N in the weft direction at different V_f. As previously mentioned, the predicted permeability before and after adding fibers in mesopores is close to experimental values. So adding fibers can be ignored for this textile since the mesopore volume is small relative to other dimensions. Figure 89 and Figure 91 show a comparison between the experimental and numerical permeability of TG-33-N in the warp and weft direction respectively, before and after adding fibers.

	TG-33-N - $K_{0°}$					
	Before Adding Fibers			After Adding Fibers		
V_f	$k_{exp}(m^2)$	$k_{num}(m^2)$	Error (%)	$k_{exp}(m^2)$	$k_{num}(m^2)$	Error (%)
V_{f1}	$2.14E^{-10}$	$1.52E^{-10}$	-28.6	$2.14E^{-10}$	$9.96E^{-11}$	-53.5
V_{f2}	$8E^{-11}$	$1.14E^{-10}$	43	$8E^{-11}$	$5.5E^{-11}$	-31.3
V_{f3}	$2.53E^{-11}$	$1.99E^{-11}$	-21.2	-	-	-

Table 60 Comparison between experimental and numerical warp permeability values of TG-33-N warp direction for different fiber volume fractions V_f.

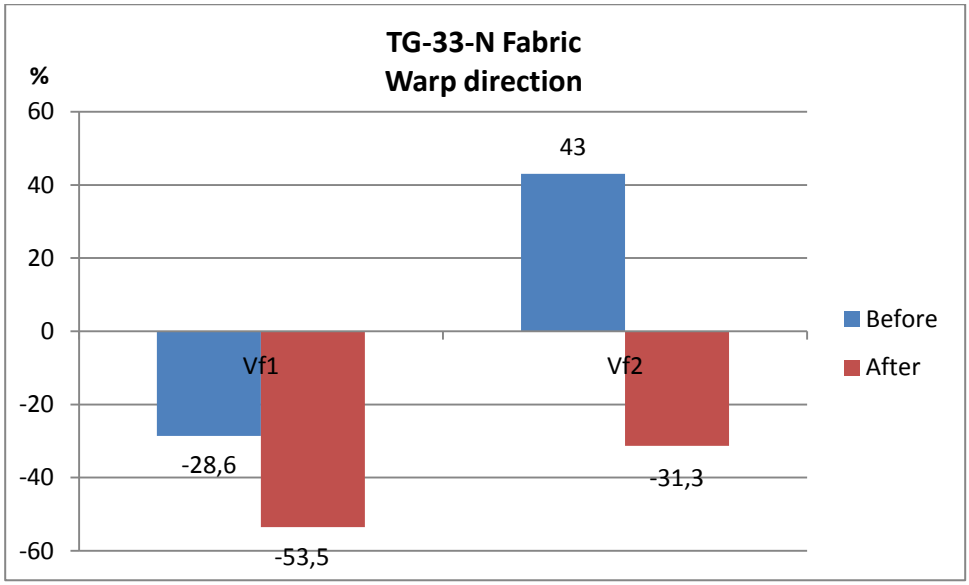

Figure 88 Comparison between error values before and after adding fibers of TG-33-N in the warp direction.

	TG-33-N – K90°					
	Before Adding Fibers			After Adding Fibers		
V_f	$k_{exp}(m^2)$	$k_{num}(m^2)$	Error (%)	$k_{exp}(m^2)$	$k_{num}(m^2)$	Error (%)
V_{f1}	$2.7E^{-10}$	$1.53E^{-10}$	-43.5	$2.7E^{-10}$	$1.55E^{-10}$	-42.7
V_{f2}	$9.68E^{-11}$	$1.22E^{-10}$	25.7	$9.68E^{-11}$	$1.2E^{-10}$	24.3
V_{f3}	$4.39E^{-11}$	$3.21E^{-11}$	-26.8	-	-	-

Table 61 Comparison between experimental and numerical weft permeability values of TG-33-N

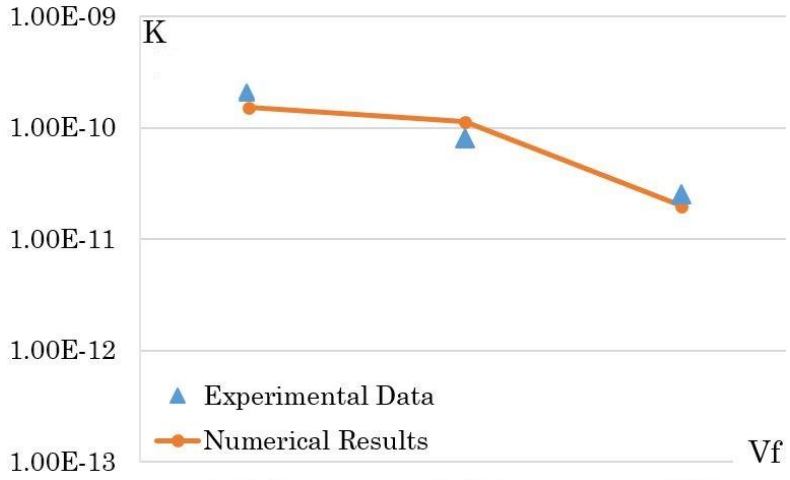

Figure 89 Comparison between numerical and experimental warp permeability results of TG-33-N

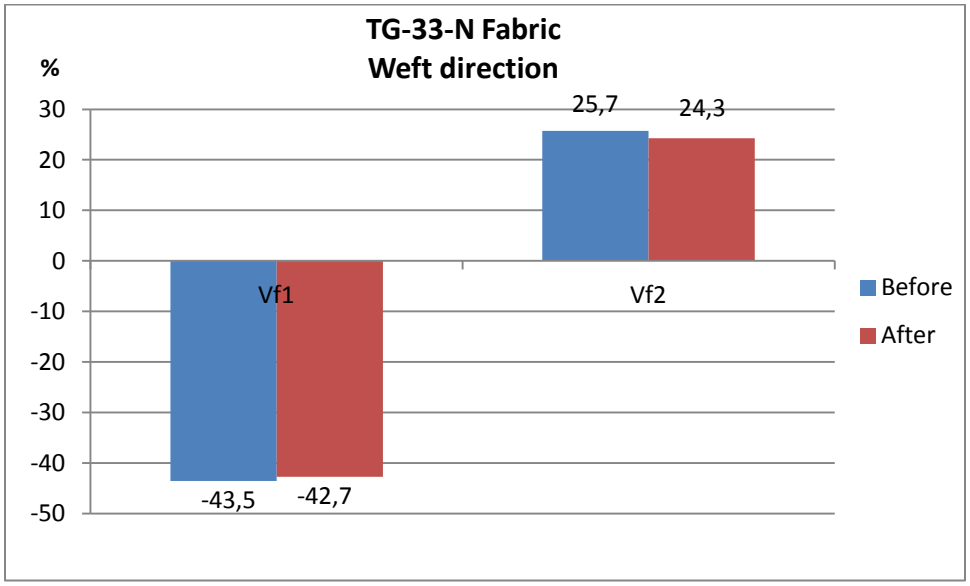

Figure 90 Comparison between error values before and after adding fibers of TG-33-N in the weft direction

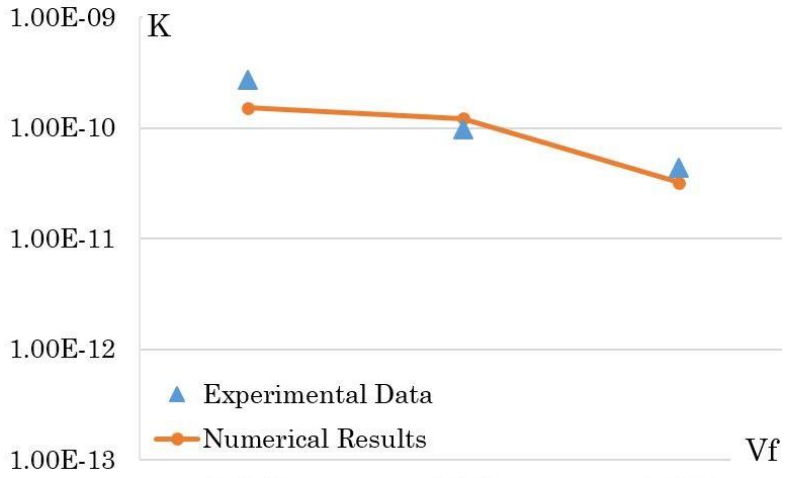

Figure 91 Comparison between numerical and experimental Transversal permeability results of TG-33-N

6.4.2 Tissa "Fabric 6" results

Table 62, Figure 92 and Figure 93 show a comparison between experimental and numerical permeability values, before and after adding fibers in mesopores, for Tissa fabric in the warp direction, for different values of V_f.

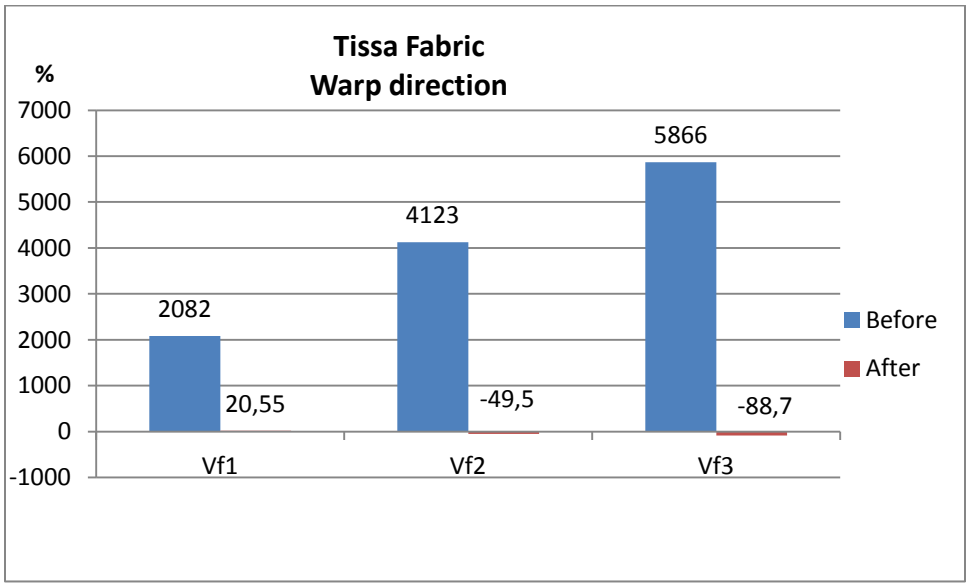

Figure 92 Comparison between error values before and after adding fibers of TISSA in warp direction

The high percentages of errors seen in Table 62 are due to the large size of mesopores which consequently leads to an overestimated fluid velocity in the numerical simulation. So, in order to control this sudden increase in velocity and to be more realistic, small

fibers were inserted. In fact, even though the width of the mesopore in the warp direction is rather small (less than 0.2 mm), but adding fibers in mesopores has shown an enhancement in permeability results due to the high mesopore volume. Hence, the error was reduced from very high values where the predicted permeability without adding the fibers is from 20 to 60 times larger than the measured values.

	TISSA Fabric – $K_{0°}$					
	Before Adding Fibers			**After Adding Fibers**		
V_f	$k_{exp}(m^2)$	$k_{num}(m^2)$	**Error (%)**	$k_{exp}(m^2)$	$k_{num}(m^2)$	**Error (%)**
V_{f1}	$1.24E^{-11}$	$2.7E^{-10}$	2082	$1.24E^{-11}$	$1.49E^{-11}$	20.55
V_{f2}	$2.77E^{-12}$	$1.17E^{-10}$	4123	$2.77E^{-12}$	$1.4E^{-12}$	-49.5
V_{f3}	$1.34E^{-12}$	$7.95E^{-11}$	5866	$1.34E^{-12}$	$1.5E^{-13}$	-88.7

Table 62 Comparison between experimental and numerical warp permeability values of Tisa's fabric

Table 63, Figure 94 and Figure 95 show the comparison for Tissa fabric between experimental and numerical permeability values, before and after adding fibers in mesopores, in the weft direction at different V_f.These results show the benefits of adding fibers where $K_{90°}$ numerically predicted was 2.5 times to 10 times larger than the values predicted after adding the fibers in the mesopores. Indeed the error without adding fibers was much larger for $K_{0°}$ than $K_{90°}$.This is explained by the bigger mesopore volume found in the warp direction.

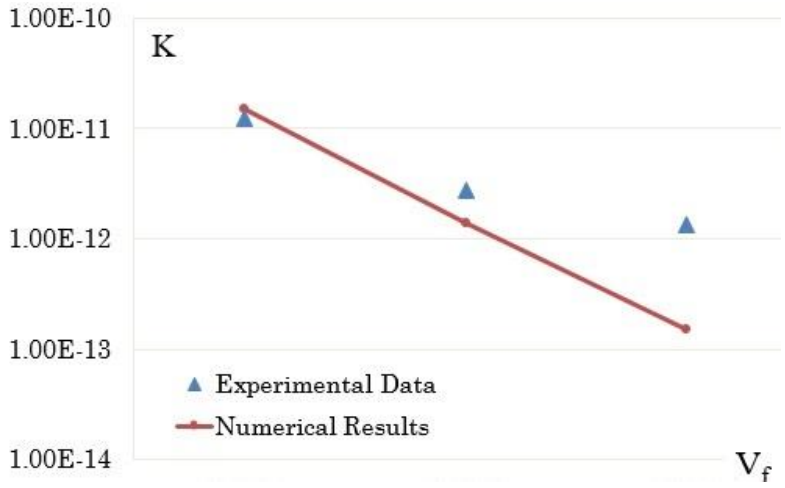

Figure 93 Comparison between experimental and numerical, after adding fibers warp permeability values of TISSA

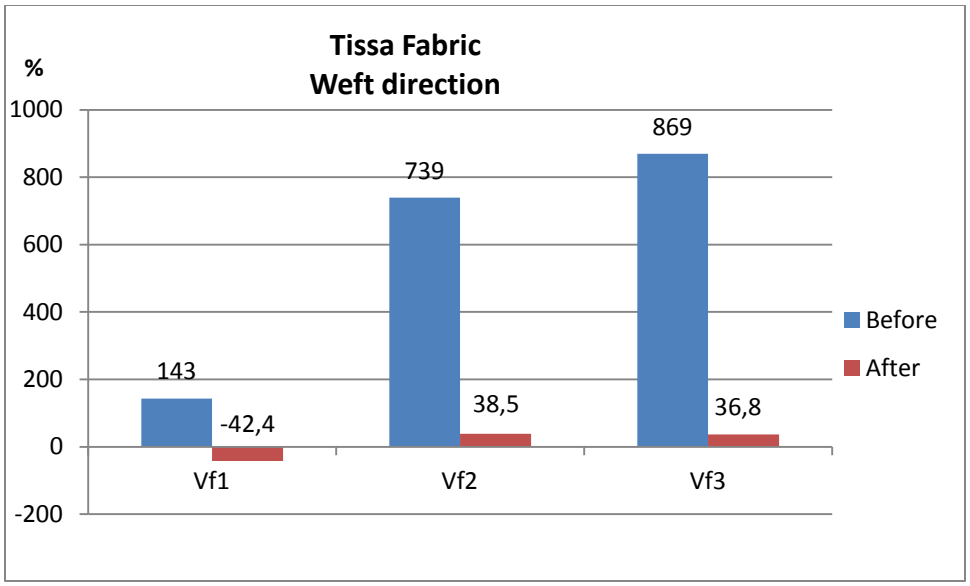

Figure 94 Comparison between error values before and after adding fibers of TISSA in weft direction

	TISSA Fabric - $K_{90°}$					
	Before Adding Fibers			After Adding Fibers		
V_f	$k_{exp}(m^2)$	$k_{num}(m^2)$	Error (%)	$k_{exp}(m^2)$	$k_{num}(m^2)$	Error (%)
V_{f1}	$7.54E^{-12}$	$1.84E^{-11}$	143	$7.54E^{-12}$	$4.34E^{-12}$	-42.4
V_{f2}	$1.9E^{-12}$	$1.6E^{-11}$	739	$1.9E^{-12}$	$2.63E^{-12}$	38.5
V_{f3}	$1.35E^{-12}$	$1.31E^{-11}$	869	$1.35E^{-12}$	$1.85E^{-12}$	36.8

Table 63 Comparison between experimental and numerical, before and after adding fibers, weft permeability values of TISSA

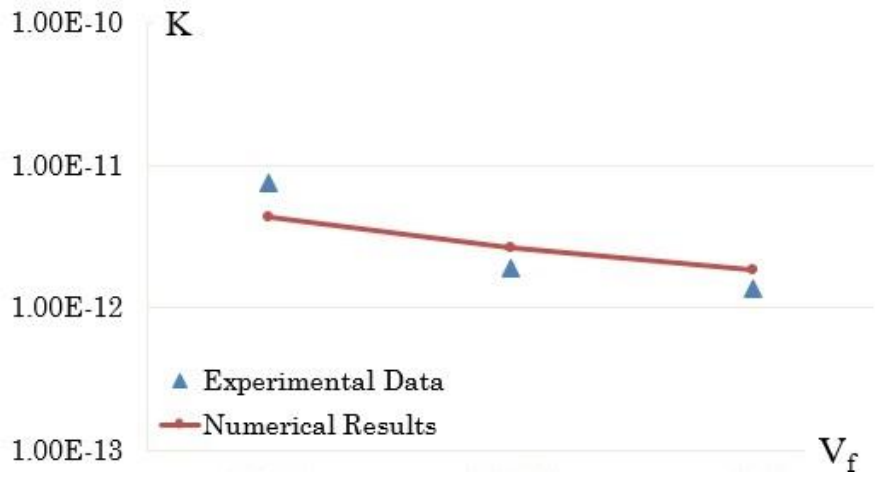

Figure 95 Comparison between experimental and numerical, after adding fibers weft permeability values of TISSA

6.4.3 TG-15-N "Fabric 1" results

Table 64, Figure 96 and Figure 97 show a comparison between experimental and numerical permeability values, before and after adding fibers in mesopores, for TG-15-N fabric in the warp direction at different V_f.

	TG-15-N - $K_{0°}$					
	Before Adding Fibers			After Adding Fibers		
V_f	$k_{exp}(m^2)$	$k_{num}(m^2)$	Error (%)	$k_{exp}(m^2)$	$k_{num}(m^2)$	Error (%)
V_{f1}	$2.39E^{-10}$	$6.4E^{-10}$	165	$2.39E^{-10}$	$2.71E^{-10}$	13.3
V_{f2}	$7.05E^{-11}$	$3.25E^{-10}$	361	$7.05E^{-11}$	$8.34E^{-11}$	18.3
V_{f3}	$1.46E^{-11}$	$5.25E^{-11}$	257	$1.46E^{-11}$	$8.55E^{-12}$	-41.4

Table 64 Comparison between experimental and numerical, before and after adding fibers, warp permeability values of TG-15-N

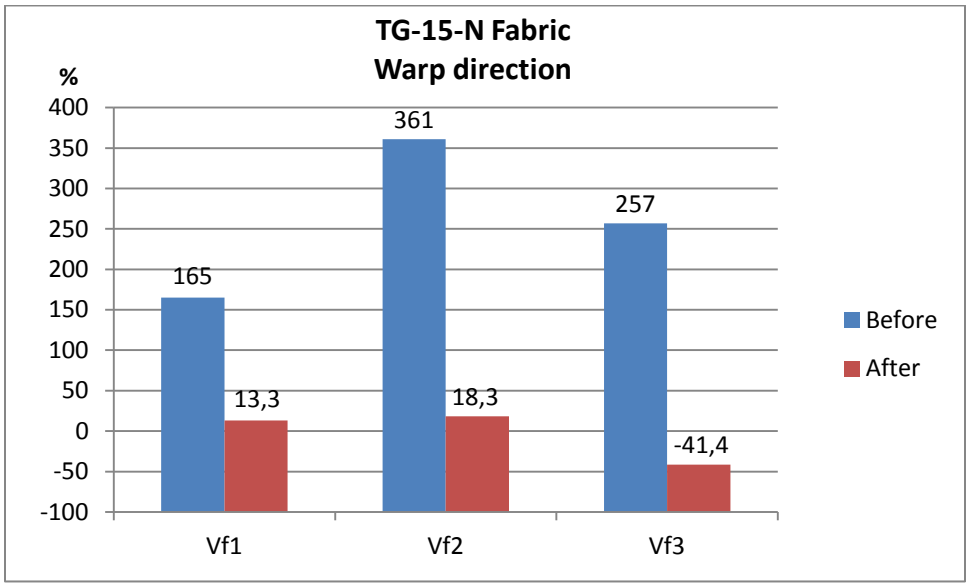

Figure 96 Comparison between errors values before and after adding fibers of TG-15-N in the warp direction

Table 65, Figure 98 and Figure 99 show a comparison between experimental and numerical permeability values, before and after adding fibers in mesopores, for TG-15-N fabric in the weft direction at different V_f.After the fibers were added, the errors were reduced. But as it is observed, adding fibers does not affect $K_{90°}$whose errors are acceptable even before adding fibers.

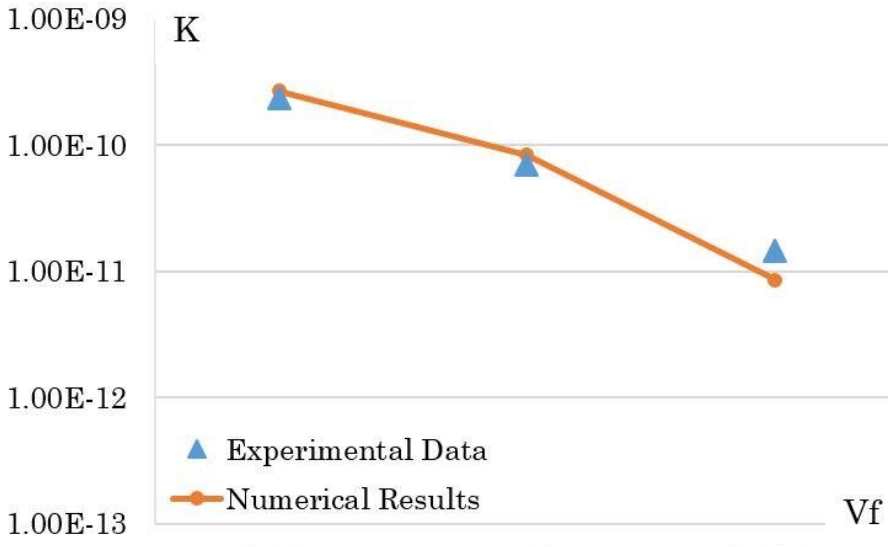

Figure 97 Comparison between experimental and numerical warp permeability values of TG-15-N, after adding fibers

	TG-15-N - $K_{90°}$					
	Before Adding Fibers			After Adding Fibers		
V_f	$k_{exp}(m^2)$	$k_{num}(m^2)$	Error (%)	$k_{exp}(m^2)$	$k_{num}(m^2)$	Error (%)
V_{f1}	$3.03E^{-10}$	$3.26E^{-10}$	7.5	$3.03E^{-10}$	$3.15E^{-10}$	4.14
V_{f2}	$7.44E^{-11}$	$7.07E^{-10}$	-5	$7.44E^{-11}$	$6.35E^{-11}$	-14.7
V_{f3}	$2.45E^{-11}$	$1.99E^{-11}$	-18.8	$2.45E^{-11}$	$1.69E^{-11}$	-31.2

Table 65 Comparison between experimental and numerical weft permeability values of TG-15-N

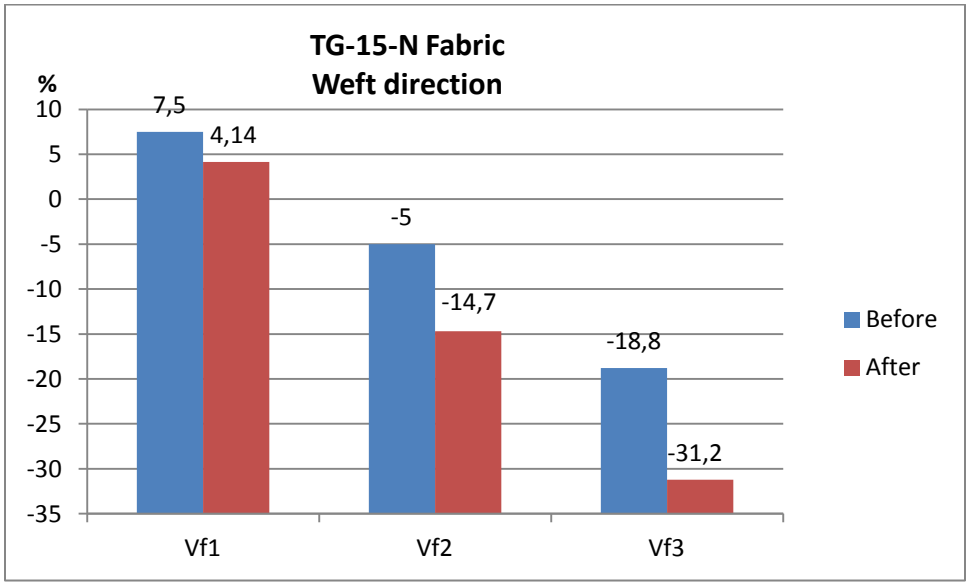

Figure 98 Comparison between errors values before and after adding fibers of TG-15-N in weft direction

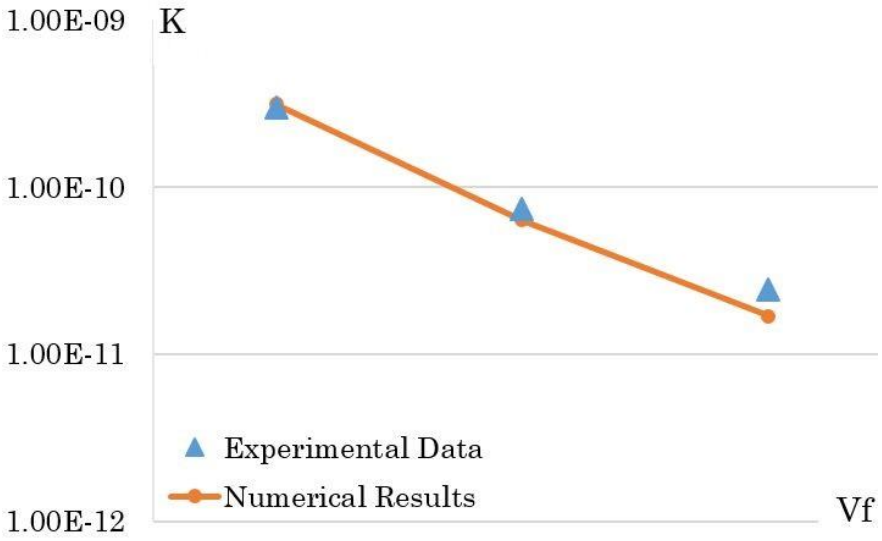

Figure 99 Comparison between experimental and numerical weft permeability values of TG-15-N after adding fibers

6.4.4 L14012 "fabric 7" results

Table 66, Figure 100 and Figure 101 show a comparison between numerical and experimental values of warp and weft permeability of L14012 at different fiber volume fraction. For the plain weave textile, the volume of mesopores is small and the bundles are interlaced, so no need to add fibers in mesopores.

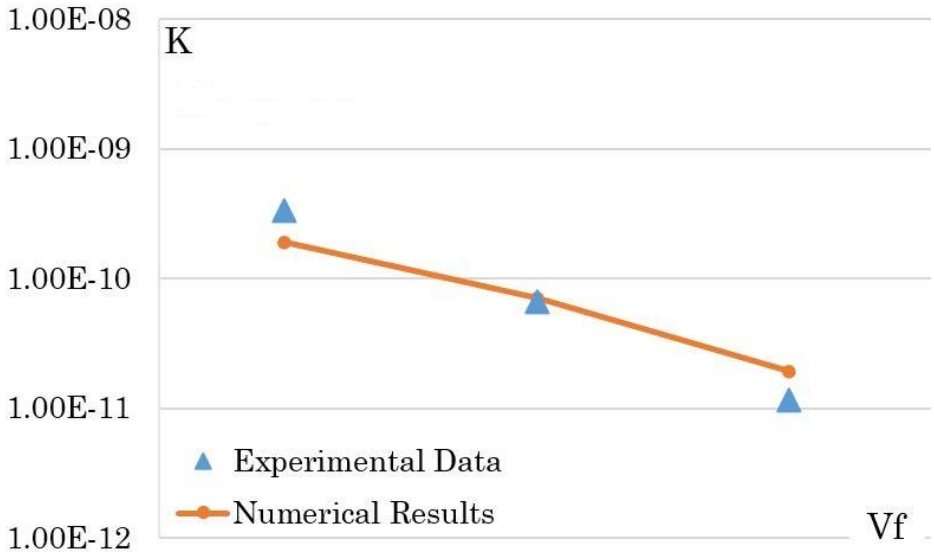

Figure 100 Comparison between numerical and experimental warp permeability results of L14012

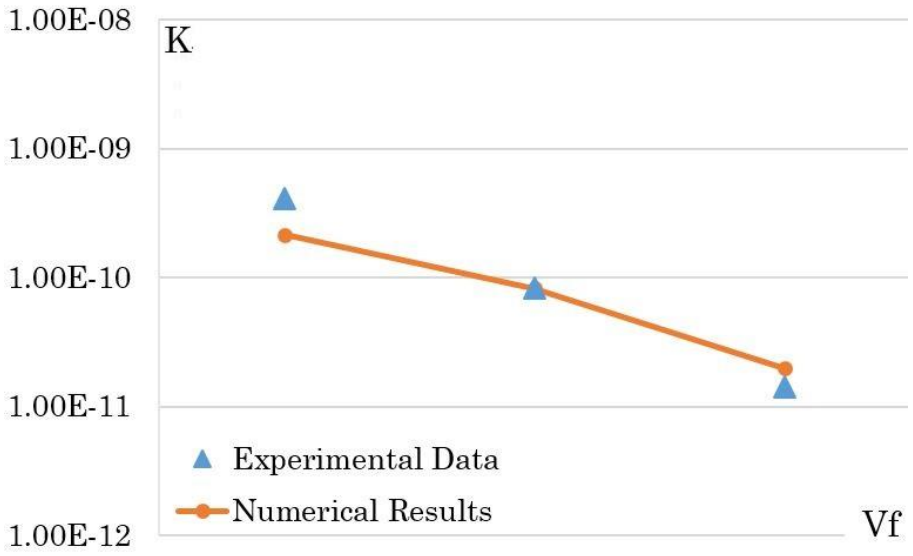

Figure 101 Comparison between numerical and experimental weft permeability results of L14012.

	L14012					
	$K_{0°}$			$K_{90°}$		
V_f	$k_{\exp}(m^2)$	$k_{\text{num}}(m^2)$	Error (%)	$k_{\exp}(m^2)$	$k_{\text{num}}(m^2)$	Error (%)
V_{f1}	$3.41E^{-10}$	$1.9E^{-10}$	-44.1	$4.08E^{-10}$	$2.16E^{-10}$	-47
V_{f2}	$6.65E^{-11}$	$7.12E^{-11}$	7.06	$8.26E^{-11}$	$8.31E^{-11}$	-0.57
V_{f3}	$1.14E^{-11}$	$1.93E^{-11}$	69	$1.43E^{-11}$	$1.98E^{-11}$	38.37

Table 66 Comparison between experimental and numerical warp and weft permeability values of L14012

6.4.5 C-weave-200P "fabric 8" results

Table 67, Figure 102 and Figure 103 show a comparison between numerical and experimental values of warp and weft permeability for Carbon fabric at different fiber volume fraction.

	Cweave200P					
	$K_{0°}$			$K_{90°}$		
Vf	$k_{\exp}(m^2)$	$k_{\text{num}}(m^2)$	Error (%)	$k_{\exp}(m^2)$	$k_{\text{num}}(m^2)$	Error (%)
V_{f1}	$3.03E^{-11}$	$1.62E^{-11}$	-46.5	$1.34E^{-11}$	$1.44E^{-11}$	7.28
V_{f2}	$6.66E^{-12}$	$3.42E^{-12}$	-48.5	$4.16E^{-12}$	$2.92E^{-12}$	-29.8
V_{f3}	$1.68E^{-12}$	$7.99E^{-13}$	-52.4	$9.51E^{-13}$	$1.08E^{-12}$	13.53

Table 67 Comparison between experimental and numerical warp and weft permeability values of Cweave200P

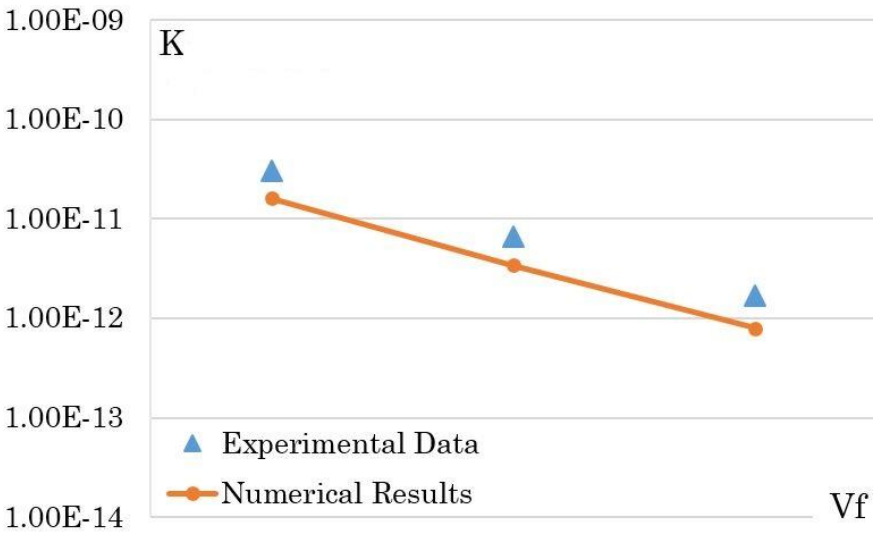

Figure 102 Comparison between numerical and experimental warp permeability results of Cweave200P

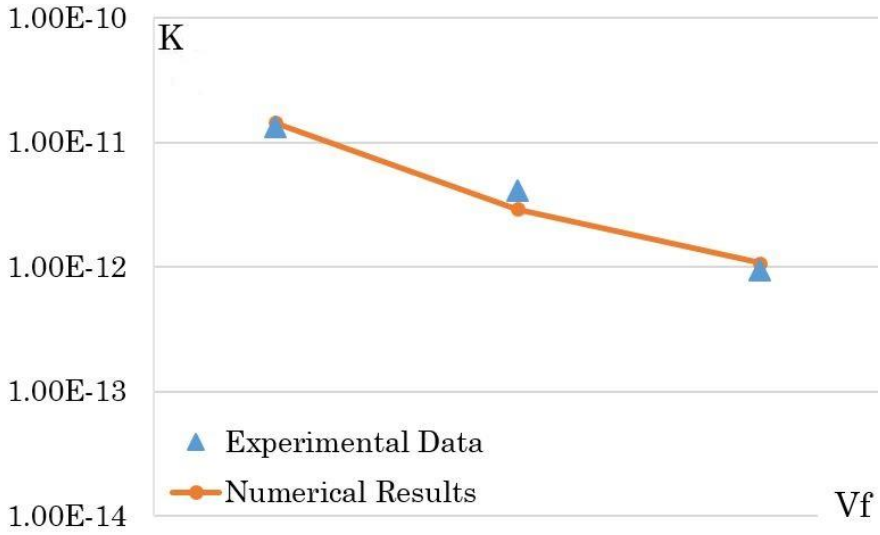

Figure 103 Comparison between numerical and experimental weft permeability results of Cweave200P

6.5 Conclusion

This work has treated the problem of permeability prediction which is essential for composite manufacturing to prevent voids' formation that causes different types of defects in the manufactured part. Using a numerical FE modeling, the warp and weft permeability values ($K_{0°}$ and $K_{90°}$) of NCF and plain-weave at different fiber volume fractions have been predicted. Moreover, adding fibers between bundles for stitched

NCFs is a pragmatic assumption that presents a more realistic simulation, leading to an improvement in permeability prediction. The numerical results obtained from those simulations after adding fibers in mesopores were compared with experimental data and they had shown a good agreement. For plain-weave textiles, numerical simulations are realistic even without adding fibers in mesopores due to the small volume of those mesopores. Results obtained from those simulations were compared with experimental data and they had shown a good agreement with an average of the absolute errors being 34.48% and 33.03% in Glass and Carbon fabrics respectively. Finally, the FE modeling done in this study has proved its efficiency, where it could be used for modeling the permeability at different fiber volume fractions and different textiles in both warp and weft directions in a fast, and accurate way.

7 Chapter 7: Conclusion and perspective

Liquid Composite Molding serves to produce high performance composite parts. The great benefit is acquired when the process is well controlled in all its stages. The most critical step is the permeability determination. Indeed, an accurate, simple and quick evaluation of permeability represents the decisive step to perform filling simulations and optimize the injection strategy. These are the main reasons motivating this investigation.

7.1 Permeability and influencing factors

As a general conclusion, permeability value depends on a certain number of interconnected factors. Each one has its own influence on the final result. For example two fabrics having the same architecture but made of different materials have different permeability tensors. The main factors influencing permeability values can be summed as follows:

- Type of fabric
- Existence of a through-thickness yarn
- Fabric material
- Areal density
- Manufacturing parameters

The qualitative influence of the above mentioned parameters is discussed briefly. ***The type of fabric*** affects the permeability where a unidirectional fabric, per example "850.0445.80.0600" has a larger permeability along the longitudinal direction of the fiber bundles than in the other directions and through-thickness direction. On the other hand, a balanced NCF has nearby the same permeability values in the warp and weft directions. 3D orthogonal fabrics have a higher permeability than NCFs. While 2D weaved and 2.5D Interlock fabrics have in general low permeability values. Permeability is directly related to the size of the mesopores and micropores and the connection sequence between them. The volume of the mesopores has a strong influence on permeability. This geometric influence is affected by the channel distribution between the warp and weft directions, where the permeability increases with the mesopore size. The connection sequence between the mesopores and the micropores affects also permeability. When the mesopores are generally connected to each other, permeability increases. When the flow

is forced to pass from a mesopore to smaller mesopores or through micropores then permeability values decreases remarkably.

Through-thickness yarn size, materials and count number have two-sided effect: on one hand, these yarns create mesopore in the peripheral layers and enhance permeability; on the other hand, they represent an obstacle by deviating the flow through the micropores hence reduce permeability.

The influence of ***fabric material*** is observed in the change of filament radius were two fabrics of similar architecture, but different filament radius exhibit different permeability values. Carbon fibers, for example in fabric TC-67-N, has a smaller radius than glass fibers in the E-glass fabric TG-96-I.The carbon fabric is less permeable than the E-glass fabric.

When the ***areal density*** increases, the permeability of fabrics of similar architecture and same material increases. This is observed for the three fabrics NCFs, TG-09-N, TG-15-N and TG-33-N, for which the areal density increases and reciprocally permeability increases. The same observations hold for the two 3D orthogonal fabrics TG-54-N and TG-96-N.

Other factors may also influence permeability tensor, namely other ***parameters*** such as nesting or the sizing inside the bundles, the tension of the stitching fiber bundles and their filament radius have also an effect on the permeability.

7.2 Permeability evaluation

Each method to evaluate permeability has its own advantages, drawbacks and limitations. The summary recalls the conclusions of this work on the experimental, numerical and analytical methods reported in the scientific literature.

7.2.1 Experimental methods

Experimental measurements still face major problems regarding the in-plane permeability. These difficulties are due to many factors such as the measurement method, the measuring device; the preparation of the sample and operator skills. In order to measure the in-plane permeability, a well-known method was adopted in the second

benchmark exercise. The in-plane permeability components of eleven different fabrics were determined in this thesis for different fiber volume fractions. The types of fabrics consist of unidirectional stitched fabric, NCFs, plain weave fabrics, and 3D orthogonal weave fabrics. Consistent results were obtained following the method used in Benchmark II.

Concerning through-thickness permeability measurements, the method used is simple to conduct; stable and repeatable tooling cost is low. This method differs from traditional techniques in the measuring procedure, where an improvement was done; in which the pressure will be measured using the data acquisition unit at alternative velocities substituting the single point measurement (pressure-velocity). The transversal permeability of seven fabrics was performed for different kinds of textiles (unidirectional, bidirectional stitched fabrics and 2D and 3D woven fabrics) is performed. The measurements are repeatable and accurate for several different geometrical fabrics. However, experimental work implies time and money.

7.2.2 Numerical methods

Different numerical methods predict permeability. An ongoing effort is focused on developing new numerical methods because no existing ones yet provide results matching experiments. This study has treated the problem of permeability prediction by resolving Navier-Stokes equation inside the mesopores.

When evaluating the permeability of unidirectional fiber beds, a random unit cell representative of the real state of the fibrous reinforcement is chosen. Static mode simulations were performed in the longitudinal and transversal directions. On the other hand, transient mode simulations performed for a transversal flow gave results consistent with the static mode simulations.

When evaluating the permeability of textiles, static mode simulations method was used under the assumption that the bundles are impermeable. This simulation shows that a primary and a secondary path are available. Primary path are mesopores directed along the flow direction, whereas secondary paths are mesopores in the perpendicular direction. In the primary path, for high volume connected mesopores, the permeability is over-

estimated. Small fibers were introduced in the mesopores; these fibers reduced the faulty velocity in the primary paths, so that the error was reduced significantly when compared to experimental results.

7.2.3 Analytical methods

7.2.3.1 Analytical models applicable on unidirectional fiber beds

Much progress was done in the bibliography on the analytical evaluation of the microscopic permeability. More than twenty models were found in the scientific literature, some are applicable for longitudinal flows, others for transversal flows. However, these models show a large scatter when compared to each other. They can be evaluated by comparing the predicted permeability with results derived from other prediction methods. This analysis showed that Bahrami and Tamayol [44], Drummond and Tahir [39], Berdichevsky and Cai ISCM and unified (square) [31, 32] models exhibit a good agreement with this data for longitudinal microscopic permeability components. Concerning the transverse microscopic permeability prediction, Berdichevsky and Cai ISCM (hexagonal) [32], Gebart (hexagonal) [33], Drummond and Tahir (hexagonal) [39], and Kuwabara [36] models were selected to be the most accurate models.

7.2.3.2 Analytical models applicable on fabrics

Conversely, few models are applicable to fabrics. This is due to the difficulties facing the research in this domain. Even though, most of the developed models are either far from the target, have a limited range of application or are hard to be applied.

A predictive model has been developed to estimate the unidirectional permeability in the warp and weft directions for a family of non-crimped and 3D orthogonal fabrics. The implementation of this model requires the knowledge of basic geometrical parameters or the fabric architecture and information concerning the compaction of the preform. Those parameters include the dimension of the mesopores and the architecture of the fiber bundles, which are determined from pictures of the fabric and from the textile data sheet. In addition, information on the average volume of mesopores and fiber bundles are required and are calculated for different fiber volume fractions taking into account a

selected unit cell in the warp and weft directions. A good agreement is found between the experimental results and the predictions of the proposed analytical model.

7.3 Perspectives

The understanding of the physical phenomena governing the flow of a liquid in the mesopores and micropores of an engineering textile represents the major contribution of this thesis to the field of composites. The latest experimental methodology was applied to measure the permeability of thirteen fabrics to form a permeability data base. Analytical models were developed for two large families of fabrics. Their generalization to other architectures of woven reinforcements such as plain weave fabrics seems possible. However, since these fabrics are geometrically more complex especially because of nesting, it is important to develop geometrical models of these fabrics based on micro-tomography x-ray combined with image reconstruction technology. Numerical simulations could then be carried out in unit cells representative of real material.

Appendix

Appendix 1 Unidirectional permeability predicting models

$$K_T = \frac{r^2}{8V_f}\left(ln\frac{1}{V_f} - \frac{V_f^2 - 1}{V_f^2 + 1}\right) \quad \text{Eq.(1)}$$

$$K_L = \frac{r^2}{4V_f}\left(ln\frac{1}{V_f} - 1.5 + 2V_f - \frac{V_f^2}{2}\right) \quad \text{Eq.(2)}$$

$$K_T = \frac{r^2}{8V_f}\left(ln\frac{1}{V_f} - 1.5 + 2V_f - \frac{V_f^2}{2}\right) \quad \text{Eq.(3)}$$

$$K_T = \frac{r^2}{8V_f}\left(-lnV_f - 1.476 + 2V_f - 1.774{V_f}^2 + 4.076{V_f}^3 + O\left({V_f}^4\right)\right) \quad \text{Eq.(4)}$$

$$K_L = \frac{r^2}{4V_f}(-lnV_f - 1.476 + 2V_f - 0.5{V_f}^2) \quad \text{Eq.(5)}$$

$$K_{Tsquare} = \frac{r^2}{8V_f}\left(-lnV_f - 1.476 + \frac{2V_f - 0.796{V_f}^2}{1 + 0.489V_f - 1.605{V_f}^2}\right) \quad \text{Eq.(6)}$$

$$K_{Thexagonal} = \frac{r^2}{8V_f}\left(-lnV_f - 1.497 + 2V_f - \frac{{V_f}^2}{2} - 0.739{V_f}^4 + \frac{2.534{V_f}^5}{1 + 1.2758V_f}\right) \quad \text{Eq.(7)}$$

$$\mathrm{K_T} = 4\mathrm{r}^2\,\frac{0.0152(1 - \mathrm{V_f})^{5.1}\pi}{\mathrm{V_f}} \quad \text{Eq.(8)}$$

$$K_T = \frac{r^2\left(\sqrt{\frac{V_a}{V_f}} - 1\right)^3}{4C\left(\sqrt{\frac{V_a}{V_f}} + 1\right)} \quad \text{Eq.(9)}$$

V_a=0.76-0.82; C=0.2 Carmen- Kozeny constant

$$K_L = \frac{8r^2}{c}\frac{(1-V_f)^3}{V_f^2} \quad \text{Eq.(10)}$$

$$K_T = r^2 * C_1\left(\sqrt{\frac{V_{f\,max}}{V_f}} - 1\right)^{5/2} \quad \text{Eq.(11)}$$

Fiber arrangement	$\mathbf{C_1}$	$\mathbf{V_{f\,max}}$	c
Quadratic	$\frac{16}{9\pi\sqrt{2}}$	$\frac{\pi}{4}$	57
Hexagonal	$\frac{16}{9\pi\sqrt{6}}$	$\frac{\pi}{2\sqrt{3}}$	53

$$K_L = \frac{r^2}{{V_f}^m} e^{(b+c*V_f)} \quad \text{Eq.(12)}$$

$$K_L = \frac{r^2}{{V_f}^m} e^{(b+c*V_f)} \quad \text{Eq.(13)}$$

Where :

$a = 0.244 + 2(0.907 - V_a)^{1.229}$, $n = 2.051 + 0.381{V_a}^{4.472}$,

$b = 5.43 - 18.5V_a + 10.7{V_a}^2$, $c = -4.27 + 6.16V_a - 7.1{V_a}^2$,

$m = -1.74 + 7.46V_a - 3.72{V_a}^2$

$$K_L = 0.211r^2\left((V_a - 0.605)\left(\frac{0.907V_f}{V_a}\right)^{(-0.181)} * \left(\frac{1-0.907V_f}{V_a}\right)^{(2.66)} + 0.292(0.907 - V_a)(V_f)^{(-1.57)}(1-V_f)^{(1.55)}\right) \quad \text{Eq.(14)}$$

$$K_T = 0.229r^2\left(\frac{1.814}{V_a} - 1\right)\left(\frac{\left(1 - \sqrt{\frac{V_f}{V_a}}\right)}{\sqrt{\frac{V_f}{V_a}}}\right)^{2.5} \quad \text{Eq.(15)}$$

$Va = 0.9069\ if\ fiber\ arrangement\ is\ Hexagonal$

$V_a = 0.7854\ if\ fiber\ arrangement\ is\ quadratic.$

$$K_T = 16r^2\frac{16r^2}{9\pi\sqrt{2}}\left(\sqrt{\frac{\pi}{4V_f}} - 1\right)^{\frac{5}{2}} \quad \text{Eq.(16)}$$

$$K_T = 4r^2\frac{(1-V_f)^3(0.7854 - V_f)}{31{V_f}^{1.3}} \quad \text{Eq.(17)}$$

$$K_T = \frac{r^2 * (1-L^2)^2}{3\sqrt{3}L^3}\left(\frac{\left(3L\ tan^{-1}\left(\sqrt{\frac{1+L}{1-L}}\right)\right)}{\sqrt{1-L^2} + {L^2}/{2} + 1}\right)^{-1} \quad where\ L = \sqrt{\left(\frac{2\sqrt{3}}{\pi}\right)V_f} \quad \text{Eq.(18)}$$

$$K_L = \frac{r^2(1-V_f)^2(3.142 - 2.157V_f)}{48(1-V_f)^2} \quad \text{Eq.(19)}$$

$$K_T = \frac{r^2\pi(1-L)\left(1-\sqrt{L}\right)^2}{24(L)^{1.5}} \quad \text{Eq.(20)}$$

$L = 2.2 * {V_f}^2 - 1.22V_f + 0.56 \qquad if\ V_f \geq 0.5$

$L = V_f \qquad if\ V_f < 0.5$

$$K_L = \frac{r^2}{4V_f}\left(-1.479 - ln\frac{1}{V_f} + 2V_f - \frac{V_f^2}{2} - 0.0186 * V_f^4\right) \quad \text{Eq.(21)}$$

$$K_T = 4r^2 \left\{ \frac{12\left(\sqrt{\varphi}-1\right)}{\varphi\sqrt{\varphi}} \times \frac{\left(2-(1.274 * V_m - 0.274)\right)}{2} + \frac{18+12(\varphi-1)}{\sqrt{\varphi}(1-\varphi)^2} + \frac{27\pi\sqrt{\varphi}}{2(\varphi-1)^{5/2}} \right\}^{-1} \quad \text{Eq.(22)}$$

$\varphi = \frac{\pi}{4V_f}$ $V_m = 1 - V_f$

$$K_{Tsquare} = \frac{0.64r^2}{\sqrt{1-V_f}} \left(\frac{\pi}{4V_f} - 3\sqrt{\frac{\pi}{4V_f}} + 3 - \sqrt{\frac{4V_f}{\pi}} \right) \quad \text{Eq.(23)}$$

$$K_{Thexagonal} = \frac{0.64r^2}{\sqrt{1-V_f}} \left(\frac{\pi}{3\sqrt{3}V_f} - 3\sqrt{\frac{\pi}{3\sqrt{3}V_f}} + 3 - \sqrt{\frac{3\sqrt{3}V_f}{\pi}} \right) \quad \text{Eq.(24)}$$

Appendix 2 In-plane permeability measurements

Tables 1 to 11 show the raw data for unidirectional permeability measurements for the Fabric A-K. These tables show the permeability values for each Fabric, for each direction for a selected fiber volume fraction. Each experiment is repeated two or three times, on a selected V_f an average permeability value is calculated for each direction.

Fabric A	*Direction*	K_{exp1} (m^2)	K_{exp2} (m^2)	K_{exp3} (m^2)	$K_{average}$
V_f =45.99	0°	3.26E-11	2.70E-11	2.92E-11	2.96E-11
	45°	4.24E-11	4.39E-11		4.31E-11
	90°	5.65E-11	6.87E-11		6.26E-11
V_f =53.65	0°	9.66E-12	1.05E-11		1.01E-11
	45°	1.39E-11	1.51E-11		1.45E-11
	90°	2.49E-11	2.70E-11		2.60E-11
V_f =61.32	0°	5.91E-12	5.54E-12		5.73E-12
	45°	7.34E-12	7.20E-12		7.27E-12
	90°	1.35E-11	1.49E-11		1.42E-11

Appendix 2-Table 1 Unidirectional permeability measurements for Fabric A

Fabric B	*Direction*	K_{exp1} (m^2)	K_{exp2} (m^2)	$K_{average}$
V_f =40.15	0°	2.21E-10	2.56E-10	2.39E-10
	45°	2.80E-10	2.79E-10	2.79E-10
	90°	3.84E-10	3.03E-10	3.43E-10
V_f =48.17	0°	8.25E-11	7.85E-11	8.05E-11
	45°	7.96E-11	6.74E-11	7.35E-11
	90°	7.44E-11	6.04E-11	6.74E-11
V_f =56.2	0°	1.34E-11	1.46E-11	1.40E-11
	45°	1.50E-11	1.81E-11	1.65E-11
	90°	2.03E-11	1.53E-11	1.78E-11

Appendix 2-Table 2 Unidirectional permeability measurements for Fabric B

Fabric C	*Direction*	K_{exp1} (m^2)	K_{exp2} (m^2)	$K_{average}$
V_f =51.44	0°	1.95E-10	2.32E-10	2.32E-10
	45°	1.6E-10	1.6E-10	1.61E-10
	90°	2.76E-10	2.65E-10	2.71E-10
V_f =58.84	0°	5.1E-11	6.1E-11	5.59E-11
	45°	5.82E-11	6.92E-11	6.37E-11
	90°	9.57E-11	9.8E-11	9.68E-11
V_f =65.87	0°	2.37E-11	2.69E-11	2.53E-11
	45°	2.5E-11	2.54E-11	2.54E-11
	90°	4.53E-11	4.5E-11	4.53E-11

Appendix 2-Table 3 Unidirectional permeability measurements for Fabric C

Fabric D	*Direction*	K_{exp1} (m^2)	K_{exp2} (m^2)	K_{exp3} (m^2)	$K_{average}$
V_f =44.94	0°	1.22E-10	1.39E-10	1.32E-10	1.31E-10
	45°	2.62E-10	2.54E-10		2.58E-10
	90°	8.1E-10	7.99E-10		8.05E-10
V_f =51.17	0°	7.93E-11	7.65E-11		7.79E-11
	45°	1.21E-10	1.24E-10		1.22E-10
	90°	3.02E-10	3.39E-10		3.21E-10
V_f =58.38	0°	3.40E-11	3.85E-11	3.78E-11	3.68E-11
	45°	4.25E-11	4.99E-11	5.19E-11	4.81E-11
	90°	1.12E-10	1.41E-10		1.26E-10

Appendix 2-Table 4 Unidirectional permeability measurements for Fabric D

Fabric E	*Direction*	K_{exp1} (m^2)	K_{exp2} (m^2)	$K_{average}$
V_f =49.84	0°	2.32E-10	2.57E-10	2.45E-10
	45°	5.22E-10	5.25E-10	5.24E-10
	90°	1.18E-09	1.12E-09	1.15E-09
V_f =54.32	0°	1.27E-10	1.03E-10	1.15E-10
	45°	1.92E-10	1.94E-10	1.93E-10
	90°	4.36E-10	4.12E-10	4.24E-10
V_f =62.7	0°	4.00E-11	3.98E-11	3.99E-11
	45°	5.57E-11	6.37E-11	5.97E-11
	90°	7.74E-11	8.81E-11	8.27E-11

Appendix 2-Table 5 Unidirectional permeability measurements for Fabric E

Fabric F	*Direction*	K_{exp1} (m^2)	K_{exp2} (m^2)	K_{exp3} (m^2)	$K_{average}$
V_f =54.58	0°	1.39E-10	1.33E-10		1.36E-10
	45°	2.18E-10	2.33E-10	2.26E-10	2.26E-10
	90°	6.15E-10	6.78E-10		6.47E-10
V_f =60.98	0°	7.01E-11	7.83E-11		7.42E-11
	45°	1.09E-10	8.55E-11		9.74E-11
	90°	1.70E-10	2.51E-10		2.10E-10
V_f =69.46	0°	7.86E-12	7.20E-12		7.53E-12
	45°	9.88E-12	9.58E-12		9.73E-12
	90°	1.48E-11	1.64E-11		1.56E-11

Appendix 2-Table 6 Unidirectional permeability measurements for Fabric F

Fabric G	*Direction*	K_{exp1} (m^2)	K_{exp2} (m^2)	$K_{average}$
Vf =52.83	0°	1.09E-10	9.90E-11	1.04E-10
	45°	1.31E-10	1.60E-10	1.46E-10
	90°	2.98E-10	3.65E-10	3.31E-10
Vf =59.02	0°	3.66E-11	2.92E-11	3.29E-11
	45°	4.62E-11	5.30E-11	4.96E-11
	90°	1.01E-10	1.00E-10	1.00E-10
Vf =67.23	0°	3.02E-12	2.96E-12	2.99E-12
	45°	2.56E-12	1.77E-12	2.56E-12
	90°	7.74E-12	9.56E-12	8.65E-12

Appendix 2-Table 7 Unidirectional permeability measurements for Fabric G

Fabric H	*Direction*	K_{exp1} (m^2)	K_{exp2} (m^2)	$K_{average}$
V_f =47.93	0°	3.01E-11	3.10E-11	3.06E-11
	45°	1.61E-11	1.56E-11	1.59E-11
	90°	1.38E-11	1.57E-11	1.47E-11
V_f =54.56	0°	1.24E-11	1.47E-11	1.35E-11
	45°	7.60E-12	7.45E-12	7.53E-12
	90°	7.54E-12	7.53E-12	7.54E-12
V_f =61.62	0°	2.62E-12	2.77E-12	2.7E-12
	45°	2.23E-12	2.26E-12	2.24E-12
	90°	3.49E-12	2.95E-12	3.22E-12

Appendix 2-Table 8 Unidirectional permeability measurements for Fabric H

Fabric I	*Direction*	K_{exp1} (m^2)	K_{exp2} (m^2)	$K_{average}$
V_f =45.59	0°	1.46E-11	1.82E-11	1.64E-11
	45°	1.50E-11	1.35E-11	1.43E-11
	90°	1.23E-11	1.21E-11	1.22E-11
V_f =52.1	0°	5.81E-12	6.61E-12	6.21E-12
	45°	6.53E-12	6.08E-12	6.30E-12
	90°	4.54E-12	4.84E-12	4.69E-12
V_f =64.87	0°	8.74E-13	8.74E-13	8.74E-13
	45°	1.08E-12	8.35E-13	9.57E-13
	90°	6.56E-13	7.02E-13	6.79E-13

Appendix 2-Table 9 Unidirectional permeability measurements for Fabric I

Fabric J	*Direction*	K_{exp1} (m^2)	K_{exp2} (m^2)	K_{exp3} (m^2)	$K_{average}$
V_f =44.51	0°	3.77E-10	3.06E-10		3.41E-10
	45°	3.01E-10	3.28E-10		3.15E-10
	90°	4.08E-10	3.63E-10		3.85E-10
V_f =53.41	0°	6.56E-11	6.75E-11		6.65E-11
	45°	6.10E-11	5.77E-11		5.94E-11
	90°	9.03E-11	7.49E-11		8.26E-11
V_f =62.31	0°	1.19E-11	1.10E-11	1.14E-11	1.14E-11
	45°	8.99E-12	9.00E-12		8.99E-12
	90°	1.51E-11	1.36E-11		1.43E-11

Appendix 2-Table 10 Unidirectional permeability measurements for Fabric J

Fabric K	*Direction*	K_{exp1} (m^2)	K_{exp2} (m^2)	K_{exp3} (m^2)	$K_{average}$
Vf =43.4	0°	3E-11	3.03E-11		3E-11
	45°	2.17E-11	1.89E-11		2E-11
	90°	1.34E-11	1.57E-11	1.34E-11	1.42E-11
Vf =52.08	0°	1.09E-11	9.69E-12		1E-11
	45°	3.73E-12	4.16E-12		3.95E-12
	90°	5.48E-12	4.16E-12		4.82E-12
Vf =60.76	0°	1.68E-12	1.68E-12		1.68E-12
	45°	1.2E-12	1.21E-12		1.21E-12
	90°	9.51E-13			9.51E-13

Appendix 2-Table 11 Unidirectional permeability measurements for Fabric K

Principal in-plane permeability values are shown in tables 12-13, tables show (K_1, $K_{2)}$ and β which represents the angle between the warp direction and biggest permeability value K_1. Figure 1 and 2 show the ellipse flow form based on table 12-13 results.

Fabric name	V_f (%)	K_1 (*$10^{-11}m^2$)	K_2 (*$10^{-11}m^2$)	β
Fabric A	V_{f1}= 45.99	6.32	2.94	84.6
	V_{f2}= 53.65	2.60	1.01	90.2
	V_{f3}= 61.32	1.46	0.56	97.5
Fabric B	V_{f1}= 39.83	30.311	25.493	87.5
	V_{f2}= 47.8	7.470	7.023	75.4
	V_{f3}= 55.76	1.801	1.387	78.6
Fabric C	V_{f1}= 49.48	55.960	16.096	131.1
	V_{f2}= 56.6	9.990	5.492	101.4
	V_{f3}= 63.36	5.385	2.324	112.2
Fabric D	V_{f1}= 44.94	83.875	12.984	84.9
	V_{f2}= 52.43	32.092	7.788	91.2
	V_{f3}= 59.99	13.527	3.609	99.3

Appendix 2-Table 12 Principal in-plane permeability values for Fabrics A-D

Fabric name	V_f (%)	K_1 (*$10^{-11}m^2$)	K_2 (*$10^{-11}m^2$)	β
Fabric E	V_{f1}= 51.26	129.518	23.887	80.2
	V_{f2}= 55.87	42.742	11.474	86.8
	V_{f3}= 64.48	8.446	3.950	82.1
Fabric F	V_{f1}= 52.83	64.662	13.600	89.9
	V_{f2}= 59.02	21.724	7.339	97.4
	V_{f3}= 67.23	1.567	0.748	93.6
Fabric G	V_{f1}= 54.08	33.662	10.360	94.8
	V_{f2}= 60.42	10.045	3.294	90.0
	V_{f3}= 68.82	3.767	0.236	118.3
Fabric H	V_{f1}= 47.93	3.486	1.388	162.3
	V_{f2}= 54.56	1.618	0.690	157.4
	V_{f3}= 61.62	0.277	0.190	179.0
Fabric I	V_{f1}= 46.21	1.500	1.193	19.1
	V_{f2}= 52.81	0.682	0.459	14.9
	V_{f3}= 65.76	0.090	0.066	18.3
Fabric J	V_{f1}= 44.51	43.059	31.176	123.9
	V_{f2}= 53.41	10.005	5.831	122.9
	V_{f3}= 62.31	2.212	0.889	127.3
Fabric K	V_{f1}= 43.4	3.046	1.571	3.9
	V_{f2}= 52.08	0.679	0.411	170.2
	V_{f3}= 60.76	0.168	0.095	179.7

Appendix 2-Table 13 Principal in-plane permeability values for Fabrics E-K

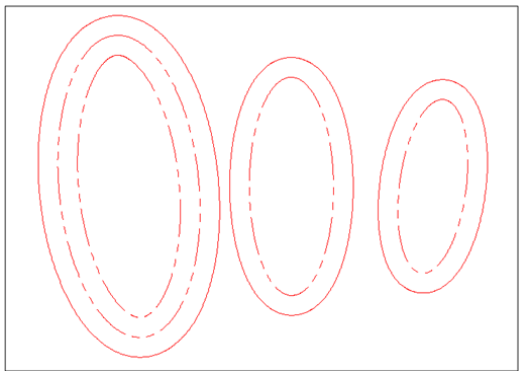

Fabric A

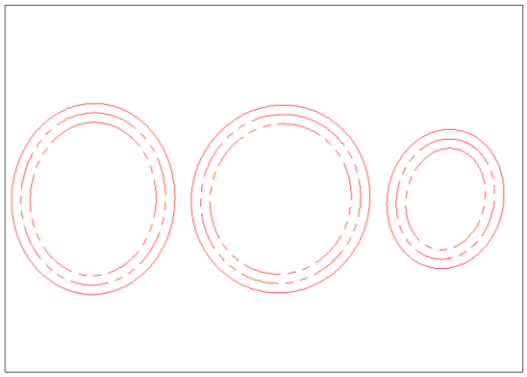

Fabric B

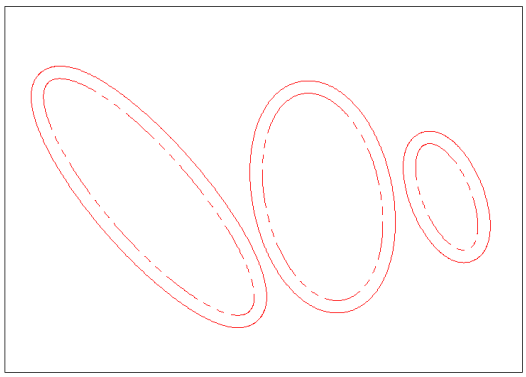

Fabric C

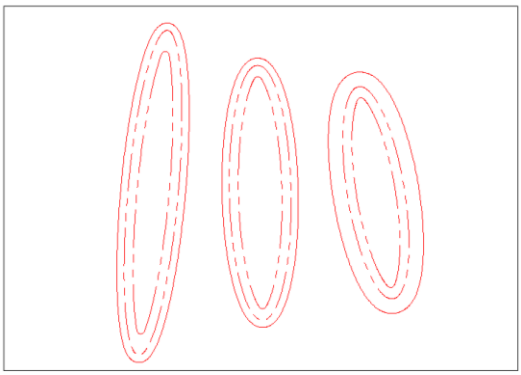

Fabric D

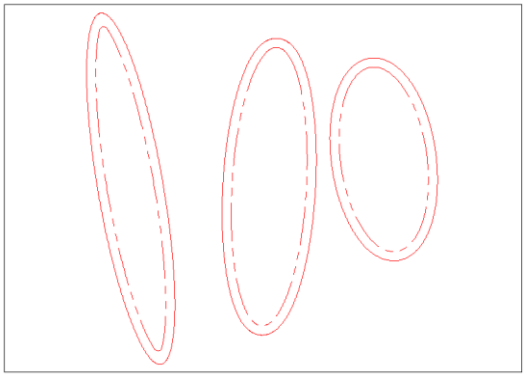

Fabric E

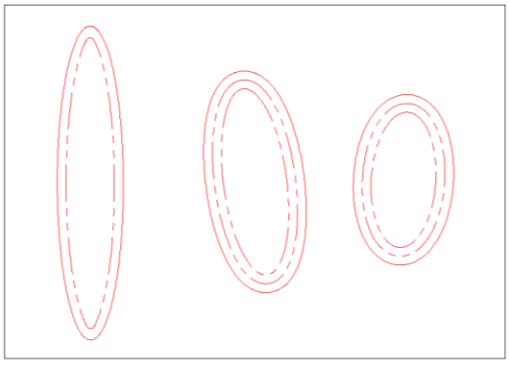

Fabric F

Appendix 2 Figure 1 Ellipse shape for an imposed injection, in each figure the right ellipse corresponds for

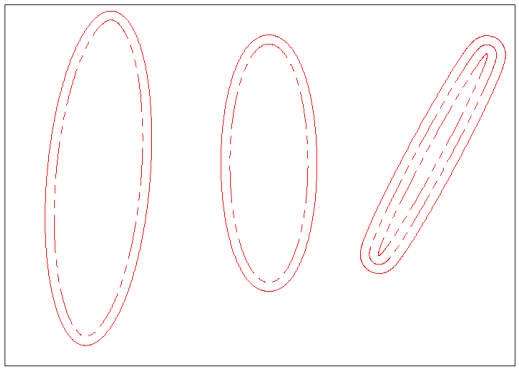

Fabric G

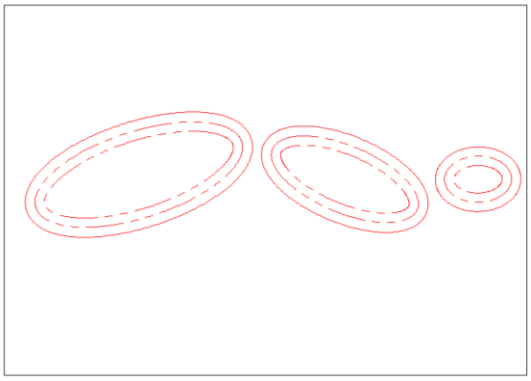

Fabric H

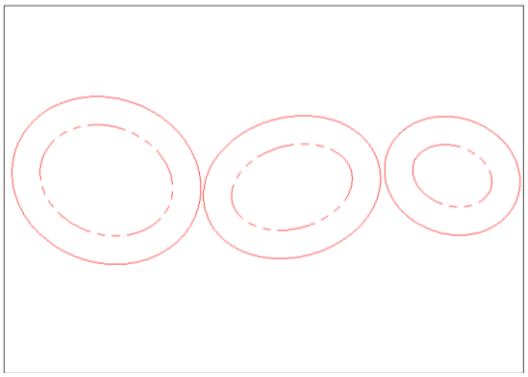

Fabric I

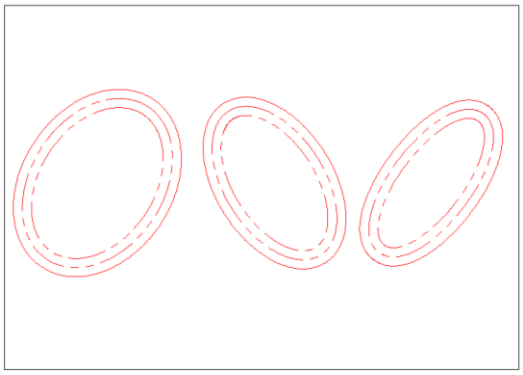

Fabric J

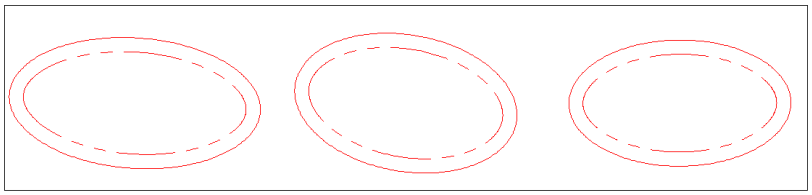

Fabric K

Appendix 2 Figure 2 Ellipse shape for an imposed injection, in each figure the right ellipse corresponds for the lower V_f. Fabrics E-K

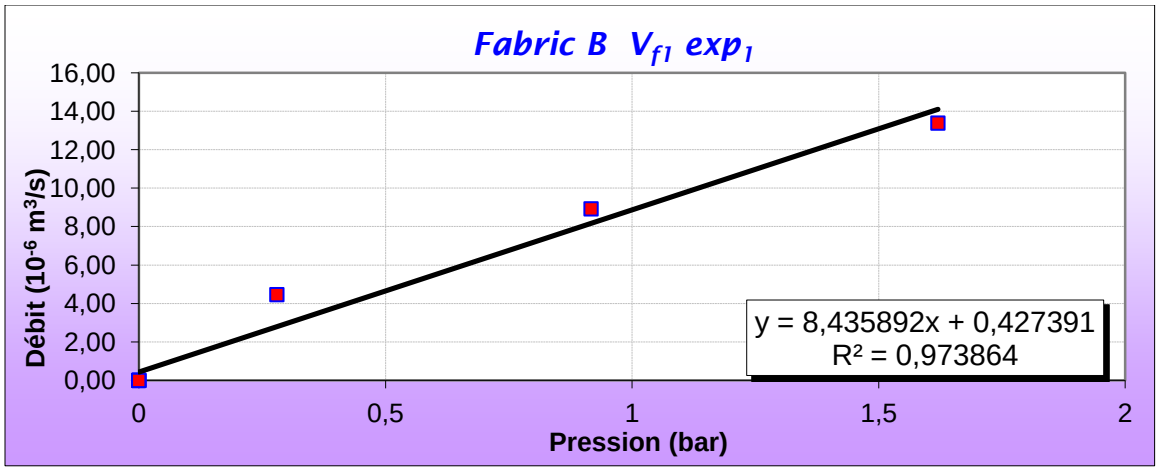

Appendix 2 Figure 3 Through-thickness permeability experiment Fabric B (V_{f1} exp_1).

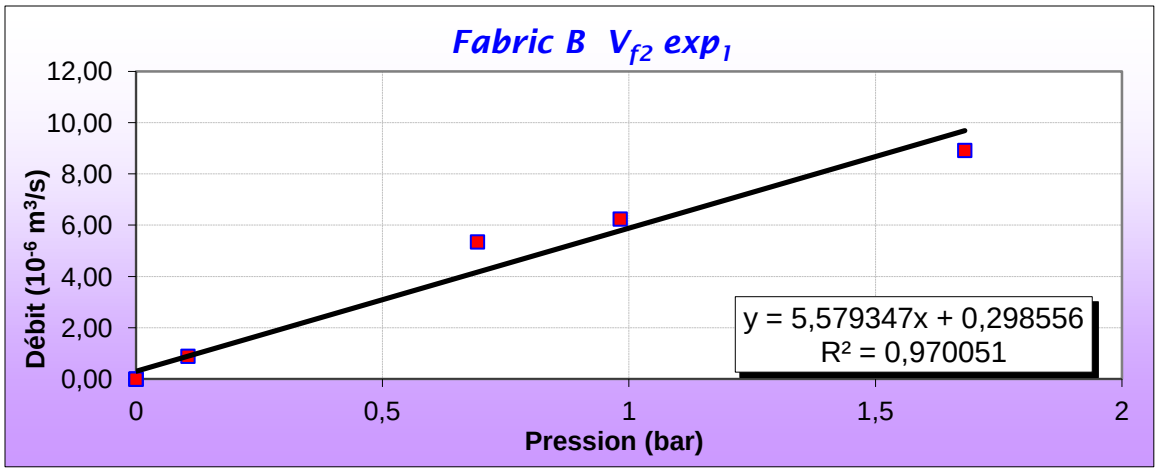

Appendix 2 Figure 4 Through-thickness permeability experiment Fabric B (V_{f2} exp_1).

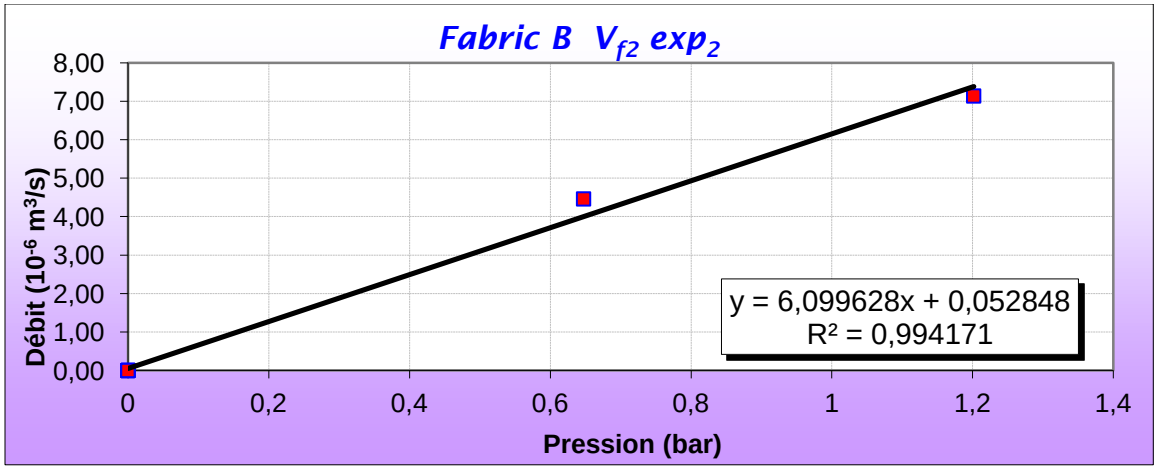

Appendix 2 Figure 5 Through-thickness permeability experiment Fabric B (V_{f2} exp_2).

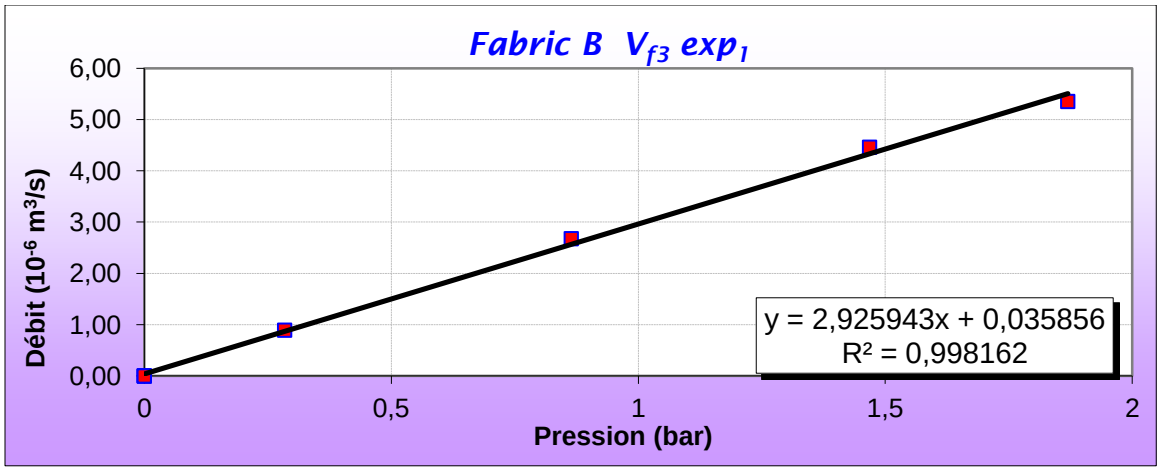

Appendix 2 Figure 6 Through-thickness permeability experiment Fabric B (V_{f3} exp_1).

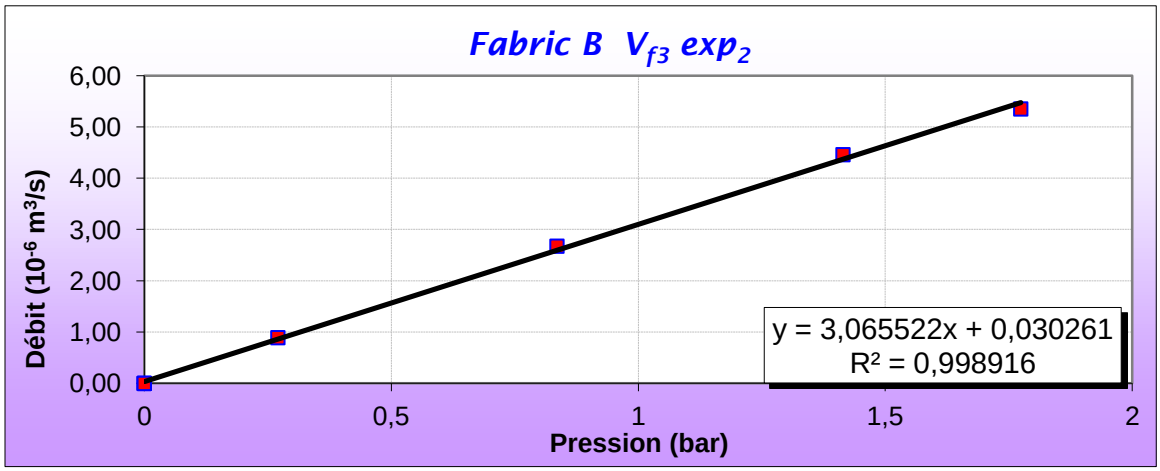

Appendix 2 Figure 7 Through-thickness permeability experiment Fabric B (V_{f3} exp_2).

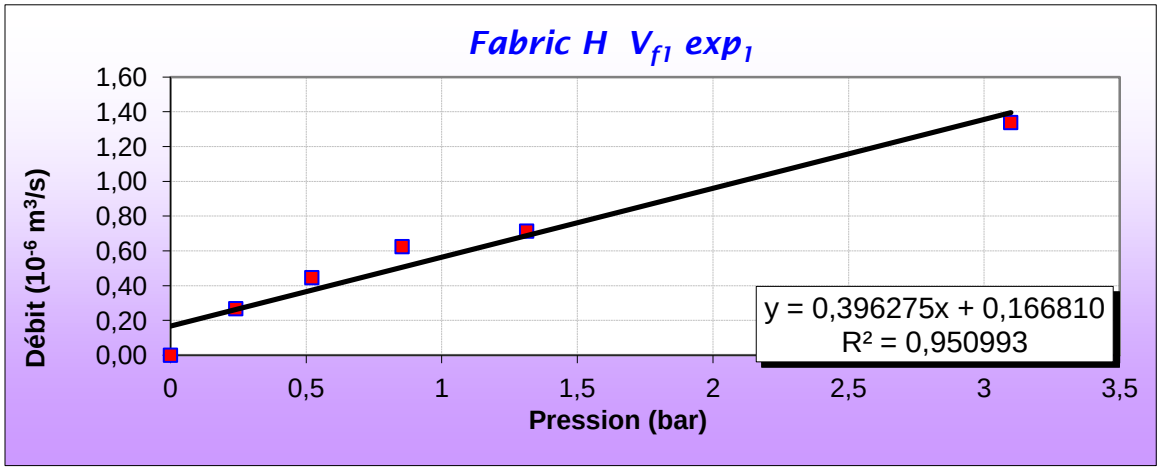

Appendix 2 Figure 8 Through-thickness permeability experiment Fabric H (V_{f1} exp_1).

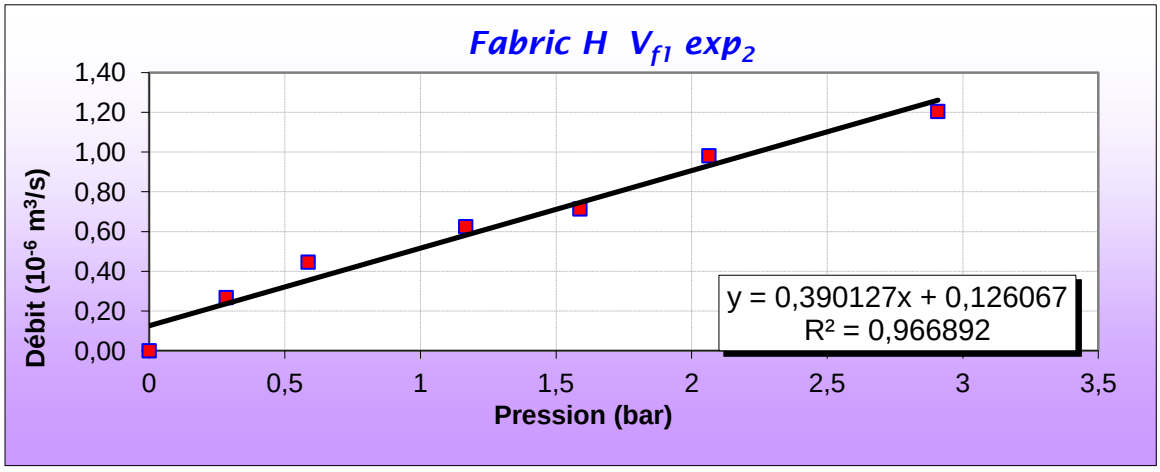

Appendix 2 Figure 9 Through-thickness permeability experiment Fabric H (V_{f1} exp_2).

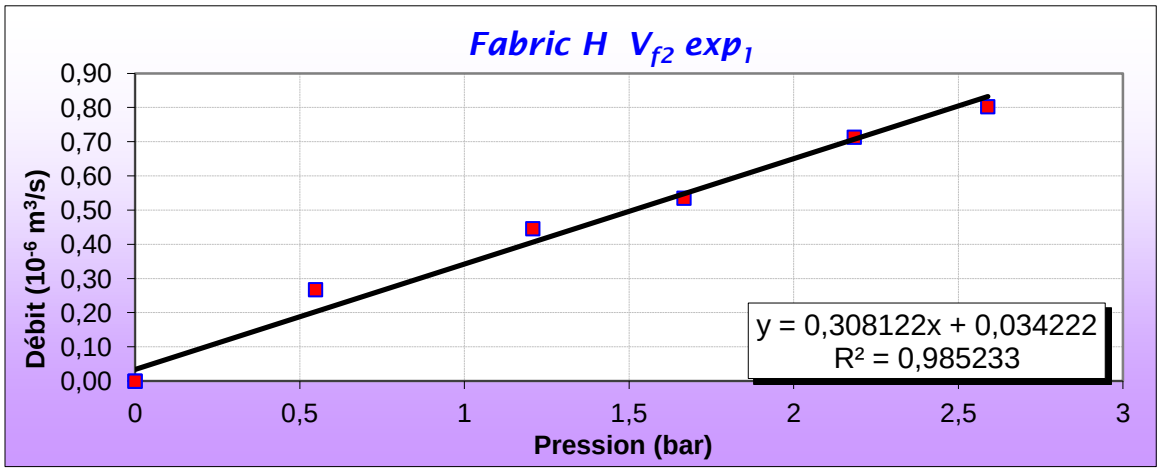

Appendix 2 Figure 10 Through-thickness permeability experiment Fabric H (V_{f2} exp_1).

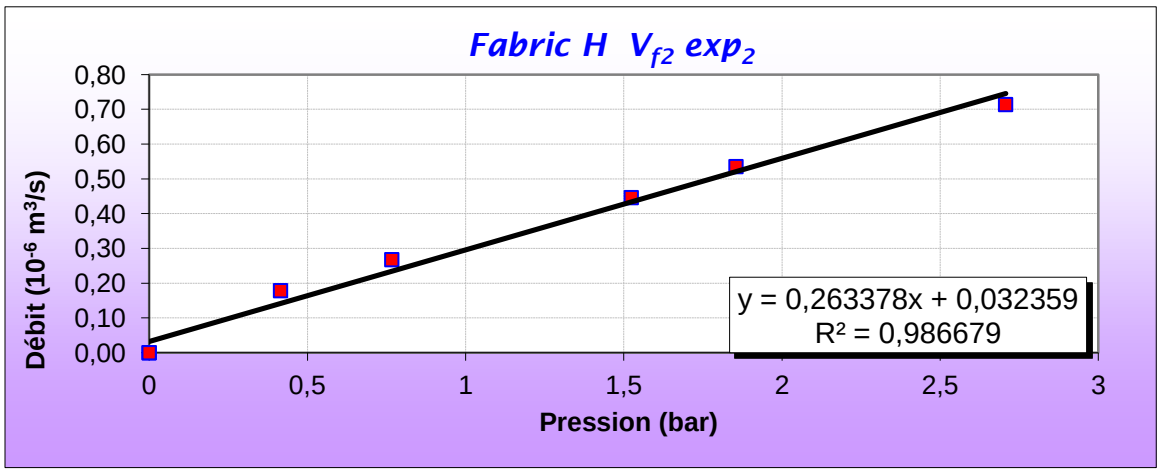

Appendix 2 Figure 11 Through-thickness permeability experiment Fabric H (V_{f2} exp_2).

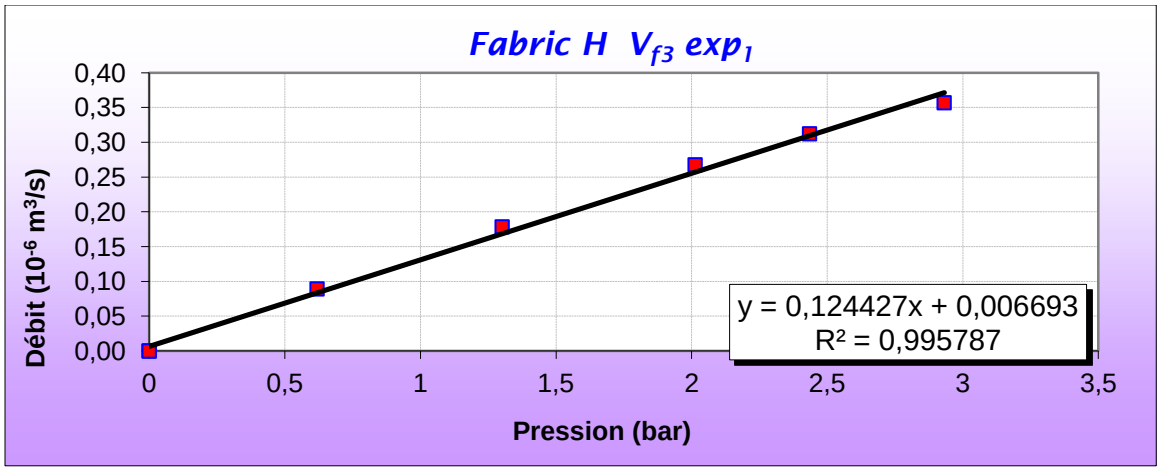

Appendix 2 Figure 12 Through-thickness permeability experiment Fabric H (V_{f3} exp_1).

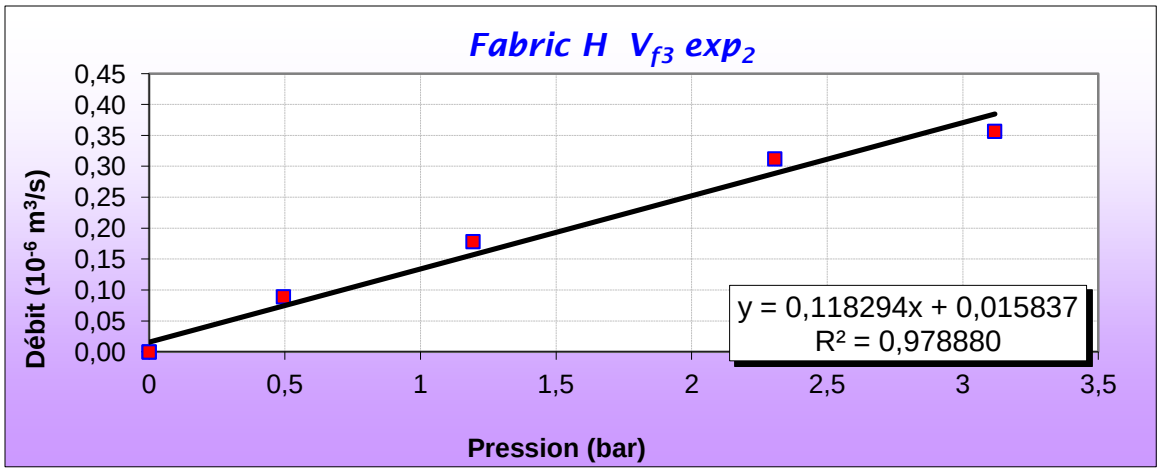

Appendix 2 Figure 13 Through-thickness permeability experiment Fabric H (V_{f3} exp_2).

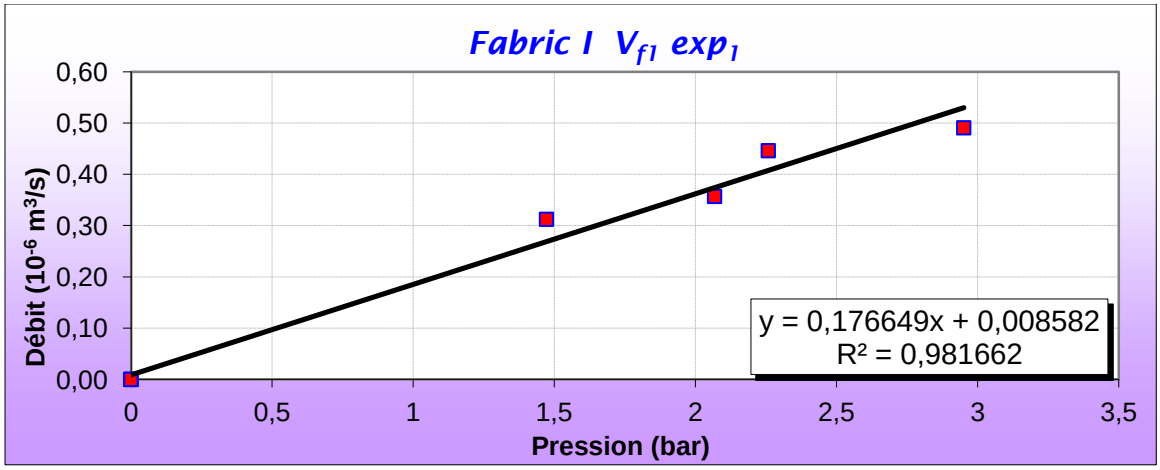

Appendix 2 Figure 14 Through-thickness permeability experiment Fabric I (V_{f1} exp_1).

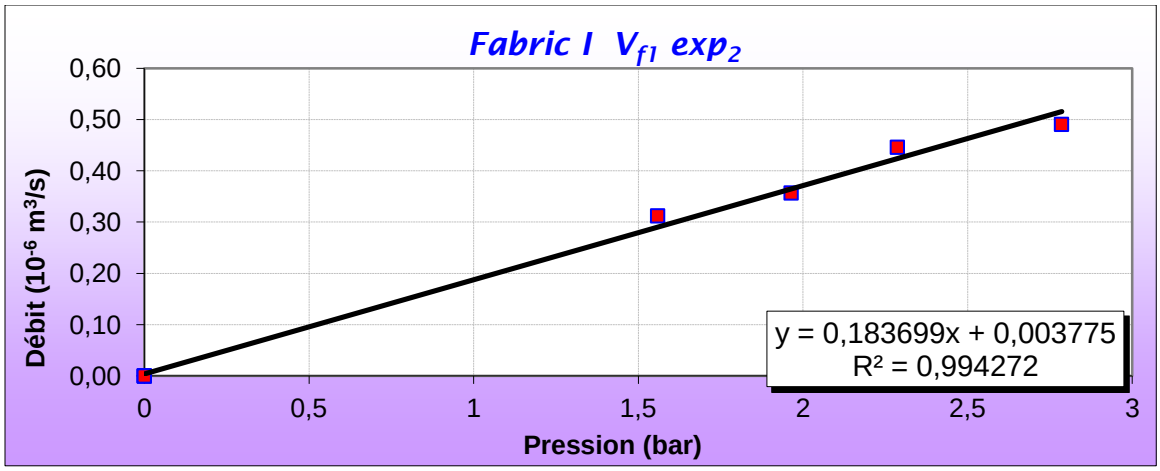

Appendix 2 Figure 15 Through-thickness permeability experiment Fabric I (V_{f1} exp_2).

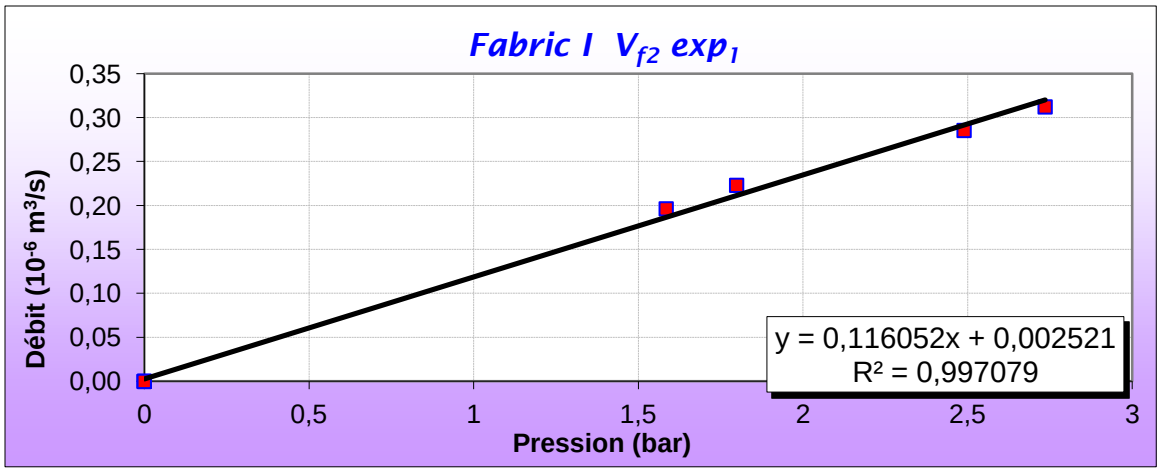

Appendix 2 Figure 16 Through-thickness permeability experiment Fabric I (V_{f2} exp_1).

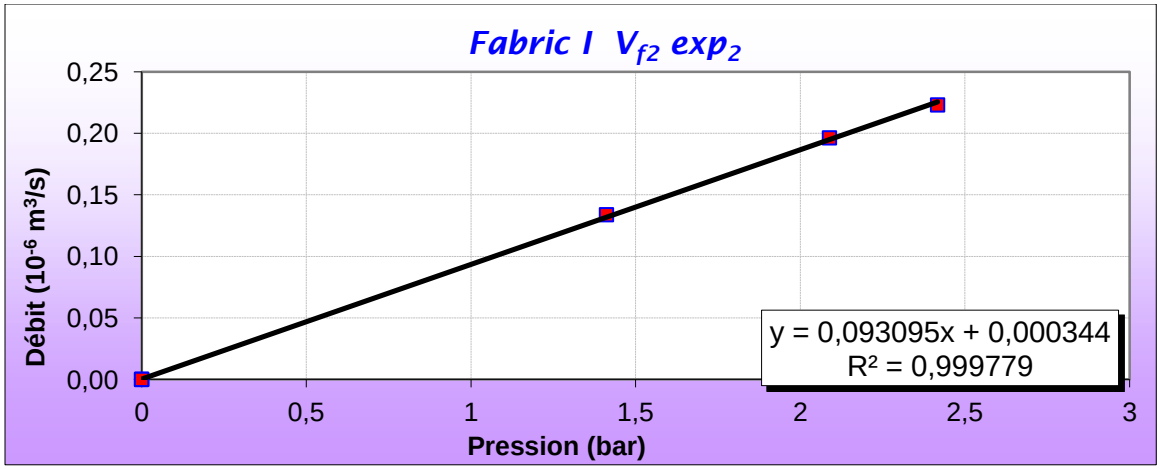

Appendix 2 Figure 17 Through-thickness permeability experiment Fabric I (V_{f2} exp_2).

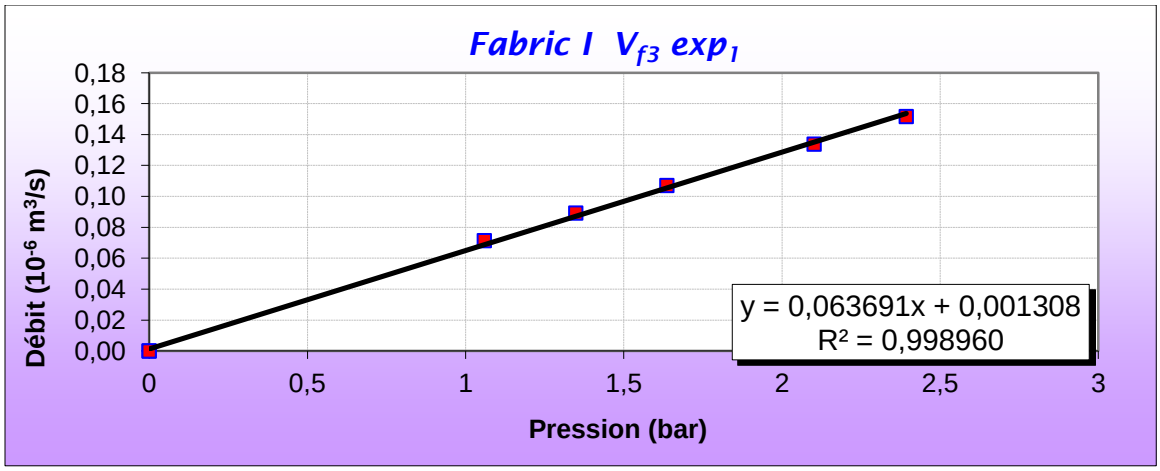

Appendix 2 Figure 18 Through-thickness permeability experiment Fabric I (V_{f3} exp_1).

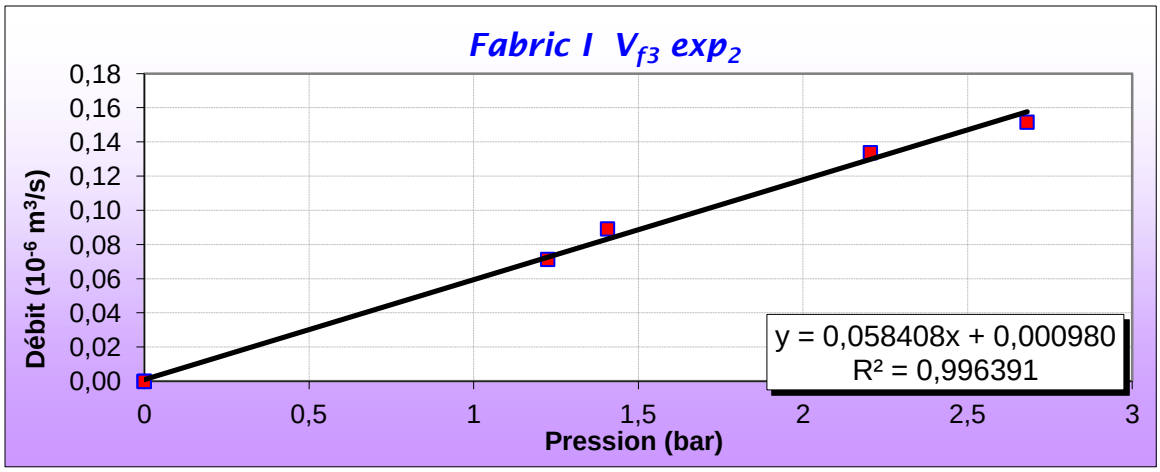

Appendix 2 Figure 19 Through-thickness permeability experiment Fabric I (V_{f3} exp_2).

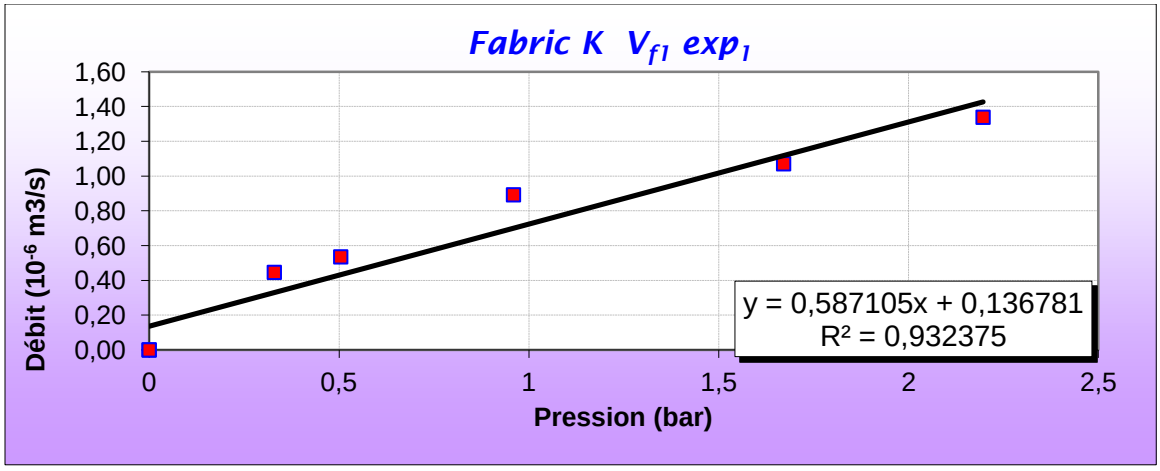

Appendix 2 Figure 20 Through-thickness permeability experiment Fabric K (V_{f1} exp_1).

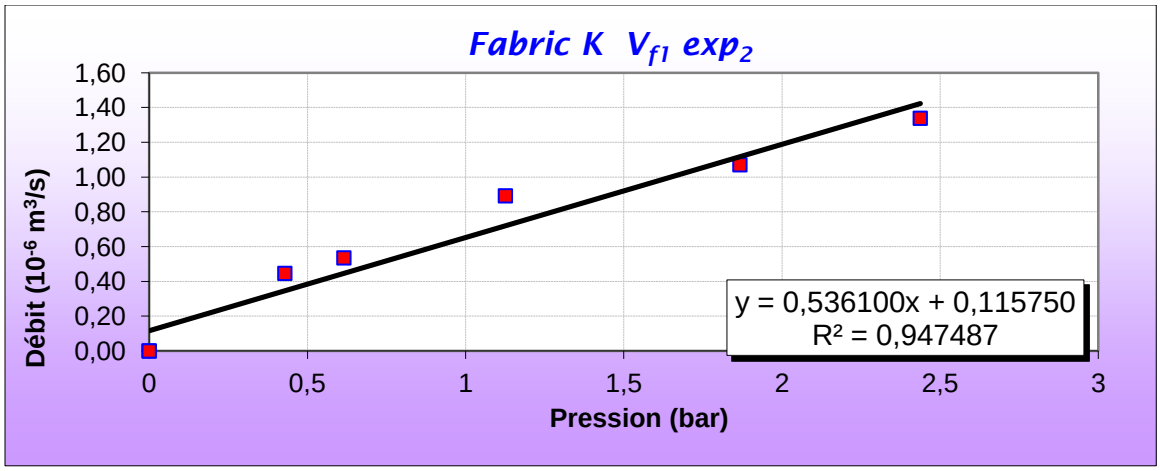

Appendix 2 Figure 21 Through-thickness permeability experiment Fabric K (V_{f1} exp_2).

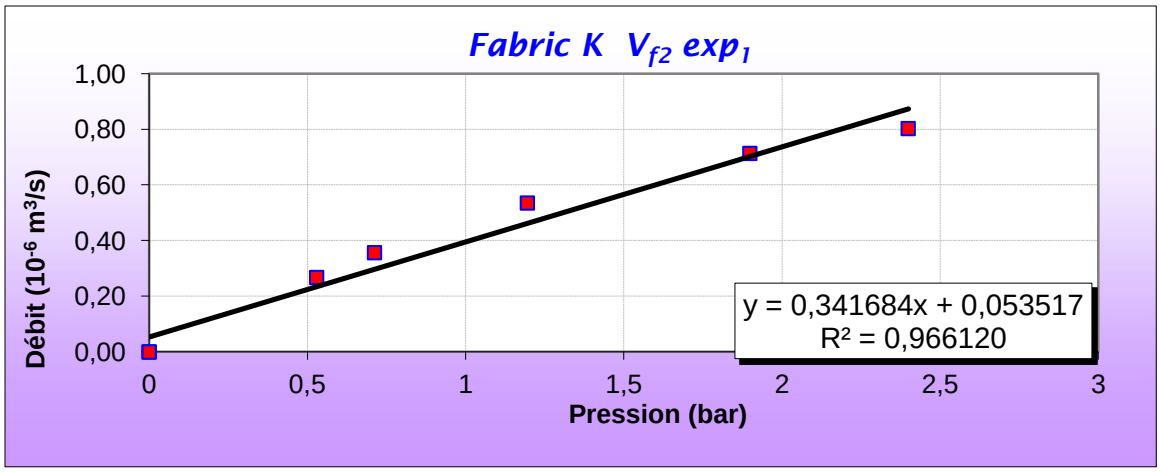

Appendix 2 Figure 22 Through-thickness permeability experiment Fabric K (V_{f2} exp_1).

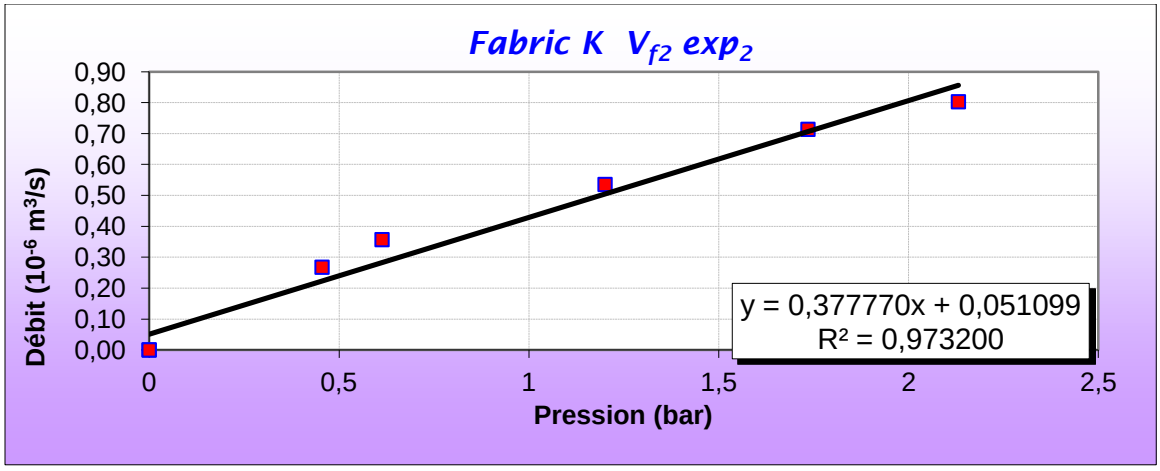

Appendix 2 Figure 23 Through-thickness permeability experiment Fabric K (V_{f2} exp_2).

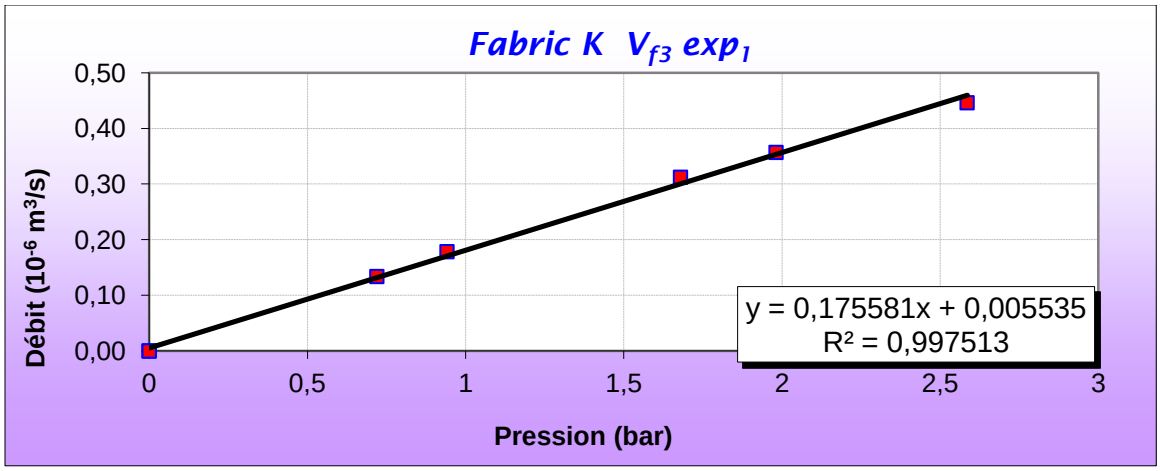

Appendix 2 Figure 24 Through-thickness permeability experiment Fabric K (V_{f3} exp_1).

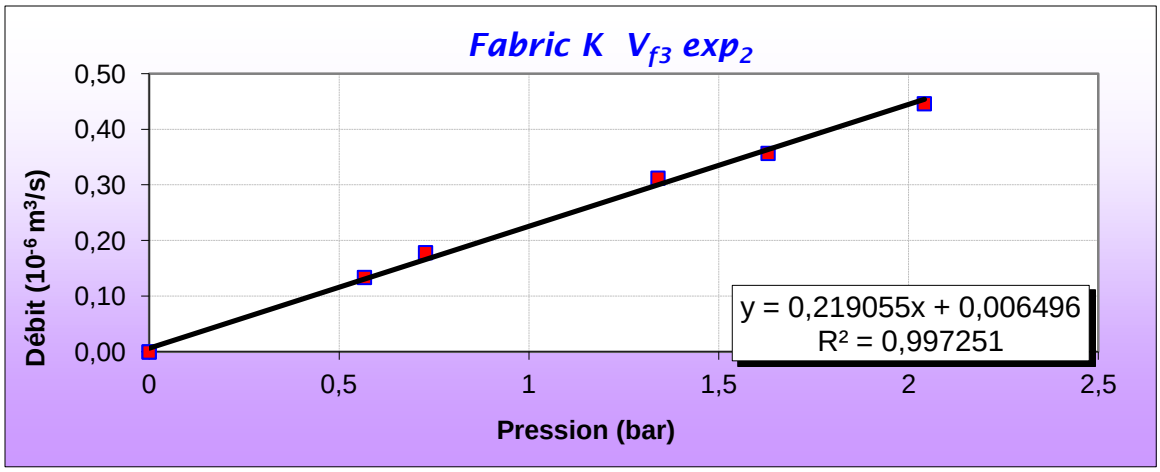

Appendix 2 Figure 25 Through-thickness permeability experiment Fabric K (V_{f3} exp_2).

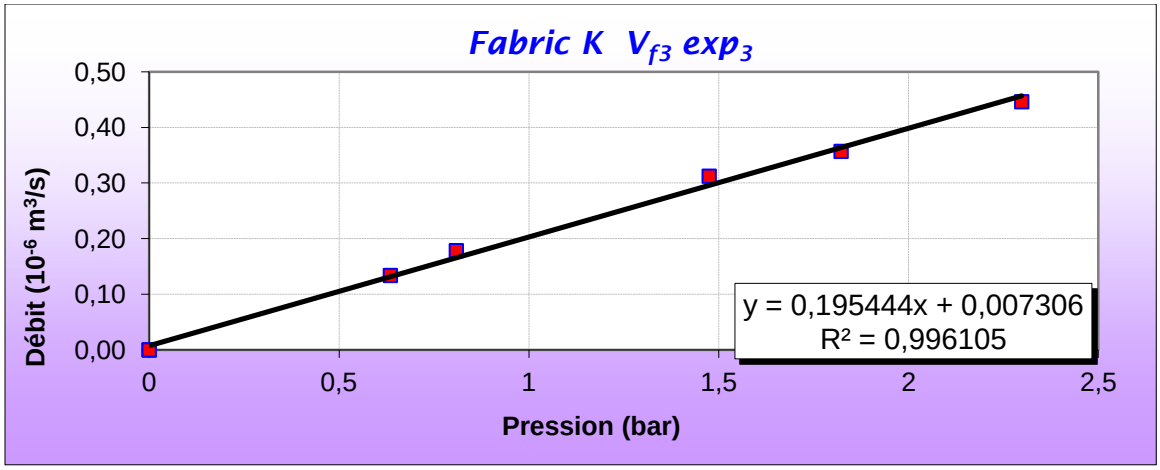

Appendix 2 Figure 26 Through-thickness permeability experiment Fabric K (V_{f3} exp_3).

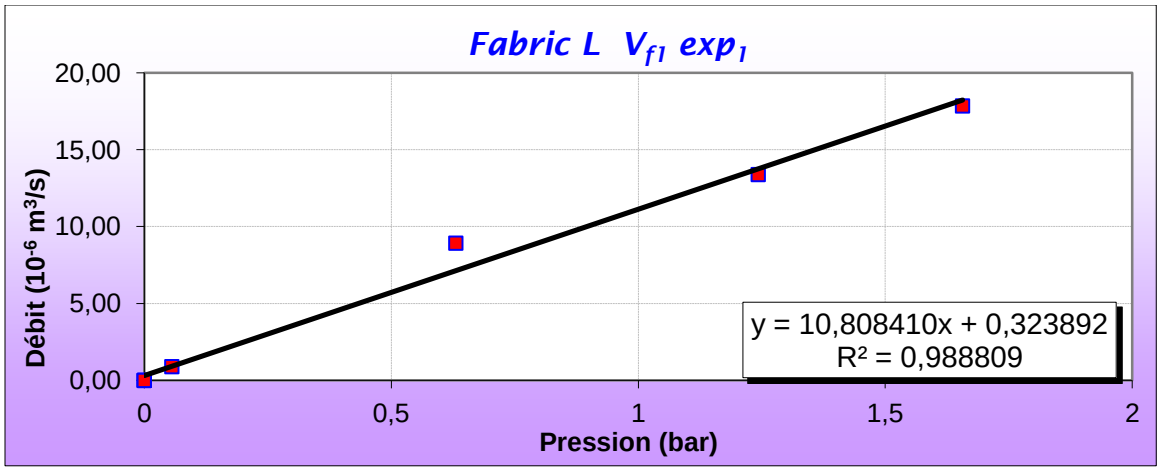

Appendix 2 Figure 27 Through-thickness permeability experiment Fabric L (V_{f1} exp_1).

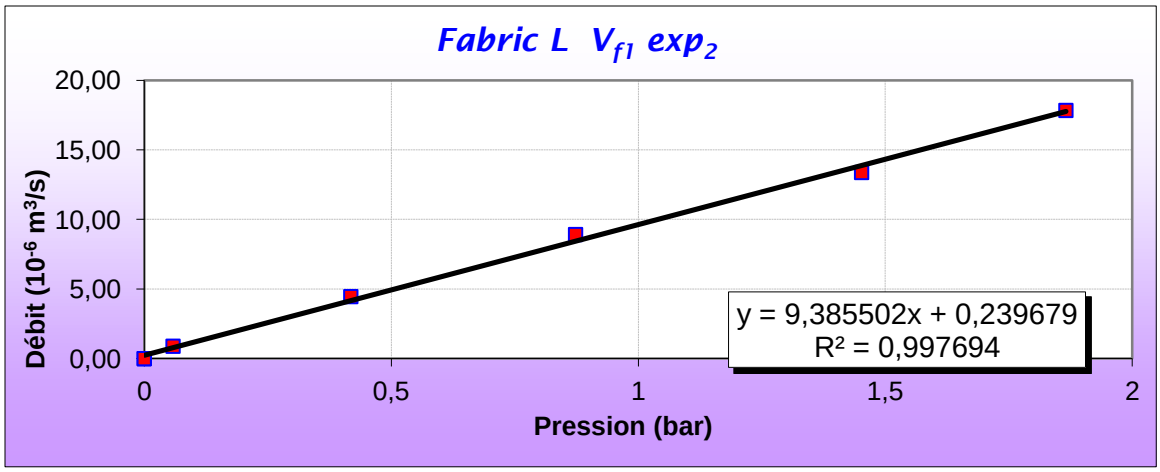

Appendix 2 Figure 28 Through-thickness permeability experiment Fabric L (V_{f1} exp_2).

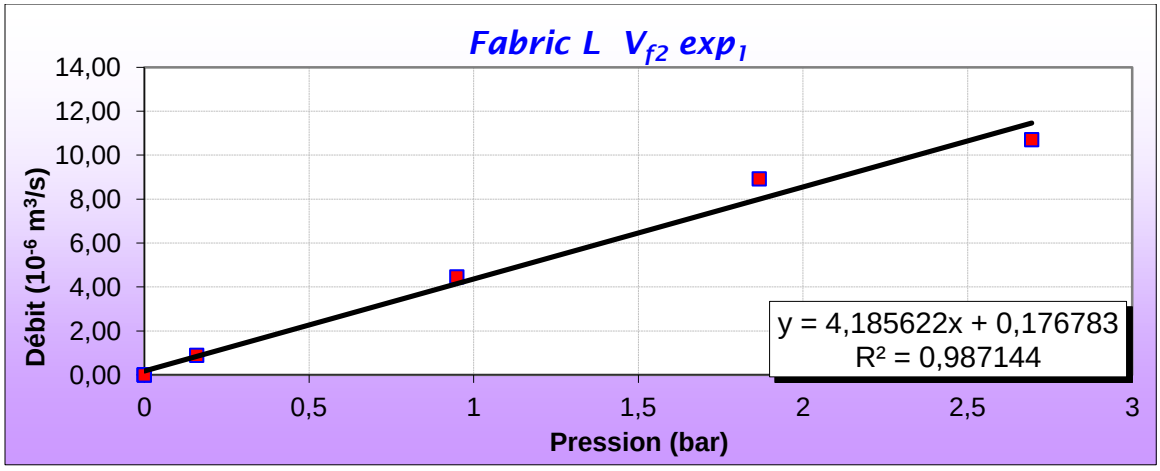

Appendix 2 Figure 29 Through-thickness permeability experiment Fabric L (V_{f2} exp_1).

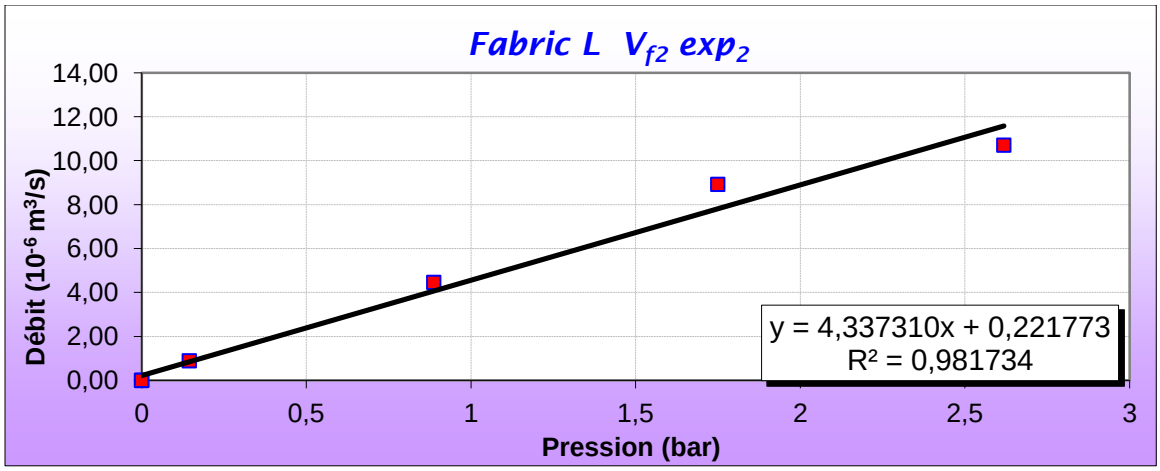

Appendix 2 Figure 30 Through-thickness permeability experiment Fabric L (V_{f2} exp_2).

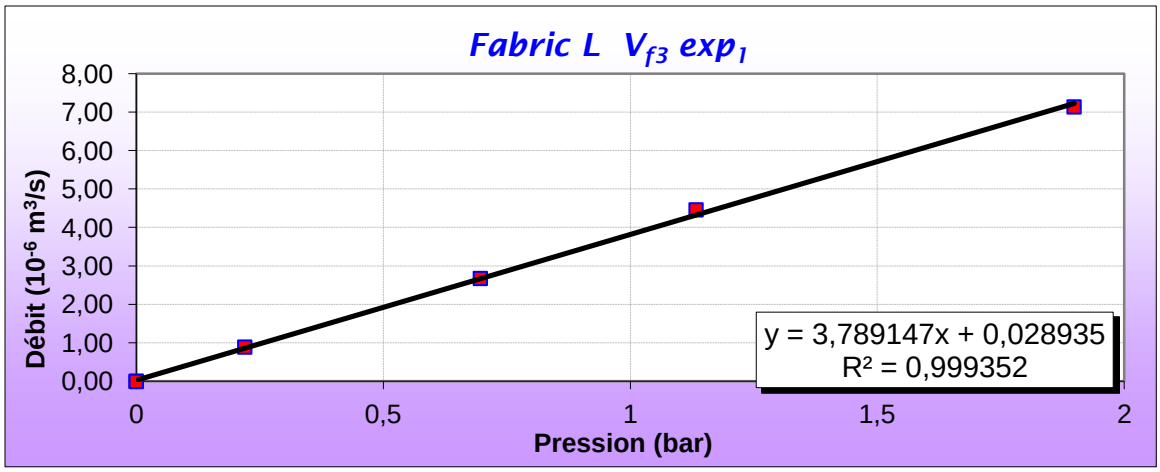

Appendix 2 Figure 31 Through-thickness permeability experiment Fabric L (V_{f3} exp_1).

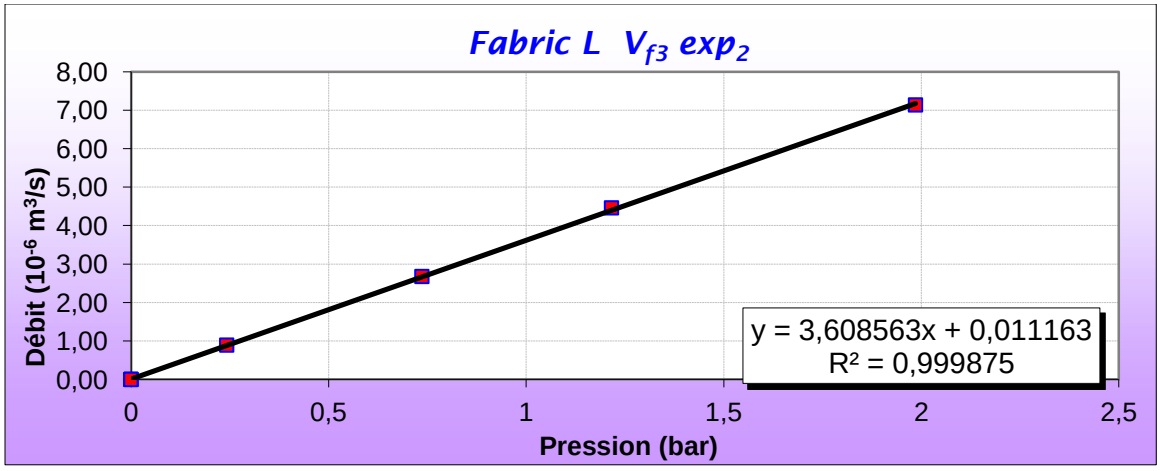

Appendix 2 Figure 32 Through-thickness permeability experiment Fabric L (V_{f3} exp_2).

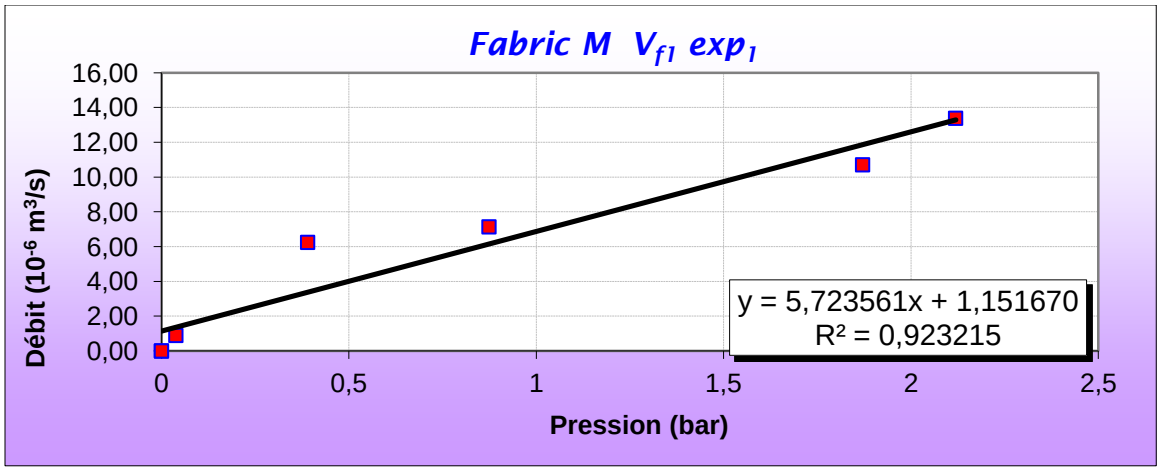

Appendix 2 Figure 33 Through-thickness permeability experiment Fabric M (V_{f1} exp_1).

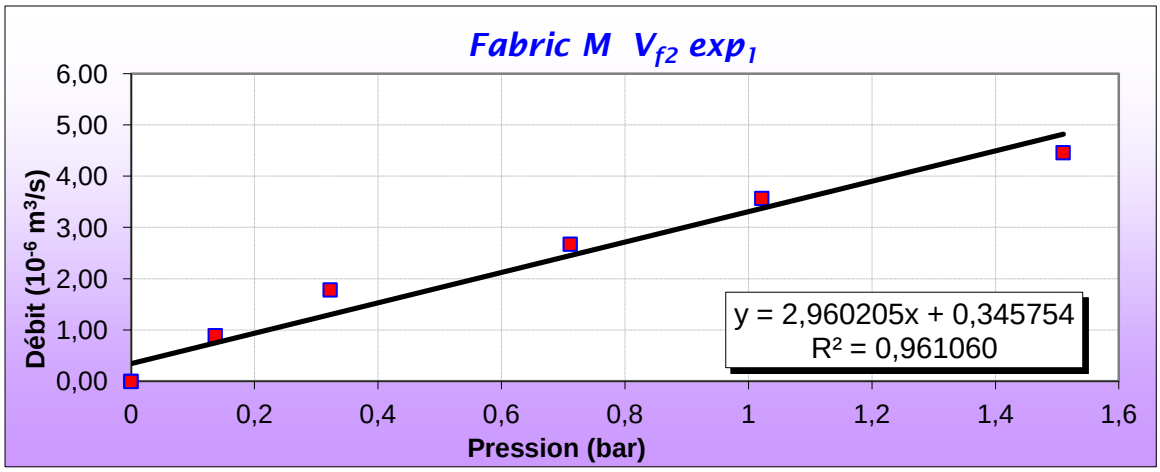

Appendix 2 Figure 34 Through-thickness permeability experiment Fabric M (V_{f2} exp_1).

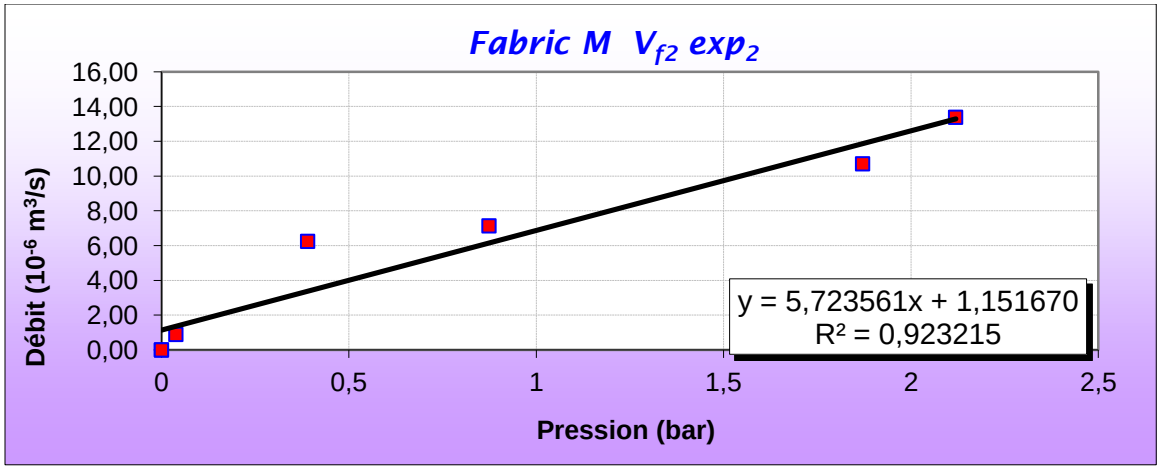

Appendix 2 Figure 35 Through-thickness permeability experiment Fabric M (V_{f2} exp_2).

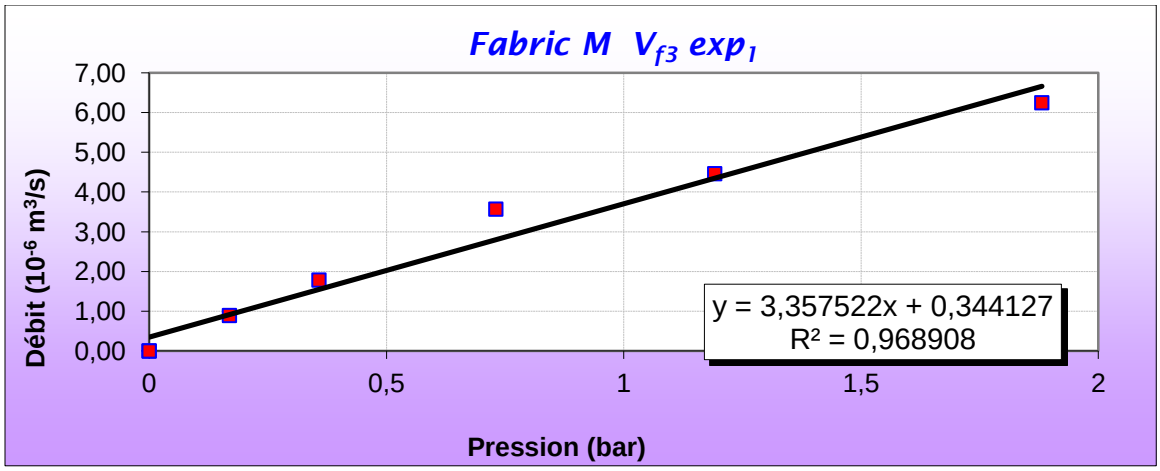

Appendix 2 Figure 36 Through-thickness permeability experiment Fabric M (V_{f3} exp_1).

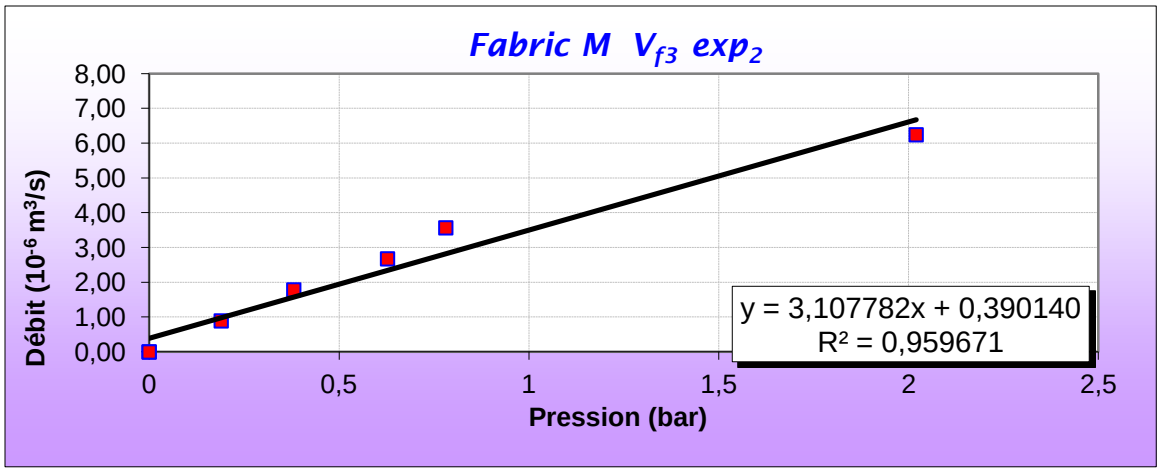

Appendix 2 Figure 37 Through-thickness permeability experiment Fabric M (V_{f3} exp_2).

Bibliography

1. Naik, N., M. Sirisha, and A. Inani, *Permeability characterization of polymer matrix composites by RTM/VARTM.* Progress in aerospace sciences, 2014. **65**: p. 22-40.
2. Shojaei, A., et al., *An experimental study of saturated and unsaturated permeabilities in resin transfer molding based on unidirectional flow measurements.* Journal of reinforced plastics and composites, 2004. **23**(14): p. 1515-1536.
3. Hoes, K., et al., *New set-up for measurement of permeability properties of fibrous reinforcements for RTM.* Composites Part A: applied science and manufacturing, 2002. **33**(7): p. 959-969.
4. Song, Y.-S. and J.-R. Youn, *Asymptotic expansion homogenization of permeability tensor for plain woven fabrics.* Composites Part A: Applied Science and Manufacturing, 2006. **37**(11): p. 2080-2087.
5. Comas-Cardona, S., C. Binetruy, and P. Krawczak, *Unidirectional compression of fibre reinforcements. Part 2: A continuous permeability tensor measurement.* Composites Science and Technology, 2007. **67**(3): p. 638-645.
6. Endruweit, A. and A. Long, *Analysis of compressibility and permeability of selected 3D woven reinforcements.* Journal of composite materials, 2010. **44**(24): p. 2833-2862.
7. Liu, Q., R.S. Parnas, and H.S. Giffard, *New set-up for in-plane permeability measurement.* Composites Part A: Applied Science and Manufacturing, 2007. **38**(3): p. 954-962.
8. Arbter, R., et al., *Experimental determination of the permeability of textiles: a benchmark exercise.* Composites Part A: Applied Science and Manufacturing, 2011. **42**(9): p. 1157-1168.
9. Vernet, N., et al., *Experimental determination of the permeability of engineering textiles: Benchmark II.* Composites Part A: Applied Science and Manufacturing, 2014. **61**: p. 172-184.
10. Hoareau, C., *Injection sur renfort: Etude du remplissage de moule et détermination théorique de la perméabilité des tissus*. 1994.
11. Šimáček, P. and S.G. Advani, *Permeability model for a woven fabric.* Polymer Composites, 1996. **17**(6): p. 887-899.
12. Ngo, N. and K. Tamma, *Microscale permeability predictions of porous fibrous media.* International Journal of Heat and Mass Transfer, 2001. **44**(16): p. 3135-3145.
13. Takano, N., et al., *Microstructure-based evaluation of the influence of woven architecture on permeability by asymptotic homogenization theory.* Composites science and technology, 2002. **62**(10): p. 1347-1356.
14. Fournier, R., *Optimisation et modélisation du procédé RTM*. 2003, École Nationale Supérieure des Mines de Paris.
15. Laine, B., et al. *Permeability of the woven fabrics*. in *Proceedings of the 8th international conference on flow processes in composite materials, Ecole des Mines de Douai, France*. 2006.
16. Loix, F., et al., *Woven fabric permeability: From textile deformation to fluid flow mesoscale simulations.* Composites Science and Technology, 2008. **68**(7): p. 1624-1630.
17. Laine, B., *Influence des déformations d'un renfort fibreux sur sa perméabilité: modélisations et expériences*. 2008, Arts et Métiers ParisTech.
18. Verleye, B., et al., *Permeability of textile reinforcements: Simulation, influence of shear and validation.* Composites Science and Technology, 2008. **68**(13): p. 2804-2810.

19. Spaid, M.A. and F.R. Phelan, *Modeling void formation dynamics in fibrous porous media with the lattice Boltzmann method.* Composites Part A: Applied Science and Manufacturing, 1998. **29**(7): p. 749-755.
20. Martys, N.S. and H. Chen, *Simulation of multicomponent fluids in complex three-dimensional geometries by the lattice Boltzmann method.* Physical review E, 1996. **53**(1): p. 743.
21. Dunkers, J.P., et al. *Permeability Prediction from Non-Destructive Imaging of Composite Microstructure*. in *Proceedings of the 59th Society of Plastics Engineers Annual Conference, Dallas, USA*. 2001.
22. Chen, H., H. Gould, and J. Tobochnik, *Discrete Boltzmann systems and fluid flows.* Computers in Physics, 1993. **7**(6): p. 632-637.
23. Zeng, X., et al., *Geometrical modelling of 3D woven reinforcements for polymer composites: Prediction of fabric permeability and composite mechanical properties.* Composites Part A: Applied Science and Manufacturing, 2014. **56**: p. 150-160.
24. Chen, Z.-R., L. Ye, and M. Lu, *Permeability predictions for woven fabric preforms.* Journal of Composite Materials, 2009.
25. Choi, M.A., et al., *Permeability modeling of fibrous media in composite processing.* Journal of Non-Newtonian Fluid Mechanics, 1998. **79**(2): p. 585-598.
26. Nordlund, M., et al., *Permeability network model for non-crimp fabrics.* Composites Part A: Applied Science and Manufacturing, 2006. **37**(6): p. 826-835.
27. Shou, D., et al., *Transverse permeability determination of dual-scale fibrous materials.* International Journal of Heat and Mass Transfer, 2013. **58**(1): p. 532-539.
28. Vernet, N. and F. Trochu. *Permeability analytical modeling of 3d interlock fabrics*. in *The 19th international conference on composite materials*. 2013.
29. Vernet, N. and F. Trochu, *Analysis of mesoscopic pore size in 3D-interlock fabrics and validation of a predictive permeability model.* Journal of Reinforced Plastics and Composites, 2016. **35**(6): p. 471-486.
30. Yu, B. and L. James Lee, *A simplified in-plane permeability model for textile fabrics.* Polymer Composites, 2000. **21**(5): p. 660-685.
31. Berdichevsky, A.L. and Z. Cai, *Preform permeability predictions by self-consistent method and finite element simulation.* Polymer Composites, 1993. **14**(2): p. 132-143.
32. Cai, Z. and A. Berdichevsky, *An improved self-consistent method for estimating the permeability of a fiber assembly.* Polymer composites, 1993. **14**(4): p. 314-323.
33. Gebart, B., *Permeability of unidirectional reinforcements for RTM.* Journal of composite materials, 1992. **26**(8): p. 1100-1133.
34. Gutowski, T., et al., *Consolidation experiments for laminate composites.* Journal of Composite Materials, 1987. **21**(7): p. 650-669.
35. Happel, J., *Viscous flow relative to arrays of cylinders.* AIChE Journal, 1959. **5**(2): p. 174-177.
36. Kuwabara, S., *The forces experienced by randomly distributed parallel circular cylinders or spheres in a viscous flow at small Reynolds numbers.* Journal of the physical society of Japan, 1959. **14**(4): p. 527-532.
37. Van der Westhuizen, J. and J.P. Du Plessis, *An attempt to quantify fibre bed permeability utilizing the phase average Navier-Stokes equation.* Composites Part A: Applied Science and Manufacturing, 1996. **27**(4): p. 263-269.
38. Bruschke, M. and S. Advani, *Flow of generalized Newtonian fluids across a periodic array of cylinders.* Journal of Rheology (1978-present), 1993. **37**(3): p. 479-498.

39. Drummond, J. and M. Tahir, *Laminar viscous flow through regular arrays of parallel solid cylinders.* International Journal of Multiphase Flow, 1984. **10**(5): p. 515-540.
40. Lee, S. and J. Yang, *Modeling of Darcy-Forchheimer drag for fluid flow across a bank of circular cylinders.* International journal of heat and mass transfer, 1997. **40**(13): p. 3149-3155.
41. Phelan, F.R. and G. Wise, *Analysis of transverse flow in aligned fibrous porous media.* Composites Part A: Applied Science and Manufacturing, 1996. **27**(1): p. 25-34.
42. Sahraoui, M. and M. Kaviany, *Slip and no-slip velocity boundary conditions at interface of porous, plain media.* International Journal of Heat and Mass Transfer, 1992. **35**(4): p. 927-943.
43. Sangani, A. and A. Acrivos, *Slow flow past periodic arrays of cylinders with application to heat transfer.* International journal of Multiphase flow, 1982. **8**(3): p. 193-206.
44. Tamayol, A. and M. Bahrami, *Analytical determination of viscous permeability of fibrous porous media.* International Journal of Heat and Mass Transfer, 2009. **52**(9): p. 2407-2414.
45. Karaki, Mohamad; Hallal, Ali; Younes, Rafic; Trochu, Francois; Lafon, Pascal; Hayek, Amin; Kobeissy, AlHadi; Fayad, Ahmad *A Comparative Analytical, Numerical and Experimental Analysis of the Microscopic Permeability of Fiber Bundles in Composite Materials.* International Journal of Composite Materials, 2017. **7**(3): p. 82-102.
46. Nehme, S., et al., *Numerical/analytical methods to evaluate the mechanical behavior of interlock composites.* Journal of Composite Materials, 2011. **45**(16): p. 1699-1716.
47. Hallal, A., et al., *Improved analytical model to predict the effective elastic properties of 2.5 D interlock woven fabrics composite.* Composite Structures, 2012. **94**(10): p. 3009-3028.
48. Landel, R.F. and L.E. Nielsen, *Mechanical properties of polymers and composites*. 1993: Crc Press.
49. Hallal, A. and R. Younes, *Improvement in failure prediction algorithm for textile composites.* International Journal of Damage Mechanics, 2018. **27**(1): p. 3-31.
50. Jinlian, H., L. Yi, and S. Xueming, *Study on void formation in multi-layer woven fabrics.* Composites Part A: Applied Science and Manufacturing, 2004. **35**(5): p. 595-603.
51. Mayer, C., X. Wang, and M. Neitzel, *Macro-and micro-impregnation phenomena in continuous manufacturing of fabric reinforced thermoplastic composites.* Composites Part A: Applied Science and Manufacturing, 1998. **29**(7): p. 783-793.
52. Shih, C.H. and L.J. Lee, *Analysis of void removal in liquid composite molding using microflow models.* Polymer composites, 2002. **23**(1): p. 120-131.
53. Lundstrom, T., B. Gebart, and C. Lundemo, *Void formation in RTM.* Journal of Reinforced Plastics and Composites, 1993. **12**(12): p. 1339-1349.
54. Sadiq, T., S. Advani, and R. Parnas, *Experimental investigation of transverse flow through aligned cylinders.* International Journal of Multiphase Flow, 1995. **21**(5): p. 755-774.
55. *PAM-RTM*. 2012.
56. S.G.Advani, *LIMS*. 2006.
57. inc., P., *Polyworx*. 2012.
58. Darcy, H., *The Public Fountains of the City of Dijon, Victor Dalmont, Paris, 1856, ch.* Appendix D.
59. Woerdeman, D.L., F.R. Phelan, and R.S. Parnas, *Interpretation of 3-D permeability measurements for RTM modeling.* Polymer Composites, 1995. **16**(6): p. 470-480.
60. Kelly, A.Z., C, *Comprehensive Composite Materials*. 1999.

61. Babadagli, T. and S. Al-Salmi, *A review of permeability-prediction methods for carbonate reservoirs using well-log data.* SPE Reservoir Evaluation & Engineering, 2004. **7**(02): p. 75-88.
62. Lai, J., et al., *A review on pore structure characterization in tight sandstones.* Earth-Science Reviews, 2017.
63. Renard, P. and G. De Marsily, *Calculating equivalent permeability: a review.* Advances in water resources, 1997. **20**(5-6): p. 253-278.
64. Patiño, I., C. Vargas, and J. Vanegas, *Methods for permeability measurements of fibrous reinforced preforms.* Revista Facultad de Ingeniería Universidad de Antioquia, 2014(72): p. 186-2002.
65. Chen, X. and T. Papathanasiou, *Micro-scale modeling of axial flow through unidirectional disordered fiber arrays.* Composites Science and Technology, 2007. **67**(7): p. 1286-1293.
66. Wang, J.F. and W.R. Hwang, *Permeability prediction of fibrous porous media in a bi-periodic domain.* Journal of composite materials, 2008. **42**(9): p. 909-929.
67. Carman, P., *The determination of the specific surface of powders.* J. Soc. Chem. Ind. Trans, 1938. **57**: p. 225.
68. Sullivan, R., *Specific surface measurements on compact bundles of parallel fibers.* Journal of Applied Physics, 1942. **13**(11): p. 725-730.
69. Happel, J. and H. Brenner, *Low Reynolds Number Hydrodynamics: With Special Applications to Particulate Media*. 1973: Noordhoff International Publishing.
70. Tamayol, A. and M. Bahrami, *Transverse permeability of fibrous porous media.* Physical Review E, 2011. **83**(4): p. 046314.
71. Carman, P.C., *Fluid flow through granular beds.* Transactions-Institution of Chemical Engineeres, 1937. **15**: p. 150-166.
72. Shih, C.H. and L.J. Lee, *Effect of fiber architecture on permeability in liquid composite molding.* Polymer Composites, 1998. **19**(5): p. 626-639.
73. Skartsis, L., B. Khomami, and J. Kardos, *Resin flow through fiber beds during composite manufacturing processes. Part II: numerical and experimental studies of Newtonian flow through ideal and actual fiber beds.* Polymer Engineering & Science, 1992. **32**(4): p. 231-239.
74. Yu, B., L.J. Lee, and H. Cao, *A fractal in-plane permeability model for fabrics.* Polymer composites, 2002. **23**(2): p. 201-221.
75. Dong, S., et al., *A new structure-related model to predict the permeability of non-crimp fabric preform.* Journal of Composite Materials, 2013. **47**(24): p. 3053-3063.
76. Adams, K.L., B. Miller, and L. Rebenfeld, *Forced in-plane flow of an epoxy resin in fibrous networks.* Polymer Engineering & Science, 1986. **26**(20): p. 1434-1441.
77. Bahrami, M., M.M. Yovanovich, and J.R. Culham, *A novel solution for pressure drop in singly connected microchannels of arbitrary cross-section.* International Journal of Heat and Mass Transfer, 2007. **50**(13): p. 2492-2502.
78. Nordlund, M. and T.S. Lundstrom, *Numerical study of the local permeability of noncrimp fabrics.* Journal of composite materials, 2005. **39**(10): p. 929-947.
79. Lundström, T., *The permeability of non-crimp stitched fabrics.* Composites part A: applied science and manufacturing, 2000. **31**(12): p. 1345-1353.
80. Papathanasiou, T., *Flow across structured fiber bundles: a dimensionless correlation.* International journal of multiphase flow, 2001. **27**(8): p. 1451-1461.
81. Laine, B., et al. *Permeability of woven fabrics: analytical and numerical predictions*. in *FPCM-10, 10th International Conference on Flow Processes in Composite Materials*. 2010.

82. *Analysis of Compressibility and Permeability of Selected 3D Woven Reinforcements.* Journal of Composite Materials, 2010. **44**(24).
83. *Transverse permeability measurement of a circular braided perform in liquid composite molding.* Korea-Australia Rheology Journal, 2007. **19**(1): p. 17-25.
84. Chae, H.S., Y.S. Song, and J.R. Youn, *Transverse permeability measurement of a circular braided preform in liquid composite molding.* Korea-Australia Rheology Journal, 2007. **19**(1): p. 17-25.
85. Trevino, L., et al., *Analysis of resin injection molding in molds with preplaced fiber mats. I: Permeability and compressibility measurements.* Polymer Composites, 1991. **12**(1): p. 20-29.
86. Weitzenböck, J., R. Shenoi, and P. Wilson, *Measurement of three-dimensional permeability.* Composites Part A: Applied Science and Manufacturing, 1998. **29**(1): p. 159-169.
87. Wu, X., J. Li, and R. Shenoi, *A new method to determine fiber transverse permeability.* Journal of composite materials, 2007. **41**(6): p. 747-756.
88. Nedanov, P.B. and S.G. Advani, *Numerical computation of the fiber preform permeability tensor by the homogenization method.* Polymer composites, 2002. **23**(5): p. 758-770.
89. Nedanov, P.B., et al., *Determination of the permeability tensor of fibrous reinforcements for VARTM.* Advances in aerospace materials and structures, 1999: p. 79-88.
90. Elbouazzaoui, O., S. Drapier, and P. Henrat, *An experimental assessment of the saturated transverse permeability of non-crimped new concept (NC2) multiaxial fabrics.* Journal of Composite Materials, 2005. **39**(13): p. 1169-1193.
91. Drapier, S., et al., *Influence of the stitching density on the transverse permeability of non-crimped new concept (NC2) multiaxial reinforcements: measurements and predictions.* Composites Science and Technology, 2002. **62**(15): p. 1979-1991.
92. Ouagne, P. and J. Bréard, *Continuous transverse permeability of fibrous media.* Composites Part A: Applied Science and Manufacturing, 2010. **41**(1): p. 22-28.
93. Scholz, S., J.W. Gillespie, and D. Heider, *Measurement of transverse permeability using gaseous and liquid flow.* Composites Part A: Applied Science and Manufacturing, 2007. **38**(9): p. 2034-2040.
94. Sangani, A.S.a.Y., C., *Transport processes in random arrays of cylinders: II-viscous flow.* American Institute of Physics, 1988. **31**(9): p. 2435-2444.
95. Skartsis, L. and J. Kardos. *The Newtonian permeability and consolidation of oriented carbon fiber beds*. in *Proceedings of the American Society for Composites. Fifth Technical Conference: Composite Materials in Transition*. 1990.
96. Kirsch, A. and N. Fuchs, *Studies on fibrous aerosol filters—II. Pressure drops in systems of parallel cylinders.* Annals of Occupational Hygiene, 1967. **10**(1): p. 23-30.
97. Chmielewski, C. and K. Jayaraman, *The effect of polymer extensibility on crossflow of polymer solutions through cylinder arrays.* Journal of Rheology (1978-present), 1992. **36**(6): p. 1105-1126.
98. Coulaud, O., P. Morel, and J. Caltagirone, *Numerical modelling of nonlinear effects in laminar flow through a porous medium.* Journal of Fluid Mechanics, 1988. **190**: p. 393-407.
99. Dave, R., J. Kardos, and M. Duduković, *A model for resin flow during composite processing part 2: numerical analysis for unidirectional graphite/epoxy laminates.* Polymer Composites, 1987. **8**(2): p. 123-132.
100. Zhong, W.H., I. Currie, and D. James, *Creeping flow through a model fibrous porous medium.* Experiments in fluids, 2006. **40**(1): p. 119-126.

101. Amico, S. and C. Lekakou, *Mathematical modelling of capillary micro-flow through woven fabrics.* Composites Part A: Applied Science and Manufacturing, 2000. **31**(12): p. 1331-1344.
102. Chan Wei, L.Z.h., Tan Hong Mu, *Laminar flow, turbulent flow and Reynolds number.*
103. Tselishchev, Y.G. and V. Val'tsifer, *Influence of the type of contact between particles joined by a liquid bridge on the capillary cohesive forces.* Colloid journal, 2003. **65**(3): p. 385-389.
104. Butt, H.-J. and M. Kappl, *Normal capillary forces.* Advances in colloid and interface science, 2009. **146**(1): p. 48-60.
105. Ferland, P., D. Guittard, and F. Trochu, *Concurrent methods for permeability measurement in resin transfer molding.* Polymer composites, 1996. **17**(1): p. 149-158.
106. Ansar, M., W. Xinwei, and Z. Chouwei, *Modeling strategies of 3D woven composites: a review.* Composite structures, 2011. **93**(8): p. 1947-1963.
107. Gutowski, T.G., et al., *Consolidation experiments for laminate composites.* Journal of Composite Materials, 1987. **21**(7): p. 650-669.
108. Zeng, X., et al., *Numerical prediction of in-plane permeability for multilayer woven fabrics with manufacture-induced deformation.* Composites Part A: Applied Science and Manufacturing, 2015. **77**: p. 266-274.
109. Smith, D., *Resin Transfer Moulding (RTM)- Advanced techniques of light resin transfer molding.*, P. University, Editor. 2008.
110. Sparrow, E. and A. Loeffler, *Longitudinal laminar flow between cylinders arranged in regular array.* AIChE Journal, 1959. **5**(3): p. 325-330.
111. Sobera, M. and C. Kleijn, *Hydraulic permeability of ordered and disordered single-layer arrays of cylinders.* Physical Review E, 2006. **74**(3): p. 036301.
112. *TexGen*. 2017; Available from: http://texgen.sourceforge.net.
113. Karaki, M., et al., *In-Plane Permeability Prediction Model for Non-Crimp and 3D Orthogonal Fabrics*. 2017: JOTI.
114. Versteeg, H.K. and W. Malalasekera, *An introduction to computational fluid dynamics: the finite volume method*. 2007: Pearson Education.
115. Kuzmin, D., *Introduction to computational fluid dynamics.* University of Dortmund, Dortmund, 2014.
116. Amico, S. and C. Lekakou, *An experimental study of the permeability and capillary pressure in resin-transfer moulding.* Composites Science and Technology, 2001. **61**(13): p. 1945-1959.
117. Rossell, S.M., *Fluid Fow Modeling Of Resin Transfer Molding For Composite Material Wind Turbine Blade Structures.*